

PhD Thesis

**UNDERSTANDING
SIZE-RESOLVED
DUST EMISSION
FROM FIELD
MEASUREMENTS
IN MOROCCO**

Cristina González Flórez

Understanding size-resolved dust emission from field measurements in Morocco

Memoria presentada para optar al grado de doctor
por la Universitat Politècnica de Catalunya.

Programa de doctorado en Ingeniería Ambiental

Departamento de Ingeniería Civil y Ambiental

Autora: Cristina González Flórez

Directores: Carlos Pérez García-Pando
Martina Klose

Tutora: María Gonçalves Ageitos



UNIVERSITAT POLITÈCNICA
DE CATALUNYA
BARCELONATECH

Understanding size-resolved dust emission from field measurements in Morocco.

PhD Thesis

Barcelona, 2023

Author: Cristina González Flórez

Copyright: Reproduction of this publication in whole or in part must include the customary bibliographic citation, including author attribution, thesis title, etc.

Cover photos: Konrad Kandler. Morocco, 2019.

The research leading to this PhD thesis has been carried out at the Earth Sciences department of the **Barcelona Supercomputing Center-Centro Nacional de Supercomputación (BSC-CNS)**.



The author acknowledges funding support from Agència de Gestió d'Ajuts Universitaris i de Recerca (AGAUR) **Ayudas destinadas a universidades, centros de investigación y fundaciones hospitalarias para la contratación de personal investigador novel (FI)** grant 2020-FI-B 00678. She also acknowledges funding support from the European Research Council under the Horizon 2020 research and innovation programme through the ERC Consolidator Grant FRAGMENT (grant agreement No. 773051) and from the AXA Research Fund (grant no. AXA Chair on Sand and Dust Storms).

*A mis queridos abuelos,
Candelas, Eutiquio, Cristina y Amador,
ejemplos inspiradores de trabajo y esfuerzo,
y amantes incondicionales de su querida tierra leonesa.*

Acknowledgements

Cuando decidí embarcarme en esta tesis, hace ya casi cinco años, el mundo del “dust” me era completamente desconocido y no iba más allá de la imagen que tenía sobre las tormentas de polvo en los desiertos y las lluvias de barro. A pesar de mi formación en física y más específicamente en meteorología, no era consciente de la multitud de procesos físicos involucrados en esta área de investigación y de la magnitud de sus impactos. Quizás, fue el desafío de entender la física detrás de la emisión de polvo o mi espíritu aventurero y curioso, probablemente una combinación de ambos, lo que me ha motivado a llegar hasta aquí. El camino, no nos vamos a engañar, ha sido duro y lleno de obstáculos, en el que he tenido la suerte de contar con muchas personas que me han ayudado y que de una manera u otra han contribuido a mi crecimiento personal y profesional. Por este motivo, quiero utilizar estas páginas para agradecerse a todos ellos.

Me gustaría empezar dando las gracias a mis directores de tesis, quienes me han enseñado todo lo que se sabe sobre el dust y con quienes he compartido muchos momentos durante las campañas de medidas. Carlos, gracias por encontrar siempre tiempo para mí en tus apretados calendarios, por estar siempre dispuesto a escuchar y ayudar en todo lo que estaba a tu alcance, y por brindarme oportunidades de crecimiento profesional. Tu pasión por este trabajo, tu curiosidad incansable, tu alto nivel de exigencia y tu calidad humana son sin duda un referente para mí. Martina, ich möchte dir dafür danken, dass du mir den Anfang meiner Promotion mit deinen Ratschlägen sowie durch die Weitergabe einiger deiner Skripte, Bücher und Notizen deutlich erleichtert hast. Deine Unterstützung bei der Lösung von Programmier- und LaTeX-Fehlern sowie bei der Überprüfung mühsamer Gleichungsentwicklungen war entscheidend für ein erfolgreiches Durchführen meiner Arbeit. Obwohl dein Abschied vom BSC deutlich spürbar war, erfüllt es mich mit Freude zu sehen, wie sehr du dich weiterentwickelt hast und wie weit du gekommen bist. Du wurdest (für mich und andere Frauen) zu einem weiblichen Vorbild in der Welt der Wissenschaft. Mi más sincera gratitud a ambos por vuestro constante apoyo, guía y dedicación a lo largo

Acknowledgements

de este camino, fundamentales para mi crecimiento como investigadora.

También quiero agradecer a mi tutora María por haber sido el mejor nexo con la UPC, siempre disponible a ayudarme con toda la burocracia y facilitarme las cosas con los trámites de la universidad.

Without any doubt, the dust field campaigns in which I have participated during my PhD have become some of the most intense experiences I have ever had in my life. I would like to express my gratitude to all the incredible colleagues, local people and technicians I had the privilege to work with before and during these campaigns, whether it was enduring over 40°C under the Saharan sun or facing the formidable force of nature in Iceland that ripped our tents out and flooded our measurement site. Thanks to each of you for creating a positive and joyful atmosphere filled with laughter, which made even the most challenging times more bearable.

Quiero dar las gracias también a toda la gente del IDAEA-CSIC, donde dediqué una considerable cantidad de tiempo realizando pruebas y preparando los instrumentos para las campañas. Especial mención a Xavi y a Andrés Alastuey, ha sido un privilegio poder aprender tanto de vosotros. Gracias también a Cristina Reche por ayudarme a corregir y sincronizar los datos de los Fidas y estar siempre dispuesta a echarme una mano. Gracias a Andrés Carrillo y Agnès por todo vuestro apoyo con los aspectos más técnicos de los Fidas.

En una nota más personal, me gustaría dar las gracias a Adolfo, siempre dispuesto a ayudar montando y desmontando los Fidas y los instrumentos meteorológicos conmigo, analizando los datos de las PSDs del suelo y sobre todo por tus risas y buen humor en los momentos más complicados de las campañas y del doctorado. Agnesh, thanks for bringing serenity and calm to the group and all the good times we have lived together. Jesús, gracias por llegar a Marruecos a recargarnos las pilas cuando ya las teníamos agotadas y nos queríamos volver, y por tus enseñanzas sobre las propiedades ópticas del dust. But above all, thank you to the three of you for your friendship.

I would like to express my gratitude to all the external collaborators, and I want to extend special thanks to Sylvain Dupont and Konrad Kandler for reviewing this thesis and providing me with valuable input and support. Also, thanks to Jasper Kok

Acknowledgements

and Yaping Shao, it was an honour for me that you revised the paper on which this thesis is based. Your thoughtful and constructive comments, though challenging to address, undoubtedly played a significant role in enhancing the quality of the paper and, consequently, this thesis.

Quiero dar las gracias también a todos los compañeros y compañeras del BSC, que de alguna manera u otra han contribuido a que esta tesis vea la luz. A Luciana y a todo el grupo de travels por toda la gestión durante las campañas de medidas. A Katia y a Judit por vuestra ayuda en las tareas administrativas y la gestión de mi beca FI. A Carles, per introduir-me al món de Linux i de PyCharm quan vaig arribar. A Francesco, per avermi aiutato con gli script per generare i file NetCDF. A Albert Vila, siempre supereficiente solucionando mis problemas técnicos con los portátiles y teniéndolos siempre a punto para las campañas. A Jerónimo, por llevar a cabo la transformación de diámetros ópticos a diámetros geométricos con la colaboración de Yue Huang. Muchas gracias al grupo de Atmospheric Composition, que siempre se ha interesado por la evolución de esta tesis, y a muchas otras personas dentro del departamento de Earth Sciences que han seguido emocionados mis aventuras en Marruecos e Islandia: Saskia, Miriam, Aude, Stella, Froila, Verónica Torralba, Enza, Sara, Elina, Vanessa, An-Chi, Victoria, Núria, Marios, Santi, Angie, Jan, Gert, Albert Martínez, Aleks, Ferran, Álvaro, Pep, Lluís, Eneko, Manu, Jaime. Gracias también a Rubén Sousse y a Roger por compartir conmigo nuestra primera EGU en Viena. Con vosotros, Héctor, Kevin, Alba y Andrea he podido compartir especialmente en este último año preocupaciones y alegrías relacionadas con el doctorado. Gracias a Verónica Martín, Paloma y Raquel por vuestro apoyo en los momentos difíciles, sabios consejos y merendolas brasileñas.

Muchas gracias a los PhD students que estaban cuando llegué al BSC o se incorporaron al poco tiempo: Bianca, Rubén Cruz, Bala, Dani, Jaume, Elisa y Carlos. Me he sentido muy acogida, gracias por tantos buenos momentos y excursiones. Especial gratitud a mis antiguos compis de piso: Jaume y Carlos. Después de pasar toda la cuarentena juntos ya sois para mi como hermanos. Merci à Anaëlle pour les mois que nous avons passés ensemble and thanks to Sube for fueling my desire to travel to India after completing this thesis. Tampoco me olvido de mis amigos de la uni a quienes les tengo tanto cariño: Coral, Adri, Pablo, Alberto, Natalia, Adrián, Carlos, Laura y Jorge, ni de mi amiga de infancia Bea, ni de mis amigos del año de

Acknowledgements

Erasmus Andrea y Alex. Gracias a todos por estar siempre tan cerca a pesar de la distancia, compartiendo todas mis alegrías y mis penas.

Quiero dar las gracias a los profesores que tuve antes de ir a la universidad, especialmente a Daniel. No solo por tu dedicación y por hacer que las matemáticas resultaran apasionantes, sino por creer en mí desde el principio y despertar en mí la curiosidad por explorar el mundo científico. Mi más sincero agradecimiento también a todos los profesores del Máster en Meteorología y Geofísica de la UCM, por transmitirme vuestros conocimientos y la pasión por la meteorología. Quiero hacer una mención especial a Luis, Belén, Encarna, Carlos Yagüe y Carlos Ordóñez, claves para que decidiera embarcarme en esta aventura del doctorado.

Además de todas estas personas, esta tesis no hubiera sido posible sin el apoyo de mi familia. Gracias a mis padres y a mi hermana por el cariño y el apoyo incondicional que me habéis brindado desde siempre. Aunque el camino no ha sido siempre fácil, vosotros siempre habéis estado ahí animándome a perseguir mis sueños, pero también consolándome cuando las cosas no iban bien. Soy consciente de los sacrificios que muchas veces habéis tenido que hacer por mí y estoy enormemente agradecida por ello. Moltes gràcies a Anna i a Ximo per acollir-me a la vostra família i per celebrar els meus èxits com si foren vostres.

I per últim, vull expressar el meu sincer agraïment a Joaquim, el meu gran company de vida. No trobe paraules suficients per agraïr-te tot el suport, comprensió i paciència infinita que has tingut amb mi. Gràcies per estar al meu costat en cada pas del camí, per compartir les alegries i les dificultats. També gràcies per les hores dedicades al disseny d'esta tesi i les constants correccions a les figures.

Contents

Summary	xv
Resumen	xix
Resum	xxiii
Publications	xxvii
List of Figures	xxxii
List of Tables	xl
List of Symbols	xli
Acronyms	xlvi

I Introduction

1 A general overview of atmospheric mineral dust	1
1.1 The atmospheric mineral dust cycle	1
1.2 Impacts on society	7
1.3 Impacts on climate	8
1.3.1 Interaction with radiation	8
1.3.2 Interaction with clouds	10
1.3.3 Interaction with atmospheric chemistry	11
1.3.4 Interaction with biogeochemistry	12
1.3.5 Interaction with cryosphere	13
1.3.6 Dust radiative forcing	14
1.4 Key dust microphysical properties	15
1.4.1 Mineralogical composition	15
1.4.2 Shape	17
1.4.3 Size	18
2 Physics of dust emission	21
2.1 Basic physical concepts	21

Contents

2.1.1	Soil particle size distribution	21
2.1.2	Wind friction velocity, u_*	22
2.1.3	Logarithmic wind profile and roughness length, z_0	24
2.1.4	Threshold friction velocity, u_{*th}	25
2.1.5	Horizontal or saltation flux, Q	27
2.1.6	Vertical or emitted dust flux, F_{emi}	27
2.2	Mechanisms of dust emission	28
2.2.1	Aerodynamic entrainment	28
2.2.2	Saltation bombardment or sandblasting	28
2.2.3	Aggregate disintegration or auto-abrasion	29
2.3	Theoretical frameworks to estimate dust emission and its PSD	30
2.4	The dust particle size distribution and its variability at emission	33
3	Objectives and structure	41
3.1	Main objectives	41
3.2	Thesis structure	41
4	Context and scope	43
4.1	Objectives of FRAGMENT	43
4.2	Locations of FRAGMENT field campaigns	45
4.3	My role in the field campaigns	47
II Data and methods		
5	The FRAGMENT dust field campaign in the Moroccan Sahara	53
5.1	Climatological analysis before the campaign	53
5.2	Experimental site	57
5.3	Measurements	60
5.3.1	Meteorological parameters	60
5.3.2	Size-resolved dust concentrations	61
5.3.3	Size-resolved saltation counts	66
5.3.4	Computation of dynamical parameters characterizing the near-surface boundary layer	66

5.3.5	Computation of size-resolved flux gradient diffusive dust flux and its uncertainty	68
5.3.6	Computation of sandblasting efficiency	73
5.4	Estimating the size-resolved dry deposition and emitted fluxes based on different parameterizations	74
III Results and discussion		
6	Overview of the atmospheric conditions and dust events during the campaign	83
7	Characterization of saltation and sandblasting efficiency	91
8	Variability of the dust PSD at emission	101
8.1	Identification and removal of the anthropogenic aerosol influence . . .	102
8.2	Differences between concentration and diffusive flux PSDs and their dependencies upon u_* and wind direction	107
8.3	PSD differences between regular and haboob events	112
9	What explains the observed PSD variations? Potential roles of dry deposition and fetch length, aggregate disintegration, and haboob gust front	113
10	Evaluation of the estimated dry deposition and emitted fluxes	119
11	Comparison with Brittle Fragmentation Theory	129
IV Conclusions and future perspectives		
12	Conclusions and future perspectives	137
12.1	Conclusions	137
12.2	Future work	140
V Appendices		

Contents

A	Analysis of correction for heavy particles	147
B	Friction velocity from the Eddy Covariance method	149
C	Additional figures related to the diffusive flux PSDs	151
D	Additional figures related to the dry deposition fluxes	157
E	Additional figures related to the estimated emitted flux PSDs	161
F	Additional figures related to the ratio of dry deposition flux to the estimated emitted flux	167
	References	170

Summary

Atmospheric mineral dust, primarily emitted by wind erosion from arid and semi-arid regions, is composed of a variety of mineral particles exhibiting distinct composition, shape, and size. The wide range of diameters exhibited by dust particles, spanning more than three orders of magnitude, partly determines their effects within the Earth System. Dust perturbs climate by absorbing and scattering both shortwave and longwave radiation. It also influences the distribution and lifetime of clouds and precipitation by acting as cloud condensation nuclei and ice nucleating particles. Once deposited to the surface, dust fertilizes ocean and land ecosystems and can alter snow albedo. Furthermore, dust has implications for agriculture, transportation and infrastructure, and its inhalation poses risks to human health.

This PhD thesis focuses on dust emission, and especially on the emitted dust particle size distribution (PSD) and its variability. The thesis has been conducted within the context of the ERC project “FRontiers in dust minerAloGical coMposition and its Effects upoN climaTe” (FRAGMENT), which aims to understand and constrain the global mineralogical composition of dust along with its effects upon climate. Dust is generated through saltation bombardment and aggregate disintegration, and less effectively by aerodynamic entrainment. Constraining its PSD at emission is crucial as it strongly affects the impacts, lifetime and global distribution of dust. Despite the extensive research performed on this topic over the last years, there are still substantial gaps in our fundamental and quantitative understanding of the emitted dust PSD, including its potential variability, its underlying causes and the fraction of dust with diameter $> 10 \mu\text{m}$.

This thesis provides new insights into the emitted dust PSD and its variability based on meteorological, saltation and size-resolved dust concentration measurements performed during the FRAGMENT dust field campaign that took place in Morocco in 2019. In particular, the measurements were performed in an ephemeral lake located in the Lower Drâa Valley of Morocco surrounded by small sand dune fields. Saltation and dust emission occurred regularly at this location, but in comparison to some

previous studies in other locations sandblasting efficiency was lower. This is probably related to the paved sediment that constituted the surface. During the campaign two types of dust events were identified: regular events and haboobs. Regular events are linked to the daily cycles of surface winds that are associated to solar heating. Haboob refers to a type of intense dust storm that occurs when downdrafts from a convective storm touch the ground, creating a front of dust and sand in its path.

A thorough analysis of the number and mass PSDs of both the concentration and diffusive flux has been conducted, identifying statistically significant dependencies of these PSDs upon friction velocity (u_*), wind direction, and type of event (regular versus haboob). One of the most noteworthy features within the observed variability of the PSD, which has caused more debate in the literature, is a shift towards finer diffusive flux PSD with increasing u_* . In this thesis, this feature has been attributed to a large extent to the effect of dry deposition, which is modulated by the wind-direction-dependent fetch length, and u_* , although an enhanced fragmentation of aggregates with u_* could still play a complementary yet arguably smaller role.

Using a resistance model constrained with field observations to estimate the dry deposition flux, and thereby also the emitted dust flux, it has been shown that the deposition flux could represent up to $\sim 90\%$ of the emitted dust flux with diameters $> 10\ \mu\text{m}$ and up to $\sim 65\%$ of the emitted flux of particles as small as $\sim 5\ \mu\text{m}$ in diameter. These results imply that the emitted dust PSD is coarser and its variability is smaller than that of the diffusive flux PSD. As far as I know, this is the first time that the effect of dry deposition upon the diffusive flux is identified and quantified experimentally, supporting recent results based on numerical modelling. It is worth noting that the influence of dry deposition can invalidate the typical assumption that the diffusive flux PSD is equivalent to the emitted dust PSD, particularly when including the particles with diameters $> 10\ \mu\text{m}$, and has consequences on the evaluation of dust emission schemes and their implementation in dust transport models.

Another noteworthy feature within the observed variability of the PSD is the difference in the PSDs associated to haboob events in comparison with regular events. During the haboobs there is a lower proportion of sub-micrometre particles for equivalent or higher u_* intervals, and more dry deposition and variability in the dust

mass fractions with diameters $> 3 \mu\text{m}$. The mechanisms proposed to explain this variability include a smaller and variable effective fetch during the haboob events, and/or an increased resistance of soil aggregates to fragmentation associated with the observed increase in relative humidity along the haboob outflow.

Finally, compared to the invariant emitted dust flux PSD predicted by Brittle Fragmentation Theory (BFT), our dust flux shows a substantially higher proportion of super-micrometre particles. Overall, these results highlight the need to adequately consider dry deposition when estimating the emitted PSD from concentration measurements, even in studies limited to size ranges $< 10 \mu\text{m}$.

Resumen

El polvo mineral atmosférico, emitido principalmente por la erosión del viento en regiones áridas y semiáridas, está compuesto por una variedad de partículas minerales que tienen una composición, forma y tamaño distintos. El amplio rango de diámetros de las partículas de polvo, que abarca más de tres órdenes de magnitud, determina en parte sus efectos dentro del Sistema Tierra. El polvo perturba el clima al absorber y dispersar la radiación de onda corta y larga. Además, influye en la distribución y tiempo de vida de las nubes y la precipitación, ya que puede actuar como núcleo de condensación de nubes líquidas y de hielo. Una vez depositado en la superficie, el polvo fertiliza los ecosistemas oceánicos y terrestres, y puede alterar el albedo de la nieve. Por otro lado, el polvo tiene implicaciones para la agricultura, el transporte y la infraestructura, y su inhalación representa riesgos para la salud humana.

Esta tesis doctoral se centra en la emisión de polvo, particularmente en la distribución de tamaños de las partículas de polvo emitidas (“PSD”, del inglés Particle Size Distribution) y la variabilidad de dicha distribución. Esta tesis se ha llevado a cabo en el contexto del proyecto ERC “FRontiers in dust minerAloGical coMposition and its Effects upoN climaTe” (FRAGMENT), que tiene como objetivo una mejor comprensión de la composición mineralógica global del polvo, así como de los efectos del polvo en el clima. El polvo se genera a través del bombardeo por saltación, la desintegración de agregados, y de manera menos efectiva mediante el arrastre aerodinámico (suspensión de partículas). Determinar la PSD del polvo en emisión es crucial, ya que afecta en gran medida a sus impactos, tiempo de vida y distribución global. A pesar de la extensa investigación realizada sobre este tema en los últimos años, todavía existen lagunas sustanciales en nuestra comprensión fundamental y cuantitativa de la PSD del polvo emitido, incluyendo su posible variabilidad, las causas subyacentes a dicha variabilidad y la fracción de polvo con diámetro $>10\ \mu\text{m}$.

Esta tesis proporciona nuevas perspectivas sobre la PSD del polvo emitido y su variabilidad basándose en las observaciones meteorológicas y las medidas de

concentración de polvo y de saltación en diferentes rangos de tamaño realizadas durante una campaña de medidas que tuvo lugar en Marruecos en 2019 dentro del proyecto FRAGMENT. En particular, las mediciones se realizaron en un lago efímero ubicado en la zona baja del valle del Drâa en Marruecos, rodeado de campos de dunas de arena pequeños. La saltación y la emisión de polvo fueron muy frecuentes en el lago efímero, pero en comparación con estudios previos en otras zonas, la eficiencia de saltación fue menor. Esto se debe probablemente al sedimento compactado que cubría la superficie. Durante la campaña se identificaron dos tipos de eventos de polvo: eventos regulares y haboobs. Los eventos regulares están asociados al ciclo diario del viento superficial, que está relacionado con el calentamiento solar. Los haboobs designan a un tipo de tormenta de polvo intensa que se origina cuando las corrientes descendentes de aire en una tormenta convectiva tocan el suelo creando a su paso una especie de frente de polvo y arena.

Se ha realizado un análisis exhaustivo de las PSDs en número y en masa tanto para la concentración como para el flujo difusivo, identificando dependencias estadísticamente significativas con la velocidad de fricción (u_*), la dirección del viento, y el tipo de evento (regular versus haboob). Una de las características más destacadas dentro de la variabilidad observada en las PSDs, que ha generado más debate en la literatura, es un desplazamiento hacia PSDs más finas en el flujo difusivo a medida que aumenta la u_* . En esta tesis, esta característica se ha atribuido en gran medida al efecto de la deposición seca, que está modulada por la u_* y la extensión de la fuente de polvo (“fetch” en inglés), ésta última dependiente de la dirección del viento. Sin embargo, una mayor fragmentación de agregados a medida que aumenta la u_* podría también desempeñar un papel complementario, aunque probablemente de menor importancia.

Se ha utilizado un modelo de deposición basado en resistencias calibrado con observaciones de campo para estimar el flujo de deposición seca y, a partir de él se ha estimado también el flujo de polvo emitido. Se ha demostrado que se puede depositar aproximadamente hasta el 90% de las partículas emitidas con diámetros $>10\ \mu\text{m}$ y hasta aproximadamente el 65% de las partículas emitidas con diámetros alrededor de $\sim 5\ \mu\text{m}$. Estos resultados implican que la PSD del polvo emitido es más gruesa y menos variable que la PSD del flujo difusivo. Ésta es la primera vez que se identifica y cuantifica experimentalmente el efecto de la deposición seca en el flujo difusivo,

respaldando resultados recientes obtenidos con modelización numérica. Cabe destacar que la influencia de la deposición seca puede invalidar la típica suposición de que la PSD del flujo difusivo es equivalente a la PSD del polvo emitido, especialmente al incluir las partículas con diámetro $>10\ \mu\text{m}$, y tiene consecuencias en la evaluación de los esquemas de emisión de polvo y su implementación en los modelos de transporte de polvo.

Otra característica destacable sobre la variabilidad de la PSD son las diferencias de ésta entre los eventos de haboob y los eventos regulares. Durante los haboobs hay una menor proporción de partículas submicrónicas para intervalos de u_* equivalentes o mayores, y una mayor deposición seca y variabilidad en las fracciones de masa de polvo con diámetros $> 3\ \mu\text{m}$. Los mecanismos propuestos para explicar esta variabilidad incluyen un “fetch” efectivo más pequeño y variable durante los eventos de haboob, y/o una mayor resistencia de los agregados del suelo a la fragmentación, que está asociada al aumento observado en la humedad relativa a lo largo del flujo de salida (“outflow”) del haboob.

Finalmente, en comparación con la PSD del flujo de polvo que propone la teoría de fragmentación de materiales frágiles (“BFT”, del inglés Brittle Fragmentation Theory), se observa una proporción sustancialmente mayor de partículas supermicrónicas en el flujo de polvo obtenido en este trabajo. En general, estos resultados sugieren que la deposición seca debe ser considerada adecuadamente cuando se estima la PSD emitida a partir de las medidas de concentración de partículas, incluso en estudios limitados a rangos de tamaño $< 10\ \mu\text{m}$.

Resum

La pols mineral atmosfèrica, principalment emesa per l'erosió del vent en regions àrides i semiàrides, està composta per una varietat de partícules minerals que tenen una composició, forma i mida diferents. L'àmplia gamma de diàmetres de les partícules de pols, que abasta més de tres ordres de magnitud, determina en part els seus efectes dins del Sistema Terra. La pols pertorba el clima a l'absorbir i dispersar la radiació d'ona curta i llarga. A més, influeix en la distribució i temps de vida dels núvols i la precipitació, ja que pot actuar com a nucli de condensació de núvols líquids i de gel. Una vegada dipositada a la superfície, la pols fertilitza els ecosistemes oceànics i terrestres i pot alterar l'albedo de la neu. Per altra banda, la pols té implicacions per a l'agricultura, el transport i la infraestructura, i la seva inhalació comporta riscos per a la salut humana.

Aquesta tesi doctoral es centra en l'emissió de pols i, més concretament, en la distribució de tamany de les partícules de pols emeses ("PSD", de l'anglès Particle Size Distribution) i la seva variabilitat. Aquesta tesi s'ha realitzat en el context del projecte ERC "FRontiers in dust minerAloGical coMposition and its Effects upon climaTe" (FRAGMENT), que té com a objectiu millorar la comprensió de la composició mineralògica global de la pols, així com dels efectes de la pols en el clima. La pols es genera a través del bombardeig per saltació, la desintegració d'agregats i, de manera menys efectiva, mitjançant l'arrossegament aerodinàmic (suspensió de partícules). Determinar la PSD de la pols en emissió és crucial, ja que afecta de manera significativa els seus impactes, temps de vida i distribució global. Malgrat la extensa investigació realitzada sobre aquest tema en els últims anys, encara existeixen mancances substancials en la nostra comprensió fonamental i quantitativa de la PSD de la pols emesa, incloent-hi la seva possible variabilitat, les causes subjacents d'aquesta variabilitat i la fracció de pols amb diàmetre $> 10 \mu\text{m}$.

Aquesta tesi proporciona noves perspectives sobre la PSD de la pols emesa i la seva variabilitat basant-se en observacions meteorològiques i mesures de concentració de pols i de saltació resoltes per tamany realitzades durant una campanya de mesures

que va tenir lloc a Marroc el 2019 dins del projecte FRAGMENT. En particular, les mesures es van realitzar en un llac efímer situat a la zona baixa de la vall del Drâa a Marroc, envoltada de camps de dunes de sorra petites. La saltació i l'emissió de pols van ser molt freqüents en el llac efímer, però en comparació amb estudis previs en altres zones, l'eficiència de saltació va ser menor. Això es deu probablement al sediment compactat que cobria la superfície. Durant la campanya es van identificar dos tipus d'esdeveniments de pols: esdeveniments regulars i haboobs. Els esdeveniments regulars estan associats al cicle diari del vent superficial, que està relacionat amb l'escalfament solar. Els haboobs fan referència a un tipus d'ensorrament de pols intens que es produeix quan les corrents descendents d'aire en una tempesta convectiva toquen el sòl creant, al seu pas, una mena de front de pols i sorra.

S'ha realitzat una anàlisi exhaustiva de les PSDs en nombre i en massa tant per a la concentració com per al flux difusiu, identificant dependències estadísticament significatives en funció de la velocitat de fricció (u_*), la direcció del vent, i el tipus d'esdeveniment (regular o haboob). Una de les característiques més destacades dins de la variabilitat observada en les PSDs, que ha generat més debat en la literatura, és el desplaçament cap a PSDs més fines en el flux difusiu a mesura que augmenta la u_* . En aquesta tesi, aquesta característica s'ha atribuït en gran mesura a l'efecte de la deposició seca, que està modulada per la u_* i l'extensió de la font ("fetch" en anglès), aquesta última dependent de la direcció del vent. No obstant això, una major fragmentació d'agregats a mesura que augmenta la u_* podria també jugar un paper complementari, encara que probablement de menor importància.

S'ha utilitzat un model de resistències calibrat amb observacions de camp per estimar el flux de deposició seca i, a partir d'aquest, s'ha estimat també el flux de pols emesa. S'ha demostrat que es pot depositar aproximadament el 90% de les partícules emeses amb diàmetres $> 10 \mu\text{m}$ i fins a aproximadament el 65% de l'emissió de partícules amb diàmetres al voltant de $\sim 5 \mu\text{m}$. Aquests resultats impliquen que la PSD de la pols emesa és més gruixuda i menys variable que la PSD del flux difusiu. Aquesta és la primera vegada que s'identifica i quantifica experimentalment l'efecte de la deposició seca en els fluxos difusius, recolzant resultats recents obtinguts amb modelització numèrica. Cal destacar que la influència de la deposició seca pot invalidar la típica suposició que la PSD del flux difusiu és equivalent a la PSD de la pols emesa, especialment a l'incloure les partícules amb diàmetre $> 10 \mu\text{m}$, i té

conseqüències en l'avaluació dels esquemes d'emissió de pols i la seva implementació en els models de transport de pols.

Una altra característica destacable sobre la variabilitat de la PSD són les diferències de PSD entre els esdeveniments de haboob i els esdeveniments regulars. Durant els haboobs hi ha una menor proporció de partícules submicròniques per a intervals de u_* equivalents o majors, i una major deposició seca i variabilitat en les fraccions de massa de pols amb diàmetres $> 3 \mu\text{m}$. Els mecanismes proposats per explicar aquesta variabilitat inclouen un “fetch” efectiu més petit i variable durant els esdeveniments de haboob, i/o una major resistència dels agregats del sòl a la fragmentació, que està associada a l'augment observat en la humitat relativa al llarg del flux de sortida (“outflow” en anglès) del haboob.

Finalment, en comparació amb la PSD del flux de pols emès que proposa la teoria de fragmentació de materials fràgils (“BFT”, de l'anglès Brittle Fragmentation Theory), s'observa una proporció substancialment més gran de partícules supermicròniques en el flux de pols obtingut en aquest treball. En general, aquests resultats suggereixen que la deposició seca ha de ser considerada adequadament per a estimar la PSD emesa a partir de les mesures de concentració de partícules, fins i tot en estudis limitats a rangs de tamany $< 10 \mu\text{m}$.

Publications

Articles in peer-review scientific journals

Publications included in this thesis

1. **González-Florez, C.**, Klose, M., Alastuey, A., Dupont, S., Escribano, J., Etyemezian, V., Gonzalez-Romero, A., Huang, Y., Kandler, K., Nikolich, G., Panta, A., Querol, X., Reche, C., Yus-Díez, J., Pérez García-Pando, C. (2023). Insights into the size-resolved dust emission from field measurements in the Moroccan Sahara. *Atmospheric Chemistry and Physics*. 2023. 23(12), 7177-7212. doi: <https://doi.org/10.5194/acp-2022-758>.

Co-author in other publications

1. Panta, A., Kandler, K., Alastuey, A., **González-Florez, C.**, González-Romero, A., Klose, M., Querol, X., Reche, C., Yus-Díez, J., Pérez García-Pando, C. (2023). Insights into the single-particle composition, size, mixing state, and aspect ratio of freshly emitted mineral dust from field measurements in the Moroccan Sahara using electron microscopy. *Atmospheric Chemistry and Physics*. 2023. 23(6), 3861-3885. doi: <https://doi.org/10.5194/acp-23-3861-2023>.
2. González-Romero, A., **González-Florez, C.**, Panta, A., Yus-Díez, J., Reche, C., Córdoba, P., Alastuey, A., Kandler, K., Klose, M., Baldo, C., Clark, R. N., Shi, Z. B., Querol, X., Pérez García-Pando, C. (2023). Variability in grain size, mineralogy, and mode of occurrence of Fe in surface sediments of preferential dust-source inland drainage basins: The case of the Lower Drâa Valley, S Morocco. *Atmospheric Chemistry and Physics*. 2023. [preprint] doi: <https://doi.org/10.5194/egusphere-2023-1120>.

Conferences presentations

1. **González-Florez, C.**, Klose, M., Pérez García-Pando, C.: “Field Observations of the Variability of Dust Emission, its Size-Spectrum and Mineralogy”. In: *7th BSC SO Doctoral Symposium*, online, 5 May 2020, <https://www.bsc.es/education/predoctoral-phd/doctoral-symposium/7th-bsc-so-doctoral-symposium,2020>.
2. Yus-Díez, Jesús, Pérez García-Pando, C., Alastuey, A. , Ivančič, M., **González-Florez, C.**, Gonzalez-Romero, A., Klose, M., Querol, X., Pandolfi, M.: “Multi-wavelengths in-situ scattering and absorption measurements of Saharan dust particles during FRAGMENT”. In: *European Aerosol Conference*, 30 Aug-4 Sep 2020.
3. **González-Florez, C.**, Klose, M., Alastuey, A., Dupont, S., Etyemezian, D., Gonzalez-Romero, A., Kandler, K., Nikolich, G., Pandolfi, M., Panta, A., Querol, X., Reche, C., Yus-Díez, J., Pérez García-Pando, C.: “Understanding size-resolved dust emission from field observations in Morocco”. In: *AGU Fall Meeting 2020*, online, 1-17 Dec 2020, A041-0005, <https://agu.confex.com/agu/fm20/meetingapp.cgi/Paper/679883>, 2020.
4. Yus-Díez, Jesús, Pandolfi, M., Alastuey, A., **González-Florez, C.**, Gonzalez-Romero, A., Ivančič, M., Kandler, K., Klose, M., Panta, A., Querol, X., Reche, C., Pérez García-Pando, C.: “Multi-wavelength scattering and absorption of freshly emitted dust during field observations in Morocco”. In: *AGU Fall Meeting 2020*, online, 1-17 Dec 2020, A041-0006, <https://agu.confex.com/agu/fm20/meetingapp.cgi/Paper/692018>, 2020.
5. Gonzalez-Romero, A., Querol, X., Alastuey, A., **González-Florez, C.**, Kandler, K., Klose, M., Pandolfi, M., Panta, A., Reche, C., Yus-Díez, J., Pérez García-Pando, C.: “Size-resolved mineralogy of dry- and wet-sieved surface sediment samples collected during a field campaign in Morocco”. In: *AGU Fall Meeting 2020*, online, 1-17 Dec 2020, A019-03, <https://agu.confex.com/agu/fm20/meetingapp.cgi/Paper/691794>, 2020.
6. Panta, A., Kandler, K., **González-Florez, C.**, Alastuey, A., Gonzalez-Romero,

- A., Klose, M., Pandolfi, M., Querol, X., Reche, C., Yus-Díez, J., Pérez García-Pando, C.: “Physico-chemical composition of freshly emitted dust aerosol collected during field observations in Morocco”. In: *AGU Fall Meeting 2020*, online, 1-17 Dec 2020, A041-0007, <https://agu.confex.com/agu/fm20/meetingapp.cgi/Paper/697082>, 2020.
7. Pérez García-Pando, C., **González-Florez, C.**, González-Romero, A., Panta, A., Yus-Díez, J., Alastuey, A., Kandler, K., Klose, M., Querol, X., Reche, C., Pandolfi, M., Dupont, S., Etyemezian, V., Nikolich, G., Escribano, J., Clark, R., Ellmann, B., Greenberger, R., Tajeddine, K., and Ivančić, M.: “Towards understanding the size distribution, composition and optical properties of freshly emitted dust and its relationship with the parent sediment”. In *EGU General Assembly 2021*, online, 19–30 Apr 2021, EGU21-13606, <https://doi.org/10.5194/egusphere-egu21-13606>, 2021.
 8. Perez Garcia-Pando, C., Kandler, K., Schepanski, K., Klose, M., **González-Florez, C.**, Gonzalez-Romero, A., Panta, A., Alastuey, A., Querol, X., Reche, C., Yus-Diez, J., Pandolfi, M., Dupont, S., Irvine, M., Etyemezian, V., Nikolich, G., Clark, R., Ehlmann, B., Greenberger, R., Green, R., Brodrick, P., Dagsson-Waldhauserova, P., Dirsch, T., Meyer, H., Urbanneck, C., Umo, N.: “Comprehensive high-latitude dust field campaign in the desert of Dyngjunsandur, Iceland”. In *AGU Fall Meeting 2021*, online, 13-17 Dec 2021, A32B-01, <https://agu.confex.com/agu/fm21/meetingapp.cgi/Paper/987437>, 2021.
 9. **González-Florez, C.**, Klose, M., Alastuey, A., Dupont, S., Etyemezian, V., González-Romero, A., Kandler, K., Nikolich, G., Pandolfi, M., Panta, A., Querol, X., Reche, C., Yus-Díez, J., and Pérez García-Pando, C.: “Size distribution of emitted dust in Morocco”. In: *EGU General Assembly 2022*, Vienna, Austria, 23–27 May 2022, EGU22-11247, <https://doi.org/10.5194/egusphere-egu22-11247>, 2022.
 10. **González-Florez, C.**, Klose, M., Alastuey, A., Dupont, S., Etyemezian, V., González-Romero, A., Kandler, K., Nikolich, G., Pandolfi, M., Panta, A., Querol, X., Reche, C., Yus-Díez, J., and Pérez García-Pando, C.: “On the emitted dust size distribution and its variability: insights from a field campaign

in an ephemeral lake of the Lower Drâa Valley, Moroccan Sahara”. In: *AGU Fall Meeting 2022*, 11-15 Dec 2022, A46D-05, <https://agu.confex.com/agu/fm22/meetingapp.cgi/Paper/1139923>, 2022.

11. **González-Florez, C.**, Klose, M., Alastuey, A., Dupont, S., Etyemezian, V., González-Romero, A., Kandler, K., Nikolich, G., Pandolfi, M., Panta, A., Querol, X., Reche, C., Yus-Díez, J., and Pérez García-Pando, C.: “Comparison of emitted dust size distributions from field campaigns in Morocco and Iceland”. In: *7th High Latitude Dust Workshop*, 14-15 Feb 2023, A46D-05, <https://icedustblog.wordpress.com/2022/12/25/high-latitude-dust-workshop-2023/>, 2023.

List of Figures

1 A general overview of atmospheric mineral dust	1
1.1 Main processes involved in dust cycle and main dust impacts on climate.	2
1.2 Main dust source regions in the world along with main dust transport patterns.	3
1.3 Scanning electron microscope image of a dust sample collected in Morocco in 2019.	16
2 Physics of dust emission	21
2.1 A general overview of dust emission: basic concepts involved.	22
2.2 Relationship between threshold friction velocity and particle diameter based on theoretical expressions and experimental measurements. . .	26
2.3 Dust emission mechanisms.	29
2.4 Illustration of the set-up needed for measuring diffusive flux through the FG and EC methods in a source region along with a schematic representation of the surface and near-surface fluxes.	38
4 Context and scope	43
4.1 Objectives and methods set by FRAGMENT.	44
4.2 Time and locations of FRAGMENT field campaigns	46
4.3 (a) Most of the FRAGMENT team during the first field campaign in Morocco. (b) Myself downloading the meteorological data.	48
5 The FRAGMENT dust field campaign in the Moroccan Sahara	53
5.1 Average annual cycles of wind speed at 3 m height and precipitation and temperature (minimum and maximum) at 2 m height at the Jebel Brahim AWS.	54
5.2 Wind roses by month at the Jebel Brahim AWS using 15 min data from 1 Jan. 2002 to 21 Aug. 2011	55

List of Figures

5.3	Daily mean wind speed at 3 m height for each month in the Jebel Brahim AWS.	55
5.4	(a) ERA5 and ERA-Interim grid points closest to our area of interest, the Jebel Brahim AWS and 3 potential field locations identified during an exploratory trip in January 2019. Comparison of annual mean wind speed between the in-situ data at the Jebel Brahim AWS and ERA5 (b) and ERA-Interim (c) data interpolated to these 3 locations. . . .	56
5.5	(a) Location of the study area in Northern Africa. (b) Zoomed-in view over Morocco and Algeria. (c) Zoomed-in view over the Lower Drâa Valley. (d) Experimental set-up in “L’Bour” (Morocco). (e) Picture of the main instruments as deployed in the field.	58
5.6	(a) Minimally-and fully-dispersed normalized mean PSDs of a sand dune (blue) and the paved sediments (orange) in L’Bour. (b) Picture of the paved sediment. (c) Picture of a small sand dune in L’Bour. . .	59
5.7	Default optical diameters (μm) of the Fidas versus geometric diameters (μm) calculated assuming that dust particles are tri-axial ellipsoids with an aspect ratio of 1.46, a height-to-width ratio of 0.45 and a refractive index of $1.49 + 0.0015 i$. (a) Representation in linear scale. (b) Representation in logarithmic scale.	64
5.8	(a) Systematic correction parameter, λ_i , and (b) Pearson coefficient, r , for each integrated size bin i	65
5.9	(a) FidasL versus FidasU (after systematic correction) number concentrations ($\# \text{m}^{-3}$) during the intercomparison period. (b) σ_r versus corrected FidasU number concentrations ($\# \text{m}^{-3}$) during the intercomparison period.	72

6 Overview of the atmospheric conditions and dust events during the campaign **83**

6.1	Time series (UTC) of 15 min average (a) temperature ($^{\circ}\text{C}$) at 1, 2, 4, and 8 m; (b) relative humidity (%) and temperature ($^{\circ}\text{C}$) at 0.5 m; (c) pressure (hPa) at 1.5 m; (d) mean wind speed (m s^{-1}) and (e) mean wind direction ($^{\circ}$) at 0.4, 0.8, 2, 5, and 10 m; (f) FidasL (1.8 m) particle concentrations in number $c_i^n (\# \text{m}^{-3})$; and (g) in mass $c_i^m (\mu\text{g m}^{-3})$. . .	84
-----	--	----

List of Figures

6.2	Time series (UTC) of 15 min averaged (a) friction velocity u_* (m s^{-1}); (b) atmospheric stability represented by z/L , where z is the reference height 2 m; (c) saltation flux ($\text{g m}^{-1} \text{s}^{-1}$); (d) bulk and size-resolved diffusive flux in number ($\# \text{m}^{-2} \text{s}^{-1}$) between 0.27 and 19.11 μm ; and (e) bulk and size-resolved diffusive flux in mass ($\mu\text{g m}^{-2} \text{s}^{-1}$) between 0.27 and 19.11 μm	85
6.3	Wind rose at 2 m height for different u_* intervals (m s^{-1}).	86
6.4	Solid lines represent the time evolution of the 15 min average total particle concentrations between 0.25 to 19.11 μm in number ($\# \text{m}^{-3}$) (a) and mass ($\mu\text{g m}^{-3}$) (b). Contour plots on the background show the size-resolved particle number (a) and mass (b) concentration fractions (%) for each time step.	88
6.5	Saltation flux ($\text{kg m}^{-1} \text{s}^{-1}$) versus wind shear stress (Pa).	89
7 Characterization of saltation and sandblasting efficiency		91
7.1	(a) Diffusive flux ($\mu\text{g m}^{-2} \text{s}^{-1}$) versus friction velocity u_* (m s^{-1}), (b) saltation flux ($\text{g m}^{-1} \text{s}^{-1}$) versus u_* (m s^{-1}), (c) sandblasting efficiency (m^{-1}) versus u_* (m s^{-1}), and (d) sandblasting efficiency (m^{-1}) versus saltation flux ($\text{g m}^{-1} \text{s}^{-1}$).	92
7.2	Analogous to Fig. 7.1 but considering only wind directions between 45–90°.	94
7.3	Analogous to Fig. 7.1 but considering only wind directions between 225–270°.	95
7.4	Relationship between 15 min averages of surface roughness length, z_0 , and friction velocity, u_* , under wind erosion conditions.	96
7.5	(a) The Charnock relationship between shear velocity and roughness length. (b) The modified Charnock relationship between shear velocity and roughness length. The points shown in both panels correspond to the 15 min values with a positive saltation flux and when $u_* > u_{*th}$	97
7.6	Analogous to Fig. 7.5 but selecting the 15 min values with a positive saltation flux and when $u_* > 0.2 \text{ m s}^{-1}$	98
8 Variability of the dust PSD at emission		101

List of Figures

8.1	Average size-resolved particle number concentration, $dN/d\ln D_i$ ($\# \text{ m}^{-3}$), from FidasL for different u_* intervals, types of events (regular or haboob), and wind directions in the range $150\text{--}330^\circ$ (a) and $330\text{--}150^\circ$ (b). Panels (c)-(d) are the same as (a)-(b) but normalized (<i>Norm. $dN/d\ln D_i$</i>) after removing the anthropogenic mode (normalization from 0.42 to $19.11 \mu\text{m}$).	103
8.2	Average size-resolved particle mass concentration, $dM/d\ln D_i$ ($\mu\text{g m}^{-3}$), from FidasL for different u_* intervals, types of events (regular or haboob), and wind directions in the range $150\text{--}330^\circ$ (a) and $330\text{--}150^\circ$ (b). Panels (c)-(d) are the same as (a)-(b) but normalized (<i>Norm. $dM/d\ln D_i$</i>) after removing the anthropogenic mode (normalization from 0.37 to $19.11 \mu\text{m}$).	104
8.3	Average size-resolved particle number concentration, $dN/d\ln D_i$ ($\# \text{ m}^{-3}$), from FidasU for different u_* intervals, types of events (regular or haboob), and wind directions in the range $150\text{--}330^\circ$ (a) and $330\text{--}150^\circ$ (b). Panels (c)-(d) are the same as (a)-(b) but normalized (<i>Norm. $dN/d\ln D_i$</i>) after removing the anthropogenic mode (normalization from 0.42 to $19.11 \mu\text{m}$).	105
8.4	Average size-resolved particle mass concentration, $dM/d\ln D_i$ ($\mu\text{g m}^{-3}$), from FidasU for different u_* intervals, types of events (regular or haboob), and wind directions in the range $150\text{--}330^\circ$ (a) and $330\text{--}150^\circ$ (b). Panels (c)-(d) are the same as (a)-(b) but normalized (<i>Norm. $dM/d\ln D_i$</i>) after removing the anthropogenic mode (normalization from 0.37 to $19.11 \mu\text{m}$).	106
8.5	Average size-resolved number diffusive flux, $dF_n/d\ln D_i$ ($\# \text{ m}^{-2} \text{ s}^{-1}$), for different u_* intervals, types of events (regular or haboob) and wind directions in the range $150\text{--}330^\circ$ (a) and $330\text{--}150^\circ$ (b). Only the samples where diffusive flux is positive in all the diameter bins above the anthropogenic mode have been selected. Panels (c)-(d) are the same as (a)-(b) but normalized (<i>Norm. $dF_n/d\ln D_i$</i>) after removing the anthropogenic mode (normalization from 0.37 to $19.11 \mu\text{m}$). Shaded areas around the lines of the regular event PSDs depict the combination of random uncertainty and standard error.	108

8.6	Average size-resolved mass diffusive flux, $dF_m/d\ln D_i$ ($\mu\text{g m}^{-2} \text{s}^{-1}$), for different u_* intervals, types of events (regular or haboob) and wind directions in the range $150\text{--}330^\circ$ (a) and $330\text{--}150^\circ$ (b). Only the samples where diffusive flux is positive in all the diameter bins above the anthropogenic mode (as discussed in Sect. 8.1) have been selected. Panels (c)-(d) are the same as (a)-(b) but normalized ($Norm. dF_m/d\ln D_i$) after removing the anthropogenic mode (normalization from 0.37 to $19.11 \mu\text{m}$). Shaded areas around the lines of the regular events PSDs illustrate the combination of random uncertainty and standard error.	109
8.7	Number and mass diffusive flux fractions for different u_* intervals, types of events (regular or haboob) and wind directions in the range $150\text{--}330^\circ$ (a)-(c) and $330\text{--}150^\circ$ (b)-(d).	111
9 What explains the observed PSD variations? Potential roles of dry deposition and fetch length, aggregate disintegration, and haboob gust front		113
9.1	Schematic representation of the fetch length during (a) regular dust events and (b) haboobs.	116
10 Evaluation of the estimated dry deposition and emitted fluxes		119
10.1	Median size-resolved dry deposition velocities v_{dep} (m s^{-1}) obtained using field measurements and applying (a) F19, (b) Z01, and (c) tuned parameterization for different u_* intervals (solid lines). The stars correspond to the median of the observation-based v_{dep} for the u_* intervals $(0 - 0.05] \text{m s}^{-1}$ (purple), $(0.05 - 0.10] \text{m s}^{-1}$ (blue), and $(0.10 - 0.15] \text{m s}^{-1}$ (cyan).	120
10.2	In situ size-resolved measurements of dry deposition velocity v_{dep} (m s^{-1}) for u_* between (a) $(0 - 0.05) \text{m s}^{-1}$, (b) $(0.05 - 0.10) \text{m s}^{-1}$, and (c) $(0.10 - 0.15) \text{m s}^{-1}$ (bar plots). Lines represent the estimated median v_{dep} applying F19 (dashed), Z01 (solid) and the tuned parameterization (dashdot) for the corresponding u_* interval.	120

List of Figures

10.3 Different configurations of the tuned parameterization for estimating v_{dep} applying different values of A_{in} , B_1 and d_c 121

10.4 Average size-resolved number dry deposition flux, $d|F_{dep.n}|/dlnD_i$ ($\# m^{-2} s^{-1}$), estimated from the v_{dep} tuned formulation for different u_* intervals, types of events (regular or haboob), and wind directions in the range 150–330° (a) and 330–150° (b). Only the samples where diffusive flux is positive in all the diameter bins above the anthropogenic mode have been selected. 122

10.5 Average size-resolved mass dry deposition flux, $d|F_{dep.m}|/dlnD_i$ ($\mu g m^{-2} s^{-1}$), estimated from the v_{dep} tuned formulation for different u_* intervals, types of events (regular or haboob), and wind directions in the range 150–330° (a) and 330–150° (b). Only the samples where diffusive flux is positive in all the diameter bins above the anthropogenic mode have been selected. 123

10.6 Average size-resolved number estimated emitted flux, $dF_{emi.n}/dlnD_i$ ($\# m^{-2} s^{-1}$) from the tuned v_{dep} parameterization, for different u_* intervals, types of events (regular or haboob), and wind directions in the range 150–330° (a) and 330–150° (b). Only the samples where diffusive flux is positive in all the diameter bins above the anthropogenic mode have been selected. Panels (c)-(d) are the same as (a)-(b) but normalized ($Norm. dF_{emi.n}/dlnD_i$) after removing the anthropogenic mode (normalization from 0.37 to 19.11 μm). 125

10.7 Average size-resolved mass estimated emitted flux, $dF_{emi.m}/dlnD_i$ ($\mu g m^{-2} s^{-1}$), for different u_* intervals, types of events (regular or haboob), and wind directions in the range 150–330° (a) and 330–150° (b). Only the samples where diffusive flux is positive in all the diameter bins above the anthropogenic mode have been selected. Panels (c)-(d) are the same as (a)-(b) but normalized ($Norm. dF_{emi.m}/dlnD_i$) after removing the anthropogenic mode (normalization from 0.37 to 19.11 μm). 126

10.8 Number and mass emitted flux fractions for different u_* intervals, types of events (regular or haboob), and wind directions in the range 150–330° (a-c) and 330–150°(b-d) 128

10.9	Ratio of dry deposition flux to the estimated emitted dust flux, determined using the v_{dep} tuned parameterization, for different u_* intervals, types of events (regular or haboob), and wind directions in the range 150–330° (a) and 330–150°(b)	128
11	Comparison with Brittle Fragmentation Theory	129
11.1	Averaged normalized PSDs considering PSL latex spheres with a refractive index of $1.59 + 0i$ removing the anthropogenic mode (normalization from 0.37 to 19.11 μm) for well-developed erosion conditions during regular events and for two PSDs during haboob events for FidasL (a-b), for diffusive flux (c-d), and for estimated emitted flux using the v_{dep} from the tuned parameterization (e-f). Panels (a,c,e) show PSDs in terms of number, and panels (b,d,f) show PSDs in terms of mass.	130
11.2	Averaged normalized PSDs considering tri-axial ellipsoids of $1.49 + 0.0015i$ removing the anthropogenic mode (normalization from 0.37 to 19.11 μm) for well-developed erosion conditions during regular events and for two PSDs during haboob events for FidasL (a-b), for diffusive flux (c-d) and for estimated emitted flux using the v_{dep} from the tuned parameterization (e-f). Panels (a,c,e) show PSDs in terms of number, and panels (b,d,f) show PSDs in terms of mass.	131
A	Analysis of correction for heavy particles	147
A.1	Mean correction factor for heavy particles per size bin.	148
B	Friction velocity from the Eddy Covariance method	149
B.1	Time series of u_* calculated from the law of the FG method (blue line) and EC method at 1 m (magenta line), 3 m (grey line) and extrapolated to the surface (orange line).	149
C	Additional figures related to the diffusive flux PSDs	151

List of Figures

C.1	Analogous to Fig. 8.5 but with shaded areas around the lines of the haboob event PSDs depicting the combination of random uncertainty and standard error.	152
C.2	Analogous to Fig. 8.6 but with shaded areas around the lines of the haboob event PSDs depicting the combination of random uncertainty and standard error.	153
C.3	Analogous to Fig. C.3 but with shaded areas around the lines depicting the standard error.	154
C.4	Analogous to Fig. C.4 but with shaded areas around the lines depicting the standard error.	155
D	Additional figures related to the dry deposition fluxes	157
D.1	Analogous to Fig. 10.4 but with v_{dep} estimated from F19.	157
D.2	Analogous to Fig. 10.5 but with v_{dep} estimated from F19.	158
D.3	Analogous to Fig. 10.4 but with v_{dep} estimated from Z01.	158
D.4	Analogous to Fig. 10.5 but with v_{dep} estimated from Z01.	159
E	Additional figures related to the estimated emitted flux PSDs	161
E.1	Analogous to Fig. 10.6 but with v_{dep} estimated from F19.	162
E.2	Analogous to Fig. 10.7 but with v_{dep} estimated from F19.	163
E.3	Analogous to Fig. 10.6 but with v_{dep} estimated from Z01.	164
E.4	Analogous to Fig. 10.7 but with v_{dep} estimated from Z01.	165
F	Additional figures related to the ratio of dry deposition flux to the estimated emitted flux	167
F.1	Analogous to Fig. 10.9 but with v_{dep} estimated from F19.	167
F.2	Analogous to Fig. 10.9 but with v_{dep} estimated from Z01.	168

List of Tables

7	Characterization of saltation and sandblasting efficiency	91
7.1	Obtained parameters a and b from each regression curve in Fig. 7.1 (all wind directions) along with their 95% confidence intervals.	93
7.2	Obtained parameters a and b from each regression curve in Fig. 7.2 (wind directions between 45–90°) along with their 95% confidence intervals.	94
7.3	Obtained parameters a and b from each regression curve in Fig. 7.3 (wind directions between 225–270°) along with their 95% confidence intervals.	95
9	What explains the observed PSD variations? Potential roles of dry deposition and fetch length, aggregate disintegration, and haboob gust front	113
10.1	Mean and standard deviation (SD) of the number and mass percentages for the four size ranges in the diffusive and emitted fluxes during regular events for each wind sector, calculated from the average values of each u_* interval shown in Figs. 8.7 and 10.8. The average of each u_* interval contributes equally to the mean, and the standard deviation is a measure of the variability across u_* interval averages. For the estimated emitted flux we used the v_{dep} from the tuned parameterization.	127
11	Comparison with Brittle Fragmentation Theory	129
11.1	Mean and standard deviation (SD) of the number and mass percentages for the four size ranges in the diffusive and emitted fluxes during regular events for each wind sector, assuming tri-axial ellipsoids. The average of each u_* interval contributes equally to the mean, and the standard deviation is a measure of the variability across u_* interval averages. For the estimated emitted flux we used the v_{dep} from the tuned parameterization.	133

List of Symbols

Symbol	Description
A_{in}	Tuning parameter in the dry deposition velocity tuned parameterization.
B_1	Tuning parameter in the dry deposition velocity tuned parameterization.
C_c	Cunningham slip correction factor.
C_{ch}	Fitting parameter of Charnock's model.
C_h	Bulk heat transfer coefficient.
C_{hp}	Correction term for heavy particles.
c	Mean dust concentration.
$c_{int}(D_i)$	Concentration at the intermediate height between the two Fidas.
c_{l_0}	Concentration from FidasL during the intercomparison period.
$c_l^n(D_i)$	Number concentrations of dust particles with diameter D_i measured by FidasL during the campaign.
c_{u_0}	Uncorrected concentration from FidasU during the intercomparison period.
$c_u^n(D_i)$	Number concentrations of dust particles with diameter D_i measured by FidasU during the campaign after systematic correction.
c_u	Corrected FidasU concentration during the campaign.
$c_{u_{uncorr.}}$	Uncorrected FidasU concentration during the campaign.
D	Diameter of dust particles, with the specific type of diameter specified in each corresponding section.
$D_g(D_i)$	Brownian diffusivity.
D_i	Mean logarithmic particle diameter in bin number i of the Fidas.
d_c	Tuning parameter in the dry deposition velocity tuned parameterization.
E_B	Collection efficiency from Brownian diffusion.

List of Symbols

E_{IM}	Impaction.
E_{IN}	Interception.
F	Diffusive dust flux.
F_{dep}	Dry deposition flux.
F_{emi}	Vertical or emitted dust flux.
F_g	Gravitational settling flux.
$F_m(D_i)$	15 min averaged mass diffusive flux with diameter D_i .
$F_n(D_i)$	15 min averaged number diffusive flux with diameter D_i .
g	Gravitational acceleration.
H	Sensible heat flux.
H_0	Null hypothesis in the test of significance.
K_d	Dust eddy diffusion coefficient.
K_m	Eddy exchange coefficient of momentum.
L	Obukhov length.
N	Number of 15 min measurements in the u_* interval.
Q	Horizontal or saltation flux.
R_1	Correction factor representing the fraction of particles that stick to the surface in Z01 parameterization.
R_a	Aerodynamic resistance.
R_s	Surface collection resistance.
S_c	Schmidt number.
S_t	Stokes number.
Sc_t	Turbulent Schmidt number.
T	Air temperature at 1,m height.
T_0	Soil surface temperature.
T_r	Temperature at reference height z_r .
$U(z)$	Mean horizontal wind speed at height z .
z	Height above the surface.
z_0	Roughness length.
z_{int}	Intermediate height between the two Fidas.
z_l	Height of FidasL.
z_r	Reference height.
z_u	Height of FidasU.

List of Symbols

α	Sandblasting efficiency.
β	Dimensionless coefficient relating the fluid Lagrangian integral time scale, the integral length scale of the Eulerian fluid velocity field and the standard deviation of the turbulent velocity.
γ	Constant in Z01 parameterization.
κ	von Karman constant.
μ	dynamical viscosity.
ν	Air kinematic viscosity.
$\partial U/\partial z$	vertical gradient of the horizontal wind speed.
ϕ_d	Similarity function for dust.
ϕ_h	Similarity function for sensible heat.
ϕ_m	Similarity function for momentum.
ψ_h	Integral of the similarity function for sensible heat.
ψ_m	Integral of the similarity function for momentum.
ρ_{air}	Air density.
ρ_d	Dust particle density.
$\sigma_{F(D_i)}$	Uncertainty in the diffusive flux.
$\sigma_{F(D_i)avg}$	Average diffusive flux uncertainty.
$\sigma_{F(D_i)j}$	Uncertainty of each 15 min size-resolved diffusive flux in the u^* interval.
$\sigma_{F_{emi}(D_i)}$	Uncertainty in the estimated emitted flux.
$\sigma_{c_u(D_i)}$	Uncertainty of the FidasU concentration with respect to the FidasL concentration.
σ_{pa}	Particle-to-air density ratio.
σ_w	Unbiased variance of turbulent velocity.
τ	Wind shear stress.
τ_M	Viscous shear stress.
τ_R	Reynolds shear stress.
τ_{th}	Impact threshold stress.
θ_r	Reference potential temperature.
$\zeta = z/L$	Stability parameter.
$\langle u'w' \rangle$	Momentum flux.
μ	Dynamical viscosity.

List of Symbols

$\partial U/\partial z$	Vertical gradient of the horizontal wind speed.
τ_{th}	Impact threshold stress.
τ_R	Reynolds shear stress.
τ_M	Viscous shear stress.
λ_i	Systematic correction parameter for each bin i of FidasU.
$\overline{w'\theta'_0}$	Surface kinematic heat flux.
u_r	Wind at reference height.
u_*	Wind friction velocity.
u_{th}	Threshold friction velocity.
$v_{dep.F19}(D_i)$	Dry deposition velocity in F19 parameterization.
$v_{dep.Z01}(D_i)$	Dry deposition velocity in Z01 parameterization.
$v_{dep.tuned}(D_i)$	Dry deposition velocity in tuned parameterization.
$v_{dep}(D_i)$	Dry deposition velocity.
$v_{diff}(D_i)$	Diffusive dry deposition velocity.
$v_g(D_i)$	Gravitational settling velocity.
v_g	Gravitational settling velocity.
$v_{diff}(D_i)$	Diffusive dry deposition velocity.
ρ_d	Dust particle density.
$\sigma_{F(D_i)}$	Uncertainty in the diffusive flux.
$\sigma_{c_u(D_i)}$	Uncertainty of the FidasU concentration with respect to the FidasL concentration.
$\sigma_{F(D_i)avg}$	Average diffusive flux uncertainty.
$\sigma_{F(D_i)j}$	Uncertainty of each 15 min size-resolved diffusive flux in the u_* interval.
$\sigma_{F_{emi}(D_i)}$	Uncertainty in the estimated emitted flux.
w	Wind velocity vertical component.

Acronyms

ABL Atmospheric Boundary Layer.

AC Atmospheric Composition.

AeroCom Aerosol Comparisons between Observations and Models.

AR Aspect Ratio.

AWS Automated Weather Station.

BC Black Carbon.

BFT Brittle Fragmentation Theory.

BSC Barcelona Supercomputing Center.

CCN Cloud Condensation Nuclei.

CESM Community Earth System Model.

DOD Dust Optical Depth.

DRE Direct Radiative Effect.

EC Eddy Covariance.

EMIT Earth Surface Mineral Dust Source Investigation.

ERC European Research Council.

FG Flux-Gradient.

FRAGMENT FRontiers in dust minerAloGical coMposition and its Effects upon
climaTe.

HiLDA Iceland as a model for high-latitude dust sources – a combined experimental
and modelling approach for characterization of dust emission and transport
processes.

HLD High Latitude Dust.

HWR Height-to-Width Ratio.

IADS Intelligent Aerosol Drying System.

IDAEA-CSIC Institute of Environmental Assessment and Water Research at the Spanish Research Council.

IGFR International Geomagnetic Reference Field.

INPs Ice Nucleating Particles.

JADE Japan-Australian Dust Experiment.

KIT Karlsruhe Institute of Technology.

LAPs Light-Absorbing Particles.

LW Longwave.

MONARCH Multiscale Online Non-hydrostatic Atmosphere Chemistry.

MWAC Modified Wilson and Cook samplers.

OGD Optical Gate Device.

OPC Optical Particle Counter.

PSD Particle Size Distribution.

PSL Polystyrene Latex Spheres.

RF Radiative forcing.

SANTRI Standalone Aeolian Transport Real-time Instrument.

SBL Surface Boundary Layer.

SSA Single-Scattering Albedo.

SW Shortwave.

TOA Top Of the Atmosphere.

TUDA Technical University of Darmstadt.

UPC Universitat Politècnica de Catalunya.

Acronyms

WIND-O-V WIND erOsion in presence of sparse Vegetation.





I Introduction

A general overview of atmospheric mineral dust

Dust research spans over different disciplines, including soil physics, meteorology, geology, air chemistry, mineralogy and microbiology. In this chapter, I provide a comprehensive introduction to atmospheric mineral dust, covering different aspects of its atmospheric life cycle, effects and properties. First, I describe the different stages involved in its atmospheric cycle, and review the most recent global dust emission estimates along with the contributions from the main dust source regions. Then, I focus on the effects dust exerts upon our society and climate. Finally, I delve into the dust physico-chemical properties.

1.1. The atmospheric mineral dust cycle

Atmospheric mineral dust, formed of tiny soil mineral particles, is the most abundant aerosol type, contributing more than two thirds of the global aerosol mass (Textor et al., 2006). Once emitted, dust particles drastically reduce visibility in source regions and are frequently carried over distances of thousands of kilometres before being deposited to land and ocean waters (Fig. 1.1). During transport dust is subject to chemical and physical transformations and interacts with radiation and clouds. The atmospheric dust cycle is controlled by factors that change at multiple spatio-temporal scales, ranging from seconds to hundreds of thousands of years and from local to global, and is connected to other cycles including the energy, water, carbon, phosphorus and iron cycles (Shao et al., 2011b).

Dust is mainly emitted from arid and semi-arid areas, where strong winds promote the movement of soil particles by saltation, and the release of fine particles (Shao, 2008). Besides wind intensity, dust emission is controlled by other factors such as soil properties (e.g. mineralogy, presence of aggregates, soil texture), surface soil conditions (e.g. crust, moisture, vegetation, roughness) and land-use (e.g. grazing, farming) (Tegen et al., 2002; Pierre et al., 2012; Perlwitz et al., 2015a,b; Klose et al.,

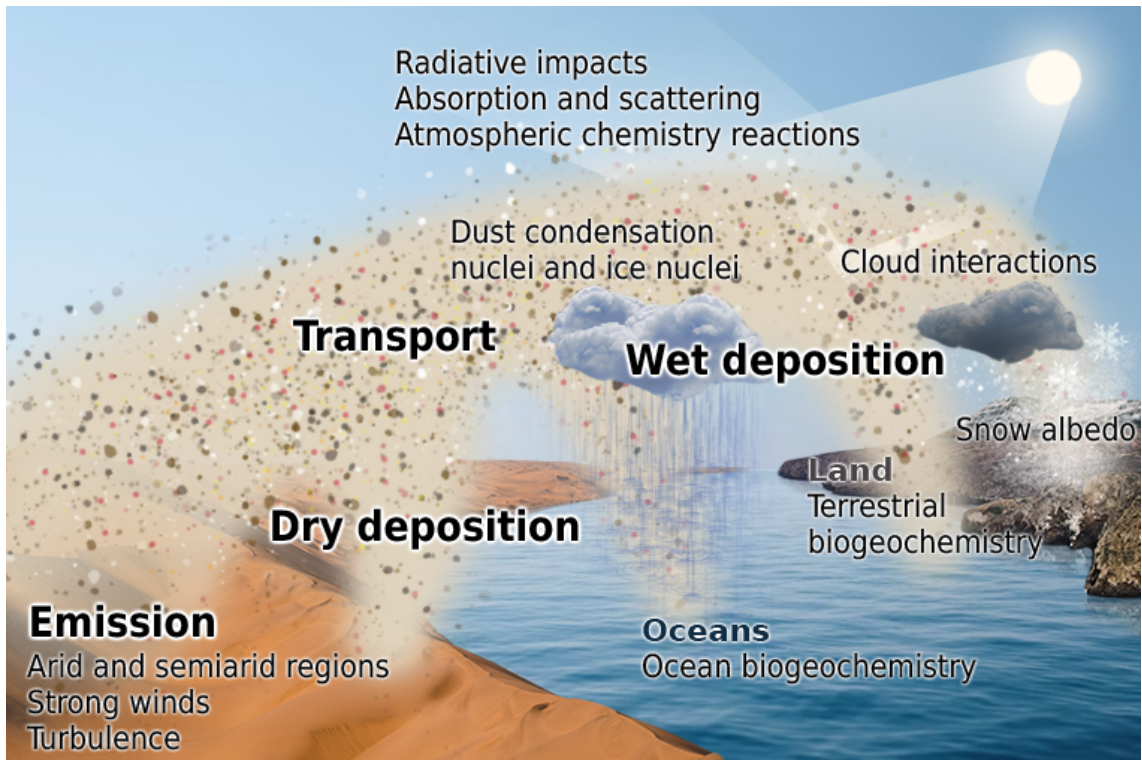


Figure 1.1: Main processes involved in dust cycle and main dust impacts on climate.

2019). As a result, although natural deserts dominate dust production, anthropogenic sources resulting from changes in land-use have been estimated to represent about 25% of the global emission (Ginoux et al., 2012). However, the uncertainty in this estimate is high (Tegen et al., 2004; Mahowald et al., 2004; Stanelle et al., 2014; Xi and Sokolik, 2016).

Prolific sources of dust aerosol are located mostly in areas where precipitation is low and there is accumulation of alluvial sediments (Fig. 1.2). Such regions comprise deserts, inland basins sporadically flooded by ephemeral surface water streams and dry lake beds (Prospero et al., 2002; Bullard et al., 2011; Ginoux et al., 2012). The largest source region on Earth is the Sahara Desert, which hosts what is thought to be the most prolific dust source of the planet: the Bodélé Depression, located in the northern Lake Chad Basin (Prospero et al., 2002; Bristow et al., 2009; Ginoux et al., 2012). Recent estimates suggest that North African source regions contribute around 50% of the total global loading of dust (Kok et al., 2021a). Other major dust source regions, representing around 40% of the total global loading of dust (Kok et al., 2021a), are the Middle East with several active sources (Pease et al.,

1.1. The atmospheric mineral dust cycle

1998; Hamidi et al., 2013; Yu et al., 2013) and the Asian continent, including the Taklamakan Desert (Ge et al., 2016), the Gobi Desert (Chen et al., 2017), the Sistan Basin (Alizadeh-Choobari et al., 2014) and the Thar Desert (Hussain et al., 2005). All these sources constitute the so-called “global dust belt” in the Northern Hemisphere, extending from the west coast of North Africa, over the Middle East, Central and South Asia, to China (Prospero et al., 2002). Dust aerosols are also emitted from deserts in Australia (Ekström et al., 2004), South Africa (Bryant et al., 2007; Vickery et al., 2013), South America (Gassó and Torres, 2019) and North America (Hand et al., 2017), but to a lesser extent. While most of the global dust originates from hot tropical and subtropical arid regions, it is estimated that up to 5 % of the global dust is emitted from cold high-latitude dust (HLD) sources ($\geq 50^\circ\text{N}$ and $\geq 40^\circ\text{S}$) (Bullard et al., 2016). In addition, the existence of a northern HLD belt has been recently suggested. This belt has been defined as the area north of 50°N , with a “transitional HLD-source area” extending at latitudes $50\text{--}58^\circ\text{N}$ in Eurasia and $50\text{--}55^\circ\text{N}$ in Canada and a “cold HLD-source area” including areas north of 60°N in Eurasia and north

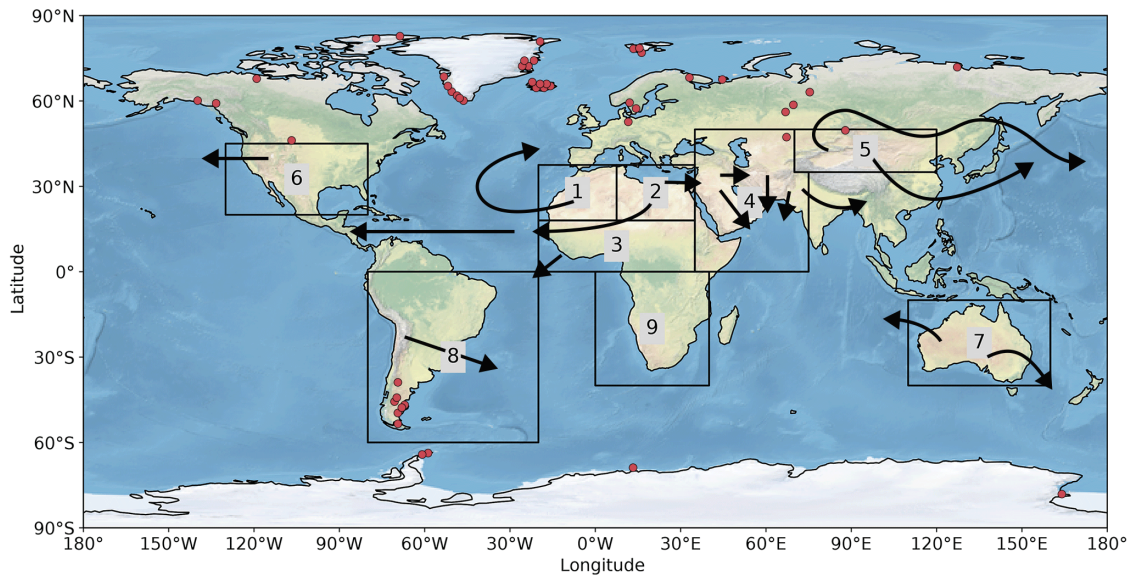


Figure 1.2: Main dust source regions in the world located in: (1) Western North Africa, (2) Eastern North Africa, (3) the Southern Sahara and Sahel, (4) the Middle East and Central Asia (which includes the Horn of Africa), (5) East Asia, (6) North America, (7) Australia, (8) South America, and (9) Southern Africa. Red points represent the high-latitude dust sources identified in Meinander et al. (2022). Black arrows reflect the main dust transport patterns described in (Shao et al., 2011b). Figure modified from Kok et al. (2021a).

of 58 °N in Canada, with currently “no dust source” area between the HLD and low-latitude dust, except for British Columbia (Meinander et al., 2022).

Recent estimates constrained by global observations of dust aerosol optical depth and size-resolved concentrations suggest that every year between 3400 and 9100 Tg yr⁻¹ are emitted globally (Kok et al., 2021a,b). These estimates, which consider dust with a geometric diameter up to 20 µm, exceed previous assessments (Huneeus et al., 2011) in great part due to higher emission of coarse and super-coarse particles. It is important to note that these estimates are sensitive to the choice of the dust emission scheme (Klose et al., 2021).

Dust emission, as described earlier, is influenced by various factors that make it sensitive to climate change and land-use and land-cover change (Jia et al., 2019). Limited research has examined the evolution of global dust sources since pre-industrial times, suggesting a likely increase in dust emission during the last century (Mahowald et al., 2010; Stanelle et al., 2014; Kok et al., 2023). Notably, the recent study conducted by Kok et al. (2023), which combines dust deposition records with constraints on the modern-day dust cycle, has estimated an increase in global dust mass loading of 55 ± 30% since pre-industrial times, driven largely by increases in dust from Asia and North Africa. However, it remains unclear whether dust emission will increase or decrease in response to future climate and land-use changes (Evan et al., 2016; Pu and Ginoux, 2017, 2018). Accurately simulating dust emission evolution is hindered by uncertainties surrounding future regional wind patterns and precipitation (Evan et al., 2016). Additionally, uncertainties arise from factors such as the influence of CO₂ fertilization on the extent of dust sources (Huang et al., 2017), the complexities of dust feedback mechanisms (Evans et al., 2019), and the effects of human activities that alter land-use, disturb soil, and involve practices such as cropping, livestock grazing, recreation, urbanization, and water diversion for irrigation (Ginoux et al., 2012).

Once dust is emitted, its lifetime in the atmosphere is strongly influenced by the environmental conditions (Pye, 1987; Kok et al., 2012; Adebisi and Kok, 2020) and the size of its particles, as small particles fall slower than larger ones (Seinfeld and Pandis, 2006). Under favourable environmental conditions, including atmospheric instability, strong convection, turbulence within the boundary layer and

strong prevailing winds in the free troposphere (Ansmann et al., 2009; Knippertz and Todd, 2012; Garcia-Carreras et al., 2015), dust particles (especially particles with geometric diameters $< 10 \mu\text{m}$) can remain suspended for several days and travel distances of thousands of kilometres through the air (Prospero et al., 1970; Carlson and Prospero, 1972). As depicted in Fig. 1.2, the main trajectories followed by dust from North Africa are (1) southward over the Sahel and the Gulf of Guinea ($\sim 60\%$ of emissions) (2) westward to the North Atlantic Ocean ($\sim 25\%$), (3) northward to Europe and the Mediterranean Sea ($\sim 10\%$) and (4) eastward to the Middle East ($\sim 5\%$) (Shao et al., 2011b). The emission and transport of dust from the Middle East and Central Asia are associated with the Indian monsoon trough, resulting in the transport of dust towards the Indian Ocean (Shao et al., 2011b; Di Biagio et al., 2021). In East Asia, dust normally follows the East Asian trough and is primarily transported toward the southeast and then the northeast, sometimes even reaching the West coast of Canada and the USA. In Australia there are two major pathways: (1) south-eastward to the Southern Pacific Ocean and (2) north-westward to the Indian Ocean (Shao et al., 2011b). Dust emitted from South America primarily undergoes transport across the South Atlantic Ocean and can even reach Antarctica (Li et al., 2010; Johnson et al., 2011). In North America, Santa Ana winds transport abundant amounts of dust from the mainland to the eastern Pacific Ocean (Muhs et al., 2007). The analysis of HLD pathways is more limited. However, some progress has been made in recent years. For instance, the study conducted by Baddock et al. (2017) has highlighted the transportation of Icelandic dust to the Northern Atlantic and sub-Arctic oceans.

There is increasing observational evidence of the long-range transport of dust particles with a geometric diameter of $2.5\text{--}10 \mu\text{m}$ (coarse) and $10\text{--}62.5 \mu\text{m}$ (super-coarse) (Jeong et al., 2014; Van Der Does et al., 2016; Weinzierl et al., 2017; van der Does et al., 2018) although the physical mechanisms responsible for this phenomenon still remain quite uncertain. Existing models, which commonly rely on the Stokes settling approximation, fail to incorporate this observed long-range transport of coarse and super-coarse dust, which is crucial for understanding the impacts of dust aerosols on the Earth System (Ryder et al., 2019; Adebisi et al., 2023). A recent study suggests that climate models are likely missing over 75% of particles with a geometric diameter larger than $5 \mu\text{m}$ (Adebisi and Kok, 2020). The transport

of coarse and super-coarse dust particles over long distances is likely influenced by atmospheric phenomena such as advection, convection, atmospheric instability, and turbulence (Ansmann et al., 2009; Knippertz and Todd, 2012; Garcia-Carreras et al., 2015). Regrettably, these important factors are not adequately represented in current models. Additionally, the impact of dust shape and orientation, as well as the potential electrification of the dust layer, which can contribute to a decrease in the settling velocity of larger particles, are typically overlooked (Ulanowski et al., 2007; Renard et al., 2018; Huang et al., 2020; Mallios et al., 2020).

Dust is removed from the atmosphere by dry deposition, including gravitational settling, impaction, interception, and diffusion, and by wet deposition, which refers to the scavenging of particles by water and their subsequent removal by precipitation (Shao, 2008; Bergametti and Foret, 2014). These processes depend strongly on dust size. The comparison between different simulations performed using seven dust models within the Aerosol Comparisons between Observations and Models (AeroCom) project, suggested that dry deposition accounts for about 65-80 % of the overall dust deposition (Textor et al., 2007). Recent findings by Kok et al. (2021a), using an inverse model, align with these results, indicating that only around 15-30 % of the overall deposition is attributed to the wet mechanism, with some seasonal and regional variations. Coarse dust particles constitute the major portion of the dry deposition flux, with this type of deposition predominantly occurring near the source regions. In contrast, wet deposition emerges as the dominant mechanism for particle deposition in regions located further away from the sources (Loye-Pilot et al., 1986; Yu et al., 2019; van der Does et al., 2020).

In general, larger errors and biases are found when simulating dust deposition compared to other variables needed to represent the dust cycle, which is partly explained by its larger spatial and temporal variability (Avila et al., 1997; Kok et al., 2021b). The models included in the AeroCom project for example simulate the yearly dust deposition within a factor ten compared to the observations (Huneus et al., 2011). Accurate quantification of this deposition, although challenging, is crucial for constraining dust transport models and understanding the overall mass budget (Bergametti and Foret, 2014).

1.2. Impacts on society

Historical archives, such as the *Samguk sagi* (History of the Three Kingdoms) spanning from 57 BC to AD 938 (Chun et al., 2008), contain the first preserved descriptions of dust events. Moreover, concepts related to dust, including phenomena such as dust devils, have been documented since Ancient Greece. For instance, dust devils appear in the Greek play “Antigone” written around 450 BC (Bowker, 2011). The concern of ancient cultures regarding dust storms was rooted in fear, as they believed it to be a punishment or warning from God to the ruler (Chun et al., 2000). Nowadays, although our knowledge and understanding of these phenomena have advanced significantly, our concern about dust remains due to its negative impacts on human health, agriculture, transport, infrastructure, and its implications for climate, as described in Sect. 1.3.

Health problems caused or aggravated by dust exposure, which occur especially in arid and semi-arid regions, include eye infections, skin irritations, cardiovascular disorders and respiratory diseases, ranging from acute infections such as bronchitis or pneumonia to chronic diseases such as asthma or emphysema (Goudie, 2014; Zhang et al., 2016; Querol et al., 2019). The size of dust particles is a key point when assessing the potential hazard to human health (Brunekreef and Holgate, 2002; Karanasiou et al., 2012). In practical terms, a distinction is made between two categories: particulate matter with an aerodynamic diameter less than 10 μm , referred to as PM_{10} or “thoracic” particles, which can penetrate into the lower respiratory system, and particulate matter with an aerodynamic diameter less than 2.5 μm , known as $\text{PM}_{2.5}$ or “respirable” particles. The latter have a higher likelihood of being deposited in the gas-exchange region of the lungs, leading to more significant adverse effects (Brunekreef and Holgate, 2002). In addition, dust can carry pathogens, allergens, fungi, pollutants and toxic substances and can contribute to the outbreak of epidemics (Griffin et al., 2001; Thomson et al., 2006; De Deckker et al., 2008; García-Pando et al., 2014).

Dust events also have repercussions on economy, as a consequence of air and land transport disruptions (Schultz and Meisner, 2009), interruption of communications and physical damages on buildings (Miri et al., 2009), reduction in solar power output (Saidan et al., 2016) and crop damage, which may lead to a decrease in production yield (Stefanski and Sivakumar, 2009). At the same time, a reduction in the crop

cover makes the soil more vulnerable to water erosion (Römken et al., 2002), but also enhances wind erosion, leading eventually to soil degradation through the removal of the nutrient-rich topsoil layer (McTainsh et al., 1990; Wang et al., 2017b).

1.3. Impacts on climate

Mineral dust plays a key role in the Earth System, with a major impact on the energy and carbon cycles, and, therefore, upon climate (Knippertz and Stuut, 2014). In this section, I explore the main mechanisms through which dust impacts climate including interactions with radiation, clouds, atmospheric chemistry, biogeochemistry, cryosphere along with an assessment of dust radiative forcing. I place special emphasis on the influence of dust composition, shape, and particularly size (further explored in Sect. 1.4) on these mechanisms.

1.3.1 Interaction with radiation

Based on the Planck's law, the Sun emits radiation with shorter wavelengths compared to the Earth due to its higher temperature. Consequently, the radiation from the Sun is referred to as shortwave (SW), while Earth's radiation is termed as longwave (LW). In the SW spectrum, approximately one quarter of the total SW radiation extinguished through scattering and absorption by all aerosol particles in the atmosphere can be attributed to dust (Kinne et al., 2006; Gliß et al., 2021). The global dust optical depth (DOD) at 550 nm is estimated to be ~ 0.032 , with the Northern Hemisphere having about 1 order of magnitude more DOD (~ 0.056) than the Southern Hemisphere (~ 0.008) (Gkikas et al., 2022). In the LW spectrum, dust is the primary aerosol responsible for radiative effects due to its coarse size and abundance (Dufresne et al., 2002; Heald et al., 2014). The direct interaction of dust with SW and LW radiation leads to changes in radiation, which are further adjusted by what are known as semi-direct radiative effects (Forster et al., 2021; Adebisi et al., 2023). These effects include modifications in temperature and water vertical profiles, cloud and precipitation distributions, wind circulation and convective processes (Knippertz and Stuut, 2014; Choobari et al., 2014; Amiri-Farahani et al., 2017; Jin et al., 2021).

The direct radiative effect (DRE) of dust is the net perturbation of the radiative

balance by dust through direct interaction with SW and LW radiation and it can be evaluated at the top of the atmosphere (TOA), in the atmosphere and at the surface. The dust DRE depends on the abundance, size, shape and complex refractive index of dust particles. The complex refractive index of mineral dust consists of a real part, strongly influenced by the mineralogy of iron oxides and hydroxides (hematite versus goethite) and clay minerals (illite versus kaolinite), that governs scattering, and an imaginary part, which is controlled mainly by the volume fraction of iron oxides and hydroxides, that governs absorption (Moosmüller et al., 2012; Highwood and Ryder, 2014; Li et al., 2021).

Furthermore, the magnitude of the DRE is influenced by the presence of clouds, the dust vertical distribution and the albedo of the underlying surface (Liao and Seinfeld, 1998; Highwood and Ryder, 2014; Li et al., 2021). A key intensive optical property of dust is the single-scattering albedo (SSA), which is defined as the fraction of the extinguished radiation that is scattered by dust particles (Highwood and Ryder, 2014). For purely absorbing particles, the SSA is 0, while for purely scattering particles, it is 1. For mineral dust, SSA values range between 0.80 and 0.99 at 550 nm (Volz, 1972; Dubovik et al., 2002; Müller et al., 2009; Formenti et al., 2011a; Rocha-Lima et al., 2018). The spatial variability of the iron content in mineral dust is considered to be the primary factor responsible for this range of values (Claquin et al., 1999; Miller et al., 2014). A recent study conducted by Di Biagio et al. (2019) presented a dataset containing SSA values of dust from eight distinct source regions in the world.

The direction in which radiation is scattered when it interacts with dust particles is also important to evaluate the radiative impact, and it is often described by the scattering phase function which depends on the relative angle between the incident and emerging beams (Miller et al., 2014).

While at the global scale in the SW spectrum mineral dust is estimated to have a cooling effect at TOA because scattering of SW radiation dominates over spectral absorption, in the LW range dust has a warming effect (Sokolik and Toon, 1996; Kok et al., 2017; Di Biagio et al., 2020; Adebiyi et al., 2023). According to recent literature, the net DRE of dust, which combines the SW and LW effects, ranges from -0.5 to $+0.35 \text{ W m}^{-2}$ (Scanza et al., 2015; Kok et al., 2017; Di Biagio

et al., 2020; Li et al., 2021; Feng et al., 2022). However, earlier studies have reported larger negative estimates (Woodward, 2001; Miller et al., 2006; Choobari et al., 2014). The uncertainty associated with these estimates largely stems from the particle size distribution of dust in models (Zhao et al., 2013; Adebisi and Kok, 2020; Adebisi et al., 2023). For instance, Kok et al. (2017) showed a reduced cooling effect of dust, approximately half of previous estimates (-0.46 to -0.20 W m^{-2}), when incorporating size-resolved dust loadings constrained by the emitted dust size distribution and lifetime. Additionally, Di Biagio et al. (2020) suggested that the inclusion of particles with geometric diameters $\geq 20 \mu\text{m}$ in models could further weaken the cooling effect of dust.

Hence, the knowledge of dust particle sizes present in the atmosphere are crucial to determine whether the net DRE of dust leads to warming or cooling of the planet (Di Biagio et al., 2020; Adebisi and Kok, 2020).

1.3.2 Interaction with clouds

Dust, acting as cloud condensation nuclei (CCN) and ice nucleating particles (INPs), indirectly affects the Earth's energy balance by influencing cloud microphysical properties (DeMott et al., 2003; Atkinson et al., 2013; Hawker et al., 2021).

Under supersaturated conditions, when the size of dust particles exceeds a critical diameter, dependent on the particle solubility and ambient conditions, they initiate the nucleation of cloud droplets. Consequently, the number of dust particles acting as CCN is significantly influenced by the dust size, composition and surface area distribution (Kelly et al., 2007; Karydis et al., 2011; Mahowald et al., 2014). Besides nucleating droplet, dust has the potential to interact with warm clouds, being captured by cloud droplets within these clouds. Due to its unique composition (being insoluble) and large particle size, dust exerts a more complex impact on the microphysics of these clouds compared to other typical CCN (Karydis et al., 2011; Mahowald et al., 2014; Adebisi et al., 2023). For example, it has been observed that the increase of dust particles acting as CCN in warm stratiform clouds leads to an increase of cloud albedo and a suppression of precipitation (Rosenfeld et al., 2001). It has been also suggested that the coarsest dust particles could act as giant CCN (Levin and Ganor, 1996). These giant CCN produce larger cloud droplets that

promote collision coalescence and thereby are thought to initiate precipitation sooner (Blyth et al., 2003). Although a conceptual case proved the latter and it is clear that large dust particles have the potential to alter cloud properties and lifetime (Levin et al., 2005), there are still considerable uncertainties (Adebisi et al., 2023).

Dust is also a prominent source of INPs, exerting considerable influence on cold cloud processes all around the planet from the surface to the top of the troposphere (Murray et al., 2012; Vergara-Temprado et al., 2017; Froyd et al., 2022). The activation of INPs is influenced by various factors, including the properties of dust such as its composition, size, and surface defects, as well as environmental factors such as particle concentration, temperature and humidity (Möhler et al., 2006; Yakobi-Hancock et al., 2013; Takeishi and Storelvmo, 2018; Hawker et al., 2021). Recent modelling studies have analyzed the impact of INPs on convective clouds (Takeishi and Storelvmo, 2018; Hawker et al., 2021). Results suggest that heterogeneous ice nucleation in the mixed-phase cloud regime can diminish the availability of water for homogeneous freezing, leading to fewer and larger ice crystals in the high-latitude cirrus anvil. This finding is noteworthy as the characteristics and duration of the anvil play a crucial role in the cloud radiative effect of a convective system, given that anvils have a larger coverage area compared to the convective core and persist long after the core dissipates (Hawker et al., 2021).

1.3.3 Interaction with atmospheric chemistry

While present in the atmosphere, dust undergoes chemical composition transformations through diverse processes, including the uptake of reactive compounds in the gas phase, photochemistry, and both in-cloud and off-cloud processing (Adebisi et al., 2023). Consequently, certain properties of mineral dust, such as its hygroscopicity, which is crucial for its role as CCN or INPs, and its solubility in water, which affects its capacity for ocean fertilization, undergo modifications (Li-Jones et al., 1998; Tobo et al., 2010; Kumar et al., 2011; Tang et al., 2016).

In turn, these dust chemical composition transformations impact the composition and oxidative capacity of the atmosphere. For example, the carbonate compounds present in dust can significantly decrease atmospheric acidity by reacting with nitric

and sulfuric acid (Gatz et al., 1986; Rastogi and Sarin, 2006). Furthermore, dust influences the balance of other atmospheric components, acting as catalyser and providing surface for heterogeneous reactions. These mechanisms lead for example to a reduction in some photochemical oxidants and ozone (Güsten et al., 1996; Bonasoni et al., 2004; Cwiertny et al., 2008), and modifications in nitric oxide cycle (Ndour et al., 2008).

1.3.4 Interaction with biogeochemistry

Beyond its effects on the atmosphere, the composition and size of dust also influences the land and ocean biogeochemistry since deposited dust constitutes an important source of nutrients, especially iron, nitrogen and phosphorus (Duce and Tindale, 1991; Okin et al., 2004; Bristow et al., 2010; Jickells and Moore, 2015). Some ocean ecosystems such as large regions of the Southern Ocean and Equatorial Pacific exhibit high content of nutrient but low phytoplankton primary production, which is attributed to iron limitation (Martin et al., 1991; Mills et al., 2004; Okin et al., 2011). Therefore, the presence of iron governs the dynamics of phytoplankton blooms, which, in turn, impact the biogeochemical cycle of carbon. Mineral dust is considered nowadays as the primary source of atmospheric iron, accounting for approximately 95 % of the total burden. The remaining 5 % is attributed to combustion sources, notably anthropogenic combustion and biomass burning aerosols (Luo and Gao, 2010; Okin et al., 2011). However, not all the iron supplied by dust is directly bioavailable for marine biota and the mechanism by which it becomes bioavailable remains poorly understood. Nevertheless, there is some evidence suggesting that solubility, which appears to be influenced by the surface area to volume ratio of dust particles, plays a significant role in this process (Baker and Jickells, 2006; Baker and Croot, 2010). Furthermore, dust generally exhibits lower solubility compared to combustion-derived iron particles (Ito et al., 2021), although solubility characteristics can vary depending on the mineralogy and source of the particles (Chuang et al., 2005; Schroth et al., 2009).

In terrestrial ecosystems, phosphorus is often the limiting nutrient for productivity. Multiple studies have demonstrated the role of dust in supplying this nutrient. For instance, it has been proved that Saharan dust regulates soil

phosphorus dynamics in the Amazon Basin (Swap et al., 1992; Okin et al., 2004). Also, the input of phosphorus from dust originating in Asia has been found to be significant in sustaining productivity in Hawaiian ecosystems (Chadwick et al., 1999).

1.3.5 Interaction with cryosphere

The snowpack, a crucial element of the cryosphere, is predominantly found in high latitude and/or high elevation environments and exerts a significant influence on the global energy balance through its high albedo (Zhang, 2018; Skiles et al., 2018; Jakobs et al., 2021). Several observations and model simulations have demonstrated that the presence of light-absorbing particles (LAPs), such as black carbon (BC) and mineral dust, within the snowpack can lead to a decrease in snow albedo. This reduction in albedo enhances the absorption of solar radiation, thereby accelerating the melting of snow, with important impacts for regional climate, hydrology and ecological systems (Liou et al., 2014; Skiles and Painter, 2019; Dumont et al., 2020). Different studies have revealed that when present in significant concentrations, dust can have a dominant impact on radiative forcing among LAPs in snow (Kaspari et al., 2014; Skiles and Painter, 2018).

Although in general dust deposition in snow areas is more sporadic than BC (Di Mauro et al., 2019), there is considerable evidence of dust outbreaks leading to deposition on the snowpack reducing the surface albedo and accelerating the snow melting rate (Painter et al., 2007; Dumont et al., 2014; Di Mauro et al., 2019; Wei et al., 2021). Several studies have made significant progress in developing snow albedo models and parameterizations that incorporate the influence of dust within the snowpack (Liou et al., 2014; Flanner et al., 2021). These studies typically assume that dust particles are spherical but as shown in Sect. 1.4.2, this assumption is not the most accurate and can result in underestimations or overestimations of the dust-induced snow albedo radiative effect. A recent study has revealed opposite effects of dust size and non-sphericity on snow albedo reduction. While this reduction decreases by up to 30% as the dust effective radius increases from 1 to 5 μm , the albedo reduction is enhanced by up to 20% when assuming spheroidal dust particles instead of spheres, with a stronger enhancement for larger dust sizes and higher dust concentrations (Shi et al., 2022).

1.3.6 Dust radiative forcing

Radiative forcing (RF) serves as a tool to evaluate and compare the factors contributing to climate change (Myhre et al., 2013). The dust radiative forcing is defined as the net change in the radiative flux by dust particles prior to any response by the climate (from pre-industrial to present day) (Hansen et al., 2005; Heald et al., 2014; Miller et al., 2014). As previously discussed, dust produces a range of effects that can be categorized as direct, involving interactions with SW and LW radiation, as well as semi-direct or adjustment effects, including modifications in temperature and water vertical profiles, changes in cloud and precipitation distributions, adjustments to wind circulation patterns, and modifications to convective processes. Each of these effects leads to a distinctive dust DRE defined at the TOA, calculated as the change in Earth’s energy balance produced by the change in global dust mass loading in the modern climate due to each effect multiplied by the global modern dust loading. The sum of all these DREs then equals the effective radiative effect of dust. From these quantities it is possible to obtain the radiative perturbation due to a change in dust loading from its value in the modern climate, and then define the effective radiative forcing of dust due to the change in dust mass loading from pre-industrial to modern times (Kok et al., 2023). Note that the term “effective” refers to the fact that when assessing the change in net TOA downward radiative flux caused by dust, it allows atmospheric temperatures, water vapor, and clouds to readjust to radiative equilibrium, while keeping the global mean surface temperature or a portion of surface conditions unchanged.

Usually the term RF denotes radiative perturbations that are entirely from anthropogenic forcing agents (Ginoux et al., 2012; Wu et al., 2020). Nevertheless, since dust is a natural aerosol that is influenced by both climate changes and human land-use changes, a radiative perturbation resulting from a historical change in dust can be attributed partly to changes in human land-use (considered a forcing) and partly to natural and anthropogenic climate changes (considered a feedback). In light of the complexity to disentangle these two contributions, the recent study conducted by Kok et al. (2023) refers to the dust effective RF encompassing the entire radiative perturbation due to the historical change in dust, that estimates to be $-0.2 \pm 0.5 \text{ W m}^{-2}$ (90 % confidence interval). This finding suggests that dust net

cools the climate. Furthermore, the study indicates that compared to pre-industrial levels, the global mass loading of dust in the modern climate has increased by $55 \pm 30\%$. This increase has resulted in a global mean effective radiative forcing of $-0.07 \pm 0.18 \text{ W m}^{-2}$, which somewhat counteracts greenhouse warming.

Unfortunately, current climate models fail to account for this increase in dust, thereby excluding the associated RF. Consequently, climate change projections and assessments of climate sensitivity are subject to bias (Kok et al., 2023). Further research is necessary to better understand and constrain the dust radiative effects on climate. An essential factor in this pursuit is the understanding of dust size, as fine dust particles tend to induce a cooling effect on a global scale, while coarse and super-coarse dust aerosols contribute to warming, thereby counteracting the cooling effect (Otto et al., 2011; Ryder et al., 2018; Adebisi et al., 2023).

1.4. Key dust microphysical properties

Figure 1.3 depicts a scanning electron microscope image of a dust sample from a field campaign conducted in Morocco in 2019, which will be further discussed in this thesis. The dust sample is composed by a variety of mineral particles exhibiting distinct composition, shapes, and sizes. In this section, I delve into these key dust microphysical properties.

1.4.1 Mineralogical composition

Dust consists of a mixture of different minerals including feldspars (albite/anorthite and orthoclase), quartz, clay minerals (mica/illite, kaolinite, palygorskite, chlorite/clinochlore and smectite/montmorillonite), carbonate minerals (mainly calcite and dolomite), salts (mainly halite and gypsum), iron oxides and hydroxides (mostly goethite and hematite) and other oxides or hydroxides of titanium, magnesium and aluminium (Schütz and Seibert, 1987; Caquineau et al., 1998; Formenti et al., 2008; Kandler et al., 2009; Shen et al., 2009; Scheuven et al., 2013; Baldo et al., 2020). In Sects. 1.2 and 1.3 I have provided an overview of how dust affects both our society and climate. Here, I highlight the specific roles of some of these dust minerals in influencing the Earth System: (1) Clay minerals have a notable impact on optical

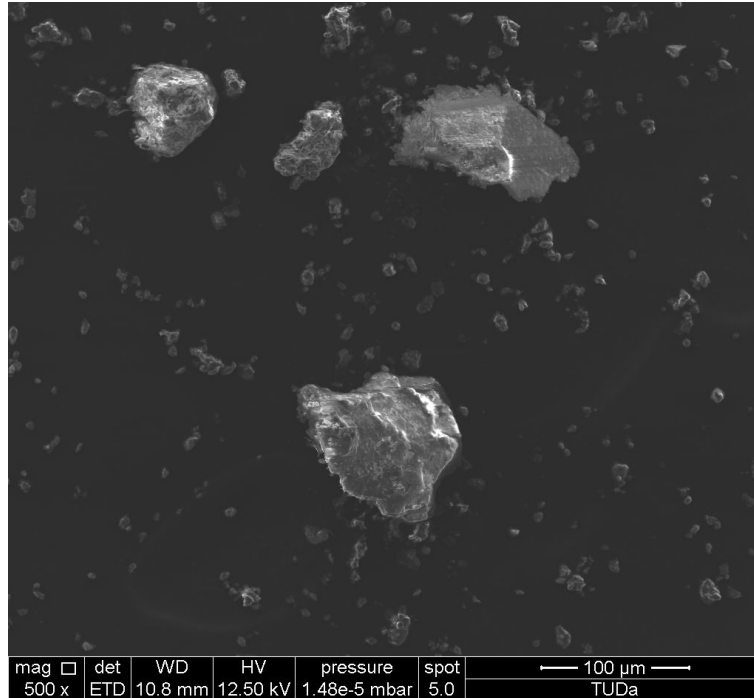


Figure 1.3: Scanning electron microscope image of a dust sample collected during the FRAGMENT field campaign in Morocco in September 2019. Image credit: A. Panta.

aspects such as SW radiation scattering and LW absorption and emission. However, their contribution to SW absorption is relatively low due to their low imaginary component of the refractive index (Sokolik et al., 1998; Sokolik and Toon, 1999); (2) Iron oxides and oxi-hydroxides, being hematite and goethite the most prevalent species, play a dominant role for radiation absorption as their imaginary component of the refractive index is significantly higher (by orders of magnitude) compared to clay minerals (Sokolik and Toon, 1999; Zhang et al., 2015); (3) k-feldspars and to a lesser extent quartz have a great efficiency as INPs, which can significantly impact cloud processes (Yakobi-Hancock et al., 2013; Atkinson et al., 2013; Harrison et al., 2019; Chatziparaschos et al., 2023); (4) Carbonates exhibit a high reactivity and can easily be involved in interactions with acids such as sulfuric or nitric acid. Through this mechanism, they have the potential to significantly enhance their hygroscopicity (Laskin et al., 2005; Matsuki et al., 2005); (5) Iron, phosphorus, calcium and magnesium compounds act as efficient nutrients for both marine and terrestrial ecosystems (Okin et al., 2004; Boyd et al., 2010; Wang et al., 2021b) and (6) Chromium and other heavy metals present a high toxicity that can alter marine

1.4. Key dust microphysical properties

primary production and exert adverse effects on human health (Paytan et al., 2009; Wood et al., 2010).

These dust minerals are usually internally or externally mixed (among themselves and with other aerosol species in the atmosphere) and exhibit several morphologies (e.g. crystalline structures, aggregates and core-shell configuration) and sizes. Clays, predominantly illite and kaolinite, are relatively more abundant in the fine fraction of dust (particles with geometric diameters $< 2.5 \mu\text{m}$) while quartz and calcium carbonate prevail in the coarser fractions (particles with geometric diameters $>2.5 \mu\text{m}$). Titanium and iron oxides are ubiquitous in all dust sizes (Kandler et al., 2007, 2009; Formenti et al., 2011b; Kandler et al., 2020).

Currently the relationship between source sediment composition and airborne dust composition is poorly understood. Also, although the type and proportions of soil minerals vary with the source region, current global atlases of mineralogical composition are poorly constrained by observations (e.g. Caquineau et al., 1998; Claquin et al., 1999; Journet et al., 2014). Clear differences in composition can be observed when comparing some high latitude sources such as those from Iceland, which are primarily composed of plagioclase and pyroxene, and contain approximately 60-90% of aluminosilicate glass (Moroni et al., 2018; Baldo et al., 2020), with mid-latitude dust, which is composed mainly of quartz, feldspars, calcite and clays (Avila et al., 1997; Shi et al., 2005; Kandler and Scheuvsens, 2019). Although smaller, there are also differences in composition among mid-latitude sources. Ratios between minerals such as I/K (I: illite, K: kaolinite) and Fe/Al (Fe: iron, Al: aluminium), and the abundance of certain minerals (i.e. carbonate content) can be sensitive tracers and compositional fingerprints of a source region (Caquineau et al., 1998; Shen et al., 2009; Formenti et al., 2011b).

1.4.2 Shape

As depicted in Fig. 1.3 and supported by numerous in situ measurements, the majority of dust particles are highly aspherical, exhibiting length-to-width (aspect ratio) and height-to-width ratios that substantially deviate from unity (e.g. Okada et al., 2001; Chou et al., 2008; Kandler et al., 2011; Huang et al., 2020; Panta et al., 2023). To account for the non-sphericity of dust, most retrieval algorithms of passive

remote sensing instruments suggest the application of spheroid models, considering an equal distribution of prolate and oblate spheroids with the same length-to-height ratio (Dubovik et al., 2006). However, in most current climate models dust particles are assumed to be spherical (Gliß et al., 2021). A recent study that compiled dozens of dust shape measurements revealed considerable discrepancies among the three perpendicular axes for the majority of dust particles and thus suggested that approximating dust shape by tri-axial ellipsoids would be more realistic (Huang et al., 2020). This study concluded that accounting for dust asphericity increases dust lifetime with respect to gravitational settling by $\sim 20\%$, which could also help to explain the transport of coarser dust particles. Furthermore, dust optical properties inferred assuming tri-axial ellipsoids agree with observations substantially better than when approximating dust by spheres or spheroids (Huang et al., 2020). This indicates that constraining dust shape is crucial to determine its optical and aerodynamic properties (Bi et al., 2009; Saito and Yang, 2021; Kong et al., 2022) and therefore make accurate estimations of dust impacts in the Earth System.

1.4.3 Size

Given the non-sphericity of dust particles, the characterization of their size requires the use of an “equivalent” diameter, defined based on a certain property or behaviour of the irregular particle that is then linked to that of a perfect sphere (Kulkarni et al., 2011). The most common equivalent diameters used in atmospheric dust studies are: (1) the volume equivalent diameter or geometric diameter; (2) the optical equivalent diameter; (3) the projected area equivalent diameter; and (4) the aerodynamic equivalent diameter.

The geometric diameter is defined as the diameter of a sphere that has the same volume and density as the irregularly shaped dust particle (Hinds, 1999). This is the prevailing equivalent diameter used in dust models (Mahowald et al., 2014). The optical equivalent diameter is the diameter of a calibration particle, usually a polystyrene latex sphere or equivalent non-absorbing material, that scatters the same amount of radiation as an irregularly shaped dust particle (Formenti et al., 2011b). This diameter is used in optical particle counters (OPC), widely employed during field campaigns for measuring size-resolved dust concentrations (Sow et al., 2009;

1.4. Key dust microphysical properties

Shao et al., 2011a; Dupont et al., 2021). The projected area equivalent diameter is the diameter of a circle having the same area as an irregularly shaped dust particle projected on a two-dimensional image (Kandler et al., 2007; Huang et al., 2020). This diameter is employed for analysing particles collected on filters using electron microscopy (Kandler et al., 2007; Panta et al., 2023). The aerodynamic equivalent diameter represents the diameter of a sphere with a standard density (1000 kg m^{-3}) exhibiting the same terminal velocity as an irregularly shaped dust particle (Hinds, 1999). This diameter is commonly used for evaluating the impact of aerosols on human health and establishing air pollution standards (Esworthy and McCarthy, 2013). It is worth highlighting that the density of dust is ~ 2.5 higher than the standard density used to define the aerodynamic diameter (Fratini et al., 2007; Reid et al., 2008; Kaaden et al., 2009; Sow et al., 2009; Kok et al., 2021b).

The conversions among diameter types depend on shape, index of refraction and dust density (Reid et al., 2003), and have been overlooked in many studies. Recent advancements in the field have enabled the establishment of conversions between the four types of diameters, while also accounting for the asphericity of dust particles assuming tri-axial spheroids (Huang et al., 2021). The findings of this study showed that (1) optical equivalent diameters exceeding approximately $8 \mu\text{m}$ tend to underestimate the corresponding geometric equivalent diameters, (2) projected-area equivalent diameters, on the other hand, exhibit an overestimation of approximately $\sim 56\%$ in comparison to geometric equivalent diameters, and (3) aerodynamic equivalent diameters surpass geometric equivalent diameters by approximately $\sim 45\%$. These conversions are key to properly compare dust observations, often expressed in optical, area or aerodynamic equivalent diameters, with models that use the geometric diameters.

While the size of an individual particle is defined by any of the previously mentioned diameters, the particle size distribution (PSD) of a dust aerosol population refers to the relative concentrations of particles across different size ranges in terms of number, mass, surface area or volume (Seinfeld and Pandis, 2006). Mathematically, the PSD is expressed as follows:

$$P(D) = \int_0^D p(D') \delta D' \quad (1.1)$$

where $p(D')$ represents the particle-size distribution density function, δ denotes differentiation and D the dust particle diameter.

Unlike other aerosols in the atmosphere, mineral dust particle sizes span more than three orders of magnitude, from $<0.1\ \mu\text{m}$ to more than $100\ \mu\text{m}$ in diameter. In atmospheric sciences, aerosols have been traditionally classified in two size modes called fine and coarse (Seinfeld and Pandis, 2006). The fine mode is in turn subdivided into the nucleation mode, an Aitken mode and accumulation mode (Whitby and Cantrell, 1976; Finlayson-Pitts and Pitts Jr, 1999). Dust particles were initially associated with the coarse mode but subsequent research has clarified their presence in the fine mode as well. Nonetheless, the boundary diameter between fine and coarse dust modes has been revised multiple times and there are inconsistencies among studies regarding the specific type of diameter used to define this boundary (Walton, 1954; Heintzenberg, 1989; Rajot et al., 2008; Mahowald et al., 2014; Adebisi and Kok, 2020). A similar situation arises with the upper limit of the coarse mode, for which there is no consensus. This situation promoted the introduction of various terms such as “large coarse-mode”, “super-coarse”, and “giant particles” in the classification of dust particle sizes (Weinzierl et al., 2011; Pérez García-Pando et al., 2016; Jeong et al., 2014). In an attempt to avoid more inconsistencies in the future and ensure comparison across the literature, the following terminology for classifying atmospheric dust particles in terms of geometric diameter (D) has been recently proposed in Adebisi et al. (2023): (1) Fine dust $D < 2.5\ \mu\text{m}$, (2) Coarse dust $2.5 < D < 10\ \mu\text{m}$, (3) Super-coarse dust $10 < D < 62.5\ \mu\text{m}$ and (4) Giant dust $D > 62.5\ \mu\text{m}$.

Dust PSD exhibits significant spatio-temporal variations and undergoes changes throughout the various stages of the dust cycle. As discussed in Sects. 1.2 and 1.3 the impacts of dust on the Earth System are strongly influenced by its size, and given the wide range of sizes, these impacts are numerous and diverse. This thesis specifically emphasizes on the dust PSD at emission, recognizing its crucial role in shaping the overall behavior of dust in the atmosphere.

Physics of dust emission

In this chapter the focus is directed towards dust emission, with special emphasis on the emitted dust PSD, which is a central component of this thesis.

2.1. Basic physical concepts

Dust emission is a dynamic process wherein soil particles become detached from arid or semiarid surfaces and are propelled into the atmosphere due to wind shear stress (Fig. 2.1). The intensity of dust emission is influenced by various factors, including the presence and size of roughness elements (such as stones, vegetation, and dunes), atmospheric conditions (such as wind shear, turbulence, and convection), topsoil properties of the source area (such as soil particle size and moisture), land-use and other factors. During a wind erosion event, two distinct fluxes can be identified: a horizontal or saltation flux, where particles hop along the surface in the direction of the wind, and a vertical or emitted dust flux. This section provides further elucidation of fundamental physical concepts associated with dust emission.

2.1.1 Soil particle size distribution

Soils contain particles with diameters ranging from less than 0.1 μm to more than 2 mm and gravel, encompassing pebbles, cobbles, and boulders that exceed 2 mm in diameter. Soil particles susceptible to being lifted by wind are typically classified based on their diameter, D , in sand ($50\text{-}63 \mu\text{m} < D \leq 2000 \mu\text{m}$), silt ($2\text{-}4 \mu\text{m} < D \leq 50\text{-}63 \mu\text{m}$) and clay ($D < 2\text{-}4 \mu\text{m}$) (Shao, 2008; Perlwitz et al., 2015a). It is important to note that the specific size intervals may vary depending on the particle size classification system used, such as those proposed by the United States Department of Agriculture or the World Reference Base for Soil Resources. Additionally, many soil particles are bound together by interparticle cohesion forces, forming larger aggregates.

The relationship between the emitted dust PSD (introduced in Chap. 1.4.3) and

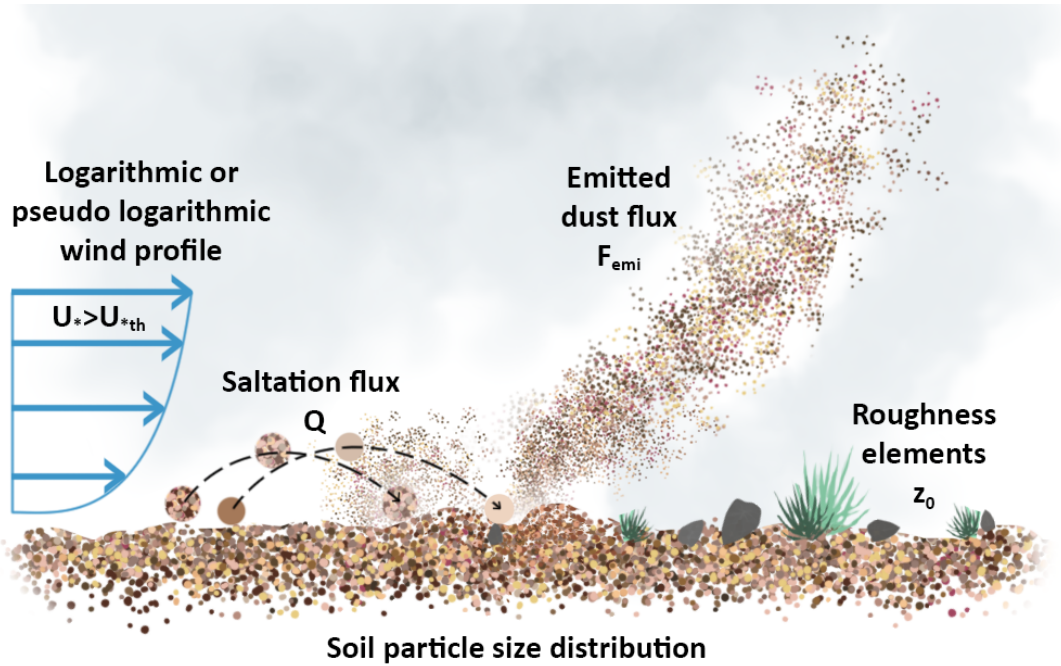


Figure 2.1: A general overview of dust emission: basic concepts involved.

its parent soil PSD is complex and is still not fully understood (Marticorena, 2014). However, as outlined in Sect. 2.3 some theoretical frameworks utilize the parent soil PSD as an input parameter (Shao, 2001, 2004; Kok, 2011a,b; Kok et al., 2014). The most commonly employed techniques for measuring the parent soil PSD are sieving and laser diffraction. Typically, two distinct types of PSDs are defined for the parent soil: (1) the minimally-dispersed PSD, denoted as $p_m(D)$, which reflects the sample subjected to minimal disturbance to preserve dust aggregates as much as possible; and (2) the fully-dispersed PSD, denoted as $p_f(D)$, representing the opposite scenario where aggregates are broken up through mechanical and chemical dispersion methods (Shao, 2008).

2.1.2 Wind friction velocity, u_*

Wind friction velocity, u_* , is generally an important scaling parameter in boundary layer meteorology and hence, it is a key parameter in wind erosion studies. The airflow in contact with the Earth's surface experiences deceleration due to drag forces, which arise from both tangential stresses and pressure gradients (Arya, 2001). Therefore, wind speed in the atmospheric boundary layer (ABL) typically increases with height.

2.1. Basic physical concepts

The force exerted on the surface by the wind along its direction is called the wind shear stress, τ , and it is transmitted downward as a momentum flux. This transfer is done through both turbulent and molecular motion. Wind shear stress can be expressed as the sum of the Reynolds shear stress, τ_R , and the viscous shear stress, τ_M :

$$\tau = \tau_R + \tau_M \quad (2.1)$$

The lowest 10 % or so of the ABL, where the Coriolis effect can be neglected, is called the surface boundary layer (SBL). In the viscous sub-layer, which is immediately adjacent to the surface, turbulence becomes negligible and molecular motion is dominant, i.e. $\tau_M > \tau_R$. In the remainder of the SBL, i.e. moving away from the viscous sub-layer, the situation is opposite. However, the total wind shear stress, τ , is approximately constant with height in the SBL (Shao, 2008). The shear stress of a flowing Newtonian fluid such as the air is proportional to the vertical gradient of the horizontal wind speed, $\partial U/\partial z$, with the dynamical viscosity, μ , being the proportionality constant:

$$\tau = \mu \frac{\partial U}{\partial z} \quad (2.2)$$

In analogy with Newton's law of viscosity (Eq. 2.2), Boussinesq (1877) proposed that the turbulent flux of momentum in the SBL could be expressed in terms of the mean horizontal wind speed through the definition of an eddy exchange coefficient of momentum, K_m , also called eddy viscosity, analogous to the molecular kinematic viscosity:

$$\tau = K_m \rho_{air} \frac{\partial U}{\partial z} \quad (2.3)$$

where ρ_{air} is the air density.

A similar flux-gradient relationship is also applied to other turbulent fluxes such as mass, heat or water vapour and is known as K-theory. This theory assumes that the turbulent transfer is done by eddies whose sizes are much smaller than the characteristic scale of mean quantity variation. By analogy to the kinetic

energy dispersion of wind due to eddy turbulence, it is possible to define a wind friction velocity (also known as shear stress velocity). This friction velocity, which is homogeneous along the vertical, is associated with the transport of momentum between the different levels. Mathematically, it is expressed as:

$$u_* = \sqrt{\frac{\tau}{\rho_{air}}} \quad (2.4)$$

2.1.3 Logarithmic wind profile and roughness length, z_0

The mean wind velocity profile can be expressed by a logarithmic or pseudo-logarithmic form in the SBL which is above a rough or smooth surface (e.g. Stull, 1988; Kaimal and Finnigan, 1994; Arya, 2001; Foken and Napo, 2008; Shao, 2008). The flow regime can be stable, neutral or unstable. In the case of a neutrally stratified SBL, the eddy viscosity, K_m , is represented by:

$$K_m = \kappa u_* z \quad (2.5)$$

where κ is the von Karman constant, u_* is the friction velocity and z the height above the surface (Shao, 2008). Applying Eq. 2.5 in Eq. 2.3 and equaling to u_* from Eq. 2.4, we obtain:

$$\frac{\partial U}{\partial z} = \frac{u_*}{\kappa z} \quad (2.6)$$

Integrating Eq. 2.6 over height z , we obtain the logarithmic wind profile:

$$U(z) = \frac{u_*}{\kappa} \left[\ln \left(\frac{z}{z_0} \right) \right] \quad (2.7)$$

where $U(z)$ denotes the mean horizontal wind speed at height z , κ is the von Karman constant and z_0 is the aerodynamic roughness length of the surface. z_0 is a widely used parameter in ABL and wind erosion studies that represents the surface's ability to absorb momentum and is related to the size of the roughness elements. According to Eq. 2.7, when $z = z_0$ the mean wind becomes to zero. In the case of a fixed mean wind speed at z , a larger z_0 corresponds to a larger u_* or greater downward momentum flux. For non-neutral conditions (stable or unstable), the wind profile

deviates from the logarithmic relationship. Monin-Obukhov similarity theory (Monin and Obukhov, 1954) allows for extending the logarithmic wind profile to non-neutral conditions introducing a correction (e.g. Stull, 1988; Kaimal and Finnigan, 1994; Arya, 2001; Foken and Napo, 2008; Shao, 2008):

$$U(z) = \frac{u_*}{\kappa} \left[\ln \left(\frac{z}{z_0} \right) - \Psi_m \right] \quad (2.8)$$

with $\Psi_m = \int_{\zeta_0}^{\zeta} [1 - \Phi_m(\zeta')] \frac{d\zeta'}{\zeta}$, where Φ_m is the similarity function for momentum, L is the Obukhov length, $\zeta = z/L$ and $\zeta_0 = z_0/L$. In the case of unstable conditions, stronger turbulence translates into a more efficient transfer of momentum from higher to lower levels, increasing the wind speed close to the surface.

2.1.4 Threshold friction velocity, u_{*th}

There are different forces acting on the soil particles under the influence of an air stream, including the gravity force, the aerodynamic drag, the aerodynamic lift and interparticle cohesive forces (electrostatic, capillary and chemical binding forces). The balance of these forces is affected by a wide range of factors, with particle size being one of the most significant. Normally, the dominant forces for large, medium and fine particles are, respectively, the gravity force (proportional to D^3), the aerodynamic force (proportional to D^2) and the cohesive forces (proportional to D when considering only Van der Waals forces in an idealized case). According to their dependence upon particle size, the decay of the interparticle cohesive forces is slower than that of gravity and aerodynamic forces (Shao, 2008).

The minimum friction velocity required to set the first particles in motion due to the fluid action is called the threshold friction velocity, u_{*th} . When $u_* > u_{*th}$, the retarding forces (weight and interparticle cohesive forces) are overcome by the aerodynamic forces, and particle movement is initiated. Bagnold (1941) was the first to propose an expression to calculate u_{*th} , based on particle diameter from the balance between aerodynamic drag and gravity forces, assuming spherical particles. As a result, u_{*th} is proportional to $D^{1/2}$, which is consistent with observations for grains larger than 100 μm but not for smaller sizes. Wind tunnel experiments revealed a minimum u_{*th} for diameters around 60-100 μm and its increase with decreasing diameters below 100 μm (Chepil, 1951). This increase was explained through cohesive

forces, whose effect on small particles cannot be neglected and was therefore included along with aerodynamic lift in new formulations proposed by Iversen and White (1982) and Greeley and Iversen (1985). Later, Shao and Lu (2000) proposed a simpler formulation based on a theoretical expression for interparticle cohesive forces, mainly attributed to van der Waals and electrostatic forces. More recently, Shao and Klose (2016) proposed a statistical treatment of interparticle cohesion due to the complex interactions of particle properties affecting this force. On this basis, they assume that a fraction of particles experiences below-average interparticle cohesion and hence below-average u_{*th} , which is most relevant for particles $<100\ \mu\text{m}$. Figure 2.2 shows u_{*th} as a function of particle diameter based on the formulations proposed by Greeley and Iversen (1985); Shao and Lu (2000) and Shao and Klose (2016) together with some measurements (Bagnold, 1937; Chepil, 1945; Zingg, 1952; Iversen et al., 1976; Fletcher, 1976a,b; Greeley et al., 2003). Moisture increases the cohesion between soil particles leading to an increase in u_{*th} (McKenna-Neuman and Nickling, 1989). This dependence is affected by the soil texture, especially by the soil clay content (Fécan et al., 1999).

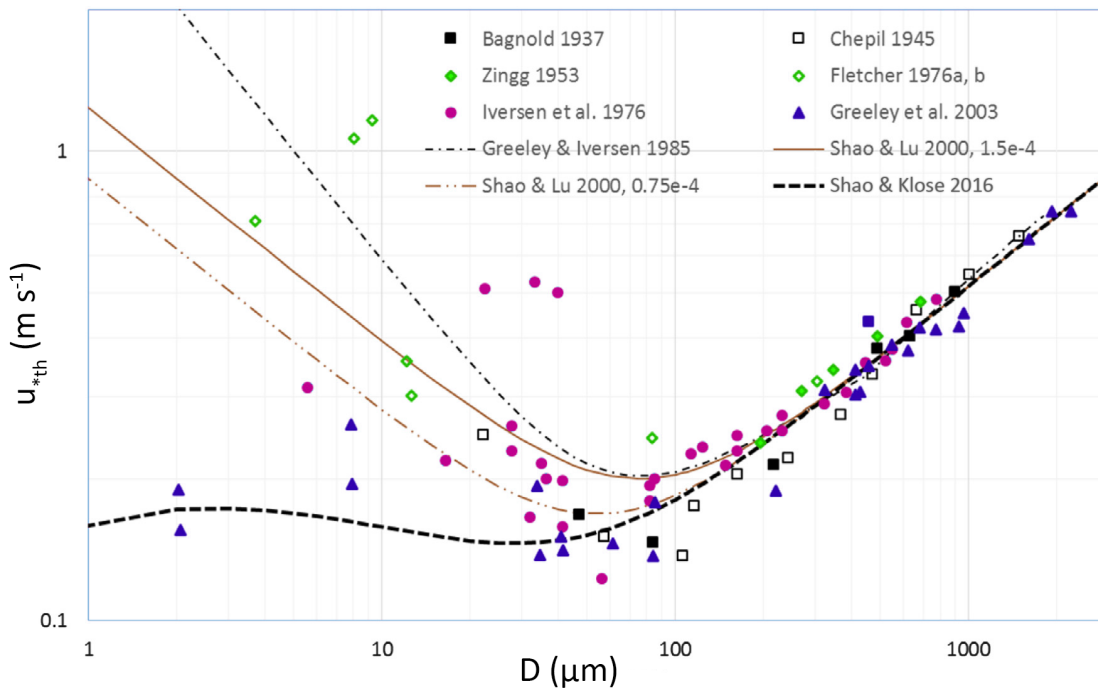


Figure 2.2: Relationship between threshold friction velocity and particle diameter based on theoretical expressions and experimental measurements. Figure modified from Shao and Klose (2016).

Traditionally, the u_{*th} has been used to describe the land surface threshold,

taking into account both soil and vegetation components. In this context, a drag partition correction calculated as a function of roughness height (Marticorena and Bergametti, 1995) or roughness density (Raupach et al., 1993) has been typically applied to the threshold to represent surface roughness effects on wind erosion. However, although phenomenologically correct, this approach overestimates the friction velocity exerted on the bare soil (Webb et al., 2014; Kok et al., 2014). Alternatively, a so-called “soil” threshold friction velocity can be considered to describe the soil surface erodibility alone, independent of roughness. In this case, the drag partitioning between roughness elements and the soil surface can be directly applied to the friction velocity (Okin, 2008; Webb et al., 2014; Klose et al., 2021; Leung et al., 2023).

2.1.5 Horizontal or saltation flux, Q

The amount of soil particles that move parallel to the ground in saltation is referred to as horizontal or saltation flux, Q . Q is defined as the mass of soil particles that crosses a unit vertical surface of infinite height perpendicular to the eroding surface per unit time, in wind direction (Marticorena and Bergametti, 1995; Alfaro and Gomes, 2001). Several studies have focused on the relationship of Q with soil particle size, surface conditions and u_* , and have proposed different numerical expressions to calculate it (Gillette, 1974a; Sørensen, 1985; Shao et al., 1993; Greeley et al., 1996; Martin and Kok, 2017a; Gillies et al., 2018). In most of these expressions Q is proportional to u_*^3 , which agrees with experimental data and theoretical considerations (Gillette and Morales, 1979; Leys and Raupach, 1991; Shao et al., 1993).

2.1.6 Vertical or emitted dust flux, F_{emi}

The vertical or emitted dust flux, F_{emi} , is defined as the mass of dust particles crossing a horizontal unit area adjacent to the surface per unit time (Marticorena and Bergametti, 1995). As described in Sect. 2.2, dust is more efficiently emitted by impacting saltating grains than directly by aerodynamic forces. F_{emi} is therefore often related to Q , establishing an indirect relationship between F_{emi} and wind. Experimentally, it has been found that according to the surface morphology and land-use, F_{emi} is proportional to u_*^n with n varying from 2.9 to 4.4 (Nickling and

Gillies, 1989, 1993; Shao, 2008). The relationship between the vertical and horizontal fluxes, i.e. the ratio between the dust mass ejected by saltation and the mass of the saltators is called the sandblasting efficiency, α .

2.2. Mechanisms of dust emission

The entrainment of particles into the atmosphere depends on the balance of the forces acting upon the soil particles resting on the Earth surface. Therefore, the following three physical mechanisms proposed for dust emission are closely related to these forces (gravity, aerodynamic and cohesive forces) and their relative importance.

2.2.1 Aerodynamic entrainment

Loose particles at the surface can be lifted by aerodynamic forces (Fig. 2.3a). The efficiency of aerodynamic dust entrainment is relatively low due to the generally strong interparticle cohesive forces acting on dust-sized particles (Loosmore and Hunt, 2000). However, due to the various factors contributing to interparticle cohesion, it can be expected that a fraction of the surface particles exhibits a substantially smaller-than-average cohesion. Dust particles can then be entrained directly by aerodynamic forces (Roney and White, 2004; Macpherson et al., 2008; Klose and Shao, 2013; Parajuli et al., 2016). This process is likely most pronounced under unstable atmospheric conditions, where atmospheric turbulence generates intense localized surface shear stresses, even under weak mean wind conditions (Klose and Shao, 2013; Klose et al., 2014).

2.2.2 Saltation bombardment or sandblasting

Wind forces set in motion sand grains or aggregates that strike the surface in a hopping motion called saltation. Often these local impacts are strong enough to break the binding forces that keep dust particles at the surface and eject them into the air (Gomes et al., 1990; Shao et al., 1993; Alfaro et al., 1997)(Fig. 2.3b). Whether particles are transported in saltation or in suspension is determined by the balance between the u_{*th} and the terminal velocity of a particle (resulting from the equilibrium of the gravitational and drag forces). Experimentally, saltation bombardment was

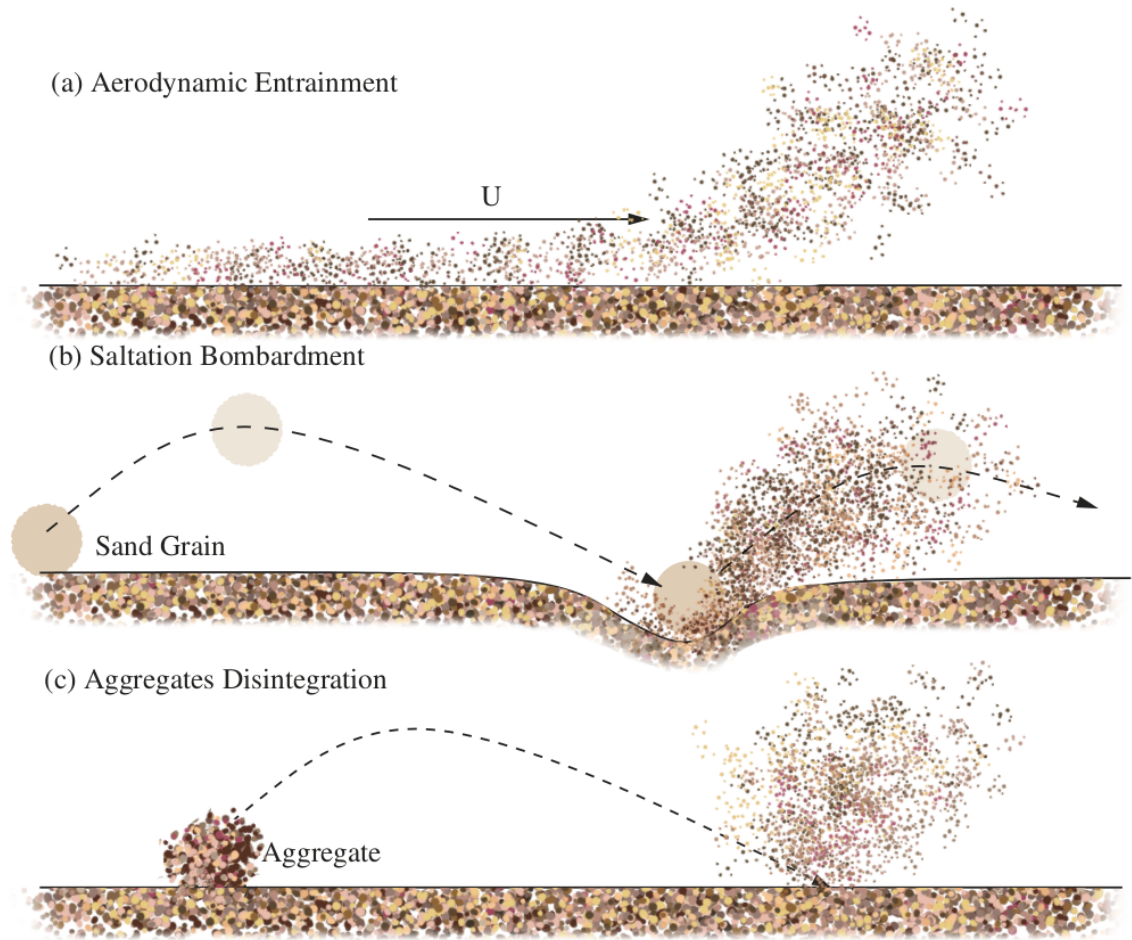


Figure 2.3: Dust emission mechanisms. (a) Aerodynamic entrainment. (b) Saltation bombardment. (c) Aggregates disintegration. Particle colors represent dust mineralogy. Figure modified from Shao (2008)

found to produce one order of magnitude more dust than aerodynamic entrainment (Shao et al., 1993). As dust emission through saltation bombardment is known to be very efficient, it is the main mechanism described in most theoretical frameworks (Sect. 2.3).

2.2.3 Aggregate disintegration or auto-abrasion

Under natural conditions saltating particle aggregates might be disintegrated when they impact the ground, leading to dust emission (Shao, 2008; Kok, 2011a)(Fig. 2.3c). The significance of this mechanism is likely comparable to that of saltation

bombardment (Shao, 2004, 2008).

2.3. Theoretical frameworks to estimate dust emission and its PSD

In the last decades different theoretical frameworks have been developed to represent dust emission, based on one or more of the mechanisms described in Sect. 2.2, and the PSD of the emitted dust. Given the significant role of saltation bombardment in dust emission (Shao et al., 1993), most of these theoretical frameworks include: (1) a quantitative characterization of saltation intensity based on specific wind, surface, and soil conditions; and (2) a description of the relationship between the dust emission rate and the intensity of saltation.

Moreover, each of these theoretical frameworks relies on specific assumptions or simplifications, making their implementation as emission schemes in models possible, but introducing inherent limitations. It is worth noting that these schemes can be categorized into two types: bulk schemes and spectral schemes. Bulk schemes predict the overall dust emission rate and then typically assume a prescribed emitted dust PSD, that can be empirically or theoretically based, whereas intrinsically spectral schemes directly predict dust emission rates for different particle size ranges or bins. In turn, all these schemes range from formulations that are simplified and semi-empirically based (e.g. Gillette and Passi, 1988; Marticorena and Bergametti, 1995) to those that aim to represent the physics of the emission processes (e.g. Shao et al., 1993, 1996; Lu and Shao, 1999; Alfaro and Gomes, 2001; Shao, 2004; Shao et al., 2011a; Kok et al., 2014; Klose et al., 2014).

First theoretical frameworks trying to represent the physics of dust emission focused on the parameterization of the saltation bombardment. On the basis of how dust emission was related to saltation, these first frameworks were classified into energy-based and volume-removal based.

In the original energy-based theoretical framework the difference of kinetic energy between the saltators impacting the surface and the particles ejected after the collision was related with the binding energy required to break the interparticle bonds between the dust grains. Several dust emission schemes used in models have been

developed in the past within this theoretical framework, including those formulated by Shao et al. (1993, 1996) and Alfaro and Gomes (2001). The concept of binding energy provides an alternative to the utilization of cohesive forces, as the latter approach requires determining the directions of these forces. However, accurately determining the binding energy between dust particles is challenging on either theoretical or experimental grounds. On the one hand, its theoretical estimates vary significantly across a broad range of values (Shao and Leslie, 1997). On the other hand, during the particle-surface collision, the kinetic energy of saltating particles is not conservative, as a proportion of it converts to heat (Shao et al., 1993). Furthermore, other factors including static electricity, moisture content, and the presence of salt also influence the binding energy (Shao, 2001). A more recent energy-based scheme was developed by Kok et al. (2014). In this case, it was assumed that dust emission is only generated when the impact energy of a saltator surpasses the energy required for dust aggregate fragmentation. This scheme is not valid for soils for which the horizontal saltation flux at a given point in time is limited by the availability of sand-sized sediment. Additionally, the application of this scheme for very erosion-resistant soils, such as crusted soils, and for soils in which dust emission is dominated by any specific process other than fragmentation might be limited.

The volume-removal based theoretical framework also considers saltation as the main mechanism for dust emission but eliminates the need to calculate the particle binding energy. This framework, supported by high-speed photography during some wind-tunnel experiments (Rice et al., 1996a,b), assumes that when a saltator impacts the surface, it generates a crater whose volume is proportional to the ejected dust. Therefore, the dust emission resulting from numerous saltating particles can be estimated by a superposition of the individual impacting events. In this case, the sandblasting efficiency depends on soil texture and soil plastic pressure (representing the soil resistance to particle impacts). Examples of dust emission schemes used in models developed within this theoretical framework include those formulated by Lu and Shao (1999); Shao (2001, 2004); and Shao et al. (2011a). The limitation of this theoretical framework stems from the lack of global-scale measurements of soil plastic pressure, which leads to make assumptions about its value based on few measurements (Zimbone et al., 1996; Rice et al., 1997; Goossens, 2004).

The schemes described above do not take into account the dust emitted by

aerodynamic entrainment. Klose and Shao (2012) and Klose et al. (2014) developed a parameterization to represent the aerodynamic entrainment of dust by convective turbulence that takes place without saltation.

Concerning the representation of the PSD at emission, the schemes developed by Alfaro and Gomes (2001) and Shao (2001, 2004) agree in that the emitted dust PSD should shift towards finer sizes with increasing wind speed. Alfaro and Gomes (2001) parameterizes the emitted dust PSD using three log-normal modes. The proportions of these modes are determined by both the binding energy of the soil aggregates and the kinetic energy of the saltators that impact the soil. As wind speed increases, the kinetic energy of the saltators also increases, resulting in the release of finer particles due to more energetic impacts with the ground. Shao (2001, 2004) assume that the PSD of the emitted dust depends on the minimally-disturbed and fully-disturbed soil size distributions and varies with wind intensity. The stronger the erosion event, the more dust contained in aggregates can be released since the increase in wind speed is seen as an extra supply of energy that allows disaggregation and therefore, an enrichment of finer emitted particles.

An alternative theoretical framework for representing the dust PSD at emission is based on the analogy with the fragmentation of brittle materials (Kolmogorov, 1941; Åström, 2006). Two examples of schemes developed within this theoretical framework are those formulated by Kok (2011a) and Meng et al. (2022). When a brittle material such as glass or gypsum receives a large amount of energy, it can be fragmented into smaller particles of different sizes. Kok (2011a) applies this concept to the release of dust particles from the soil or from saltating aggregates. The advantage of this framework is that the size distribution of the resulting fragments follows a potential law (Åström, 2006) and is thus scale invariant (Bak et al., 1987). This means that in contrast to other theories, this theoretical framework assumes that the PSD of the emitted dust does not depend on either wind speed or the minimally-disturbed soil PSD. However, this theory is not applicable for aerodynamically lifted dust, for very cohesive soils, or for dust larger than $\sim 20 \mu\text{m}$ in diameter, whose emission is not always due to fragmenting impacts. Very recently this theory has been extended to account for these coarser particles (Meng et al., 2022). This updated parameterization has been implemented in the Community Earth System Model (CESM) and although it reproduces the abundance of dust larger than $\sim 20 \mu\text{m}$ in diameter close to dust

source regions, the CESM model still substantially underestimates it in dust outflow regions. Meng et al. (2022) suggests that the underestimation of the presence of dust with diameters larger than $\sim 20 \mu\text{m}$ by models is in part due to its underestimation at emission. In Sect. 2.4 I focus on the current observations of the emitted dust PSD and its variability.

2.4. The dust particle size distribution and its variability at emission

As described in Sect. 2.3 some theoretical frameworks predict a higher proportion of emitted fine particles with increasing wind speed during saltation along with dependencies of the PSD on soil properties (Alfaro and Gomes, 2001; Shao, 2001, 2004). In contrast, the emitted PSD is posited to be relatively independent of wind speed and soil properties in another theoretical framework, based on Brittle Fragmentation Theory (BFT) (Kok, 2011b; Meng et al., 2022). These theoretical frameworks aim to capture our knowledge of the emitted dust PSD and its variability. However, this knowledge remains still quite uncertain regarding: (1) the sensitivity of the emitted dust PSD to u_* , and (2) whether the dependence of the emitted dust PSD with u_* varies between dust emission occurring under transport-limited conditions, where sediment entrainment is controlled by the wind force and other aerodynamic factors such as ABL stability, and under supply-limited conditions, in which sediment entrainment is controlled by the amount of loose erodible material at the soil surface. Our knowledge is based on available limited measurements of the emitted dust PSD.

These measurements have been conducted in near source areas, typically on surfaces that are considered “near-ideal” for dust emission, i.e. bare agricultural fields or unvegetated surfaces with near-unlimited supply of loose erodible material, and fetch sufficient for transport-limited equilibrium saltation (Gillette et al., 1972; Gillette, 1974b; Gillies and Berkofsky, 2004; Zobeck and Van Pelt, 2006; Fratini et al., 2007; Sow et al., 2009; Shao et al., 2011a; Huang et al., 2019; Dupont et al., 2021), but sometimes also in presence of sparse vegetation and crusts (e.g. Klose et al., 2019; Webb et al., 2021). Additionally, wind tunnel experiments have been carried out recreating dust emission under controlled conditions, enabling the assessment of the

sensitivity of dust PSD to different factors (i.e. temperature, moisture, saltators and bed composition) (Gillette et al., 1974; Shao et al., 1993; Rice et al., 1996b; Alfaro et al., 1997, 1998; Alfaro, 2008; Wang et al., 2021a).

Available measurements of the emitted dust PSD show discrepancies in its variability. On the one hand, most wind tunnel experiments have reported a higher proportion of emitted fine particles with increasing wind speed during saltation (Alfaro et al., 1997, 1998; Alfaro, 2008; Wang et al., 2021a). Additionally, a study based on in situ measurements conducted by Sow et al. (2009) in a bare agricultural field also found a significant enrichment of fine particles in the diffusive flux PSD during a convective dust event, which was more energetically driven, compared to two Monsoon dust events with lower energy. However, the diffusive flux PSDs during each event appeared to be independent of u_* . In view of the fact that these events took place a year apart, the differences could be attributed to changes in soil surface conditions, such as soil moisture and soil aggregation.

By analysing in situ measurements conducted under near-idealized conditions for dust emission Kok (2011a) and Kok et al. (2014) suggest that there is no statistically significant dependence of the emitted dust PSD on u_* (Gillies and Berkofsky, 2004; Zobeck and Van Pelt, 2006; Fratini et al., 2007; Sow et al., 2009; Shao et al., 2011a; Park et al., 2011). This finding is supported by empirical investigations (e.g. Creyssels et al., 2009; Martin and Kok, 2017b) and theoretical models that show that mean saltator impact speed, which determines bombardment intensity, exhibits minimal dependence on mean wind speed during equilibrium saltation (Durán et al., 2011; Kok et al., 2012). However, some studies have identified potential conditions leading to variability in the emitted dust PSD with u_* including limited-supply of loose erodible material, i.e. crusted surfaces (Gillette and Chen, 2001; Klose et al., 2019), variability in turbulent momentum fluxes from surface roughness and buoyancy in the ABL (Dupont et al., 2019; Li and Bo, 2019) and variability in cohesive properties of soil that influences surface deformation, and abrasion during saltation (Houser and Nickling, 2001). A recent study based on in situ measurements from vegetated, supply-limited aeolian systems shows a dependence of the dust PSD at emission on u_* , particularly the fine fraction ($<5\ \mu\text{m}$ in diameter) (Webb et al., 2021). As a result, this finding supports the hypothesis that the lack of dependence of the PSD on u_* may not be generalizable to crusted soils with vegetation.

In addition, in recent years there has been also growing questioning regarding the influence of atmospheric stability on the dust PSD at emission. A study conducted by Khalfallah et al. (2020) suggested that the diffusive flux measured between 2 and 4 m above the eroding surface was sensitive to the thermal stratification of the SBL. The authors interpreted these findings as indicative of the dependency of the particle eddy diffusivity on both the particle size and the thermal stability. In view of these results, Shao et al. (2020), re-analyzed the data from the Japan-Australian Dust Experiment (JADE), focusing on 12 specific events. Among these events, three were singled out as case studies due to their contrasting thermal stratification or different surface state. This re-analysis supported the dependency of the dust PSD at emission not only on thermal instability but also on wind speed. To explain these results the authors suggested that in unstable conditions the wind speed exhibited greater variability compared to neutral conditions. Consequently, at similar average u_* , wind speed peaks at higher values in unstable surface layers, transmitting more kinetic energy to saltating soil aggregates and resulting in the emission of finer dust particles. The significance of the atmospheric stability in shaping the dust PSD at emission has also been acknowledged in a recent study by Alfaro et al. (2022), while it has been contradicted by Dupont (2022). Dupont (2022) discussed and investigated the arguments given by Khalfallah et al. (2020) and Shao et al. (2020) using the WIND erOsion in presence of sparse Vegetation (WIND-O-V) 2017 data set. Dupont (2022) found the transfer velocity of sub-micrometre dust to be similar to that of coarser dust, thus not observing an enhanced vertical turbulent transport of sub-micrometre dust in unstable conditions. Also, Dupont (2022) suggests that the fluctuations in the PSD of the emitted dust were likely caused by changes in the surface soil conditions and/or the energy needed to release particles from soil aggregates, rather than an improved eddy diffusivity of sub-micrometre dust. Concerning the argument given by Shao et al. (2020), Dupont (2022) found it to be applicable only during the transition between windy and free convection regimes when u_* is close to its erosion threshold value. However, this intermediate regime appears more convective than the erosion event from which this explanation was proposed.

When comparing the existing emitted dust PSD measurements and studying its variability, it is important to understand their different measurement techniques along with the associated limitations and uncertainties. One of the limitations of the wind

tunnel experiments is that the majority of them lack the ability to represent convective turbulence (Zhang et al., 2022). Concerning the techniques frequently employed for measuring PSD in the literature, they can be categorized into five groups, depending on the underlying principles utilized in particle size measurements (Hinds, 1999). Here are examples of instruments that work based on each method: (1) Aerodynamic method: aerodynamic particle sizer and cascade impactors; (2) Optical method: optical particle counters (OPCs), light scattering particle analyzers, and dynamic light scattering instruments; (3) Electrical sensing zone method: coulter counter; (4) Electrical mobility and condensation method: differential mobility analyzer combined with condensation nuclei counter, and scanning mobility particle sizer; (5) Electron microscopy: scanning electron microscope and transmission electron microscope. Depending on the instrument used, PSDs in the literature are reported based on different types of diameter (described in Chap. 1.4.3). For example, optical sizing instruments use the optical diameter while coulter counters use geometric diameter. It is important to be aware of the specific diameter used in the measurements to ensure accurate comparisons. During the first intensive dust field campaigns, most dust PSD observations were obtained through the analysis in the laboratory of samples collected on filters. Technological advancements have facilitated the continuous and high-temporal-resolution measurement of dust PSD using OPCs, whose measurements are still in many cases complemented by the analysis of filter samples.

One of the most important challenges in studying the dust PSD at emission is the presence of particles with diameters larger than $10\ \mu\text{m}$. The emission of these particles is associated with greater uncertainty compared to smaller particles for several reasons. Firstly, accurately measuring these particles is more challenging due to their substantial inertia, resulting in significant losses during sampling through inlets and transmission to particle samplers (Adebiyi et al., 2023). As a result, there are fewer available measurements for analysis. Secondly, the lower abundance of particles in these size ranges leads to increased uncertainties. Lastly, the physics governing the emission of these larger particles introduce additional complexities. Notably, these particles exhibit substantial terminal fall speeds, ranging from 0.5 to $50\ \text{cm s}^{-1}$, resulting in a non-negligible dry deposition effect upon the calculated diffusive fluxes (Dupont et al., 2015; Fernandes et al., 2019; Adebiyi et al., 2023).

When discussing about the emitted dust PSD it is important to distinguish

between the PSD of dust suspended in the air (concentration) and the PSD of the emitted dust flux, although in many studies they are used indistinctly. Ideally the emitted dust PSD would be the PSD of dust suspended in the air at dust source at height zero. However, to my knowledge this has never been measured, and it is typically approximated based on the diffusive dust flux obtained from measured concentrations at some, often different, heights (Shao et al., 2020). The diffusive dust flux PSD describes how vertical dust concentration gradient depends on particle size. It is calculated using flux-gradient (FG) or eddy covariance (EC) methods (Gillette et al., 1972; Stull, 1988; Fratini et al., 2007; Foken and Napo, 2008; Wang et al., 2017a). The FG method offers the advantage of relying solely on local mean quantities, eliminating the need for high-frequency measurements. Only the measurements of mean dust concentration at two different heights and the mean wind velocity profile are required. However, this method is dependent on several assumptions, including a constant flux layer and the assumption of similarity in turbulent transport between dust and momentum (Dupont et al., 2021).

The EC method offers an alternative to the FG method, as it provides a direct approach to estimate diffusive dust flux without relying on assumptions about eddy diffusion coefficients or empirical constants for thermal stratification, unlike the FG method. Nevertheless, the main challenge of the EC method arises from the difficulty of simultaneously measuring high-frequency wind velocity components and particle concentration. Additionally, the EC method assumes that particles behave like gases, meaning that they passively follow turbulent motions. However, for dust, this assumption only holds for particles smaller than $10\ \mu\text{m}$ in diameter (Fratini et al., 2007). Larger particles are not easily carried by turbulent eddies due to their inertia and gravity, resulting in a phenomenon known as the particle trajectory crossing effect (Csanady, 1963; Fratini et al., 2007; Shao, 2008). The recent study conducted by Dupont et al. (2021) presents the first intercomparison between these two methods to estimate size-resolved diffusive dust fluxes during several erosion events. This study concludes that both methods yield similar predictions for particles smaller than about $4\ \mu\text{m}$ in diameter while for coarser particles, the EC method predicts a smaller diffusive flux than the FG method.

Figure 2.4 shows a typical example for the set-up needed to measure the diffusive flux through the FG and EC methods in a source region, and a schematic

representation of the surface and near-surface fluxes. At the surface, we have the emitted dust flux, F_{emi} , and the dry deposition flux, F_{dep} , while at the intermediate level between the two instruments measuring dust concentrations (on the right) which coincides with the height of the instruments measuring dust concentration and wind at high resolution (on the left), there are the diffusive flux, F , and the gravitational settling flux, F_g .

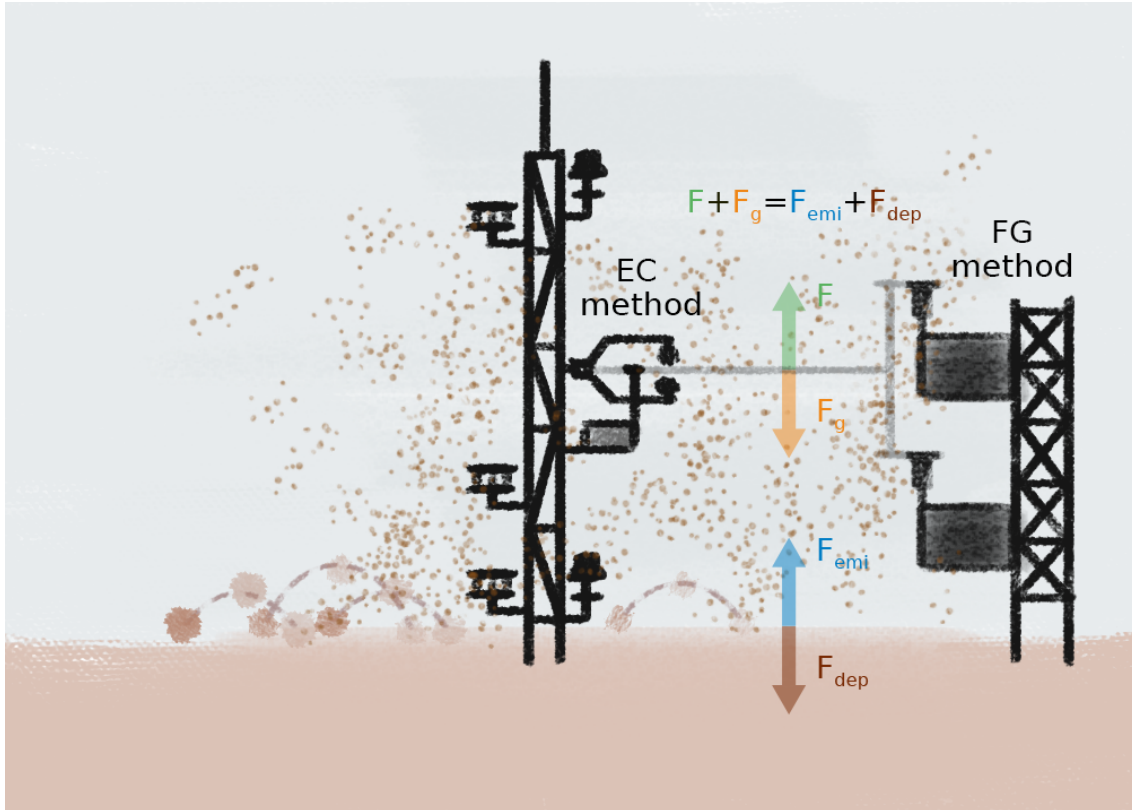


Figure 2.4: Illustration of the set-up needed for measuring diffusive flux through the FG and EC methods in a source region along with a schematic representation of the surface and near-surface fluxes. A few meters above the surface there are the diffusive flux, F , and the gravitational settling flux, F_g , while at the surface there are the emitted flux, F_{emi} , and the dry deposition flux, F_{dep} .

It is worth noting that most studies often relate the diffusive flux PSD to the emitted dust flux at the surface, assuming a constant dust flux layer and neglecting gravitational settling and turbulent dry deposition (Dupont et al., 2021). The gravitational settling term is assumed to be small for dust smaller than $\sim 10 \mu\text{m}$ in diameter (Fratini et al., 2007). The diffusive flux PSD is afterward used directly to constrain or evaluate some of the dust emission schemes presented in Sect. 2.3, neglecting the deposition component of the net dust flux at the surface. However,

recent modelling studies conducted by Dupont et al. (2015) and Fernandes et al. (2019) revealed a higher amount of small particles in the modelled diffusive flux PSD compared to the modelled emitted dust PSD. This enrichment in small particles was observed to remain below a few percent of the total diffusive dust flux (in number) for fetch distances less than 100 m, while for fetch distances longer than 1 km, this enrichment could exceed 10 %. Note that the fetch length is defined as the distance between the measurement location and the upwind border of the source area (Dupont et al., 2021). These modelling studies suggested that dry deposition modulated by the fetch length may have a significant impact on the diffusive flux PSD and could potentially explain the differences observed between the modelled diffusive flux and emitted flux PSDs.

The dry deposition of dust particles involves multiple physical processes, with gravitational settling, turbulent diffusion, interception and inertial impaction being the most prominent ones (Junge, 1963; Sehmel, 1980; Shao, 2008; Bergametti et al., 2018). The majority of dust transport models employ resistance-based dry deposition parameterizations, which combine gravitational settling velocity, v_g , with different types of resistances that counteract the deposition, including aerodynamic resistance, R_a , and surface collection resistance, R_s . The way in which the different deposition processes and their combination are represented can significantly vary among different parameterizations (e.g. Giorgi, 1986; Zhang et al., 2001; Petroff and Zhang, 2010; Kouznetsov and Sofiev, 2012; Zhang and Shao, 2014; Fernandes et al., 2019). Most of these dry deposition parameterizations are calibrated with deposition data collected in wind tunnel experiments rather than direct measurements performed close to the dust source regions. This approach is due to the fact that measurements carried out under natural emission conditions present additional technical challenges and, as a result, are scarce (Lamaud et al., 1994; Goossens and Rajot, 2008; Marticorena et al., 2017; Bergametti et al., 2018). Nevertheless, while wind tunnel experiments have been valuable in validating dust deposition schemes over the past few decades, they do have limitations, and discrepancies between field observations and wind tunnel experiments exist and require further analysis (Zhang and Shao, 2014). Consequently, dry deposition parameterizations are affected by large uncertainties (Huneeus et al., 2011; Zhang et al., 2019).

As far as I know, up to now the influence of dry deposition on shaping the

PSD at emission has been only assessed by a few modelling studies (Dupont et al., 2015; Fernandes et al., 2019), but it has never been evaluated with observations. Nevertheless, given the importance of an accurate parameterization of the dust PSD at emission, it is clear that the role of dry deposition should be further explored with experimental data. If the potentially significant impact of dry deposition is confirmed, corrections to the diffusive flux PSD might be needed before using it to constrain dust emission schemes.

In summary, despite the advancements performed in the last decades regarding the physics of dust emission, specifically concerning the emitted dust PSD and its variability, there are still some open questions and challenges. To address these gaps and further enhance our comprehension of the size resolved dust emission under varying meteorological and soil conditions, additional detailed and targeted measurements are needed. In this context, as detailed in Chap. 4, several intensive dust field campaigns have been recently conducted. This thesis, as described in Chaps. 3 and 4, aims at addressing some of these unresolved questions based on the measurements performed during one of these recent campaigns.

Objectives and structure

3.1. Main objectives

The overall aim of this thesis is to improve our fundamental and quantitative understanding of the emitted dust PSD and its variability, based on measurements from an intensive dust field campaign conducted in Morocco in 2019 in which I participated actively. This aim is addressed through the specific objectives detailed below.

- Identify and characterise the dust events occurred during the campaign based on the near-surface boundary layer conditions, bulk diffusive and saltation fluxes, and sandblasting efficiency at the experimental site.
- Quantify the size-resolved diffusive dust flux and its uncertainty from dust concentration measurements.
- Determine the variability of the PSDs of dust concentration and diffusive flux, and identify their potential drivers.
- Understand quantitatively the role of dry deposition upon the diffusive flux PSD and its variability.
- Estimate the emitted dust flux PSD.
- Compare the PSDs of dust concentration, diffusive flux, estimated emitted flux, and available observationally constrained theoretical references.

3.2. Thesis structure

Most of the content of this thesis has been recently published in a high-impact open access journal in the scientific field of atmospheric physics from the European Geoscience Union, namely *Atmospheric Chemistry and Physics*: González-Flórez et al. (2023).

Besides the current **Part I: Introduction**, this thesis is structured into three additional parts that aim at achieving the described goals.

Part II: Data and methods. This part comprises **Chapter 5**, which provides the characteristics of the specific location chosen to perform the dust field campaign in Morocco in 2019, as well as the instrumentation employed, and the data analysis and treatment methods utilized throughout this thesis.

Part III: Results and discussion. This part is divided into 6 chapters that tackle the specific objectives of this thesis. **Chapter 6** presents an overview of the near-surface boundary layer conditions and dust events occurred during the campaign. **Chapter 7** focuses on the bulk saltation and diffusive fluxes as well as the sandblasting efficiency at the experimental site. **Chapter 8** makes an exhaustive analysis of the concentration and diffusive flux PSDs and its variability with u_* , wind direction and type of dust event (regular or haboob). **Chapter 9** discusses the potential mechanisms that may explain these PSD variations including the effect of dry deposition modulated by the fetch length, aggregate disintegration during wind erosion, and the impact of the haboob gust front. **Chapter 10** analyses in detail the role of dry deposition on shaping the dust concentration and diffusive flux PSDs, which had already been suggested in numerical simulations but never confirmed with experimental data. Dry deposition flux is estimated based on a resistance-based parameterization of dry deposition velocity, and then employed to estimate the emitted dust flux PSD. Finally, **Chapter 11** tackles the last specific objective by making a comparison between the measured PSDs of dust concentration, diffusive flux, estimated emitted flux and observationally constrained theoretical references.

Part IV: Discussion and conclusion. This part is composed by **Chapter 12** that presents a summary of the main outcomes of this thesis and some ideas for the continuation of this work.

Finally, **Part V: Appendices** contains 6 appendices to support the information given in the chapters.

Context and scope

This PhD thesis has been conducted in the Earth Sciences department of the Barcelona Supercomputing Center (BSC) within the context of the ERC project “FRontiers in dust minerAloGical coMposition and its Effects upoN climaTe” (FRAGMENT). FRAGMENT is a multidisciplinary project that combines theory, field measurements, laboratory analyses, remote spectroscopy and modelling to quantify the global mineralogical composition of dust and its effects upon climate. The project is coordinated and led by Dr. Carlos Pérez García-Pando, co-leader of the Atmospheric Composition (AC) Group within the Earth Sciences department at BSC, who, together with Dr. Martina Klose, the head of the Helmholtz Young Investigator Group “A big unknown in the climate impact of atmospheric aerosol: Mineral soil dust” at the Karlsruhe Institute of Technology (KIT), have advised my thesis. In addition to the AC Group at BSC, the main team includes experts on modelling from the NASA Goddard Institute for Space Studies, on field measurements and laboratory analyses from the Institute of Environmental Assessment and Water Research at the Spanish Research Council (IDAEA-CSIC), the Technical University of Darmstadt (TUDA, Germany) and the KIT, and on spectroscopy from the Planetary Science Institute (PSI, USA), the California Institute of Technology (Caltech, USA) and the NASA Jet Propulsion Laboratory (JPL, USA). The list of collaborators has grown since the beginning of the project and includes researchers from Desert Research Institute (DRI, NV, USA), Institut National de la Recherche Agronomique (INRAE, France), Agricultural University of Iceland and Cadi Ayyad University (Morocco).

4.1. Objectives of FRAGMENT

FRAGMENT has set three major objectives to address three major key challenges (Fig. 4.1). The first objective is to reduce the uncertainties related to dust emission, focusing on the emitted dust PSD and sized-resolved mineralogy, and its relationship with the parent soil. For this purpose, the project has conducted several coordinated field campaigns in different dust source regions of the world, collecting samples of

dust particles and soils. These samples are undergoing thorough laboratory analyses, which serve two purposes: to delve deeper into the current theories about the physical processes related to dust emission, and to assess the validity of these theories.

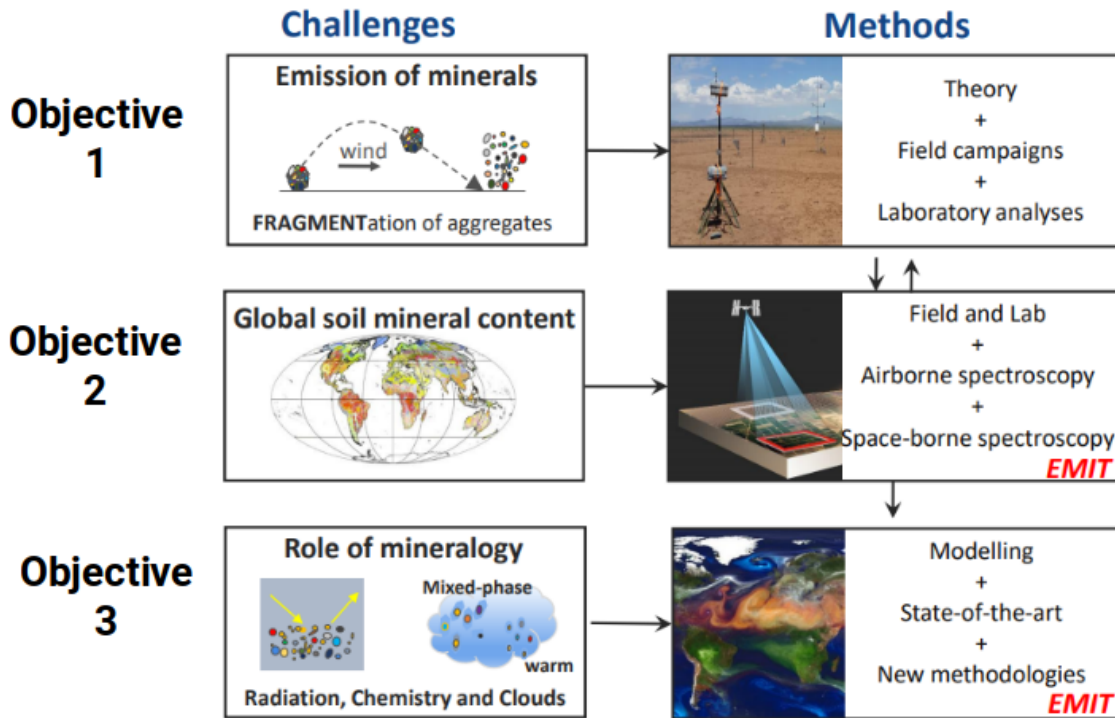


Figure 4.1: Objectives and methods set by FRAGMENT project. Image credit: C. Pérez García-Pando, principal investigator of FRAGMENT.

The second objective is to improve soil mineralogy global atlases for implementation in Earth System models. To that end, the project is evaluating airborne hyperspectral imaging conducted during the campaigns. These results will be helpful for validating the high-quality and high-resolution spaceborne hyperspectral measurements that are being performed as part of the “Earth Surface Mineral Dust Source Investigation” (EMIT) project. EMIT is a project funded by NASA that mounted an advanced imaging spectrometer to the exterior of the international space station in July 2022, with the objective of determining the mineral composition of dust sources that produce dust aerosols at global scale. The PI with other members of FRAGMENT are part of the science team of EMIT.

The third objective is to assess the role of dust mineralogy upon clouds, atmospheric chemistry and radiation. For this purpose modelling experiments are being carried out using the Multiscale Online Non-hydrostatic Atmosphere Chemistry

model (MONARCH) (Pérez et al., 2011). By applying data assimilation techniques, the new constraints on the emitted PSD and mineralogy derived from the field measurements are taken into account.

The topic and goals of my thesis, explained in Chap. 3, fall within the scope of the first objective of FRAGMENT.

4.2. Locations of FRAGMENT field campaigns

FRAGMENT has performed an unprecedented set of field campaigns from an interdisciplinary point of view in coordination with other international projects and research centers (Fig. 4.2). These campaigns have been motivated by the incomplete understanding of the physical processes and the paucity and incompleteness of available measurements, introduced in Chap. 2. The locations chosen for conducting these campaigns met several key criteria including accessibility, dust source areas, variety of soil types, textures and landforms, local/regional collaborators that helped with the logistics, and relevance to respond to different open questions in the literature.

Before the campaigns, we conducted two weeks of tests in a relatively dry region in Aragón (Spain) during the first half of 2019. Aragón was chosen as the test location due to its proximity to Barcelona and the potential susceptibility to wind erosion of agricultural plots under strong Cierzo wind events (Gomes et al., 2003a). The testing phase involved activities such as instrument installation, evaluation of required supplies and energy consumption, development of device and field procedures, and identification of potential improvements.

The first field campaign took place at “L’ Bour”, a dry lake located at the edge of the Sahara in Morocco. The campaign was organized with the collaboration of the Cadi Ayyad University in Marrakesh. The location of the campaign was relatively close to Tinfou and Zagora, where the Saharan Mineral Dust Experiment (SAMUM) I (Heintzenberg, 2009) took place and where a meteorological station was installed within the enerMENA Project (Schüler et al., 2016). This thesis is based exclusively on the measurements obtained during this specific field campaign. Additional information regarding this campaign is provided in Chap. 5.

The second and third field campaigns were initially planned for spring 2020 in

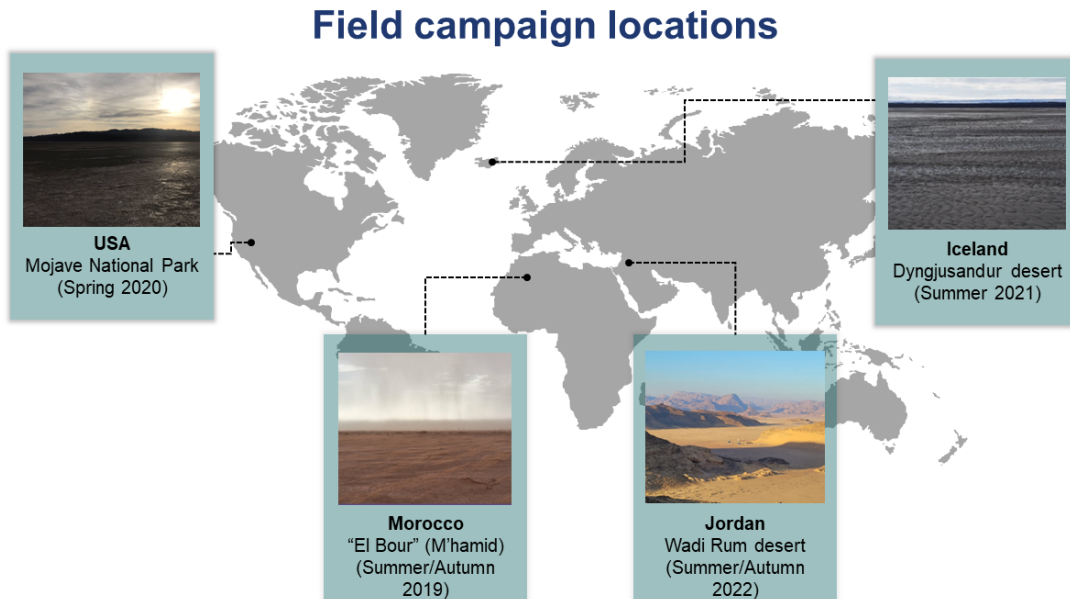


Figure 4.2: Time and locations of FRAGMENT field campaigns

the Mojave National Preserve (California, USA) and for summer 2020 in the desert of Dyngjusedur (Iceland), respectively. However, due to the COVID-19 pandemic and the resulting lockdowns and travel restrictions, both campaigns had to be postponed. Finally, the field campaign in the desert of Dyngjusedur (Iceland) was conducted in summer 2021. This campaign was mainly a joint effort between the projects FRAGMENT and HiLDA (“Iceland as a model for high-latitude dust sources – a combined experimental and modelling approach for characterization of dust emission and transport processes”) funded by the German Science Foundation. Other projects involved to a lesser extent in this campaign were funded by the NASA Jet Propulsion Laboratory, the Helmholtz Association of German Research Centers, the Icelandic Centre for Research and the Czech Science Foundation. As mentioned in Chap. 1.1, although most dust emissions occur predominantly in the subtropics, recent estimates suggest that up to 5% is emitted from cold high latitude sources (Bullard et al., 2016). In particular, Iceland is the largest Arctic as well as European desert (Dagsson-Waldhauserova et al., 2014), which significantly influences glacier albedo, ocean productivity, and arctic cloud formation (Meinander et al., 2016; Arnalds et al., 2016; Sanchez-Marroquin et al., 2020). The measurements obtained during this campaign provide a unique opportunity to rigorously test dust emission theories

4.3. My role in the field campaigns

in an environment with distinct soil properties and conditions that differ greatly from those observed in arid source regions at mid-latitudes.

The originally planned campaign in the Mojave National Preserve (California, USA) was replaced by only a week of soil sampling in spring 2022. This region has multiple environments for dust emission, including dry ephemeral washes, interdune areas, and exposed lake sediments. The main reason for performing a campaign in the USA was the existing availability of airborne hyperspectral imaging spectroscopy measurements (Kruse et al., 2003; Hamlin et al., 2011). In addition, EMIT has recently produced its initial mineral maps, allowing the FRAGMENT measurements to be used for verifying the accuracy of EMIT's measurements.

The fourth and last field campaign called J-WADI (Jordan Wind erosion And Dust Investigation) was conducted North of Wadi Rum in Jordan in autumn 2022. This region is characterised by a multitude of valleys with varying widths, separating sandstone formations. During periods of heavy rainfall, sediments are transported downstream and accumulate in the desert plain, forming mud flats and salt lakes that are susceptible to be eroded when the dry season arrives (Powell et al., 2014; Yusuf, 2007). This campaign was co-organized between FRAGMENT and the Helmholtz Young Investigator Group “A big unknown in the climate impact of atmospheric aerosol: Mineral soil dust” in collaboration with the University of Jordan and mineral dust experts from multiple institutions across Europe, Jordan, and the USA. Giant dust particles were of special interest during this campaign.

Except for the American campaign, all campaigns lasted approximately one month.

4.3. My role in the field campaigns

Throughout my PhD thesis, I have strongly contributed to the implementation and evaluation of the FRAGMENT field campaigns, particularly those in Morocco and Iceland. My involvement in the campaigns has encompassed various tasks and responsibilities, starting with a climatological analysis of field campaign locations based on available data such as satellite remote sensing, in-situ observations and model reanalyses. In addition, I became acquainted with the instruments and their

operation before the campaigns which involved technical meetings, outdoor tests at the IDAEA-CSIC facilities and in Aragón, and instrument maintenance, inventory and packaging. I was present throughout the entire measurement periods in both the Moroccan and Icelandic field campaigns, participating actively in instrument deployment and routine measurements, following established protocols. These tasks were shared with the experimental FRAGMENT team, particularly with two other PhD students from BSC/IDAEA-CSIC and TUDA. Figure 4.3a shows a picture of most of the people involved in the field campaign in Morocco and in Fig. 4.3b, I appear downloading meteorological data from the datalogger.

After the field campaigns, I focused on processing the data from the meteorological instruments and optical particle counters. Details of the data analysis and data treatment are included in Chap. 5.

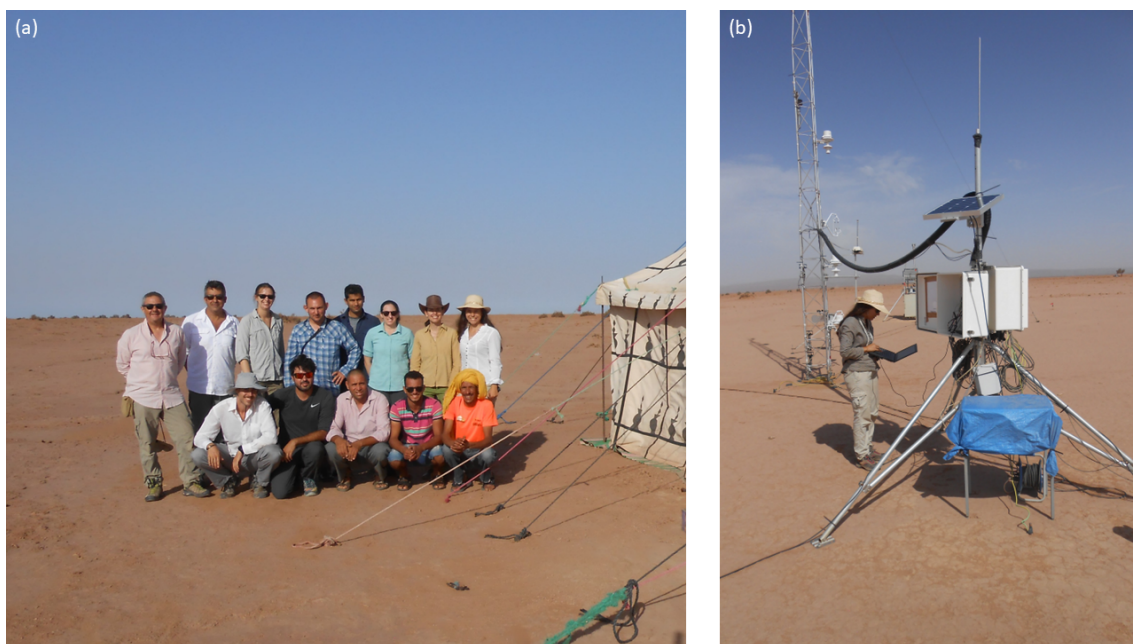


Figure 4.3: (a) Most of the FRAGMENT team during the first field campaign in Morocco. (b) Myself downloading the meteorological data.





II

Data and methods

The FRAGMENT dust field campaign in the Moroccan Sahara

5.1. Climatological analysis before the campaign

The specific location and time period for the field campaign in Morocco was selected considering both scientific criteria, which involved assessing available data from satellite remote sensing, in-situ observations, and model reanalyses, as well as logistical considerations such as the procurement of permits and accessibility. In addition, some members of the group conducted an exploratory trip and consulted with local people a few months prior to carrying out the campaign.

I analysed in advance the available in-situ observations close to Zagora, Tinfou and M'Hamid El Ghizlane from Automated Weather Stations (AWS) maintained by the IMPETUS and FENNEC projects (Christoph et al., 2008; Washington et al., 2012; Schulz and Fink, 2016) and the enerMENA initiative (Schüler et al., 2016). The goal was to determine the time periods and locations with the highest probability of dust emission occurrence in that region. Figure 5.1 shows the annual average cycles of mean wind speed at 3 m height and precipitation and maximum and minimum temperature at 2 m height at the Jebel Brahim AWS. This AWS was the closest one to M'Hamid El Ghizlane and had available data every 15 min during most of the period from 2002 to 2011 (Schulz and Fink, 2016). This dataset allowed identifying two prominent peaks of monthly mean wind speeds: the highest peak reaching $\sim 4 \text{ m s}^{-1}$ in spring followed by a peak of $\sim 3.9 \text{ m s}^{-1}$ at the end of summer and the beginning of autumn. Maximum monthly mean temperatures exceeding 40°C were recorded during July and August, and monthly accumulated precipitation mostly remained below 10 mm, which is typical for a desert area, with a peak occurring in October.

Determining the prevailing wind direction beforehand was crucial to define instrument locations at the selected field site, avoiding shadowing between instruments. Figure 5.2 illustrates that the South West and North East were the most frequent

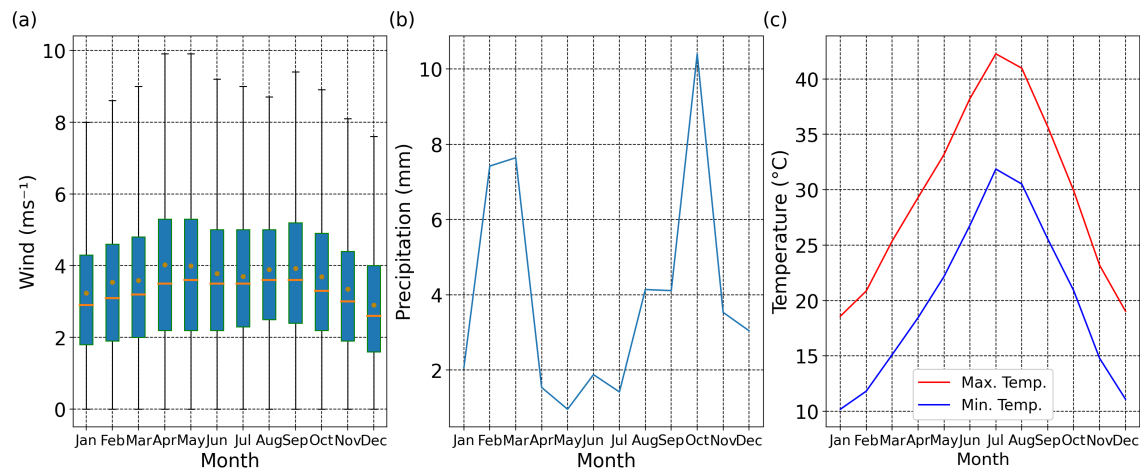


Figure 5.1: Average annual cycles of wind speed at 3 m height and monthly cumulative precipitation and temperature (minimum and maximum) at 2 m height at the Jebel Brahim AWS. In (a) the horizontal orange lines within each boxplot represent the median, and the orange points indicate the mean. Data from Schulz and Fink (2016).

wind directions throughout the year at the Jebel Brahim AWS. Additionally, the strongest winds, exceeding 6 m s^{-1} , were predominantly observed in spring and autumn, originating from the South West.

Figure 5.3 shows the mean daily wind cycle for each month. April, which exhibited the highest monthly mean wind, displayed its maximum peak at 15 LT (local time), whereas May, the month with the second highest monthly mean wind, featured two peaks: a primary peak at 18 LT and a secondary peak at 10 LT. April, along with August and September, exhibited the highest mean daily wind peak, surpassing 5 m s^{-1} , occurring between 15-18 LT.

The wind at the Jebel Brahim AWS was afterwards compared with ERA5 and ERA-Interim global reanalysis data (Balsamo et al., 2015; Hersbach, 2019) interpolated to 3 potential field locations identified during the exploratory trip using bilinear interpolation (Fig. 5.4). One of the differences between ERA5 and ERA-Interim lies in their spatial and temporal resolution: ERA5 has a grid spacing of 31 km and hourly resolution, while ERA-Interim has a grid spacing of 79 km and 6-hourly resolution. In addition, ERA5 incorporates improved parameterizations of physical processes and benefits from advancements in modelling techniques and data assimilation methods compared to ERA-Interim (Hersbach, 2019). As shown in Fig. 5.4b and c, the global reanalysis data qualitatively agreed with the in-situ

5.1. Climatological analysis before the campaign

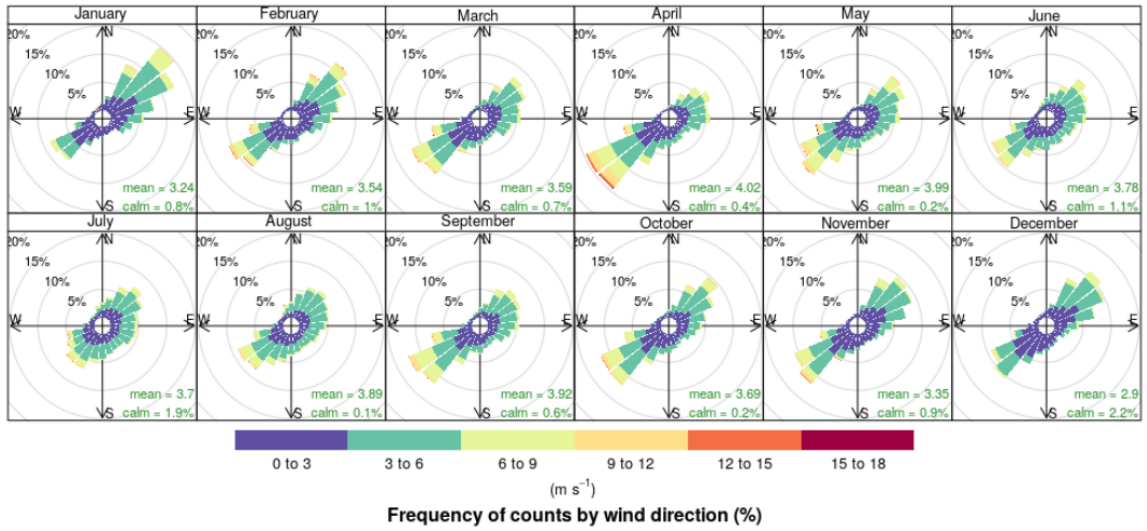


Figure 5.2: Wind roses by month at Jebel Brahim AWS using 15 min data from 1 Jan. 2002 to 21 Aug. 2011, with a gap between 10 Apr. 2009 to 19 May 2009. Data from Schulz and Fink (2016).

observations in representing the two prominent peaks of monthly mean wind speeds in April and September. However, ERA-Interim tended to overestimate the maximum peak in spring compared to ERA5, while the secondary peak was overestimated by ERA-Interim and underestimated by ERA5. Part of these discrepancies may be

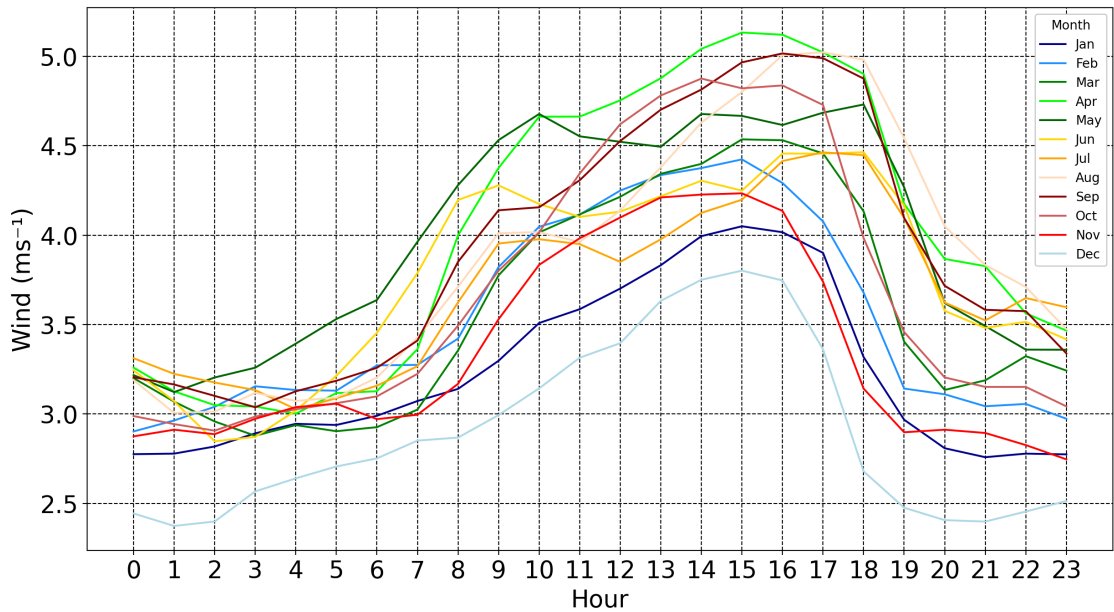


Figure 5.3: Daily mean wind speed at 3 m height for each month in the Jebel Brahim AWS. Data from Schulz and Fink (2016).

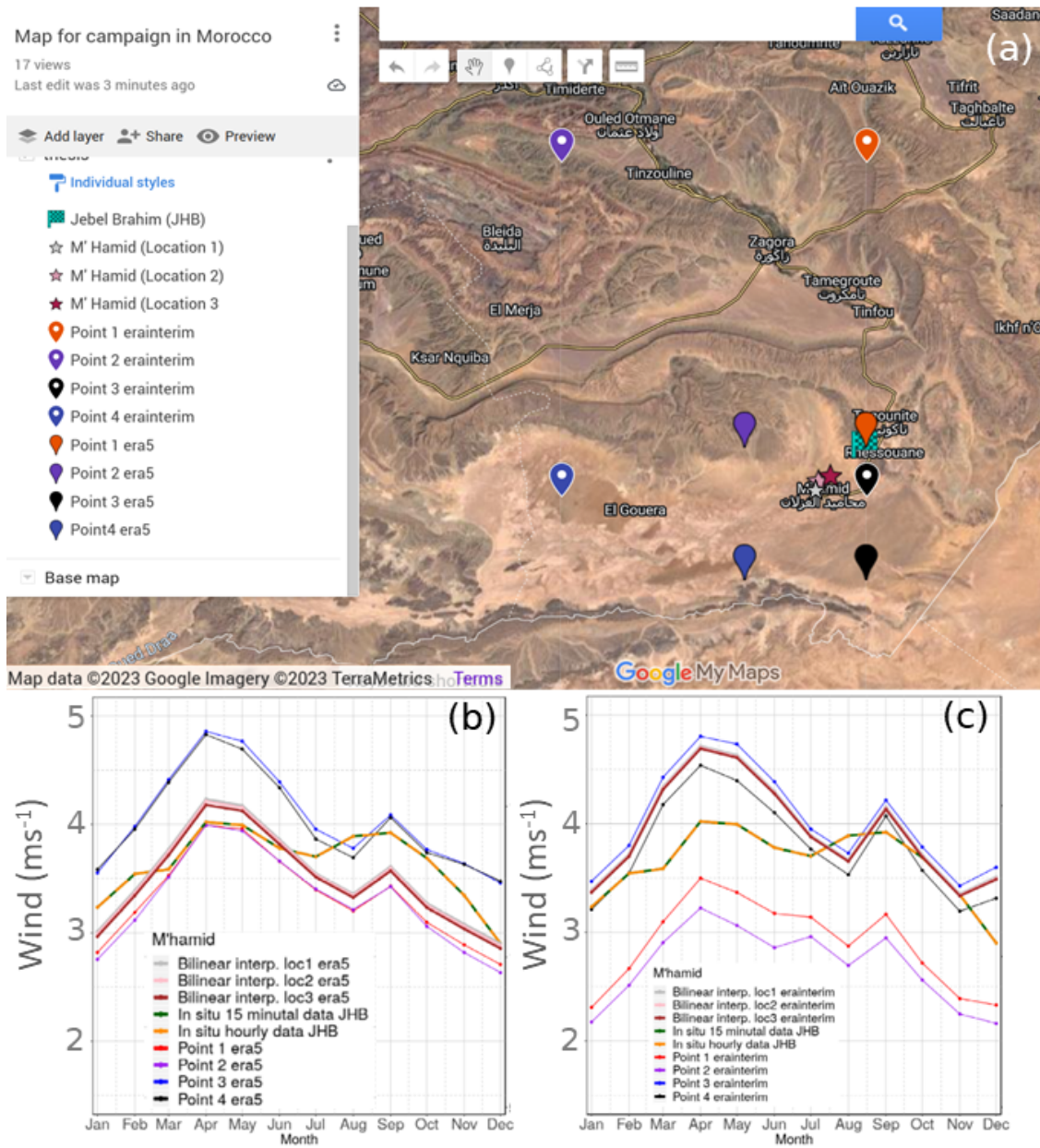


Figure 5.4: (a) ERA5 and ERA-Interim grid points closest to our area of interest, the Jebel Brahim AWS and 3 potential field locations identified during an exploratory trip in January 2019. Comparison of annual mean wind speed between the in-situ data at the Jebel Brahim AWS and ERA5 (b) and ERA-Interim (c) data interpolated to these 3 locations.

attributed to small-scale topography, which is not well captured by the reanalysis products.

Considering the meteorological conditions described above and logistical aspects, the most suitable period for carrying out the field campaign in Morocco was found to

be between late August and early October. This timeframe corresponded to a period of relatively high wind activity and a low likelihood of precipitation.

5.2. Experimental site

The final decision on the specific location for the field campaign was made after conducting an on-site inspection the week prior to the campaign, as well as considering local advice. Finally, the first FRAGMENT field campaign took place in September 2019 in a small ephemeral lake, locally named “L’Bour”, located in the Lower Drâa Valley of Morocco. L’Bour (29°49’30” N, 5°52’25” W) lies at the edge of the Saharan Desert, ~15 km west of M’Hamid El Ghizlane, ~70 km east of Lake Iriki, ~50 km east of the Erg Chigaga dune field, ~1.5 km north of the dry Drâa river, ~30 km north of the Moroccan-Algerian border, and ~25 km south of the Jebel Hassan Brahim mountain range (840 m.a.s.l) (Fig. 5.5a, b and c).

L’Bour was approximately flat and devoid of vegetation or other obstacles within a radius of ~1 km around our measurement location. Small sand dune fields surrounded the lake, and dunes south of the site were accompanied by some vegetation and shrubs during the campaign. The surface of L’Bour consisted of a smooth hard crust (hereafter referred to as paved sediment) mostly resulting from drying and aeolian erosion of paleo-sediments. Figure 5.6b and c illustrate a close-up of a small dune and the lake’s paved sediment surface. In Fig. 5.6a, their respective PSDs analysed using dry dispersion (minimally dispersed) and wet dispersion (fully dispersed) techniques are depicted. The laboratory analysis was conducted by Adolfo González Romero (BSC/IDAEA-CSIC). Details on the sampling and analysis methods are provided in González-Romero et al. (2023). The paved sediment PSDs exhibited two prominent modes peaking at ~100 μm and ~10 μm (Fig. 5.6a). The fully dispersed PSD of the paved sediment showed disaggregation of silt aggregates observed at sand sizes in the minimally dispersed PSD. The sand dune PSDs displayed a dominant mode ranging between ~50 and ~400 μm , peaking at ~150 μm , and containing only a small fraction of particles smaller than 50 μm . The fully dispersed PSD of the sand dune showed disaggregation of clay aggregates observed at silt sizes in the minimally dispersed PSD. The volume median diameter of sand dune particles (and therefore of the saltators) for minimally and fully dispersed techniques were 132.2 μm and 137.6 μm ,

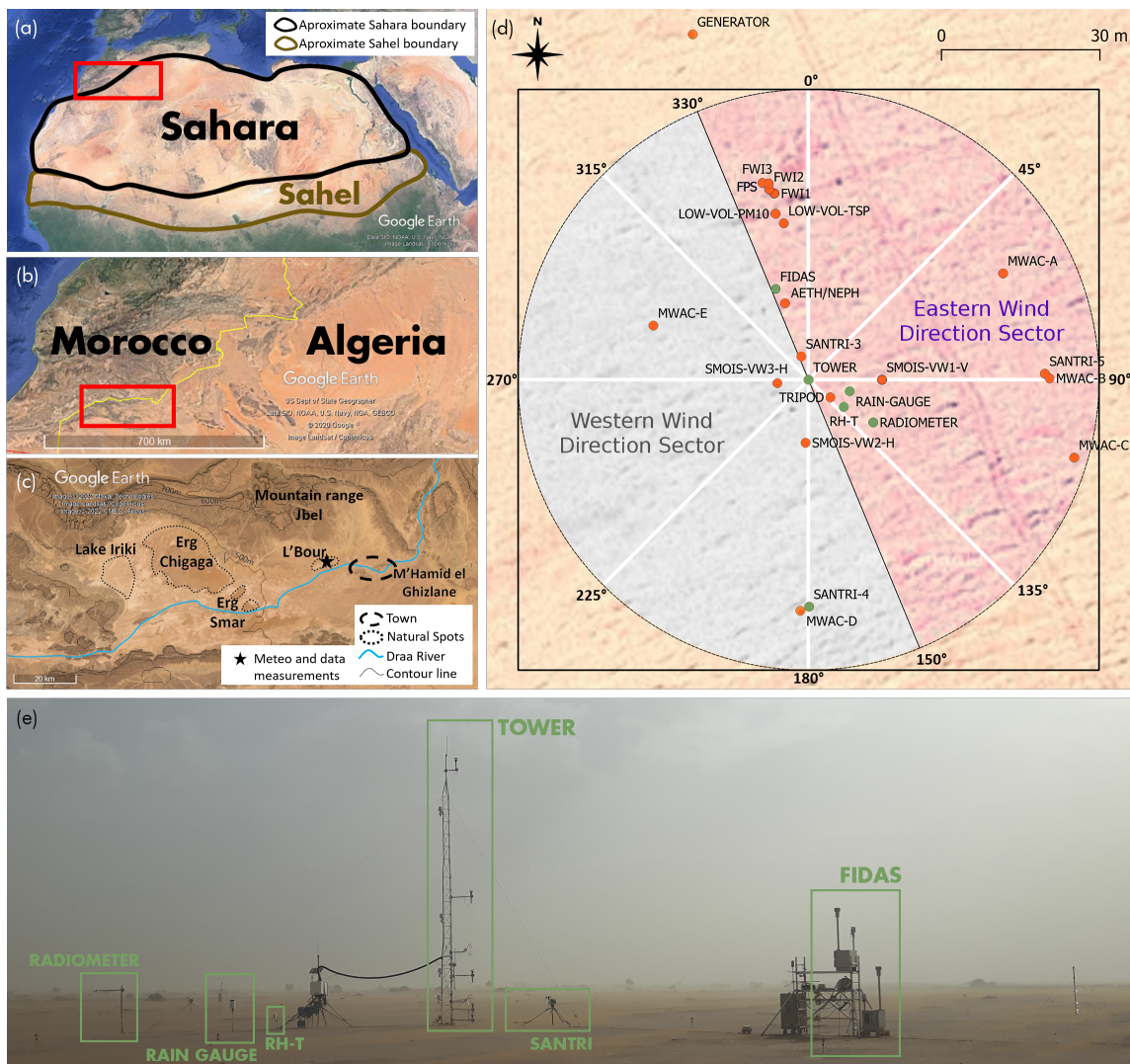


Figure 5.5: (a) Location of the study area in northern Africa. (b) Zoomed-in view over Morocco and Algeria. (c) Zoomed-in view over the Lower Drâa Valley. (d) Experimental set-up in “L’ Bour” (Morocco). The diagonal black line is perpendicular to the approximate predominant wind direction estimated based on prior data analysis. Green circles highlight the instruments used for this paper: TOWER (meteorological tower equipped with five 2-D sonic anemometers and four aspirated shield temperature sensors), FIDAS (two Fidas optical particle counters at 1.8 and 3.5 m height, respectively), RAIN GAUGE, RADIOMETER (four-component net radiometer), RH-T (temperature and relative humidity probe at 0.5 m), and SANTRI-4 (size-resolved saltation particle counter). Red circles indicate instruments not used in this thesis but discussed in other studies: FWI1, FWI2, and FWI3 (free-wing impactors); FPS (flat-plate deposition sampler); LOW-VOL-PM10 and LOW-VOL-TSP (low-volume samplers); AETH/NEPH (multi-wavelength aethalometer and polar nephelometer); MWAC (modified Wilson and Cook samplers); SMOIS (soil moisture sensors); and TRIPOD (pressure and data loggers). (e) Picture of the main instruments as deployed in the field.

5.2. Experimental site

respectively. According to the fully dispersed PSD, the texture of the surface paved sediment was loam (McKee, 1983). During the campaign, we did not observe any substantial change in the paved sediment. We observed some growth of vegetation in nearby areas, particularly to the south, after a flooding event that took place during the night of 6 September. The flooding, which did not affect our site, was caused by a convective storm that produced heavy rain upstream of the Drâa river and whose cold pool outflow generated a strong “haboob” dust storm that passed our site (see Chap. 6).

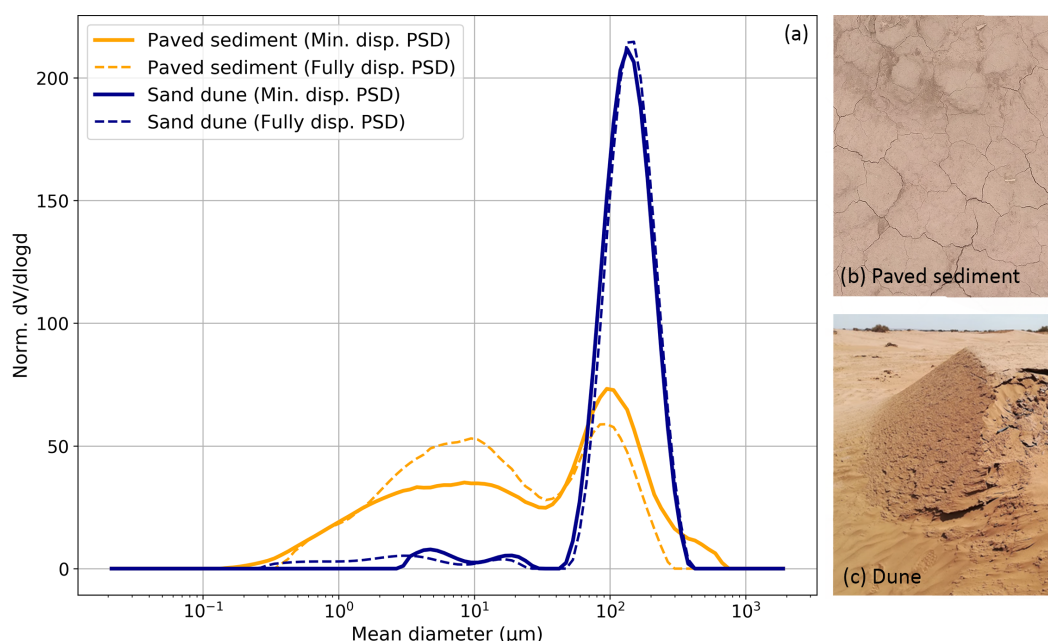


Figure 5.6: (a) Minimally- and fully-dispersed normalized mean PSDs of a sand dune (blue) and the paved sediments (orange) in L’Bour. (b) Picture of the paved sediment. (c) Picture of a small sand dune in L’Bour.

L’Bour was surrounded by other dust sources in all directions, including dunes concentrated in small flat areas and other ephemeral lakes such as Iriki and Erg Smar (Fig. 5.5c). Therefore, the fetch length, i.e. the distance between the measurement location and the upwind border of the source area (Dupont et al., 2021), was not limited to the dimensions of L’Bour. In the western and eastern predominant wind directions, which were approximately parallel to the Drâa river bed and perpendicular to the alignment of our instruments (Fig. 5.5c and d), we estimated long fetches of approximately 60 km and 10 km, respectively.

5.3. Measurements

The site layout is shown in Fig. 5.5d and e. As explained in Sect. 5.1 the alignment of the instruments was informed by prior analyses of available data, which suggested a southwesterly predominant wind direction. To avoid shadowing between instruments as much as possible, instruments were aligned roughly perpendicular to this predominant wind direction. Below I describe only the instruments and measurements used in this thesis. Measurements performed during the campaign with other instruments displayed in Fig. 5.5d are discussed in e.g. Panta et al. (2023); González-Romero et al. (2023); Yus-Díez et al. (prep).

5.3.1 Meteorological parameters

At the centre of the experimental site (Fig. 5.5d) we deployed a 10-m meteorological tower equipped with five 2-D sonic anemometers (Campbell Scientific WINDSONIC4-L) at 0.4 m, 0.8 m, 2 m, 5 m, and 10 m height and four aspirated shield temperature sensors (Campbell Scientific 43502 fan-aspirated shield with a 43347 RTD temperature probe) at 1 m, 2 m, 4 m, and 8 m height to measure wind and temperature profiles, respectively (Fig. 5.5e). Wind measurements were recorded every 2 s and temperature every 1 s. We also placed two 3-D sonic anemometers measuring at 50 Hz at 1 m and 3 m height. All anemometers were oriented toward the north using a magnetic compass. I applied a site-specific correction for magnetic declination using the International Geomagnetic Reference Field IGRF model (1590-2024) as a post-processing, which translated into a anticlockwise adjustment of $\sim 1^\circ$ to the measured wind direction relative to the true north. In the vicinity of the tower, we installed a Young tipping bucket rain gauge (Campbell Scientific 52203 unheated Rain Gauge) at 1 m height, a four-component net radiometer (Campbell Scientific NR01-L radiometer) measuring short-wave and long-wave upwelling and downwelling radiative fluxes at 1.5 m, and a temperature and relative humidity probe (Campbell Scientific HC2A-S3) at 0.5 m (Fig 5.5e). Pressure was recorded inside the data logger cabinet in a tripod near the tower.

After the campaign I carefully examined the time series of the aforementioned

measurements to identify and eliminate invalid values. Most of these values corresponded to periods of testing at the beginning of the campaign or instrument cleaning, which I manually identified and eliminated. Subsequently, I calculated the average values of all meteorological variables over 15 min intervals. This time averaging interval is consistent with the choice made for computing the dynamic parameters that characterize the near-surface boundary layer (see Sect. 5.3.4). Previous studies, such as Dupont et al. (2018), have shown that this averaging period accounts for all significant turbulent structures carrying momentum flux.

5.3.2 Size-resolved dust concentrations

At a distance of ~ 18 m from the tower, we placed two Fidas 200S (Palas GmbH) optical particle counters (OPCs) on a scaffolding (Fig 5.5e) at 1.8 m (referred to as FidasL) and 3.5 m height (FidasU) from which I calculated the diffusive dust flux (see Sect. 5.3.5). We recorded 2 min average number concentrations of suspended dust in 63 diameter size bins of equal logarithmic width between 0.2 and 19.1 μm . After the campaign, I averaged these values over 15 min intervals. Subsequently, the 15 min concentration PSDs were averaged over u_* intervals, considering two wind direction sectors and the type of dust event (regular or haboob). I didn't use data from the first three bins as they showed an unrealistic abrupt descent of the concentration (border measurement limitations). Therefore, the Fidas was considered to be efficient from the fourth bin (from $d_{min}=0.25 \mu\text{m}$). The sampling system of the Fidas operated with a volume flow of 4.8 l min^{-1} and was equipped with a Sigma-2 sampling head (manufacturer Palas GmbH). The Sigma-2 sampler has been validated by the Association of German Engineers (VDI-2119, 2013) and tested in various studies, concluding that it is a reliable collector for coarse and super-coarse particles (Dietze et al., 2006; Tian et al., 2017; Waza et al., 2019; Rausch et al., 2022). The Sigma-2 head ensures a wind-sheltered, low-turbulence air volume inside the sampler (Tian et al., 2017), but the sampling efficiency as function of wind speed and particle size has not been quantified. However, it has been shown to be largely insensitive to wind intensity at least up to $\sim 6 \text{ m s}^{-1}$ in the PM_{10} range (Waza et al., 2019). The inlet includes a drying line (Intelligent Aerosol Drying System, IADS, Palas GmbH), connecting the sampling head to the control unit, whose temperature is regulated according to the ambient temperature and humidity, avoiding condensation

effects. Moisture compensation is guaranteed through a dynamic adjustment of the IADS temperature up to a maximum heat capacity of 90 W. Unlike most of the meteorological instruments that were connected to a battery, the two Fidas depended exclusively on a generator. Therefore, there were some gaps in the time series associated with generator maintenance periods and some short power outages.

The two Fidas were calibrated in the field at the start of the campaign using monodisperse (non-absorbing) polystyrene latex spheres (PSLs). Therefore, the (default) optical diameters typically used to report the PSDs obtained with OPCs are diameters of PSLs that produce the same scattered light intensity as the measured dust particles. As in the majority of previous studies (e.g. Fratini et al., 2007; Sow et al., 2009; Shao et al., 2011a; Ishizuka et al., 2014; Dupont et al., 2021), I use optical diameters to analyse the PSDs and their variability throughout most of this thesis. I also compare these “optical diameter” PSDs with the theoretical framework from Kok (2011a), based on BFT, where the emitted dust PSD is derived by analogy to the fragmentation of brittle materials such as glass spheres constrained by PSD measurements unharmonized in terms of diameter type. Since dust is aspherical and light-absorbing, I additionally provide a synthesis of the results after transforming the optical diameters into dust geometric diameters assuming a more realistic shape and composition (see types of diameters in Chap. 1.4.3). In this way, these results can also be compared with an updated version of BFT that accounts more realistically for super-coarse dust emission (Meng et al., 2022) and that was constrained with measured PSDs harmonized to dust geometric diameters assuming tri-axial ellipsoids (Huang et al., 2021).

The transformation of the default PSL diameters into dust geometric diameters was performed by Jerónimo Escribano (BSC) following Huang et al. (2021), which involved calculating the theoretical scattered intensities of the PSLs and the aspherical dust. Following this, the comparison of both scattered intensities allows remapping the PSL into dust geometric diameters if both functions are monotonic with diameter. The calculation of the scattered intensity depends in the first order on the wavelength of the light beam used in the OPC, the scattering angle range of the OPC’s light sensor, and the shape and refractive index of the particles, which are specified below:

Wavelength of the light beam and scattering angle: The Fidas determines

the number and size of particles using a poly-chromatic unpolarized LED light source. Each particle that moves through the measurement volume generates a scattered light impulse that is detected at an angle of $90 \pm 5^\circ$. Unfortunately, neither the characteristics of the polychromatic light beam of the Fidas nor the spectral sensitivity of the sensor were provided by the manufacturer. However, the manufacturer provided a software that allowed us converting the obtained PSDs with PSLs to PSDs of spherical particles assuming 16 different refractive indices. This information together with the information on the scattering angle, and the Lorenz-Mie code used in Escribano et al. (2019) was useful to infer a light spectrum that could best reproduce the software conversions between spherical aerosol types. In this case, the optimization problem was constrained to fit a sum of Gaussian spectra over the wavelength domain. The resulting single-Gaussian optimal spectrum had a centre wavelength of 389 nm and a standard deviation of 77 nm. This spectrum was later used to convert the optical PSL diameters to dust geometric diameters. The obtained spectrum was consistent with the apparent bluish LED light of the Fidas.

Shape: The sideward scattered intensity depends on particle shape. Since PSLs are spherical, their single-scattering properties were obtained based on Lorenz-Mie theory. Since recently extensive measurements have found that dust particles are three-dimensionally aspherical (Huang et al., 2021), here dust particles were assumed to be tri-axial ellipsoids. To quantify dust asphericity, an aspect ratio (AR) of 1.46 has been used, resulting from the median AR of the more than 300.000 individual dust particles collected during the campaign and analysed in the laboratory using scanning electron microscopy (SEM) coupled with energy-dispersive X-ray spectrometry (EDX) (Panta et al., 2023). We did not perform measurements of the height-to-width ratio (HWR), so we assumed $\text{HWR}=0.45$, which is the closest value to the global median of 0.4 obtained in Huang et al. (2021). The AR and HWR were combined with the database of shape-resolved single-scattering properties of ellipsoidal dust particles (Meng et al., 2010), following Huang et al. (2021).

Refractive index: The preliminary analyses of the optical properties (Yus-Díez et al., prep) and mineralogical composition (Panta et al., 2023; González-Romero et al., 2023) of the campaign suggest imaginary parts of the refractive index between 0.0015 and 0.002, consistent with chamber-based re-suspension estimates using Moroccan soil samples in Di Biagio et al. (2019). A value of 0.0015 was utilized for the imaginary

part in this thesis, and a value of 1.49 for the real part was assumed, as obtained in Di Biagio et al. (2019) with their Moroccan samples.

Figure 5.7 compares the obtained geometric diameters with the default optical diameters. Based on this transformation, the optical diameters overestimate the dust diameters between ~ 0.5 and $\sim 13 \mu\text{m}$ and underestimate them at finer and coarser sizes due to the combined effects of dust refractive index and asphericity.

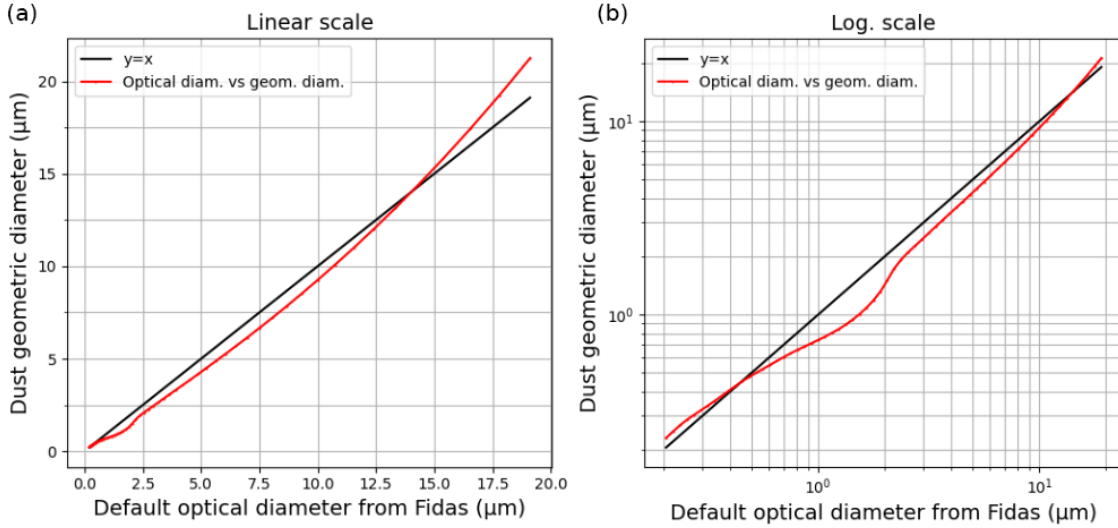


Figure 5.7: Default optical diameters (μm) of the Fidas versus geometric diameters (μm) calculated assuming that dust particles are tri-axial ellipsoids with an aspect ratio of 1.46, a height-to-width ratio of 0.45 and a refractive index of $1.49 + 0.0015i$. (a) Representation in linear scale. (b) Representation in logarithmic scale.

By the end of the campaign, the two Fidas were intercompared bin by bin (in the original size bin resolution) at the same height (1.8 m) from 1 October at 10:15 UTC to 2 October at 08:00 UTC. The goal of the intercomparison was to (1) obtain a correction factor per bin that removed the systematic differences between sensors, and (2) estimate the (random) uncertainty in the size-resolved diffusive flux (see Sect. 5.3.5). The intercomparison period was affected by a regular event from ~ 14 to 17 UTC reaching maximum 15 min number and mass concentrations of $\sim 9 \times 10^7 \# \text{m}^{-3}$ and $\sim 2700 \mu\text{g} \text{m}^{-3}$, respectively, which are very far from the maximum 15 min dust number and mass concentrations of $\sim 1 \times 10^9 \# \text{m}^{-3}$ and $\sim 44700 \mu\text{g} \text{m}^{-3}$, respectively, measured during the campaign.

The FidasL was selected as the reference device, therefore I corrected the

5.3. Measurements

systematic deviation of the FidasU. The systematic correction parameter, λ_i , for each bin i shown in Fig. 5.8a was calculated as the slope of the regression between the concentration of the two Fidas during the intercomparison period:

$$c_{l_0}(D_i) = \lambda_i c_{u_0}(D_i) \quad (5.1)$$

where c_{l_0} is the concentration from FidasL and c_{u_0} is the uncorrected concentration from FidasU with diameter D_i during the intercomparison period. If $\lambda_i > 1$ the concentration of FidasU is lower and if $\lambda_i < 1$ the concentration FidasL is higher. Figure 5.8a shows λ_i in the integrated size bin resolution both in terms of number (green line) and mass (black line) concentrations. Note that number concentrations were transformed to mass concentrations in the original size bin resolution before obtaining the integrated size bin concentrations used to calculate these λ_i . As shown in Fig. 5.8b the Pearson correlation coefficient, r , was above 0.95 for all bins, except for the two coarsest ones where it decays to ~ 0.88 and ~ 0.75 , respectively.

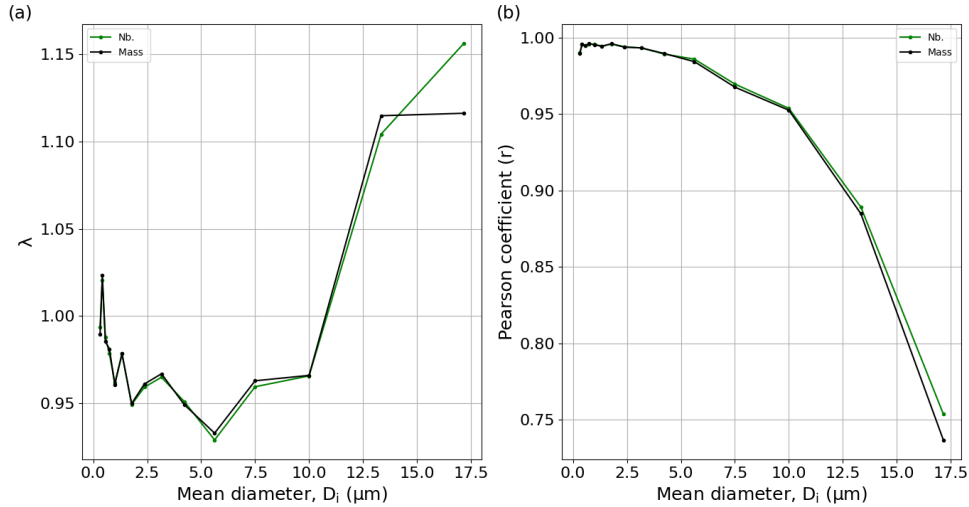


Figure 5.8: (a) Systematic correction parameter, λ_i , and (b) Pearson coefficient, r , for each integrated size bin i . Green (black) lines depict these variables in terms of number (mass) of particles.

The corrected FidasU concentration, c_u , during the campaign was then obtained by simply scaling the uncorrected concentration over the whole campaign, $c_{u_{uncorr.}}$, with λ_i :

$$c_u(D_i) = \lambda_i c_{u_{uncorr.}}(D_i) \quad (5.2)$$

Similarly, the corrected FidasU concentration, $c_{u_0corr.}$, during the intercomparison period was

$$c_{u_0corr.}(D_i) = \lambda_i c_{u_0}(D_i) \quad (5.3)$$

5.3.3 Size-resolved saltation counts

Time- and size-resolved saltation counts were measured with three SANTRI (Standalone AeoliaN Transport Real-time Instrument) platforms (Etyemezian et al., 2017; Goossens et al., 2018). Two SANTRIs (SANTRI-4 and SANTRI-5 in Fig. 5.5d) consisted of duplicate optical gate devices (OGDs, Etyemezian et al., 2017) at 5 cm height, single OGDs at 15 and 30 cm heights, and a cup anemometer and wind vane at ~ 1.1 m height and measured at 1 s intervals. Saltation counts were recorded in 7 size bins, whose lower and upper diameter limits were calculated from the recorded sensor reference voltage levels. The two bins with the smallest and largest diameters, respectively, were excluded from further analysis due to a large noise level for the former and an absent upper diameter limit for the latter. On average, the remaining size range extended roughly from 85 to 450 μm in diameter. A third SANTRI (SANTRI-3 in Fig. 5.5d) collected data from two OGDs at multiple kilohertz frequencies but has not been analysed in this thesis. Due to technical issues with SANTRI-5, results presented here have focused on SANTRI-4 using the front one of the two bottom sensors together with the upper ones.

5.3.4 Computation of dynamical parameters characterizing the near-surface boundary layer

In this thesis, I calculated u_* from the law of the wall approach, based on Eq. 2.8. The determination of $\Psi_m = \int_{\zeta_0}^{\zeta} [1 - \Phi_m(\zeta')] \frac{d\zeta'}{\zeta}$ (introduced in Chap. 2.1.3) is a requirement for this calculation. The specific expressions for Ψ_m used in this thesis are given by:

$$\Psi_m = \begin{cases} -6(\zeta - \zeta_0) & \text{if } \zeta > 0 \\ \text{(Businger et al., 1971; Högström, 1988)} \\ -\ln\left(\frac{(\xi_0^2+1)(\xi_0+1)^2}{(\xi^2+1)(\xi+1)^2}\right) - 2[\tan^{-1}(\xi) - \tan^{-1}(\xi_0)] & \text{if } \zeta \leq 0 \\ \text{(Benoit, 1977)} \end{cases} \quad (5.4)$$

5.3. Measurements

with $\xi = (1 - 19.3\zeta)^{1/4}$ and $\xi_0 = (1 - 19.3\zeta_0)^{1/4}$ (Benoit, 1977; Högström, 1988), where $\zeta = z/L$ and $\zeta_0 = z_0/L$. The Obukhov length, L , needed to determine ζ and ζ_0 , can be derived as follows (Foken and Napo, 2008):

$$L = -\frac{\theta_r u_*^3}{\kappa g \overline{w'\theta'_0}} \quad (5.5)$$

where θ_r is a reference potential temperature, $g = 9.81 \text{ m s}^{-2}$ is the gravitational acceleration and $\overline{w'\theta'_0}$ is the surface kinematic heat flux. Heat flux ($H = \rho_{air} c_p \overline{w'\theta'_0}$ with air density ρ_{air} and specific heat capacity of air at constant pressure $c_p = 1004 \text{ J kg}^{-1} \text{ K}^{-1}$) can be also estimated from the bulk aerodynamic formulation for the sensible heat flux (e.g. Shao, 2008; Klose et al., 2019)

$$H = \rho_{air} c_p \left(\frac{T_0 - T_r}{r_a} \right) \quad (5.6)$$

where T_r is the temperature at reference height z_r , T_0 the soil surface temperature, $r_a = (C_h u_r)^{-1}$ the bulk aerodynamic resistance between z_0 and z_r with u_r the wind at reference height and $C_h = \kappa^2 / ([\ln(\frac{z}{z_0}) - \Psi_m][\ln(\frac{z}{z_0}) - \Psi_h])$ (e.g. Stull, 1988; Arya, 2001) the bulk heat transfer coefficient, where $\Psi_h = \int_{\zeta_0}^{\zeta} [1 - \Phi_h(\zeta')] \frac{d\zeta'}{\zeta'}$, with Φ_h the similarity function for sensible heat. The expressions used in this thesis to calculate Ψ_h are given by:

$$\Psi_h = \begin{cases} 0.05 \ln\left(\frac{z}{z_0}\right) - 7.8(\zeta - \zeta_0) & \text{if } \zeta > 0 \\ \text{(Businger et al., 1971; Högström, 1988)} & \\ 0.05 \ln\left(\frac{z}{z_0}\right) - 1.9 \ln\left(\frac{(\lambda_0+1)}{(\lambda+1)}\right) & \text{if } \zeta \leq 0 \\ \text{(Benoit, 1977; Högström, 1988)} & \end{cases} \quad (5.7)$$

with $\lambda = (1 - 11.6\zeta)^{1/2}$ and $\lambda_0 = (1 - 11.6\zeta_0)^{1/2}$ (Benoit, 1977; Högström, 1988).

Therefore, $\overline{w'\theta'_0}$, needed for calculating L , can be inferred from Eq. 5.6. The reference height z_r was chosen as 2 m since temperature and wind measurements were available at this height. T_0 was obtained from radiometer measurements of surface longwave radiative flux, and ρ_{air} was determined from relative humidity and temperature measurements at 0.5 m height and pressure at 1.5 m height by making use of Tetens' formula (Tetens, 1930) and the ideal gas law (e.g. Stull, 1988).

Applying a linear regression based on Eq. 2.8, the following equation was derived:

$$\bar{U}(z) = m[\ln(z) - \Psi_m] + n \quad (5.8)$$

where m and n are the slope and intercept of the linear regression, respectively. Thus, $u_* = m\kappa$ and $z_0 = \exp(-n/m)$. An iterative procedure was performed to deduce u_* , z_0 and L for every 15-minute period. This iterative procedure assumes neutral conditions as a first guess, and then corrects for stability using the expressions shown before. As in previous studies, this procedure was applied only when wind increased with height and for wind speeds at 2 m height larger than $\sim 1 \text{ m s}^{-1}$ (Marticorena et al., 2006; Khalfallah et al., 2020). In addition, results were only considered when the difference between the computed and measured wind profile was less than 10% and when the resulting dimensionless height $\zeta_r = z_r/L$ was in the range $(-10, 2)$. This is the range for which Monin-Obukhov theory seems to be valid (Kramm et al., 2013).

Furthermore, u_{*th} (introduced in Chap. 2.1.4) was calculated fitting the saltation flux, Q , versus the wind shear stress, τ . Both the classical models, considering the involvement of fluid lifting in particle entrainment resulting in nonlinear $3/2$ stress-flux scaling (i.e., $Q \sim \tau^{3/2}$ or alternatively $Q \sim u_*^3$), as well as the more recent models, considering splash-dominated entrainment leading to linear or nearly linear stress-flux scaling (i.e., $Q \sim \tau$ or alternatively $Q \sim u_*^2$), were taken into account, following the methodology of Martin and Kok (2017b).

5.3.5 Computation of size-resolved flux gradient diffusive dust flux and its uncertainty

In this thesis, I estimated the near-surface vertical diffusive flux, F , using the flux-gradient method (Gillette et al., 1972). This approach, by analogy with Fick's law for molecular diffusion, assumes that the diffusive dust flux is proportional to the vertical gradient of the local mean dust concentration, c , where the dust eddy diffusion coefficient, K_d , is the constant of proportionality. Thermal stratification effects are accounted for following the Monin-Obukhov theory (Monin and Obukhov, 1954) through the similarity function for dust Φ_d , that translates into an adjustment

5.3. Measurements

of K_d . This yields

$$F = -\frac{K_d}{\Phi_d} \frac{\partial c}{\partial z} \quad (5.9)$$

Similar to Eq. 5.9, the momentum flux $\langle u'w' \rangle$ can be expressed proportionally to the vertical gradient of the horizontal wind speed, u , as

$$\langle u'w' \rangle = -\frac{K_m}{\Phi_m} \frac{\partial U}{\partial z} \quad (5.10)$$

where K_m is the momentum eddy diffusion coefficient and Φ_m is the similarity function for momentum. In this thesis, trajectory crossing effects (Csanady, 1963; Shao et al., 2011a) were estimated to be negligible for particle diameters smaller than 20 μm (see more details in Appendix A). Therefore, it was assumed that K_m and K_d were equivalent, the turbulent Schmidt number $Sc_t = K_m/K_d = 1$, and $\Phi_m = \Phi_d$. In addition, when a constant momentum flux layer is assumed, then $\langle u'w' \rangle = -u_*^2$.

The widely used expression proposed in Gillette et al. (1972) for calculating the diffusive dust flux is obtained by dividing Eqs. 5.9 and 5.10, taking into account the aforementioned assumptions and substituting from Eq. 2.8:

$$F_n(D_i) = u_* \kappa \frac{c_u^n(D_i) - c_l^n(D_i)}{\ln\left(\frac{z_u}{z_l}\right) - \Psi_m\left(\frac{z_u}{L}\right) + \Psi_m\left(\frac{z_l}{L}\right)} \quad (5.11)$$

where $c_u^n(D_i)$ and $c_l^n(D_i)$ are the number concentrations of dust particles with diameter D_i measured by the two Fidas at $z_u = 3.5\text{ m}$ and $z_l = 1.8\text{ m}$ in bin i . Note that the FidasU concentrations include the systematic corrections derived from the intercomparison of the two Fidas by the end of the campaign (explained in Sect. 5.3.2).

Eq. 5.11 was applied to each of the 63 size intervals of the Fidas using 15 min average concentrations. Thus, the total number and mass diffusive fluxes were obtained by summing over all size bins. The mass flux in each bin is inferred from its respective number flux as

$$F_m(D_i) = F_n(D_i) \frac{1}{6} \rho_d \pi D_i^3 \quad (5.12)$$

where $D_i = \sqrt{d_{max} \cdot d_{min}}$ is the mean logarithmic diameter in bin number i , d_{min} and d_{max} are the minimum and maximum particle diameters of bin i , $F_n(D_i)$ and $F_m(D_i)$ are the 15 min averaged number and mass diffusive fluxes with diameter D_i and

ρ_d is the dust particle density, which is assumed to be 2500 kg m^{-3} (Fratini et al., 2007; Reid et al., 2008; Kaaden et al., 2009; Sow et al., 2009; Kok et al., 2021b). All diameters can be either the default optical or the obtained geometric ones.

All calculations were performed using the original size bins of the Fidas (63 bins ranging from $0.2 \mu\text{m}$ to $19.1 \mu\text{m}$). However, such a high bin resolution lead to substantial noise in the coarse and super-coarse bins of the mass PSDs. Therefore, the 63-bin PSDs were integrated into 16 bins to represent the mass concentration and number and mass diffusive flux PSDs. The size-resolved diffusive flux can exhibit positive and negative values, with the former representing an upward (net emission) flux and the latter a downward (net deposition) flux. Well-developed erosion conditions are normally characterized by positive fluxes. For this reason, when analysing the diffusive flux PSDs those PSDs containing at least one negative value in all the integrated number or mass bins with $D_i > 0.42 \mu\text{m}$ (where as shown in Chap. 8.1 the anthropogenic aerosol influence is negligible) were excluded. Similar to dust concentrations PSDs, the 15 min diffusive flux PSDs were afterwards averaged over u_* intervals, considering two wind direction sectors and the type of dust event (regular or haboob).

Concerning the calculation of the uncertainty of each 15 min size-resolved diffusive flux obtained from the flux gradient method, it is important to note that there are three main sources of uncertainty : (1) u_* , (2) the difference between FidasU and FidasL concentrations and (3) the difference in stability between the two levels. The uncertainties on u_* and stability were neglected because they are size-independent and small compared to the size-resolved concentration uncertainties (Dupont et al., 2018), and the main interest of this thesis is the PSD.

As the FidasL was selected as the reference device, the uncertainty in the diffusive flux $\sigma_{F(D_i)}$ only depends on the uncertainty of the FidasU concentration with respect to the FidasL concentration $\sigma_{c_u(D_i)}$, where σ represents the standard deviation:

$$\sigma_{F(D_i)} = u_* \kappa \frac{\sigma_{c_u(D_i)}}{\ln\left(\frac{z_u}{z_l}\right) - \Psi_m\left(\frac{z_u}{L}\right) + \Psi_m\left(\frac{z_l}{L}\right)} \quad (5.13)$$

Figure 5.9a displays the number concentrations measured by the FidasU after the systematic correction (see Sect. 5.3.4) versus the FidasL concentrations in each

5.3. Measurements

integrated size bin during the intercomparison period. As the number concentration decreases, a clear relative increase in the scatter is observed both for each bin and across bins. In other words, the relative uncertainty of the number concentration is strongly dependent upon the number concentration, which is orders of magnitude smaller for large particles than for fine particles. Based on this, the relative uncertainty σ_r can be expressed as follows:

$$\sigma_r = e(c_u^n)^f \quad (5.14)$$

where c_u^n is the FidasU number concentration in any size bin and e and f are constants that can be obtained by fitting the data as described below.

Being able to express the uncertainty as a function of the number concentration independent of size is key to avoid overestimating the uncertainty of the diffusive flux because the concentrations measured during the campaign were generally much higher than the ones measured during the intercomparison period. In order to fit Eq. 5.14, the ratio λ_{ij}^n of the FidasL to the corrected FidasU number concentrations is obtained for each bin i and time step j (every 15 min) during the intercomparison period as follows:

$$\lambda_{ij}^n = c_{l_0}^n (D_i)_j / c_{u_{0corr.}}^n (D_i)_j \quad (5.15)$$

where $c_{l_0}^n$ and $c_{u_{0corr.}}^n$ are the FidasL and corrected FidasU number concentrations.

Then, the standard deviation of these ratios σ_{rk} within k number concentration intervals is calculated as follows:

$$\sigma_{rk} = \sqrt{\frac{\sum (\lambda_{ij}^{nk} - \overline{\lambda^{nk}})^2}{N - 1}} \quad (5.16)$$

where λ_{ij}^{nk} are the ratios λ_{ij}^n within each k interval, $\overline{\lambda^{nk}} \approx 1$ is the average ratio within each interval k , and N is the number of samples in each interval k .

Four k intervals with the following number concentration ranges: 10^3 – 10^4 , 10^4 – 10^5 , 10^5 – 10^6 , and 10^6 – 10^7 # m⁻³, covering the range of most of the points during the intercomparison period were selected (Fig. 5.9a). The σ_{rk} values associated to each of the four intervals are displayed in Fig. 5.9b as a function of c_u^n , which is taken as the geometric mean c_u^n within each interval. Using these values, σ_r was fitted, obtaining $e = 51.3$ and $f = -0.45$ with $R^2 = 0.98$ (Fig. 5.9b).

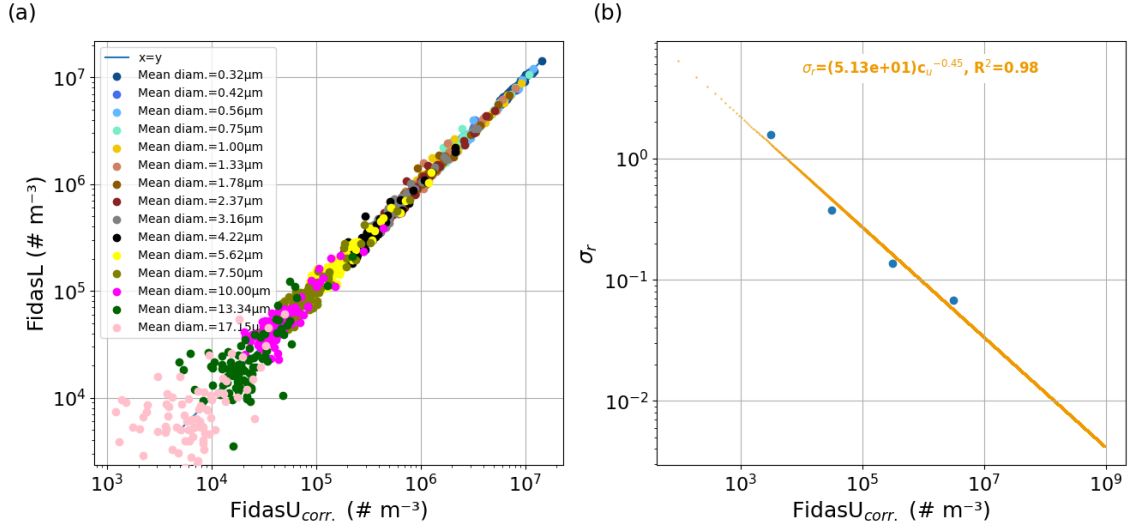


Figure 5.9: (a) FidasL versus FidasU (after systematic correction) number concentrations ($\# \text{ m}^{-3}$) during the intercomparison period. Concentrations in each bin are represented with different colours. (b) σ_r versus corrected FidasU number concentrations ($\# \text{ m}^{-3}$) during the intercomparison period. The line in (b) represents the regression curve of the form $a \cdot c_u^b$.

Finally, the uncertainty of the FidasU number concentration for each bin i and time step j during the campaign can be calculated as follows:

$$\sigma_{c_u^n(D_i)_j} = \sigma_r c_u^n(D_i)_j = 51.3(c_u^n)^{0.55}, \quad (5.17)$$

and the uncertainty of the FidasU mass concentration as:

$$\sigma_{c_u^m(D_i)_j} = \sigma_{c_u^n(D_i)_j} \frac{1}{6} \rho_d \pi D_i^3 \quad (5.18)$$

where $c_u^m(D_i)_j$ is the corrected mass concentration of FidasU in each bin i and time step j during the campaign; $D_i = \sqrt{d_{max} \cdot d_{min}}$ is the mean logarithmic diameter in bin number i , d_{min} and d_{max} are the minimum and maximum particle diameters of bin i , respectively; and ρ_d is the dust particle density, which is assumed to be 2500 kg m^{-3} .

The average total uncertainty for each u_* interval was calculated as the square root of the quadratic sum of the standard error and the average diffusive flux uncertainty within each u_* interval. The average diffusive flux uncertainty, $\sigma_{F(D_i)_{avg}}$, for each u_* is given by:

$$\sigma_{F(D_i)_{avg}} = \sqrt{\sum \sigma_{F(D_i)_j}^2 / N} \quad (5.19)$$

where $\sigma_{F(D_i)_j}$ is the uncertainty of each 15 min size-resolved diffusive flux in the u_*

interval, N is the number of 15 min measurements in the u_* interval, i is the size bin and j is the measurement time index within each u_* interval.

Additionally, the number and mass fractions of the diffusive flux integrated over four size ranges : $\sim 0.37 < D_i < 1 \mu\text{m}$, $\sim 1 < D_i < 2.5 \mu\text{m}$, $\sim 2.5 < D_i < 10 \mu\text{m}$ and $D_i > 10$

To analyse if the differences in the diffusive flux PSDs both between wind sectors and u_* intervals were statistically significant, one-tailed tests of significance were performed (Gorgas et al., 2011). This type of test allows evaluating if the mean of a population is statistically higher than the mean of another population. In this thesis I consider that: (1) our populations follow a normal distribution, (2) their variance are unknown, (3) the sum of the number of samples from each population is above 30 and (4) the number of samples of both populations is similar. Following these assumptions, I used the test statistic, z , which follows a normal distribution and is defined as:

$$z = \frac{\bar{x}_1 - \bar{x}_2}{\sqrt{\frac{s_1^2}{n_1} + \frac{s_2^2}{n_2}}} \quad (5.20)$$

where \bar{x}_i , s_i and n_i represent the mean, variance and number of samples of each population i .

The null hypothesis, H_0 , defined as the contrary of what our data show, is accepted if $z \leq z_\alpha$ and rejected if $z > z_\alpha$, where the significance level α is 0.05. This test was applied both considering certain fractions of diffusive flux and considering individually certain integrated size bins (see Chap. 8.2).

5.3.6 Computation of sandblasting efficiency

As explained in Chap. 2.1.6, sandblasting efficiency, α , is defined as the ratio of total vertical (diffusive) dust flux to horizontal (saltation) flux in mass, $\alpha = F/Q$. The total streamwise saltation flux, Q , defined as the vertical integral of the height-dependent streamwise saltation flux densities derived from the measured saltation counts, was computed by Martina Klose (KIT) using the same method as described in Klose et al. (2019). This means assuming an exponentially decreasing vertical profile of saltation flux density and using least-squares curve fitting for the three measurement heights. Profiles with coefficients of determination $R^2 < 0.5$ were excluded. Of the remaining

profiles, more than 99% had $R^2 > 0.95$ and more than 98% had $R^2 > 0.99$. For this thesis, I used these data in conjunction with the vertical flux data (calculated by myself) to estimate the sandblasting efficiency. It is important to note that in this calculation I excluded the vertical flux values in which either the net flux was negative or any of the integrated mass and number bins where $D_i > 0.42 \mu\text{m}$ was negative.

5.4. Estimating the size-resolved dry deposition and emitted fluxes based on different parameterizations

As discussed in Chap. 2.4, most studies have traditionally assumed that the diffusive flux PSD obtained a few metres above the surface is equivalent to the emitted dust PSD at the surface, neglecting the gravitational settling and the turbulent dry deposition flux. Considering the schematic shown in Fig. 2.4, the emitted flux, F_{emi} , can be estimated as the diffusive flux, F , plus the gravitational settling, F_g , at the intermediate level between the two Fidas minus the dry deposition flux at the surface, F_{dep} :

$$\begin{aligned} F_{emi}(D_i) &= F(D_i) + v_{dep}(D_i)c_{int}(D_i) - v_g(D_i)c_{int}(D_i) = \\ &= F(D_i) + (v_{dep}(D_i) - v_g(D_i))c_{int}(D_i) \end{aligned} \quad (5.21)$$

where $v_{dep}(D_i)$ is the dry deposition velocity; $v_g(D_i)$ is the gravitational settling velocity; $c_{int}(D_i) = (c_u(D_i) + c_l(D_i))/2$ is the concentration at the intermediate height between the two Fidas, being $c_u(D_i)$ the FidasU concentrations after systematic correction and $c_l(D_i)$ FidasL concentration; and D_i is the mean logarithmic diameter of each bin i . The gravitational settling velocity is calculated as $v_g(D_i) = C_c \sigma_{pa} g D_i^2 / (18\nu)$ where C_c is the Cunningham slip correction factor, $\nu = 1.45 \times 10^{-5} \text{ m}^2 \text{ s}^{-1}$ is the air kinematic viscosity and $\sigma_{pa} = (\rho_d - \rho_{air}) / \rho_{air}$ is the particle-to-air density ratio. Note that this expression assumes a Stokes regime, which is applicable to particles with $D_i \sim 10 \mu\text{m}$ or less. Furthermore, it is important to acknowledge that, as an approximation, I employed the concentration at the intermediate height between the two Fidas to estimate the dry deposition flux at the surface, rather than extrapolating it directly to the surface.

Experimentally, $v_{dep}(D_i)$ can be calculated as the sum of the diffusive dry deposition velocity, $v_{diff}(D_i)$, and $v_g(D_i)$. $v_{diff}(D_i)$ for each 15 min period was

5.4. Estimating the size-resolved dry deposition and emitted fluxes based on different parameterizations

obtained in this thesis as $v_{diff}(D_i) = -F(D_i)/c_{int}(D_i)$ (Junge, 1963; Shao, 2008; Bergametti et al., 2018). $v_{diff}(D_i)$ is positive when downward, so the diffusive flux in integrated size bin resolution, $F(D_i)$, must be negative. Due to the presence of dust emission, these observation-based estimates of v_{dep} had to be restricted to periods when dust emission was negligible, i.e. for $u_* < u_{*th}$.

In the absence of observation-based $v_{dep}(D_i)$ during wind erosion conditions ($u_* > u_{*th}$), two different resistance-based dry deposition velocity parameterizations were tested to estimate $v_{dep}(D_i)$ for all u_* values: (1) the parameterization used in Fernandes et al. (2019) (referred to as F19) and (2) the scheme proposed in Zhang et al. (2001) (referred to as Z01). The dry deposition velocity in F19 is parameterized as follows:

$$v_{dep.F19}(D_i) = \frac{1}{R_a + R_s(D_i) + R_a R_s(D_i) v_g(D_i)} + v_g(D_i) \quad (5.22)$$

where $R_a = \ln(\frac{z_{int}}{z_0})/(\kappa u_*)$ represents the turbulent transfer close to the surface, z_{int} is the intermediate height between the two Fidas, and z_0 the aerodynamic roughness length computed as explained in Sect. 5.3.4. The surface or quasi-laminar resistance $R_s = [u_*(S_c^{-2/3} + 10^{-3/S_t})]^{-1}$ accounts for losses by Brownian motion and inertial impaction; $S_c = \nu/D_g(D_i)$ is the Schmidt number, and $S_t = u_*^2 v_g(D_i)/(g\nu)$ the Stokes number for smooth surfaces, where $D_g(D_i) = \kappa T C_c/(3\pi \rho_{air} \nu D_i)$ is the Brownian diffusivity, κ is the Boltzmann constant, T is the air temperature at 1 m height, C_c is the Cunningham slip correction factor, and $\nu = 1.45 \times 10^{-5} \text{ m}^2 \text{ s}^{-1}$ is the air kinematic viscosity. The settling velocity, $v_g(D_i)$, is calculated for each size bin as $v_g(D_i) = C_c \sigma_{pa} g D_i^2/(18\nu)$ where $\sigma_{pa} = (\rho_d - \rho_{air})/\rho_{air}$ is the particle-to-air density ratio.

The dry deposition velocity in Z01 is parameterized as follows:

$$v_{dep.Z01}(D_i) = \frac{1}{R_a + R_s(D_i)} + v_g(D_i) \quad (5.23)$$

where in this case $R_a = (\ln(\frac{z_{int}}{z_0}) - \Psi_h)/(\kappa u_*)$, with Ψ_h being the integral of the similarity function for sensible heat (defined in Sect. 5.3.4), and $R_s = [\epsilon_0 u_*(E_B + E_{IM} + E_{IN})R_1]^{-1}$, where ϵ_0 is an empirical constant set to 3; E_B , E_{IM} , E_{IN} are, respectively, the collection efficiency from Brownian diffusion, the impaction, and the interception; and R_1 is the correction factor representing the fraction of

particles that stick to the surface. In this scheme some parameters are ascribed to different land use categories. For this study, I selected the values recommended for the “desert” (land use category 8) category. The efficiency from Brownian diffusion $E_B = S_c^{-\gamma}$ is a function of the Schmidt number, and the constant γ is set to 0.54. The impaction $E_{IM} = (S_t/(\alpha + S_t))^2$, where α is set to 50. Desert bare surfaces in this parameterization are considered totally smooth surfaces, and hence the interception E_{IN} is set to 0, and I assume $R_1 = 1$.

In Chap. 10, it will be demonstrated that these parameterizations significantly underestimated our observationally-based estimates of v_{dep} . Consequently, I sought a better model representation to fit the observation-based estimates for $u_* < u_{*th}$. To that end, some aspects of the newest scheme proposed by Zhang and Shao (2014) were incorporated into the Zhang et al. (2001) scheme. While sharing some similarities, the parameterization from Zhang and Shao (2014) does not consider desert bare surfaces as totally smooth surfaces, allowing the interception of dust particles by micro-roughness elements. The resulting tuned dry deposition velocity parameterization is given by:

$$v_{dep.tuned}(D_i) = \frac{1}{B_1 R_a + R_s(D_i)} + v_g(D_i) \quad (5.24)$$

where R_a and R_s are defined as in Eq. 5.23. The differences in the tuned parameterization with respect to Eq. 5.23 are as follows: (1) R_a is multiplied by a correction factor $B_1 > 0$; (2) in the impaction term E_{IM} , the constant α is now set to 0.6; (3) the form of the Stokes number for vegetated surfaces (Slinn, 1982) is now used, which is given by $S_t = u_* v_g(D_i)/(g d_c)$, where d_c is the diameter of the roughness elements; and (4) the interception is now $E_{IN} = A_{in} u_* 10^{-S_t} 2D_i/d_c$, where the term A_{in} is an empirical parameter that accounts for the effect of micro-roughness characteristics (Zhang and Shao, 2014).

By adjusting the values of B_1 , d_c and A_{in} , this tuned parameterization could reasonably fit the observation-based estimates. Subsequently, this parameterization was used to estimate the dry deposition flux, which was then employed to estimate the emitted dust flux for all u_* conditions using Eq. 5.21. Results of dry deposition and emitted fluxes obtained using F19 and Z01 are also provided in Appendices D and E. The dry deposition and emitted dust fluxes were estimated for the same 15 min samples used for diffusive flux, and subsequently were averaged over the same u_*

5.4. Estimating the size-resolved dry deposition and emitted fluxes based on different parameterizations

intervals.

Compared to the diffusive flux (see Sect. 5.3.5) there is an extra source of uncertainty for the estimated emitted flux: v_{dep} . However, there are two factors to consider. First, as there is only observation-based v_{dep} for the first three u_* intervals, it is not possible to estimate its uncertainty for the rest of the u_* intervals. Second, dry deposition parameterizations, such as those employed in this thesis, are prone to significant structural uncertainties, as evidenced by their disparities with observations. Future work may explore the use of other deposition models that better fit our measurements, but is out of the scope of this thesis and for this reason the uncertainty of v_{dep} has been neglected in the calculation of the uncertainty of the emitted flux. So, as for the diffusive flux, the uncertainty of the estimated emitted flux in each bin and timestamp was calculated assuming the FidasL as the reference device, correcting the systematic deviation of the FidasU and only propagating the random uncertainty as follows:

$$\sigma_{F_{emi}(D_i)} = u_* \kappa \frac{\sigma_{c_u(D_i)}}{\ln\left(\frac{z_u}{z_l}\right) - \Psi_m\left(\frac{z_u}{L}\right) + \Psi_m\left(\frac{z_l}{L}\right)} + \frac{v_{dep}(D_i) - v_g(D_i)}{2} \sigma_{c_u(D_i)} \quad (5.25)$$

Thus, the uncertainty in the estimated emitted flux $\sigma_{F_{emi}(D_i)}$ only depends on the uncertainty of the FidasU concentration with respect to the FidasL concentration $\sigma_{c_u(D_i)}$. Finally, the average total uncertainty within each u_* interval for each bin is calculated as the square root of the quadratic sum of the standard error of the estimated emitted flux (selecting all the timestamps belonging to that u_* interval) and the average estimated emitted flux uncertainty within each u_* interval, $\sigma_{F_{emi}(D_i)_{avg}}$. The latter is calculated for each u_* interval as $\sigma_{F_{emi}(D_i)_{avg}} = \sqrt{\sum \sigma_{F_{emi}(D_i)_j}^2} / N$ where $\sigma_{F_{emi}(D_i)_j}$ is the uncertainty of each 15 min size-resolved emitted flux in the u_* interval, N is the number of 15 min measurements in the u_* interval, i is the size bin and j is the measurement time index within each u_* interval.

Likewise, I calculated the number and mass fractions of the emitted dust flux using the v_{dep} tuned formulation integrated over the size ranges: $\sim 0.37 < D_i < 1 \mu\text{m}$, $\sim 1 < D_i < 2.5 \mu\text{m}$, $\sim 2.5 < D_i < 10 \mu\text{m}$ and $D_i > 10 \mu\text{m}$ for the different u_* intervals, type of event and the two wind direction sectors (Chap. 10). Analogous tests of


significance as those described in Sect. 5.3.5 were also applied for the estimated emitted flux.





III

Results and discussion



Overview of the atmospheric conditions and dust events during the campaign

Times series of measured atmospheric conditions and near-surface dust concentrations are displayed in Fig. 6.1; u_* and atmospheric stability, along with saltation and diffusive fluxes, are displayed in Fig. 6.2. As expected, the daily cycles of temperature and relative humidity are anti-correlated (Fig. 6.1b), and temperature inversions (Fig. 6.1a), along with atmospheric stability (Fig. 6.2b), are prevalent during nighttime. Temperature at 2 m height ranges from slightly less than 20 °C during the night to up to ~40 °C during the day, and surface relative humidity ranges from as low as 6 % during the day to up to ~65 % during the night. There is a shift after 14 September, with substantial increases in temperature and decreases in relative humidity, with the exception of 17-18 September, when relative humidity appears to be temporarily high.

The diurnal cycles of surface wind (Fig. 6.1d) and u_* (Fig. 6.2a), along with the associated cycles of dust concentration (Fig. 6.1f and g) and saltation and diffusive fluxes (Fig. 6.2c, d and e) are generally associated to the diurnal cycle of solar heating. In the early morning, as the surface starts to warm and releases turbulent sensible heat, the lower atmosphere becomes unstable. As the day evolves, momentum is mixed downward from the stronger winds aloft increasing wind speed and u_* , while stability progressively tends towards neutrality (Fig. 6.2b). Winds are generally channelled through the valley, broadly parallel to the Drâa river, alternating between two opposite and preferential wind directions, centred around 80 ° and 240 ° (Fig. 6.1e). The distribution of wind direction and u_* during the campaign is shown in Fig. 6.3. We refer to the dust events associated to these recurring diurnal cycles as “regular” events, for which maximum winds at 10 m can reach 15 min average values up to $\sim 11 \text{ m s}^{-1}$ (Fig. 6.1d). From 22 to 25 September winds remain relatively

Chapter 6. Overview of the atmospheric conditions and dust events during the campaign

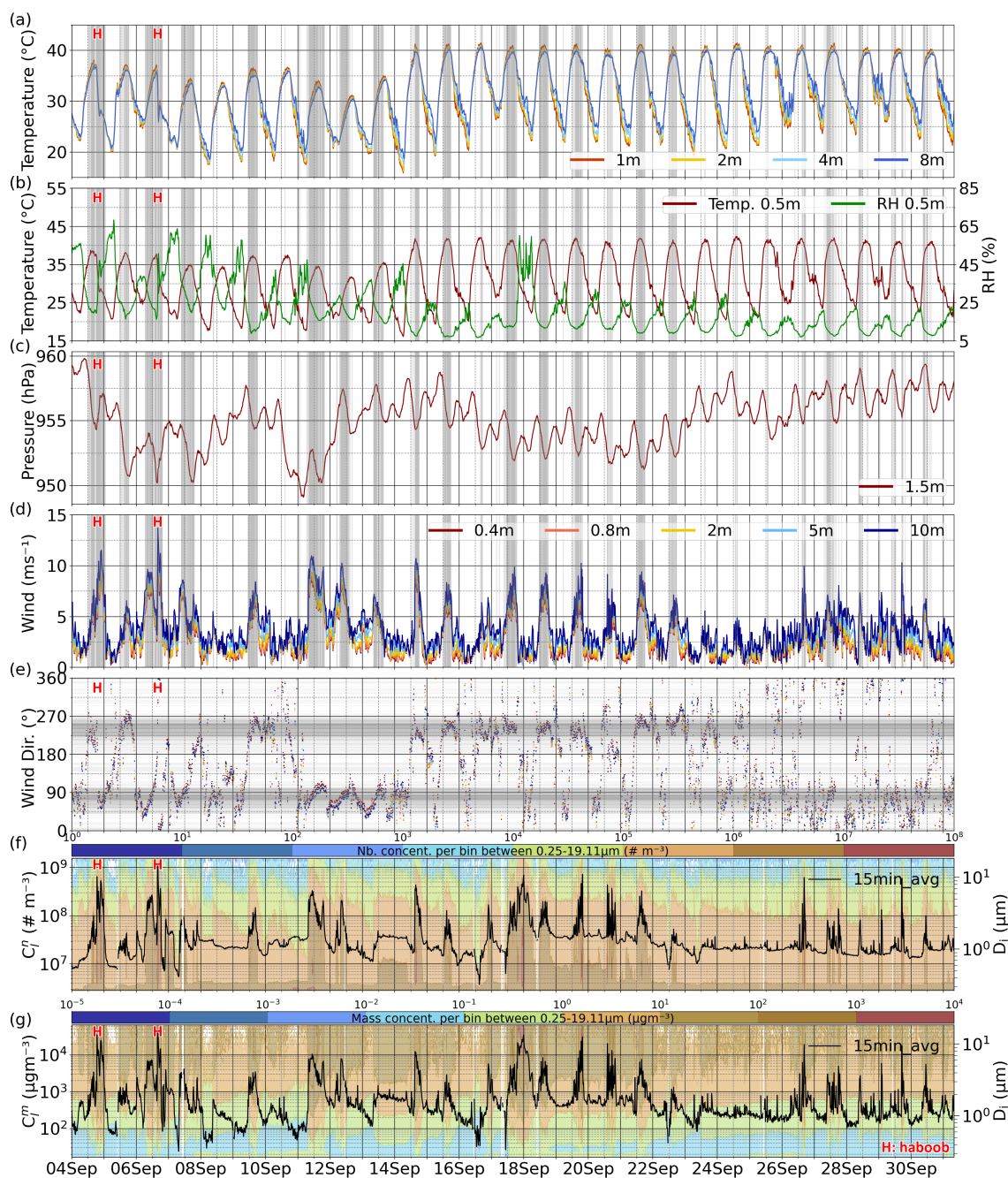


Figure 6.1: Time series (UTC) of 15 min average (a) temperature ($^{\circ}\text{C}$) at 1, 2, 4, and 8 m; (b) relative humidity (%) and temperature ($^{\circ}\text{C}$) at 0.5 m; (c) pressure (hPa) at 1.5 m; (d) mean wind speed (m s^{-1}) and (e) mean wind direction ($^{\circ}$) at 0.4, 0.8, 2, 5, and 10 m; (f) FidasL (1.8 m) particle concentrations in number $c_i^n (\# \text{ m}^{-3})$; and (g) in mass $c_i^m (\mu\text{g m}^{-3})$. In (f) and (g) the total concentrations are represented as lines (left y axis), whereas size-resolved concentrations are shown as colour contours (right y axis) in the original size bin resolution. Vertical grey lines in (a)-(d) and horizontal grey lines in (e) highlight, respectively, periods and wind directions for which $u_* > u_{*th}$. The time series of u_* is depicted in Fig. 6.2a.

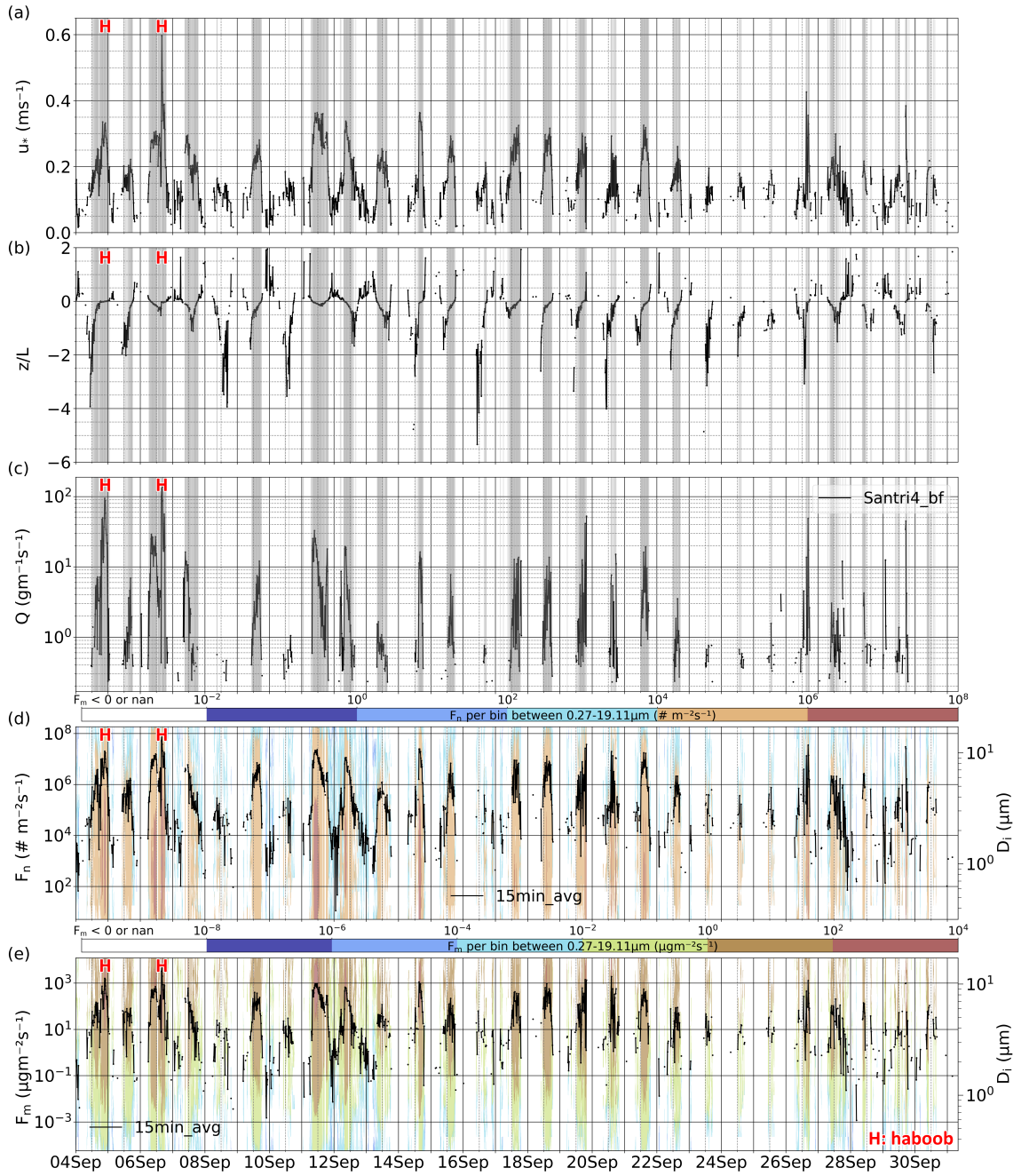


Figure 6.2: Time series (UTC) of 15 min averaged (a) friction velocity u_* (m s^{-1}); (b) atmospheric stability represented by z/L , where z is the reference height 2 m; (c) saltation flux ($\text{g m}^{-1} \text{s}^{-1}$); (d) bulk and size-resolved diffusive flux in number ($\# \text{ m}^{-2} \text{s}^{-1}$) between 0.27 and 19.11 μm ; and (e) bulk and size-resolved diffusive flux in mass ($\mu\text{g m}^{-2} \text{s}^{-1}$) between 0.27 and 19.11 μm . Grey areas in (a)-(c) highlight times with $u_* > u_{*th}$. Data gaps in u_* , atmospheric stability, and diffusive fluxes result from limits in the applicability of the law of the wall method. The size-resolved diffusive fluxes are shown in the integrated size bin resolution. Only the bulk and size-resolved diffusive fluxes that are positive are represented.

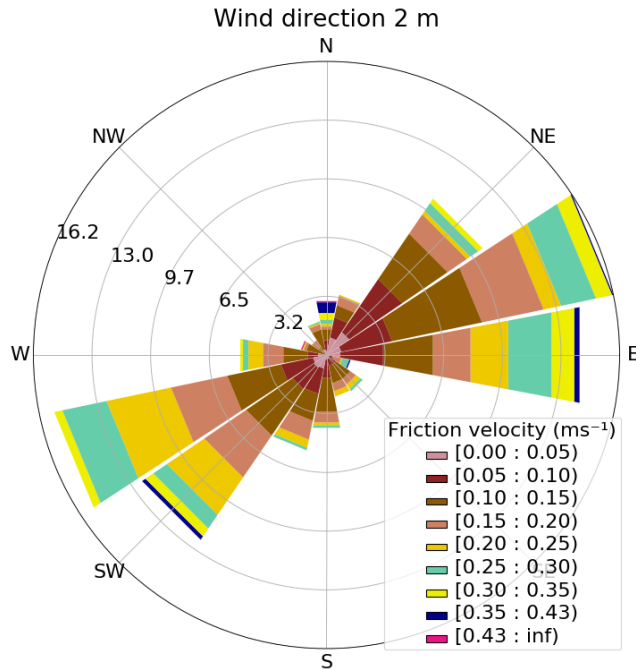


Figure 6.3: Wind rose at 2 m height for different u_* intervals (m s^{-1}). The length of each bar represents the fraction of time the wind blows from that direction.

calm, and after 25 September diurnal cycles are less marked and dust events are more intermittent and short-lived.

In addition to these regular events, we also captured two strong cold pool outflows (hereafter referred to as “haboob” events) in the evening of 4 September and in the afternoon of 6 September, both marked with a red “H” in Figs. 6.1 and 6.2. Cold pool outflows result from density currents created by latent heat exchange of evaporating rain in deep convective downdrafts. The arrival of sharply defined dust walls, caused by the gust fronts at the leading edge of the outflow winds, were not only directly witnessed by the field campaign team but can be also clearly detected in the measurements. A 1 min frequency time-lapse video recorded from the Fidas location during 6 September clearly shows the arrival of the haboob in the afternoon (FRAGMENT team, 2023). Both haboob events are characterized by the highest 10 m winds recorded during the campaign (15 min averages of $\sim 11.5 \text{ m s}^{-1}$ and $\sim 14 \text{ m s}^{-1}$, respectively) and unusually fast changes in atmospheric conditions with values consistent with previous haboob studies (Miller et al., 2008): sudden

increases in wind speed, decreases in 2 m temperature of $\sim 8\text{--}9^\circ\text{C}$, increases in relative humidity of $\sim 24\text{--}32\%$, and a rise of $\sim 2\text{ hPa}$ in surface pressure (Fig. 6.1c). During these events, precipitation was not detected by our rain gauge, but during the night of 6 September there was water flowing downriver, which caused flooding of large areas in the vicinity of our lake on the next day (not affecting the lake itself), suggesting that heavy showers occurred over the mountain range to the north of our location (Fig. 5.5c).

Dust concentration (Fig. 6.1f and g) exhibits peaks of varying intensity about every $\sim 1\text{--}2$ days, consistent with the wind speed and u_* patterns. Number and mass concentrations were $5 \times 10^7 \# \text{ m}^{-3}$ and $1243 \mu\text{g m}^{-3}$ on average, respectively, and there were 10 days when the 15 min dust mass concentration exceeded $10^4 \mu\text{g m}^{-3}$. As expected for dust, the number concentration was dominated by fine particles, and the mass concentration was dominated by coarse and super-coarse dust. Dust concentration is generally correlated with saltation (Fig. 6.2c) and diffusive fluxes (Fig. 6.2d and e), with the notable exception of an event that extends over the evening of 17 September and the morning of 18 September. During this event, concentrations reached values that are among the highest recorded during the campaign (Fig. 6.1f and g), although winds were low (Fig. 6.1d), saltation was absent (Fig. 6.2c), and diffusive fluxes were negative (note that negative fluxes are not represented in Fig. 6.2d and e). The latter implies that dust was transported from elsewhere and deposited, but it was not emitted from our site. Given that convective storms were spotted from a distance during that evening and the event was characterized by high relative humidity values (Fig. 6.1b), we hypothesize that those highly dust-loaded air masses that slowly and persistently reached our site were generated by precedent haboob activity upwind.

Additionally, the presence of anthropogenic aerosols with diameters below $\sim 0.4 \mu\text{m}$ was detected during the campaign. Its influence becomes more noticeable when winds are weak and mass concentrations are low. This feature is better appreciated in Fig. 6.4, where the size-resolved concentrations from FidasL (shown as colour contours on the right y axis) are depicted as percentages of number and mass fractions, compared to Figure 6.1f and g, where the size-resolved concentrations from FidasL (also shown as color contours on the right y axis) are represented as absolute concentrations. These findings are consistent with measured optical

Chapter 6. Overview of the atmospheric conditions and dust events during the campaign

properties analysed in Yus-Díez et al. (prep). Notably, during the period between 8 and 10 September, when there were low winds coming from the east (i.e. from M’Hamid), the influence of these anthropogenic aerosols was particularly evident. The presence of such anthropogenic aerosols in the lower size range of the measured PSD is further supported and discussed in Chap. 8.1.

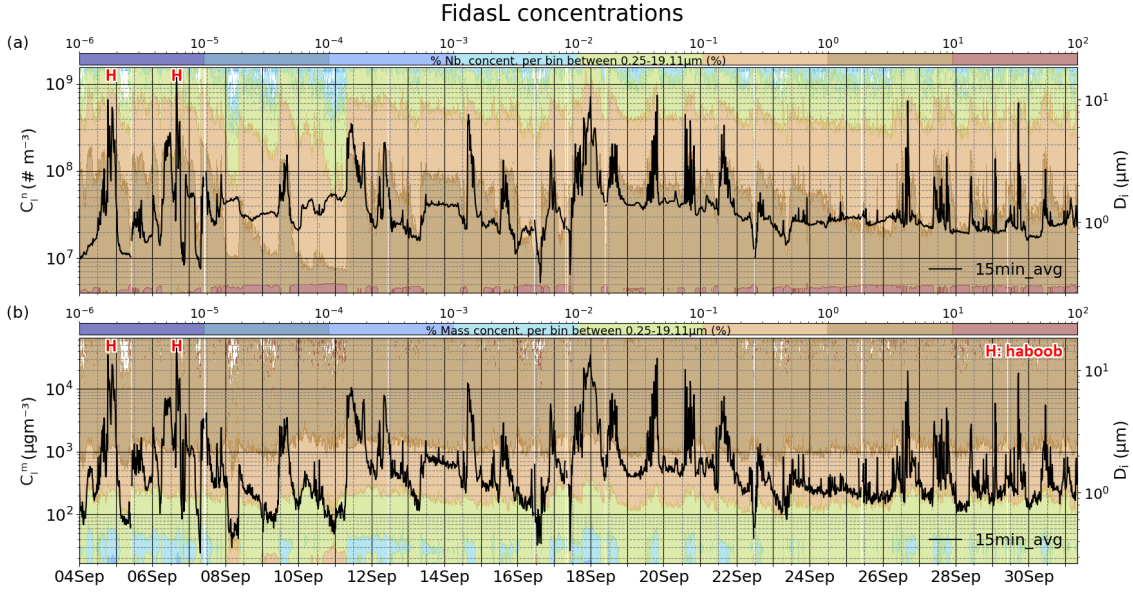


Figure 6.4: Solid lines represent the time evolution of the 15 min average total particle concentrations between 0.25 to 19.11 μm in number ($\# \text{m}^{-3}$) (a) and mass (μgm^{-3}) (b). Contour plots on the background show the size-resolved particle number (a) and mass (b) concentration fractions (%) for each time step.

Saltation and diffusive fluxes are highly correlated and occur regularly throughout the campaign, peaking typically between 12:00 and 18:00 UTC in accordance with maximum surface winds and u_* . Figure 6.5 displays Q against τ , along with the regression curves of the form $Q = Cu_*(\tau - \tau_{th})$ (magenta line) and $Q = C(\tau - \tau_{th})$ (green line). The fitting parameters, denoted as C and the impact threshold stress, τ_{th} , are reported in the graph along with the standard error of the estimate for each regression model. Our measurements seem to slightly better fit the 3/2 form (magenta line) than the linear fit (green line). Therefore, in this study u_{*th} is assumed to be 0.16 m s^{-1} , which is reached nearly every day. u_* shows peaks up to $\sim 0.4 \text{ m s}^{-1}$ during regular events and reaches up to $\sim 0.6 \text{ m s}^{-1}$ during the haboob event that occurred on the afternoon of 6 September (Fig 6.2a). Wind erosion occurs mostly under unstable or close to neutral atmospheric conditions (Fig. 6.2b). For

$u_* > u_{*th}$, the 15 min average of total vertical diffusive flux in terms of number and mass are on average $3.7 \times 10^6 \# \text{ m}^{-2} \text{ s}^{-1}$ and $191 \mu\text{g m}^{-2} \text{ s}^{-1}$, respectively, reaching maximum values of $8.4 \times 10^7 \# \text{ m}^{-2} \text{ s}^{-1}$ and $5116 \mu\text{g m}^{-2} \text{ s}^{-1}$ on 6 September.

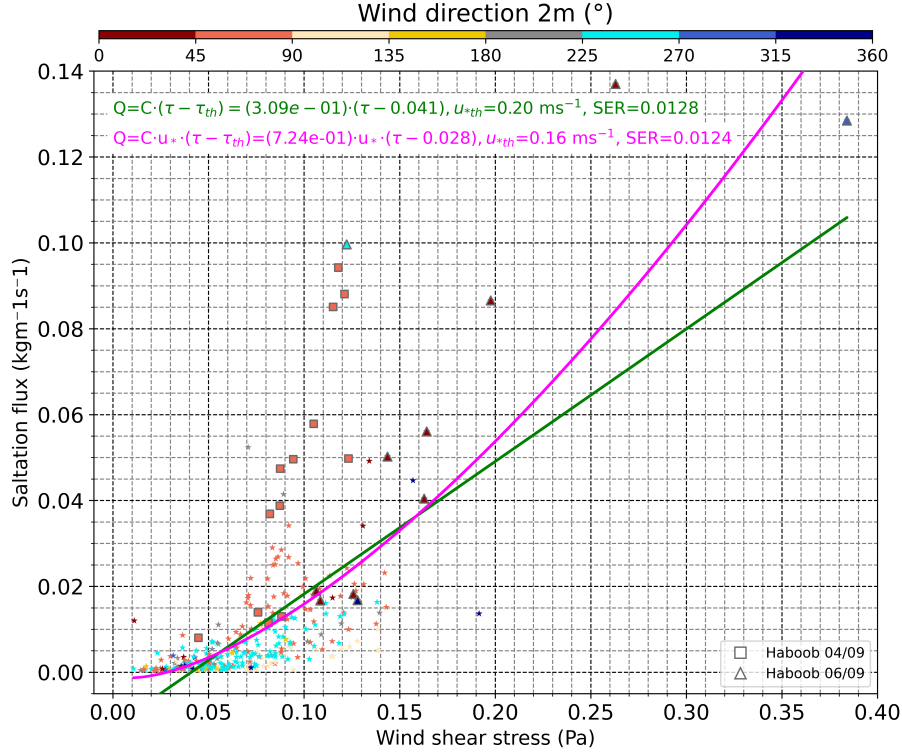


Figure 6.5: Saltation flux ($\text{kg m}^{-1} \text{ s}^{-1}$) versus wind shear stress (Pa). The points correspond to the 15 min values in which (1) there is a simultaneous net positive diffusive flux and saltation flux, (2) the diffusive flux is positive in all size bins above $0.4 \mu\text{m}$ and (3) $u_* > 0.1 \text{ m s}^{-1}$. The mean air density under these conditions used to infer u_{*th} was $\overline{\rho_{air}} = 1.07 \text{ kg m}^{-3}$. Squares and triangles are used to identify the values corresponding to haboobs on 4 and 6 September, respectively. The green and magenta lines represent respectively the regression curves of the form $Q = C \cdot (\tau - \tau_{th})$ and $Q = C \cdot u_* \cdot (\tau - \tau_{th})$. The fitting parameters C and τ_{th} for these respective linear and 3/2 fits are shown in the graph along with the standard error of the estimate for each case.

Characterization of saltation and sandblasting efficiency

Figure 7.1a, b and c display the diffusive flux, saltation flux, and sandblasting efficiency against u_* . I used coincident 15 min data between saltation and diffusive flux, and only when the diffusive flux was positive in all dust size bins with $D_i > 0.4 \mu\text{m}$, i.e. the bulk diffusive flux is considered between 0.37 and 19.11 μm (see Chap. 8.1 for more details). The points corresponding to the haboobs on 4 and 6 September are depicted with squares and triangles, respectively. Regression curves of the form $a \cdot u_*^b$ are also represented for $u_* > u_{*th}$. The 95% confidence intervals of the parameters of each regression curve are shown in Table 7.1. Figures 7.2 and 7.3 are analogous to Fig. 7.1, but are done selecting only the 15 min values corresponding to the two predominant wind directions (45–90° and 225–270°, respectively). Similarly, Tables 7.2 and 7.3 are analogous to Table 7.1.

Considering all the available measurements (Fig. 7.1), the diffusive flux ranges mostly between $\sim 10^1$ and $\sim 10^3 \mu\text{g m}^{-2} \text{s}^{-1}$ and the power law exponent b is 3.88 (Fig. 7.1a). The obtained exponent is within the range shown in Ishizuka et al. (2014) (their Fig. 5), where b varies between approximately 3 and 6 across different datasets gathered from the literature (Gillette, 1977; Nickling, 1983; Nickling and Gillies, 1993; Nickling et al., 1999; Gomes et al., 2003b; Rajot et al., 2003; Sow et al., 2009); this is likely due to differences in soil type and soil surface conditions.

The saltation flux ranges between about 10^{-1} and $10^2 \text{g m}^{-1} \text{s}^{-1}$. The power law exponent b is slightly higher than that obtained for the diffusive flux, i.e. $b = 4.31$ (Fig. 7.1b). This value is larger than that reported in Gillette (1977) for most soils ($b \approx 3$). Additionally, the saltation flux is higher for similar ranges of u_* compared to Alfaro et al. (2022) (their Fig. 4), where data of two major dust field campaigns (JADE and WIND-O-V) are re-analysed. For $u_* \approx 0.25\text{--}0.45 \text{m s}^{-1}$, our 15 min saltation flux varies between 10^0 and $10^2 \text{g m}^{-1} \text{s}^{-1}$, while the 1 min and 16 min measurements from the JADE and WIND-O-V campaigns, respectively, vary between

10^{-1} and $10^1 \text{ g m}^{-1} \text{ s}^{-1}$. Using the same instrument (SANTRI) as in this study, Klose et al. (2019) reported a maximum 1 min saltation flux of almost $10^1 \text{ g m}^{-1} \text{ s}^{-1}$ for $u_* > 0.8 \text{ m s}^{-1}$, approximately an order of magnitude smaller than our 15 min maximum values occurring during the haboobs for smaller u_* . The large saltation fluxes suggest, despite the hard surface crusting, that the sand supply was such that our site did not experience considerable supply limitation, i.e. that saltation transport was mainly driven by atmospheric momentum and not by particle availability.

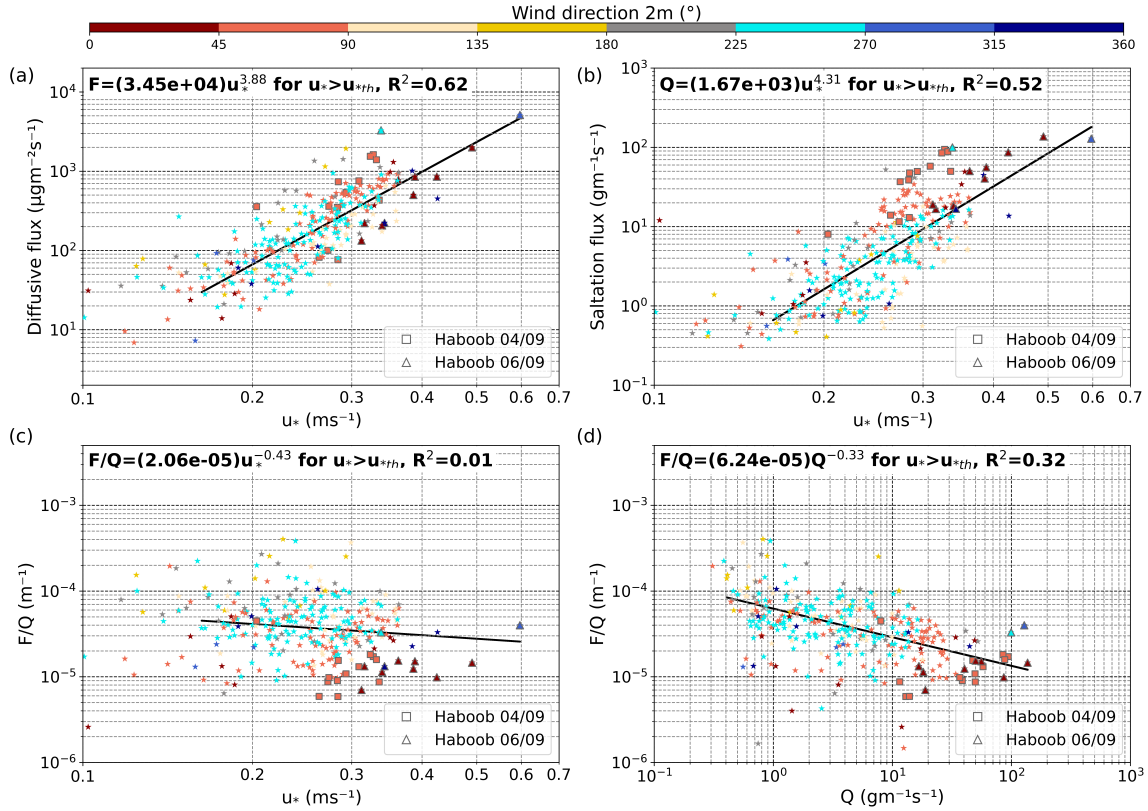


Figure 7.1: (a) Diffusive flux ($\mu\text{g m}^{-2} \text{ s}^{-1}$) versus friction velocity u_* (m s^{-1}), (b) saltation flux ($\text{g m}^{-1} \text{ s}^{-1}$) versus u_* (m s^{-1}), (c) sandblasting efficiency (m^{-1}) versus u_* (m s^{-1}), and (d) sandblasting efficiency (m^{-1}) versus saltation flux ($\text{g m}^{-1} \text{ s}^{-1}$). Colours represent the wind direction ($^\circ$). The points shown in all panels correspond to the 15 min values in which there is a simultaneous net positive diffusive flux and saltation flux, and when the diffusive flux is positive in all size bins with $D_i > 0.4 \mu\text{m}$, i.e. the bulk diffusive flux is considered between 0.37 and 19.11 μm . Sandblasting efficiency is defined as the ratio of the vertical and horizontal fluxes in mass. Squares and triangles are used to identify the values corresponding to haboobs on 4 and 6 September, respectively. The lines in (a)-(d) represent the regression curves of the form $a \cdot u_*^b$ for $u_* > u_{*th}$. The coefficient of determination (in logarithmic space) of each regression curve is shown in its respective graph, and the 95% confidence intervals of a and b are reported in Table 7.1.

Table 7.1: Obtained parameters a and b from each regression curve in Fig. 7.1 (all wind directions) along with their 95% confidence intervals.

a	a [95% C.I.]	b	b [95% C.I.]
$F = a \cdot u_*^b$			
$3.45 \cdot 10^4$	$[2.15, 5.53] \cdot 10^4$	3.88	[3.54, 4.23]
$Q = a \cdot u_*^b$			
$1.67 \cdot 10^3$	$[0.88, 3.17] \cdot 10^3$	4.31	[3.85, 4.78]
$F/Q = a \cdot u_*^b$			
$2.06 \cdot 10^{-5}$	$[1.19, 3.55] \cdot 10^{-5}$	-0.43	[-0.83, -0.04]
$F/Q = a \cdot Q^b$			
$6.24 \cdot 10^{-5}$	$[5.58, 6.98] \cdot 10^{-5}$	-0.33	[-0.39, -0.28]

Comparison of the height-dependent saltation flux obtained with SANTRI4 with that from the co-located MWAC sampler (not shown) confirmed that both were largely consistent, with SANTRI4 tending to record slightly higher fluxes. This is in qualitative agreement with the comparison of saltation measurement devices from Goossens et al. (2018).

The intensity of saltation impacts the aerodynamic roughness length z_0 due to momentum absorption by the saltating particles (Owen, 1964; Gillette et al., 1998). Figure 7.4 displays the roughness length z_0 against u_* under saltation conditions, that is 15 min values with a positive saltation flux, in our site. I only used the values in which at the same time $u_* > u_{*th}$. z_0 ranges mostly between 10^{-5} and 10^{-4} m and shows quite a lot of scatter, particularly for u_* below 0.2 m s^{-1} . Furthermore, z_0 increases with u_* . This increase was also observed in Dupont et al. (2018) and Field and Pelletier (2018), although our roughness lengths were about one order of magnitude smaller, consistent with values obtained in other playas (Marticorena et al., 2006). z_0 is also sensitive to wind direction, with values about one order of magnitude higher for wind directions $135\text{--}180^\circ$ and $315\text{--}360^\circ$, the latter one close to the alignment of our instruments. There are also differences, albeit relatively small, between the two predominant wind directions, $225\text{--}270^\circ$ and $45\text{--}90^\circ$ (Fig. 7.4).

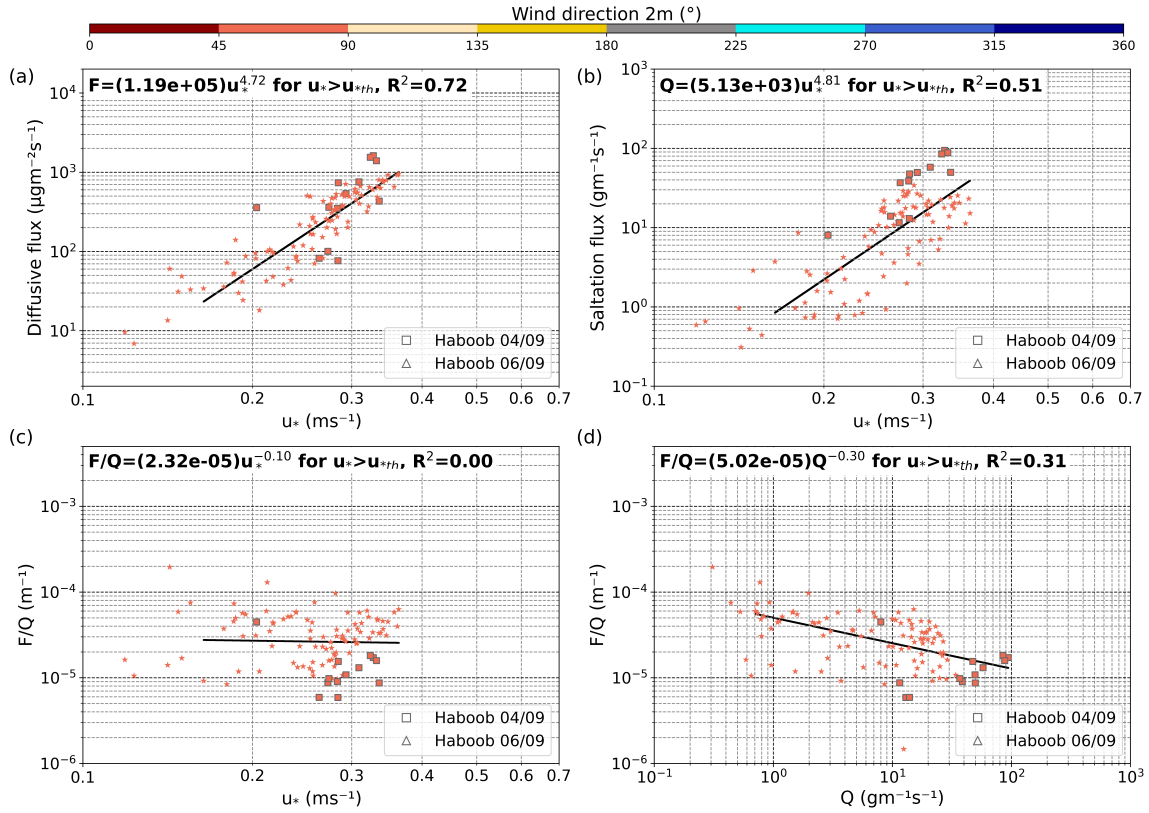


Figure 7.2: Analogous to Fig. 7.1 but considering only wind directions between 45–90°. Fitting parameters along with their respective 95% confidence intervals are reported in Table 7.2.

Table 7.2: Obtained parameters a and b from each regression curve in Fig. 7.2 (wind directions between 45–90°) along with their 95% confidence intervals.

a	a [95% C.I.]	b	b [95% C.I.]
$F = a \cdot u_*^b$			
$1.19 \cdot 10^5$	$[0.54, 2.64] \cdot 10^5$	4.72	[4.13, 5.31]
$Q = a \cdot u_*^b$			
$5.13 \cdot 10^3$	$[1.47, 17.98] \cdot 10^3$	4.81	[3.88, 5.75]
$F/Q = a \cdot u_*^b$			
$2.32 \cdot 10^{-5}$	$[0.89, 6.04] \cdot 10^{-5}$	-0.10	[-0.81, 0.62]
$F/Q = a \cdot Q^b$			
$5.02 \cdot 10^{-5}$	$[4.02, 6.26] \cdot 10^{-5}$	-0.30	[-0.39, -0.21]

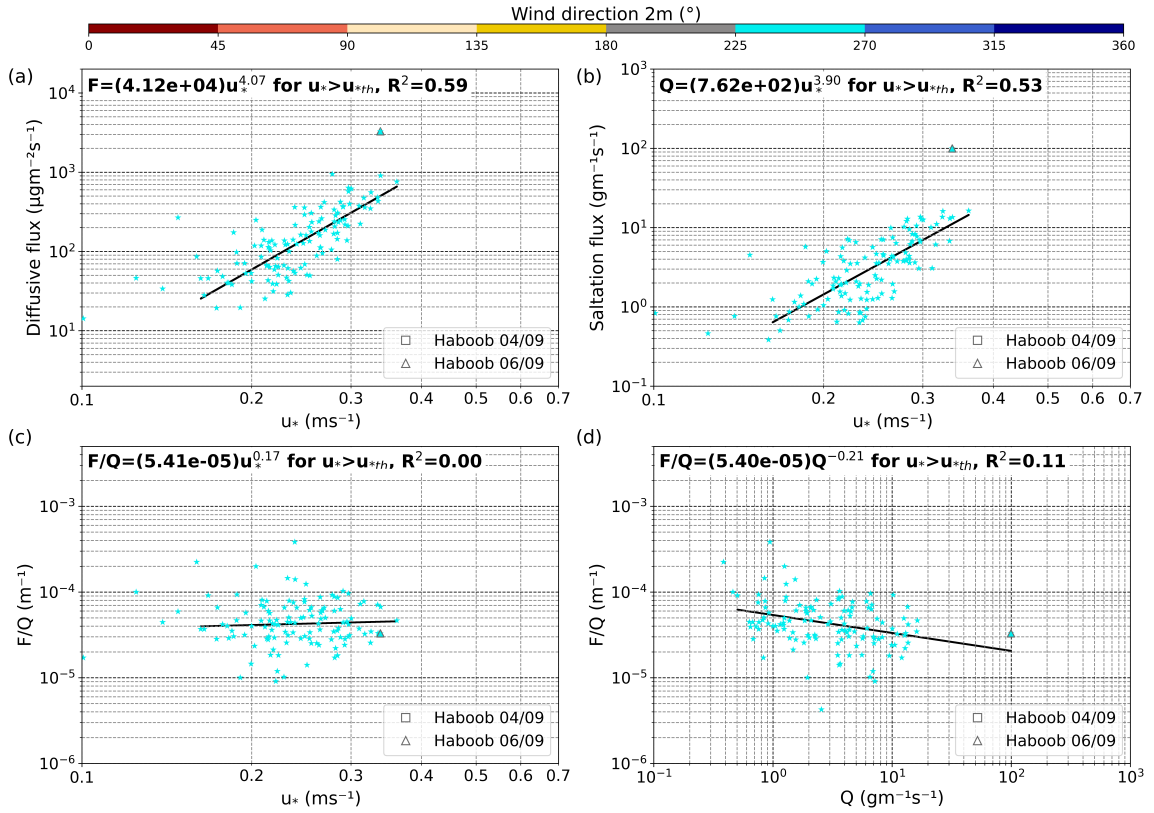


Figure 7.3: Analogous to Fig. 7.1 but considering only wind directions between 225–270°. Fitting parameters along with their respective 95% confidence intervals are reported in Table 7.2.

Table 7.3: Obtained parameters a and b from each regression curve in Fig. 7.3 (wind directions between 225–270°) along with their 95% confidence intervals.

a	a [95% C.I.]	b	b [95% C.I.]
$F = a \cdot u_*^b$			
$4.12 \cdot 10^4$	$[1.69, 10.06] \cdot 10^4$	4.07	[3.44, 4.69]
$Q = a \cdot u_*^b$			
$7.62 \cdot 10^2$	$[2.90, 19.98] \cdot 10^2$	3.90	[3.22, 4.57]
$F/Q = a \cdot u_*^b$			
$5.41 \cdot 10^{-5}$	$[2.23, 13.10] \cdot 10^{-5}$	0.17	[-0.45, 0.79]
$F/Q = a \cdot Q^b$			
$5.40 \cdot 10^{-5}$	$[4.59, 6.35] \cdot 10^{-5}$	-0.21	[-0.32, -0.10]

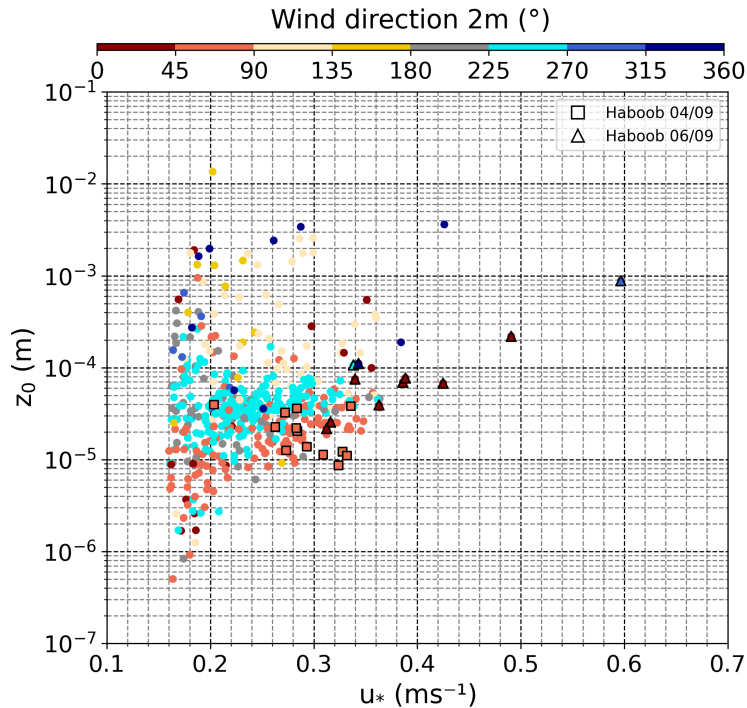


Figure 7.4: Relationship between 15 min averages of surface roughness length, z_0 , and friction velocity, u_* , under wind erosion conditions. Colors indicate wind direction at 2 m height. Squares and triangles are used to identify the values corresponding to haboobs on 4 and 6 September, respectively.

Our measurements are also fitted in Fig. 7.5a to the relationship $z_0 = C_{ch} \cdot u_*^2/g$ originally derived by Charnock (1955) for water surfaces, but also applicable for sand and snow surfaces (Owen, 1964; Chamberlain, 1983). A value of $C_{ch} = 0.02$ is obtained when taking into account all data, although the dispersion is very high and R^2 (in logarithmic space) very low. This value coincides with that obtained by Owen (1964) and that derived in Dupont et al. (2018) for some of the wind erosion events during the WIND-O-V 2017 Experiment. Smaller values of $C_{ch} = 0.007$ and 0.004 and a higher R^2 (in logarithmic space) are obtained, when considering separately the predominant wind directions $225\text{--}270^\circ$ and $45\text{--}90^\circ$, respectively (Fig. 7.5a). Our measurements are fitted as well to the modified Charnock's model proposed by Sherman (1992), which uses a more physical relation and accounts for the presence of a threshold: $z_0 - (2D_{50}/30) = C_{ch} \cdot (u_* - u_{*th})^2/g$, where $2D_{50}/30$ represents the minimum plausible roughness length, being D_{50} the mean grain diameter of the saltators, and $u_* - u_{*th}$ the excess shear velocity. For this fitting it was considered that $u_{*th} = 0.16 \text{ m s}^{-1}$ (as described in Chap. 6) and that $D_{50} = 0.13 \text{ mm}$. A value

of $C_{ch} = 0.07$ is obtained when taking into account all data and $C_{ch} = 0.02$ and 0.01 , when considering separately the predominant wind directions $225\text{--}270^\circ$ and $45\text{--}90^\circ$, respectively (Fig. 7.5b). A lower R^2 (in logarithmic space) is obtained in the three cases compared to Charnock's model. In Fig. 7.5, I used 15 min data with a positive saltation flux and when $u_* > u_{*th}$ while in Fig. 7.6 only the values when $u_* > 0.2\text{ m s}^{-1}$ were selected. In the latter, C_{ch} values remain without many changes but it is worth noting the significant increase in R^2 (in logarithmic space).

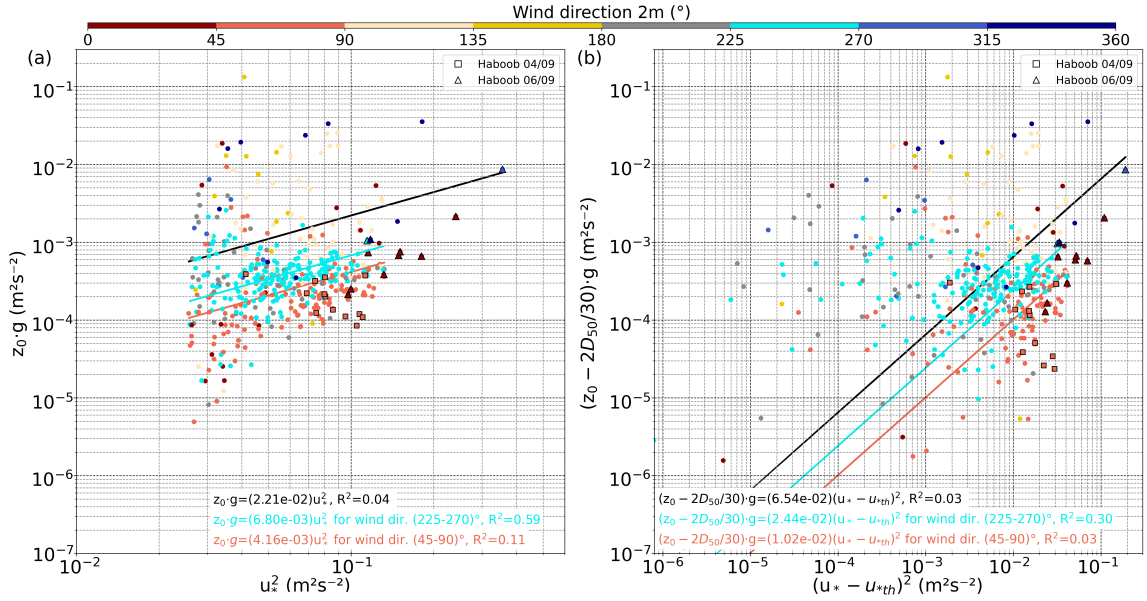


Figure 7.5: (a) The Charnock relationship between shear velocity and roughness length. (b) The modified Charnock relationship between shear velocity and roughness length. The points shown in both panels correspond to the 15 min values with a positive saltation flux and when $u_* > u_{*th}$. Colours indicate wind direction at 2 m height. The respective lines represent the regression curves for all the data (grey) and for wind directions between $45\text{--}90^\circ$ (orange) and $225\text{--}270^\circ$ (blue). The resulting fit-parameters and coefficients of determination are given in the figure. Squares and triangles are used to identify the values corresponding to haboobs on 4 and 6 September, respectively.

The sandblasting efficiency ranges between about 10^{-6} and 10^{-3} m^{-1} , although most values are concentrated between 10^{-5} and 10^{-4} m^{-1} (Fig. 7.1c). These results are similar to those obtained in Gomes et al. (2003b) (corresponding to a soil nominally of silt loam texture in Spain), Gomes et al. (2003c) (for a sandy soil with a very low clay and silt content in Niger), and the results of the soils 4 (sandy), 5 (sandy) and 9 (clay) reported in Gillette (1977). However, our values are on the lower end of the range reported in Gillette (1977) and Alfaro et al. (2022), where most sandblasting

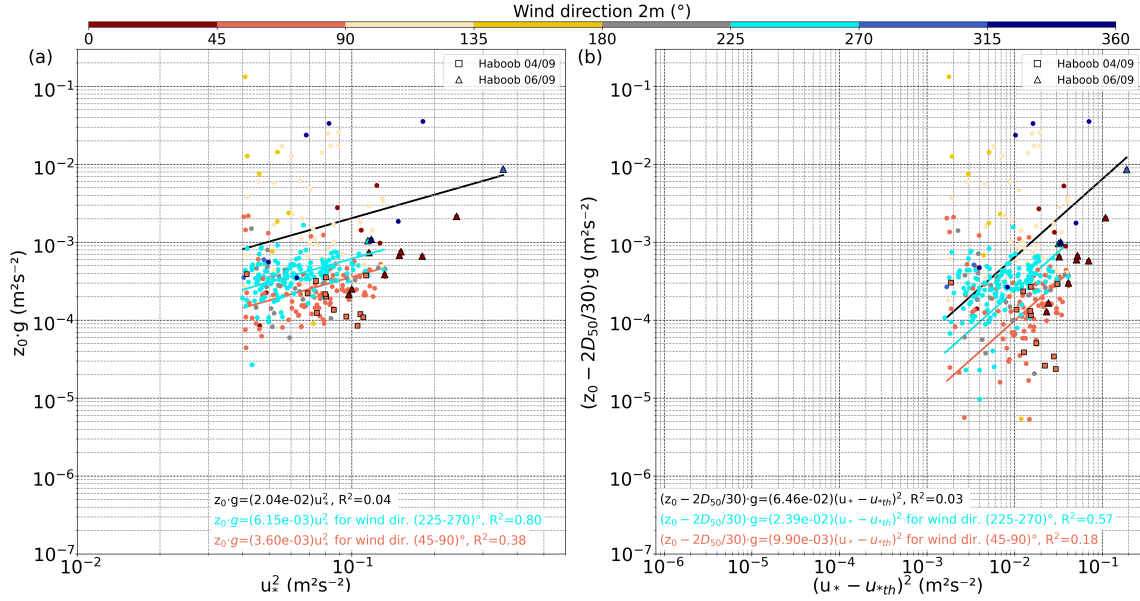


Figure 7.6: Analogous to Fig. 7.5 but selecting the 15 min values with a positive saltation flux and when $u_* > 0.2 \text{ m s}^{-1}$.

efficiencies are above 10^{-4} m^{-1} . The sandblasting efficiency tends to decrease slightly with increasing u_* when considering all wind directions, i.e. the exponent of the power law is negative ($b = -0.43$), but R^2 (in logarithmic space) is very small. There is some dependency of the sandblasting efficiency upon wind direction. For example, sandblasting efficiencies are higher under southeasterly winds (135–180°) than under the dominant wind directions (45–90° and 225–270°). The exponent of the power law also changes between predominant wind directions (See Figs. 7.2 and 7.3), but the amount of data is rather small and shows significant scatter, and R^2 (in logarithmic space) is small. Interestingly, some of the lowest sandblasting efficiency values ($\sim 10^{-5} \text{ m}$) are obtained during the haboob events, at least in part due to an enhanced reduction of coarse and super-coarse particles in the diffusive fluxes during the haboob events as discussed in Chap. 8.3.

There is a more robust decrease in sandblasting efficiency with increasing saltation fluxes (Fig. 7.1d), which is also evident in each of the two dominant wind directions (See Figs. 7.2 and 7.3). Such decreases in the sandblasting efficiency with increasing u_* and saltation flux are also found in Alfaro et al. (2022) using data from the JADE and WIND-O-V field campaigns. To explain this result, Alfaro et al. (2022) suggests that the proportion of emitted fine particles produced by sandblasting should increase with Q due to enhanced aggregate disintegration, which leads to lower

sandblasting efficiencies. We discuss in Chap. 9 a variety of potential mechanisms to explain the variations in the diffusive flux PSD with u_* that contribute to the decrease in sandblasting efficiency with increasing u_* .

All in all, our results highlight the prominence of saltation in our site, which produces strong diffusive fluxes despite the relatively low sandblasting efficiencies. These features are consistent with the measured surface sediment properties. On the one side, L'Bour was surrounded by small dunes with a minimally dispersed volume median diameter of $132.2\ \mu\text{m}$ and a considerable amount of saltators below $100\ \mu\text{m}$ (See Fig. 5.6), which translates into rather optimal saltation conditions. For instance, saltation is detected even when $u_* < u_{*th}$ based on 15 min averages (Fig. 7.1b). During such situations, saltation was typically intermittent during the 15 min period; hence, instantaneous momentum fluxes could be large enough to enable particle transport. On the other side, the low sandblasting efficiencies are attributed to the paved sediment that constituted the surface of the ephemeral lake.

Variability of the dust PSD at emission

In this chapter, variations in the dust PSD are analysed after the identification and removal of any potential anthropogenic aerosol influence. To provide a comprehensive view, the number and mass normalized and non-normalized PSDs of concentration (Figs. 8.1 and 8.2) and diffusive flux (Figs. 8.5 and 8.6) are studied. Regarding the forthcoming discussion on dust concentrations, the concentrations being referred to are those derived from FidasL. Nevertheless, analogous results are obtained using data from FidasU after correcting for the systematic deviation (Figs. 8.3 and 8.4), albeit with the typical decrease in dust concentration as height increases. For concentration PSDs all available measurements covering the full range of u_* are considered, but for diffusive flux PSDs, they are only considered when $u_* > 0.15 \text{ m s}^{-1}$, i.e. well-developed erosion conditions, and when the diffusive flux is positive in all size bins with $D_i > 0.4 \mu\text{m}$ (this minimum size is taken to avoid any anthropogenic aerosol contamination as discussed in Sect. 8.1). Figs. 8.1–8.6 group the PSDs into u_* intervals, types of events (regular versus haboob events), and wind directions (for the sake of simplicity only two 180° wind direction sectors are shown to the east and west of the alignment between the Fidas and the 10 m tower, as depicted in Fig. 5.5d). A preliminary analysis did not show any effect of atmospheric stability independent of u_* upon the PSD, in agreement with Dupont (2022) and in contrast with some recent studies (Khalfallah et al., 2020; Shao et al., 2020), likely due to the small range of stability conditions during our campaign (Chap. 6). However, this aspect was not analysed in detail and will require further analysis in the future.

8.1. Identification and removal of the anthropogenic aerosol influence

The analysis of the number PSDs shows the influence of non-geogenic (anthropogenic) particles for $D_i < 0.4 \mu\text{m}$. The number concentration PSDs show a sharp increase in particles with $D_i < 0.4 \mu\text{m}$ during regular events that is particularly evident for small u_* (Fig. 8.1a and b). This feature tends to diminish and even disappear with increasing u_* in the number concentration PSD, which demonstrates its small dependence upon wind erosion. It also disappears in the number diffusive flux (Fig. 8.5a and b), which further confirms the transport and not the emission of small anthropogenic particles in our measurement site. This result is further confirmed in other studies conducted by other researchers from the FRAGMENT project based upon the analysis of airborne samples with electron microscopy (Panta et al., 2023) and measurements of optical properties (Yus-Díez et al., prep). It is also consistent with the anthropogenic sulfate and carbonaceous particle mode detected at Tinfou ($\sim 50 \text{ km}$ northeast of L’Bour, beyond the mountain range and the enclosed desert basin) during the SAMUM field campaign (Kaaden et al., 2009; Kandler et al., 2009).

Compared to regular events, haboob events show markedly less anthropogenic influence (Fig. 8.1b). This could be related to the fresher air masses (carrying less background anthropogenic aerosols) within the cold pool outflows from the convective storms originated in the vicinity of our measurement location.

The analysis of the PSD evolution with u_* shows that the influence of anthropogenic aerosol upon the number concentration is negligible for $D_i > 0.4 \mu\text{m}$. It is worth noting that similar potentially anthropogenic features can be recognized around $0.3 \mu\text{m}$ in PSDs from other wind erosion studies such as in Sow et al. (2009) (their Fig. 8) and Fratini et al. (2007) (their Fig. 5). In this study, in order to avoid any anthropogenic aerosol contamination (particularly for low u_*), the normalized PSDs shown in linear and logarithmic scales in Figs. 8.1c-d, 8.2c-d, 8.5c-d, and 8.6c-d consider only $D_i > 0.4 \mu\text{m}$.

8.1. Identification and removal of the anthropogenic aerosol influence

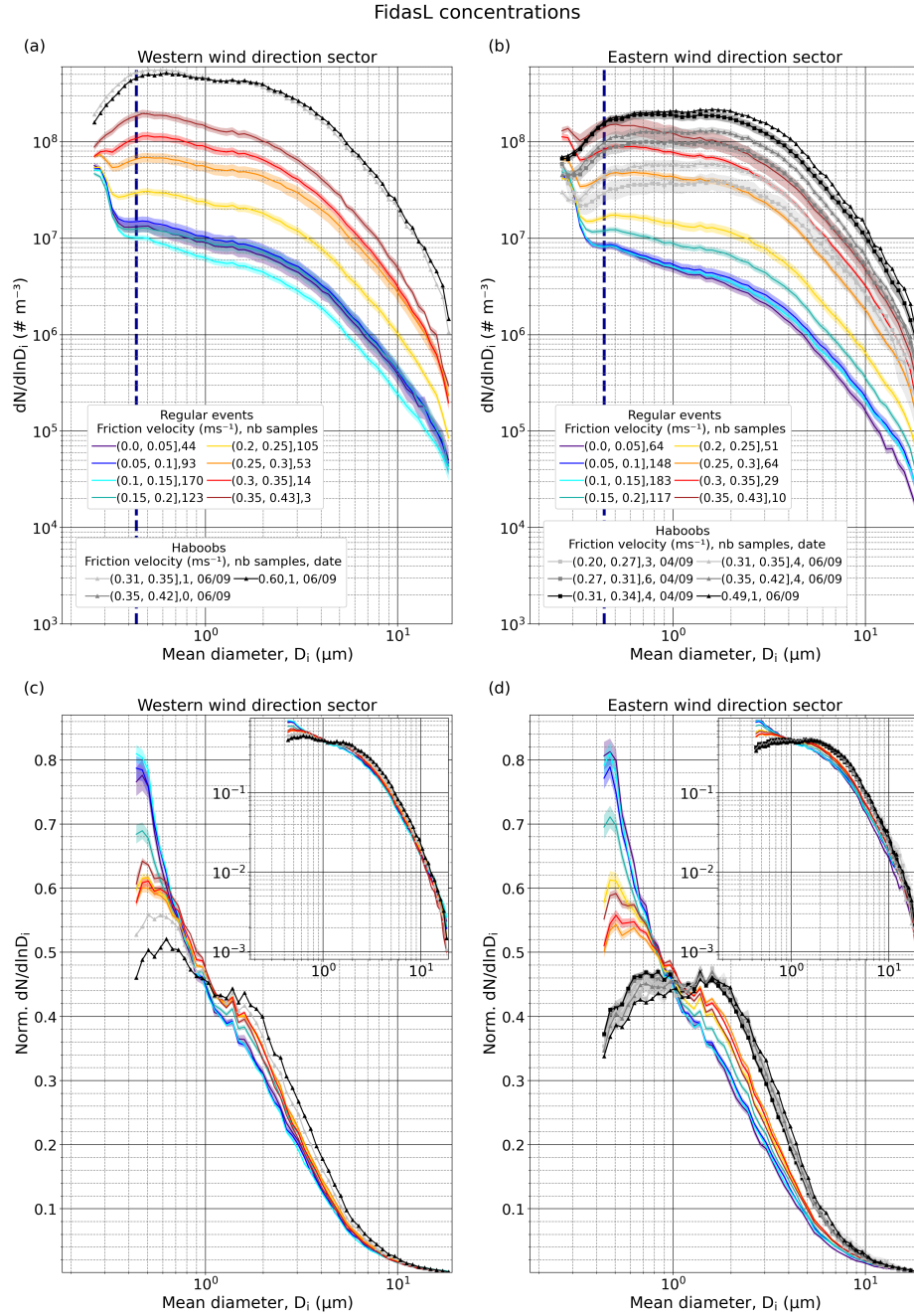


Figure 8.1: Average size-resolved particle number concentration, $dN/dlnD_i$ ($\# m^{-3}$), from FidasL for different u_* intervals, types of events (regular or haboob), and wind directions in the range $150\text{--}330^\circ$ (a) and $330\text{--}150^\circ$ (b). The number of available 15 min average PSDs in each u_* interval is indicated in the legend. Panels (c)-(d) are the same as (a)-(b) but normalized ($Norm. dN/dlnD_i$) after removing the anthropogenic mode (normalization from 0.42 to $19.11 \mu m$). The insets show the same data but with logarithmic ordinate axis scaling. Shaded areas around the lines depict the standard error. In (a) and (b) the dashed dark blue line marks the end of the anthropogenic mode ($D_i = 0.44 \mu m$). Data are shown using original size bin resolution, but the first 3 bins are not represented as Fidas is only considered efficient from the fourth one onward.

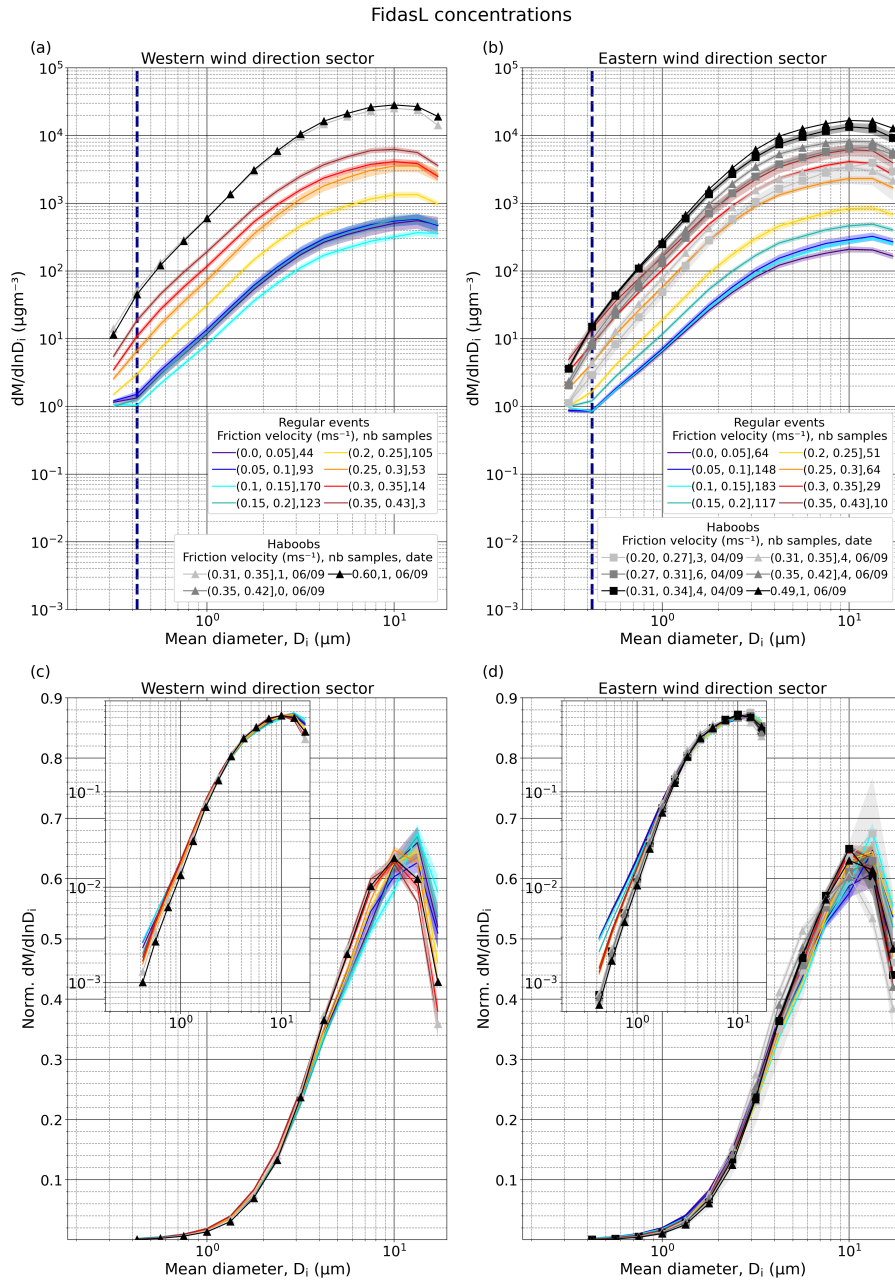


Figure 8.2: Average size-resolved particle mass concentration, $dM/d\ln D_i$ ($\mu\text{g m}^{-3}$), from FidasL for different u_* intervals, types of events (regular or haboob), and wind directions in the range $150\text{--}330^\circ$ (a) and $330\text{--}150^\circ$ (b). The number of available 15 min average PSDs in each u_* interval are indicated in the legend. Panels (c)-(d) are the same as (a)-(b) but normalized ($\text{Norm. } dM/d\ln D_i$) after removing the anthropogenic mode (normalization from 0.37 to $19.11 \mu\text{m}$). The insets show the same data but with logarithmic ordinate axis scaling. Shaded areas around the lines depict the standard error. In (a) and (b) the dashed dark blue line marks the end of the anthropogenic mode ($D_i = 0.42 \mu\text{m}$). In this case, the original size resolution of FidasL has been reduced by integrating 4 consecutive bins, except for the last one that contains 3, resulting in 16 bins. The first integrated bin is not represented as Fidas is considered efficient from the second one onward.

8.1. Identification and removal of the anthropogenic aerosol influence

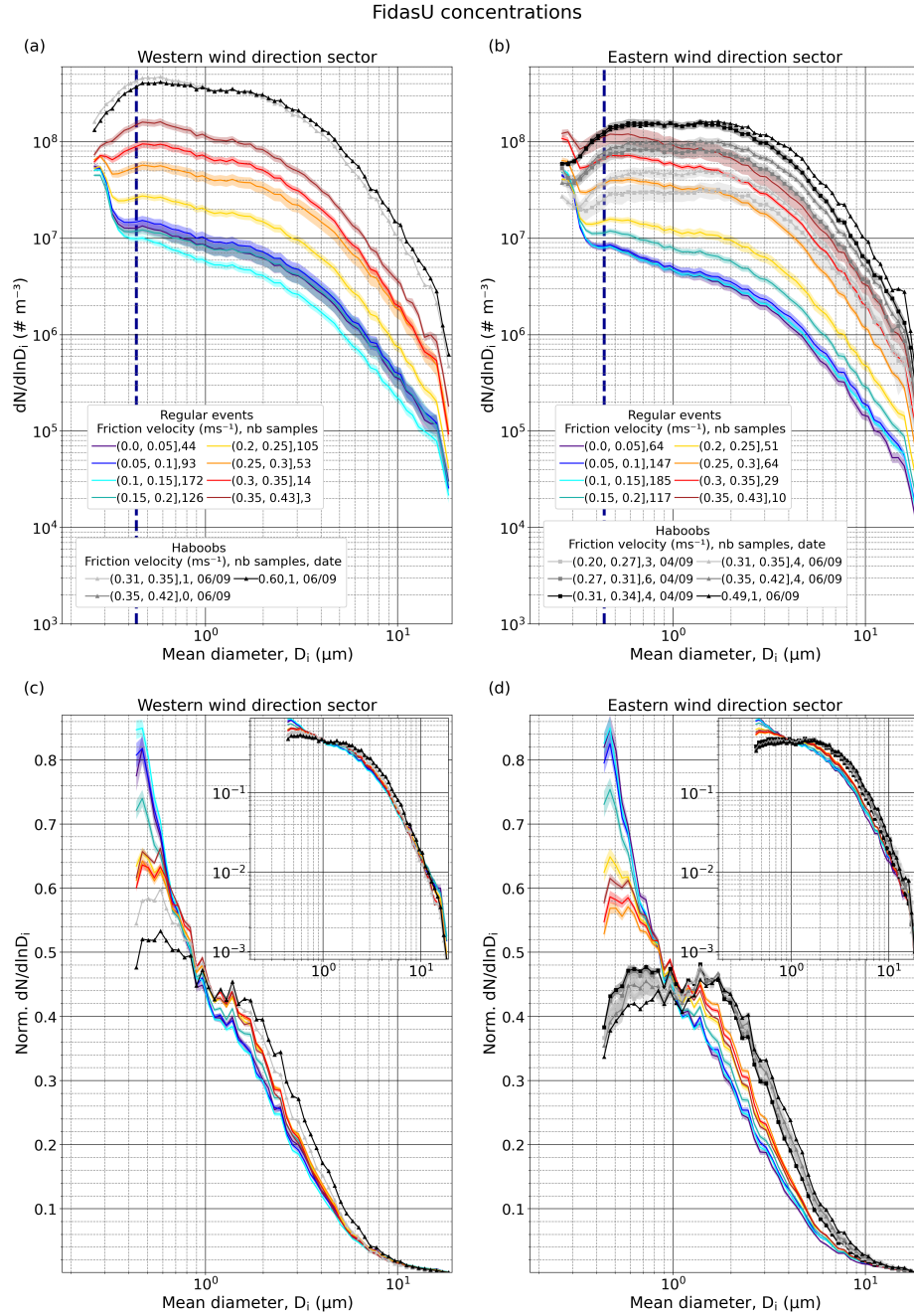


Figure 8.3: Average size-resolved particle number concentration, $dN/d\ln D_i$ ($\# m^{-3}$), from FidasU for different u_* intervals, types of events (regular or haboob), and wind directions in the range $150\text{--}330^\circ$ (a) and $330\text{--}150^\circ$ (b). The number of available 15 min average PSDs in each u_* interval is indicated in the legend. Panels (c)-(d) are the same as (a)-(b) but normalized ($Norm. dN/d\ln D_i$) after removing the anthropogenic mode (normalization from 0.42 to $19.11 \mu m$). The insets show the same data but with logarithmic ordinate axis scaling. Shaded areas around the lines depict the standard error. In (a) and (b) the dashed dark blue line marks the end of the anthropogenic mode ($D_i = 0.44 \mu m$). Data are shown using original size bin resolution, but the first 3 bins are not represented as Fidas is only considered efficient from the fourth one onward.

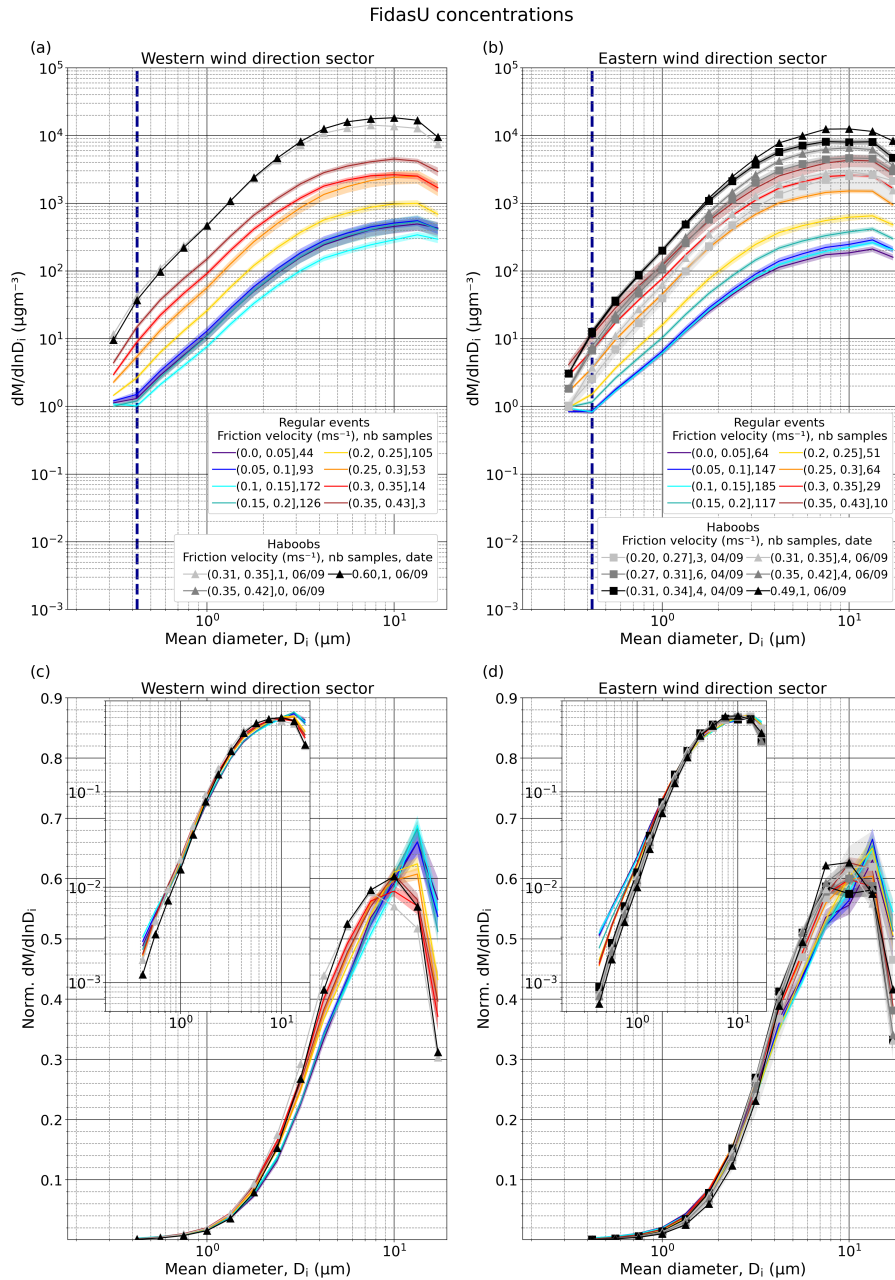


Figure 8.4: Average size-resolved particle mass concentration, $dM/d\ln D_i$ ($\mu\text{g m}^{-3}$), from FidasU for different u_* intervals, types of events (regular or haboob), and wind directions in the range $150\text{--}330^\circ$ (a) and $330\text{--}150^\circ$ (b). The number of available 15-min average PSDs in each u_* interval are indicated in the legend. Panels (c)-(d) are the same as (a)-(b) but normalized ($\text{Norm. } dM/d\ln D_i$) after removing the anthropogenic mode (normalization from 0.37 to $19.11 \mu\text{m}$). The insets show the same data, but with logarithmic ordinate axis scaling. Shaded areas around the lines depict the standard error. In (a) and (b) the dashed dark blue line marks the end of the anthropogenic mode ($D_i = 0.42 \mu\text{m}$). In this case, the original size resolution of FidasU has been reduced by integrating 4 consecutive bins, except for the last one that contains 3, resulting in 16 bins. The first integrated bin is not represented as Fidas is considered efficient from the second one onward.

8.2. Differences between concentration and diffusive flux PSDs and their dependencies upon u_* and wind direction

The non-normalized number (Fig. 8.1a and b) and mass concentration PSDs (Fig. 8.2a and b) show the expected strong scaling of concentration with u_* for all size bins, where the number is dominated by fine dust and the mass by coarse and super-coarse dust. For equivalent u_* intervals, concentrations are higher when the wind comes from the western sector. The normalized number PSDs (Fig. 8.1c and d) further depict how the shape of the concentration PSD depends upon u_* and wind direction. Overall, there is a relative decrease in sub-micrometre dust particles and a relative increase in super-micrometre particles, especially around 1.5–2 μm , with increasing u_* , from calm (purplish and blueish lines) to well-developed erosion conditions (yellow, orange, and reddish lines). However, it can be observed that for $u_* > 0.25 \text{ m s}^{-1}$ during regular events (orange, red and dark red lines) the fraction of sub-micrometre particles slightly increases with increasing u_* , which is even more evident for the eastern sector. Also for these cases (orange, red, and dark red lines), the number fraction of sub-micrometre particles is higher when winds come from the western sector (maxima at 0.6–0.7) than from the eastern sector (maxima at 0.5–0.6).

The normalized mass concentration PSDs (Fig. 8.2c and d) provide further insights into the dependencies of the concentration PSD upon u_* . During regular events, the mass fraction of coarse particles with $D_i \sim (4\text{--}10) \mu\text{m}$ tends to increase and that of super-coarse particles with $D_i > 10 \mu\text{m}$ tends to decrease as u_* increases. The peak of the mass PSD, which appears in the super-coarse fraction, tends to shift towards smaller diameters as u_* increases. These features are broadly similar for both wind direction sectors.

Figures 8.5 and 8.6 depict the diffusive flux PSDs in terms of number and mass, respectively. The PSDs in these figures include the uncertainty (adding both the standard error and the average random uncertainty obtained as described in Chap. 5.3.5) for each u_* range. For the sake of figure clarity, the uncertainty is shown only for regular events. Appendix C contains similar figures including only

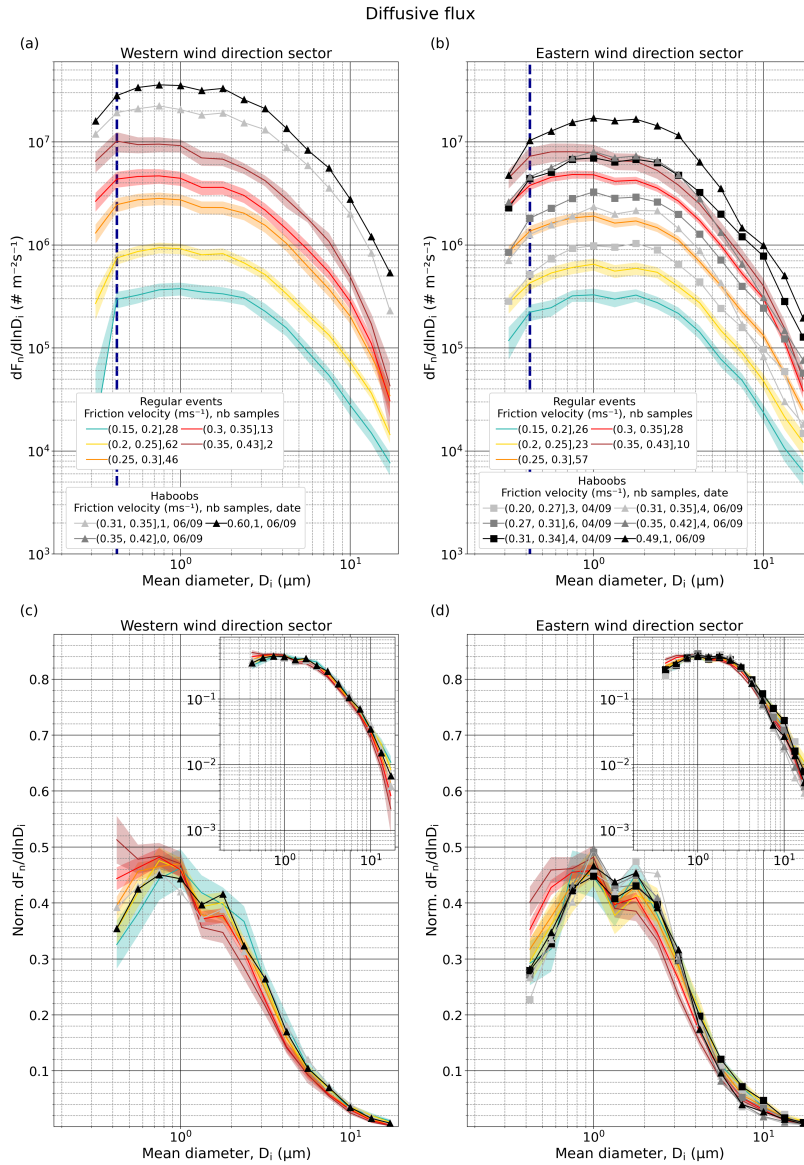


Figure 8.5: Average size-resolved number diffusive flux, $dF_n/d\ln D_i$ ($\# m^{-2} s^{-1}$), for different u_* intervals, types of events (regular or haboob) and wind directions in the range $150\text{--}330^\circ$ (a) and $330\text{--}150^\circ$ (b). The number of available 15-min average PSDs in each u_* interval are indicated in the legend. Only the samples where diffusive flux is positive in all the diameter bins above the anthropogenic mode (as discussed in Sect. 8.1) have been selected. Panels (c)-(d) are the same as (a)-(b) but normalized (Norm. $dF_n/d\ln D_i$) after removing the anthropogenic mode (normalization from 0.37 to $19.11 \mu m$). The insets show the same data, but with logarithmic ordinate axis scaling. Shaded areas around the lines of the regular event PSDs depict the combination of random uncertainty and standard error. In (a) and (b) the dashed dark blue line marks the end of the anthropogenic mode ($D_i = 0.42 \mu m$). In this case, the original size resolution of FidasL has been reduced by integrating 4 consecutive bins except for the last one that contains 3, resulting in 16 bins. The first integrated bin is not represented as Fidas is considered efficient from the second one onward. Results are shown only for well-developed erosion conditions ($u_* > 0.15 m s^{-1}$).

8.2. Differences between concentration and diffusive flux PSDs and their dependencies upon u_* and wind direction

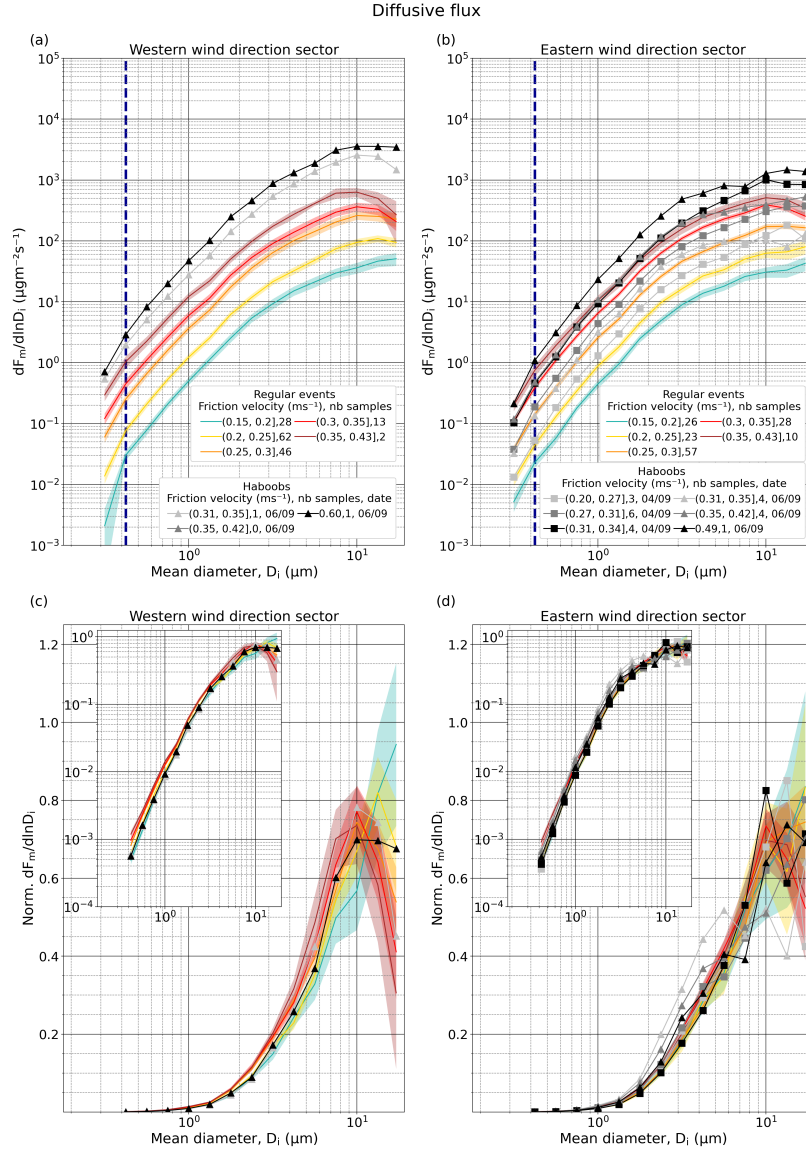


Figure 8.6: Average size-resolved mass diffusive flux, $dF_m/d\ln D_i$ ($\mu\text{g m}^{-2} \text{s}^{-1}$), for different u_* intervals, types of events (regular or haboob) and wind directions in the range $150\text{--}330^\circ$ (a) and $330\text{--}150^\circ$ (b). The number of available 15-min average PSDs in each u_* class are indicated in the legend. Only the samples where diffusive flux is positive in all the diameter bins above the anthropogenic mode (as discussed in Sect. 8.1) have been selected. Panels (c)-(d) are the same as (a)-(b) but normalized ($\text{Norm. } dF_m/d\ln D_i$) after removing the anthropogenic mode (normalization from 0.37 to $19.11 \mu\text{m}$). The insets show the same data but with logarithmic ordinate axis scaling. Shaded areas around the lines of the regular events PSDs illustrate the combination of random uncertainty and standard error. In (a) and (b) the dashed dark blue line marks the end of the anthropogenic mode ($D_i = 0.42 \mu\text{m}$). In this case, the original size resolution of FidasL has been reduced by integrating 4 consecutive bins except for the last one that contains 3, resulting in 16 bins. First integrated bin is not represented as Fidas is considered efficient from the second one onward. Results are shown only for well-developed erosion conditions ($u_* > 0.15 \text{ m s}^{-1}$).

the uncertainties for each u_* range associated with the haboob events (Figs. C.1 and C.2). Additionally, the diffusive flux PSDs with uncertainties accounting only for standard errors are also provided (Figs. C.3 and C.4).

Figure 8.7 displays the number and mass fractions of diffusive flux between $\sim 0.37 < D_i < 1 \mu\text{m}$, $\sim 1 < D_i < 2.5 \mu\text{m}$, $\sim 2.5 < D_i < 10 \mu\text{m}$ and $D_i > 10 \mu\text{m}$ for the different u_* intervals, types of events (regular or haboob), and the two wind directions sectors. The diffusive flux PSDs show consistent but more marked dependencies upon u_* and wind direction in comparison to the concentration PSDs for well-developed erosion conditions. During regular events, the proportion of sub-micrometre particles is lower and increases with u_* more strongly in the diffusive flux than in the concentration for both wind sectors (Figs. 8.5c and d versus 8.1c and d). The opposite is observed for super-micrometre particles. The differences between, for instance, the u_* intervals $(0.30\text{--}0.35] \text{ m s}^{-1}$ and $(0.15\text{--}0.20] \text{ m s}^{-1}$ for the two smallest size bins ($0.37\text{--}0.49 \mu\text{m}$ and $0.49\text{--}0.65 \mu\text{m}$) and the two wind sectors are statistically significant (p value < 0.05 ; see Chap. 5.3.5 for details on the tests of significance). The u_* interval $(0.35\text{--}0.43] \text{ m s}^{-1}$ was not used due to the small number of samples, especially in the western sector. After integration (Fig. 8.7a and b) the sub-micrometre number fractions when u_* is in the $(0.30\text{--}0.35] \text{ m s}^{-1}$ interval are $\sim 15\%$ and $\sim 13\%$ higher for the western and eastern sectors, respectively, than when u_* is in the $(0.15\text{--}0.20] \text{ m s}^{-1}$ interval. However, these differences are not statistically significant at a significance level of 0.05 (p values are 0.11 and 0.07 for the western and eastern sectors, respectively). The sub-micrometre fraction of diffusive flux is also more enhanced when the winds come from the western sector than from the eastern sector. The differences between wind sectors, for instance, for the two smallest size bins and when u_* is in the $(0.25\text{--}0.30] \text{ m s}^{-1}$ interval (this u_* interval was chosen as we had similar number of samples in both wind sectors) are statistically significant (p value < 0.05). Yet again, while the sub-micrometre fraction of diffusive flux is $\sim 6\%$ higher in the western sector than in the eastern sector (Fig. 8.7a and b) this difference is not statistically significant for a significance level of 0.05 (p value = 0.2358).

Likewise, the diffusive flux PSDs show more marked variations in coarse and super-coarse particles with increasing u_* compared to the corresponding concentration PSDs, a feature that can be better recognized in terms of mass (Fig. 8.6). During regular events, as u_* increases, there is a strong decrease in

8.2. Differences between concentration and diffusive flux PSDs and their dependencies upon u_* and wind direction

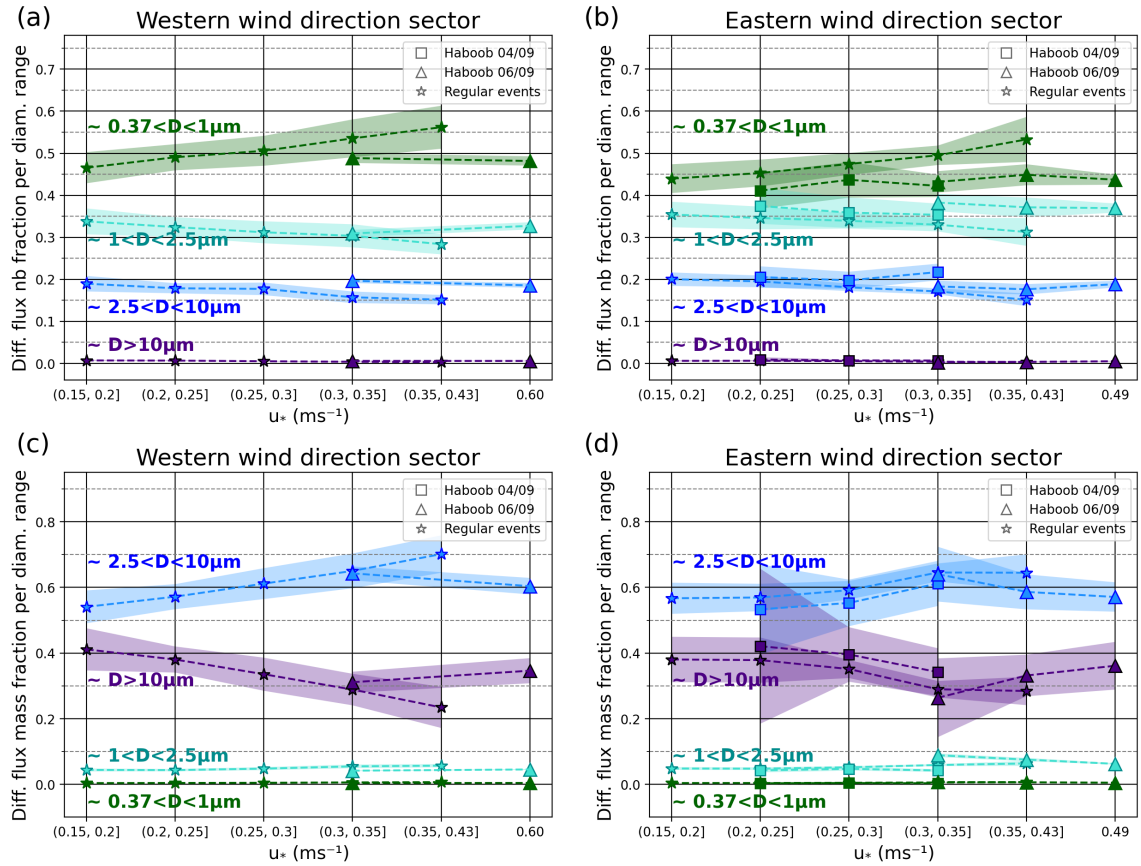


Figure 8.7: Number and mass diffusive flux fractions for different u_* intervals, types of events (regular or haboob) and wind directions in the range 150–330° (a)-(c) and 330–150° (b)-(d).

the super-coarse mass fraction and an increase in the coarse mass fraction (Figs. 8.6c, d and 8.7c and d). Also, as in the case of concentration, there is a shift in the mass diffusive flux PSD towards lower mass median diameters with increasing u_* . For the regular events, the uncertainties in the normalized PSDs can partly overlap between contiguous u_* intervals. However, both the largest size bin (Fig. 8.6c and d) and the super-coarse mass fraction ($D_i > 10 \mu\text{m}$) (Fig. 8.7c and d) show statistically significant differences. For instance, the differences between the u_* intervals (0.30–0.35] m s⁻¹ and (0.15–0.20] m s⁻¹ are statistically significant (p value < 0.05) for both wind sectors.

In summary, the dependencies of diffusive flux PSDs with u_* and wind direction are consistent with those from concentration for well-developed wind erosion conditions. However, there are relevant differences among them that preclude the use of near-surface concentration as a proxy for the diffusive flux or the emitted dust

PSD.

8.3. PSD differences between regular and haboob events

The PSDs obtained during the haboob events differ substantially from the PSDs obtained during the regular events even for equivalent u_* values and wind direction. When winds come from the eastern sector, the haboob number concentration PSDs (Fig. 8.1b and d) show peaks between 1 and 2 μm (in stark contrast to the 0.5–0.6 μm peak for equivalent u_* during regular events), and the negative slope between 0.4 and 2 μm becomes even positive. In terms of diffusive flux, there is also a clear increase in the super-micrometre number fraction and a decrease in the sub-micrometre number fraction compared to the regular PSDs (Fig. 8.5d). The coarse and super-coarse dust fractions with $D_i > 5 \mu\text{m}$ in the diffusive mass flux PSDs during the haboob events show more variability than during the regular events (Fig. 8.6d). In some cases we observe a more pronounced decrease in the super-coarse mass fraction and an increase in the coarse fraction in comparison with the regular events.

When winds come from the western sector, the haboob number concentration PSDs also tend to show an increase in the super-micrometre fraction, especially between 1 and 2 μm (Fig. 8.1a and c), although in this case the maximum fraction of particles still peaks below 1 μm (Fig. 8.1c). This last feature is consistent with the regular PSDs in that direction showing a more enhanced sub-micrometre influence.

In contrast to the regular PSDs, an increase in sub-micrometre particles with increasing u_* in the haboob normalized number diffusive flux PSDs is not detected in either wind direction (Fig. 8.5c and d). The normalized PSDs associated with the haboob u_* intervals are characterised by larger uncertainties, particularly with increasing particle size, than the PSDs associated with the regular events (see Figs. C.1 and C.2), which is largely due to the smaller number of haboob measurements in each u_* interval.

What explains the observed PSD variations? Potential roles of dry deposition and fetch length, aggregate disintegration, and haboob gust front

In chapter 8 it has been shown how and to what extent the concentration and diffusive flux PSDs depend upon u_* , wind direction, and type of event (regular versus haboob). Here, I discuss the potential mechanisms that may explain these PSD variations, which include the effect of dry deposition modulated by the fetch length, aggregate disintegration during wind erosion, and the impact of the haboob gust front.

The proportion of sub-micrometre particles decreases in the concentration PSD between calm (purplish and blueish lines) and well-developed erosion conditions (yellow, orange and red lines) (Fig. 8.1c and d). When u_* is low, i.e. in the absence of local emission, the PSDs represent background conditions and therefore present a smaller fraction of super-micrometre particles due to their shorter lifetime. As u_* increases, the concentration becomes increasingly dominated by freshly emitted dust, reducing the influence of the background dust and hence enhancing the proportion of super-micrometre dust. However, during regular dust events, the proportion of sub-micrometre particles increases and that of super-micrometre particles decreases in the diffusive flux PSD as u_* increases (Fig. 8.5c and d). This is also observed, although to a lesser extent, in the concentration PSDs for well-developed erosion conditions when $u_* > 0.25 \text{ m s}^{-1}$ (Fig. 8.1c and d). This could be compatible with two different mechanisms or the combination thereof. On the one side, it could be due to a reduction in super-micrometre particles by dry deposition, which increases with u_* (Dupont et al., 2015). On the other side, the relative enhancement of sub-micrometre

Chapter 9. What explains the observed PSD variations? Potential roles of dry deposition and fetch length, aggregate disintegration, and haboob gust front

particles may be the result of more aggregate disintegration with increasing u_* (Alfaro et al., 1997; Shao, 2001). These two hypotheses are examined more thoroughly below.

The potentially large effect of dry deposition upon the diffusive flux PSDs has been recently suggested based on numerical experiments (Dupont et al., 2015; Fernandes et al., 2019). More specifically, these studies clearly illustrated the key roles of the dust fetch length and u_* in this process. As indicated in Chap. 2.4, the dust fetch is defined as the uninterrupted upwind area generating dust emissions. This differs from the flux footprint, which is the upwind area that contributes substantially to the concentration at the measurement location (Schuepp et al., 1990), and which is here much smaller than the dust fetch, a couple of hundred metres versus several kilometres, respectively. For a given surface and uniform u_* along the fetch, the deposition of dust particles, which is size dependent, slowly increases with the fetch as the concentration of dust is enhanced. This way, a longer fetch results in a higher enrichment of the diffusive dust flux in small particles (Fernandes et al., 2019). Additionally, for a given fetch, an increasing u_* can substantially modify the diffusive flux PSD by enhancing the deposition of super-micrometre particles through impaction, i.e. the direct collision of particles to a surface resulting from their inertia, and hence reducing the fraction of these particles. Our observations suggest a major role of dry deposition in shaping the variations in the concentration and diffusive flux PSDs. On the one side, for equivalent u_* intervals during regular events, there are in general higher total number and mass concentrations for the western sector (Figs. 8.1a and 8.2a versus 8.1b and 8.2b, respectively), consistent with the longer fetch in that direction (60 km versus 10 km in the western and eastern sectors, respectively, as described in Chap. 5.2). Furthermore, in the normalized number concentration and diffusive flux PSDs a higher proportion of sub-micrometre particles is observed in the western sector compared to the eastern sector (Figs. 8.1c and 8.5c versus 8.1d and 8.5d). On the other side, during regular events when u_* increases, the mass fraction of super-coarse particles ($D_i > 10 \mu\text{m}$) decreases and that of fine and coarse particles ($D_i < 10 \mu\text{m}$) increases, both in the concentration and the diffusive flux PSDs (Figs. 8.2c, d, 8.6c and d). This effect is more visible when winds come from the western sector, which has a longer fetch. Our hypothesis is further confirmed when applying the tuned resistance-based dry deposition velocity parameterization described in Chap. 5.4, whose results are discussed in detail in Chap. 10.

Parallel to the effect of deposition, at least part of the enhancement in sub-micrometre particles with u_* could be attributed to an increased aggregate disintegration. However, while this explanation can hold for regular events, there is no detectable increase in the proportion of sub-micrometre particles with increasing u_* in the haboob events in either direction. In addition, the proportion of sub-micrometre particles during the haboob events is lower than during regular events although the former are associated with equivalent or higher u_* values (Fig. 8.1c and d). This further favours the prevalence of the fetch-deposition mechanism over any potential enhanced aggregate disintegration with u_* .

It is indeed quite remarkable that haboob events tend to show a much higher proportion of super-micrometre particles, especially for $D_i \sim (1-5) \mu\text{m}$, and a lower proportion of sub-micrometre particles than the regular events for equivalent or higher u_* intervals in the normalized number concentration PSDs (Fig. 8.1c and d). In terms of normalized number diffusive flux PSDs (Fig. 8.5c and d), haboob events are similar to the regular events for the u_* interval $(0.15-0.2] \text{m s}^{-1}$, although coarse and super-coarse dust mass fractions with $D_i > 3 \mu\text{m}$ during the haboob events show much more variability than during the regular events (Fig. 8.6d). To try to explain these features the formation process of a haboob is revisited. A convective storm or thunderstorm is formed when there is vertical transport of heat and moisture in the atmosphere (convection) that produces updrafts. As the convective storm matures, besides updrafts there are also downdrafts caused by evaporative cooling. When these downdrafts are very strong and hit the ground in a dust source area, large amounts of sand and dust are lifted into the air and can spread several kilometres wide horizontally, producing a wall of dust and strong wind gusts, a phenomenon known as a “haboob”. Therefore, a haboob is formed from the outflow of a convective storm. The location where the downdraft of the thunderstorm hits the surface could be seen as a new beginning of the dust fetch, which would be closer to our experimental site than the original start (Fig. 9.1). Following the argument given to explain the differences in PSDs between western and eastern sectors, this shorter “effective” fetch could at least partially explain the relative reduction in sub-micrometre particles and the increase in super-micrometre particles. At the same time, despite the overall increase in the fraction of super-micrometre particles, dry deposition visibly more strongly affects the fractions of coarse particles ($D_i > 3 \mu\text{m}$) and super-coarse

Chapter 9. What explains the observed PSD variations? Potential roles of dry deposition and fetch length, aggregate disintegration, and haboob gust front

particles ($D_i > 10 \mu\text{m}$) in the diffusive flux PSDs during the haboob events than during the regular events (Figs. 8.5b and 8.6b). This is because the dry deposition flux scales with the concentration, and during the haboobs the concentration of the super-micrometre particles is substantially higher (Fig. 6.1f and g). In addition, a haboob is not a static phenomenon and its gust front, where u_* and dust emission are maximized, moves towards and away from our measurement site. Therefore, there is non-uniformity of u_* and dust emission across the fetch, which may explain the higher variability in the haboob PSDs.

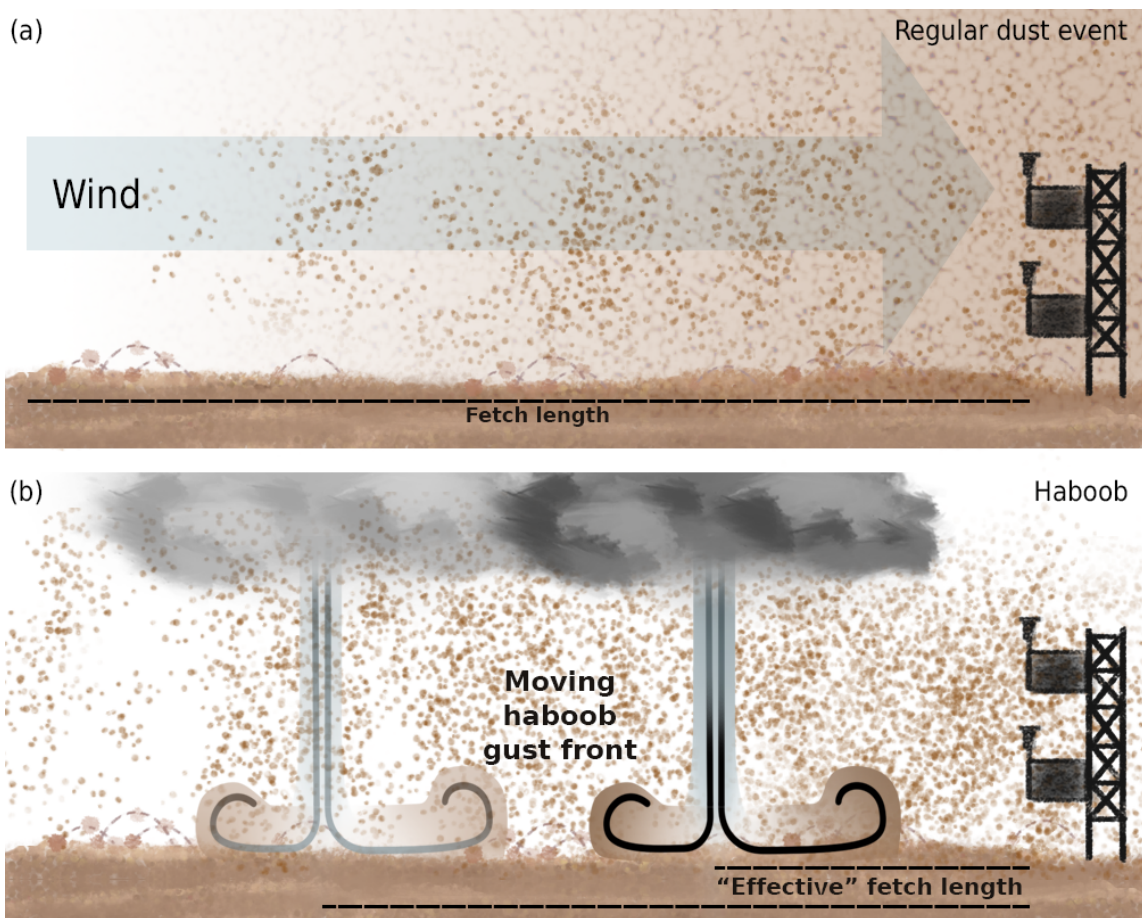


Figure 9.1: Schematic representation of the fetch length during (a) regular dust events and (b) haboobs. The “effective” fetch length during a haboob is shorter and more variable, which could explain the differences in the PSDs between regular events and haboobs.

Finally, higher air humidity along the haboob outflow and its potential effect upon the soil bonding forces cannot be discarded. During the haboob events, the relative humidity at our site increased substantially, from 15–25 % to ~ 50 % (Fig.

6.1b). Although our near-surface soil moisture measurements (2–3 cm deep) (not shown) did not register any associated increase, it has been argued that wet bonding forces in the soil surface, which are dominated by adsorption in arid regions, increase with relative humidity within approximately the observed variation range (Ravi et al., 2006). This mechanism would be consistent with the smaller proportion of sub-micrometre particles due to an increased resistance of soil aggregates to disintegration with increasing relative humidity as suspected in Dupont (2022).

Evaluation of the estimated dry deposition and emitted fluxes

If the deposition process causes the variability observed in the diffusive flux PSD, the emitted dust PSD should have a higher coarse and super-coarse fraction while showing less variability than the diffusive flux PSD. To test this hypothesis, I calculated the emitted dust flux, which required estimating the dry deposition flux (see Eq. 5.21) for the same 15 min samples used in Figs. 8.5 and 8.6. Fig. 10.1a and b display for different u_* intervals the median dry deposition velocities v_{dep} (solid lines) obtained by applying the parameterizations described in Chap. 5.4 of Fernandes et al. (2019) (referred to as F19) and Zhang et al. (2001) (referred to as Z01), respectively, for which field measurements have been used. In both cases v_{dep} increases strongly with particle size from $D_i \sim 1.5 \mu\text{m}$ due to gravitational settling. At the same time, v_{dep} scales with u_* , which is more noticeable in F19 for coarse particles in the size range $2.5 < D_i < 10 \mu\text{m}$ (Fig. 10.1a). In Z01 the scaling of coarse particles with u_* is much more subtle than for particles with $D_i < 2.5 \mu\text{m}$ (Fig. 10.1b). The stars in purple, blue, and cyan represent the median observation-based v_{dep} for the first three intervals of u_* . The two parameterizations predict v_{dep} reasonably well for $u_* < 0.05 \text{ m s}^{-1}$ and $D_i > \sim 1 \mu\text{m}$ but strongly underestimate it for the u_* intervals $(0.05\text{--}0.10] \text{ m s}^{-1}$ and $(0.10\text{--}0.15] \text{ m s}^{-1}$. For instance, for the u_* interval $(0.10\text{--}0.15] \text{ m s}^{-1}$ F19 and Z01 underestimate the observed v_{dep} (cyan star) by a factor of ~ 3 for particles with $D_i = 17.15 \mu\text{m}$. Note that as shown in Fig. 10.2 our observation-based estimates are broadly consistent with measurements reported by Bergametti et al. (2018) (magenta points), corresponding to an intense dust deposition event occurred in June 2006 in Niger.

Given the systematic underestimation of the parameterized v_{dep} applying F19 and Z01, I updated and tuned Z01 v_{dep} parameterization to best fit the observation-based estimates as described in Chap. 5.4. Fig. 10.3 shows the sensitivity of the tuned v_{dep} parameterization to different values of A_{in} , B_1 and d_c . The

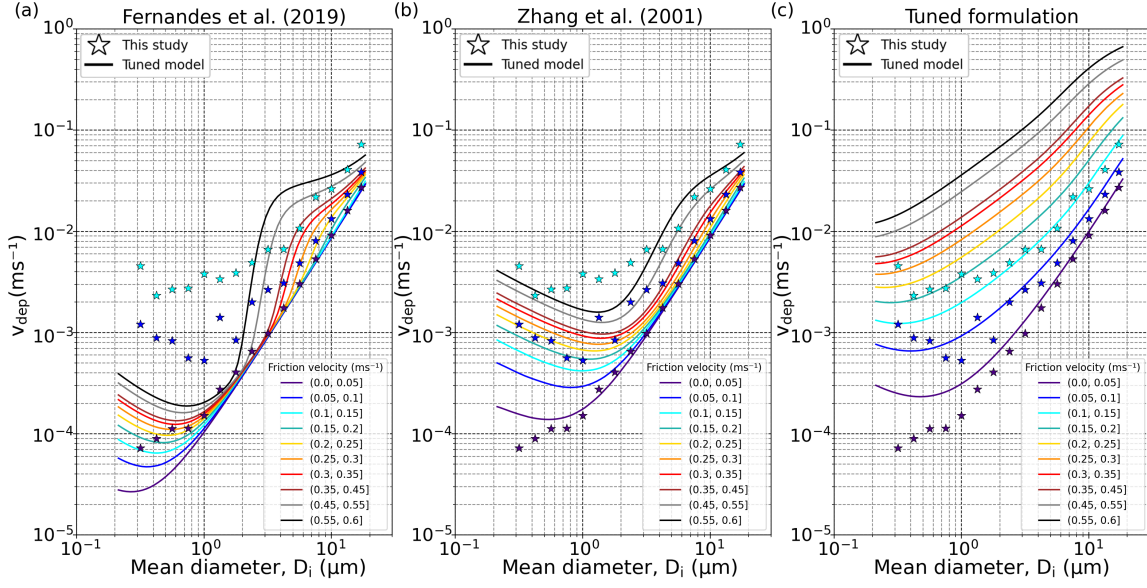


Figure 10.1: Median size-resolved dry deposition velocities v_{dep} (ms^{-1}) obtained using field measurements and applying (a) F19, (b) Z01, and (c) tuned parameterization for different u_* intervals (solid lines). The stars correspond to the median of the observation-based v_{dep} for the u_* intervals $(0 - 0.05] \text{ ms}^{-1}$ (purple), $(0.05 - 0.10] \text{ ms}^{-1}$ (blue), and $(0.10 - 0.15] \text{ ms}^{-1}$ (cyan).

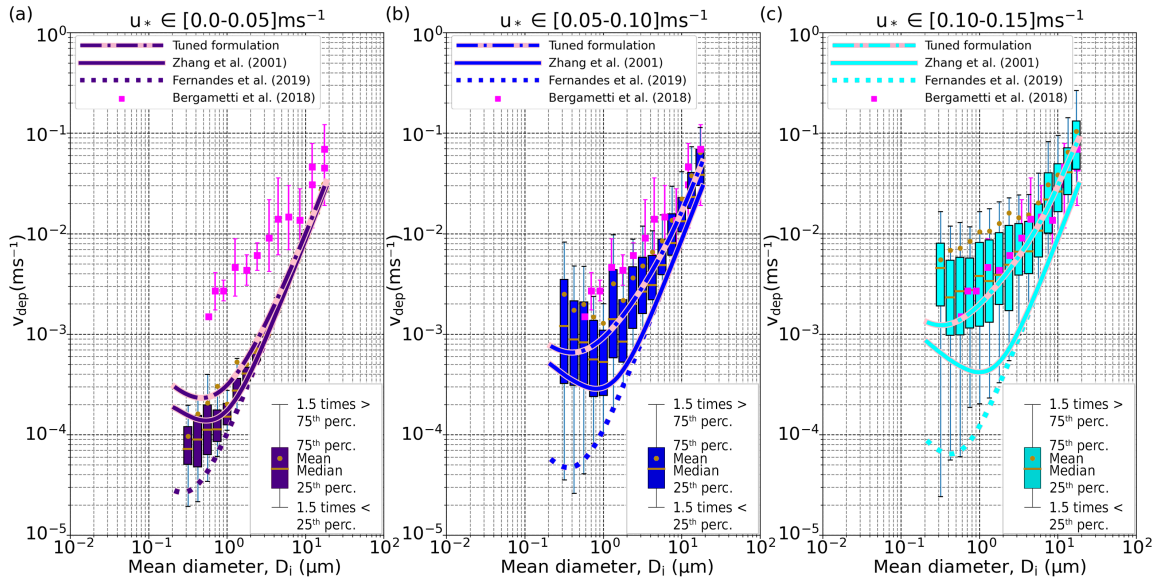


Figure 10.2: In situ size-resolved measurements of dry deposition velocity v_{dep} (ms^{-1}) for u_* between (a) $(0 - 0.05) \text{ ms}^{-1}$, (b) $(0.05 - 0.10) \text{ ms}^{-1}$, and (c) $(0.10 - 0.15) \text{ ms}^{-1}$ (bar plots). Lines represent the estimated median v_{dep} applying F19 (dashed), Z01 (solid), and the tuned parameterization (dashdot) for the corresponding u_* interval. For the tuned configuration we set $B_1 = 0.02$, $d_c = 0.0009 \text{ m}$ and $A_{in} = 15$. The points in magenta represent the measurements from Bergametti et al. (2018).

separation between curves for particles with fine, intermediate and coarse diameters is mostly controlled by the variation in A_{in} , B_1 and d_c , respectively. The more suitable configuration was achieved for $B_1 = 0.02$, $d_c = 0.0009$ m and $A_{in} = 15$ (Fig. 10.1c). It is worth noting the low value required for the scaling factor of the aerodynamic resistance B_1 .

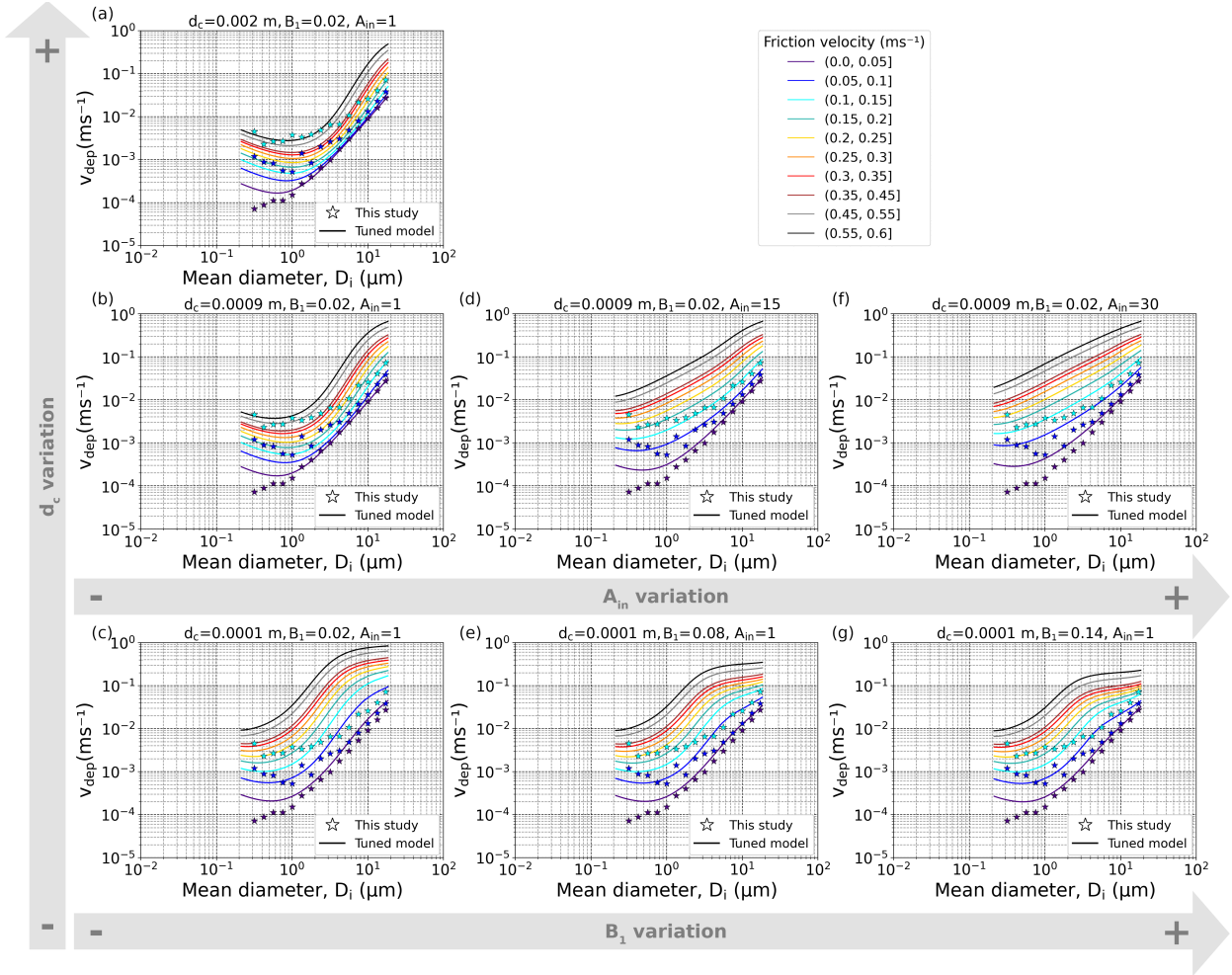


Figure 10.3: Different configurations of the tuned parameterization for estimating v_{dep} applying different values of A_{in} , B_1 and d_c .

Figures 10.4 and 10.5 represent, respectively, the size-resolved number and mass dry deposition fluxes calculated in absolute terms as $|F_{dep}(D_i)| = v_{dep}(D_i)c_{int}$ for different u_* intervals, types of events (regular and haboob events), and wind direction (Eastern and Western sectors) using the tuned parameterization for v_{dep} ($B_1 = 0.02$, $d_c = 0.0009$ m and $A_{in} = 15$). Analogous plots are obtained using F19 (Figs. D.1 and D.2) and Z01 (Figs. D.3 and D.4). Significant higher values of dry deposition

fluxes are obtained when using the tuned parameterization, reaching values above $10^7 \# \text{ m}^{-2} \text{ s}^{-1}$ in terms of number and $10^3 \mu\text{g m}^{-2} \text{ s}^{-1}$ in mass, compared to F19 and Z01. Also the shape of the curves changes considerably between the different schemes.

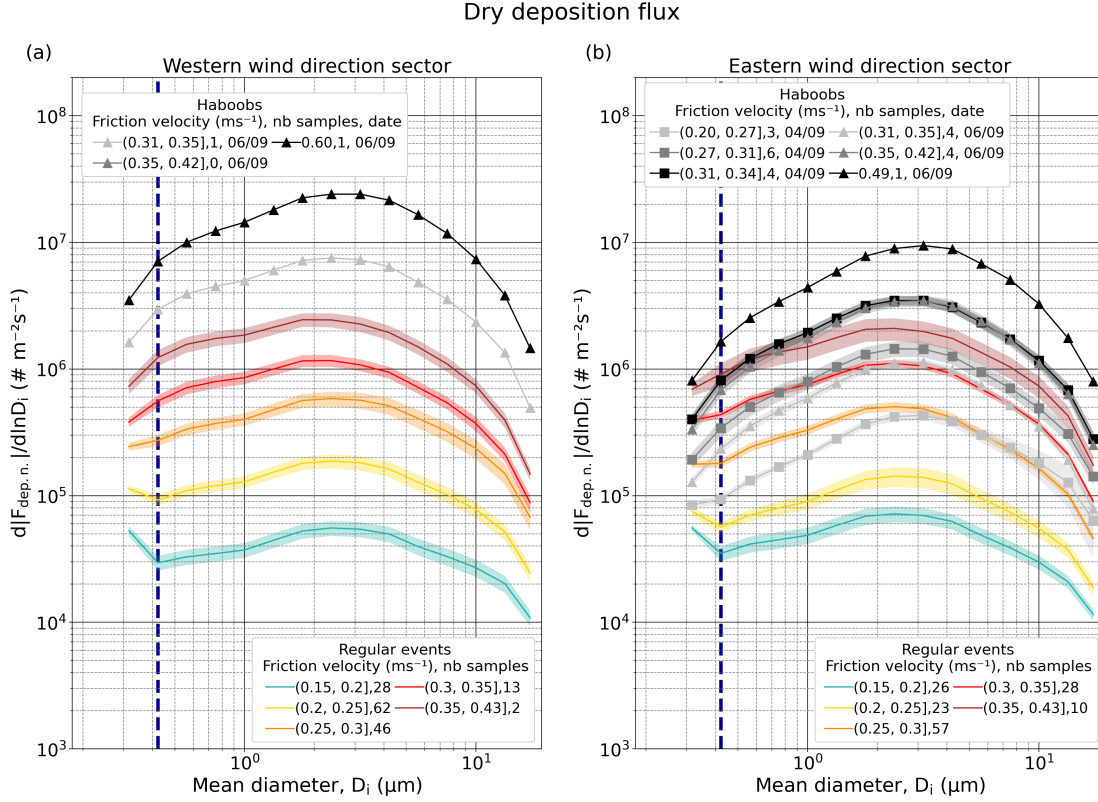


Figure 10.4: Average size-resolved number dry deposition flux, $d|F_{dep,n}|/d\ln D_i$ ($\# \text{ m}^{-2} \text{ s}^{-1}$), estimated from the v_{dep} tuned formulation for different u_* intervals, types of events (regular or haboob), and wind directions in the range $150\text{--}330^\circ$ (a) and $330\text{--}150^\circ$ (b). Only the samples where diffusive flux is positive in all the diameter bins above the anthropogenic mode (as discussed in Chap. 8.1) have been selected. The number of available 15 min average PSDs in each u_* interval are indicated in the legend. Shaded areas around the lines depict the standard error. In (a) and (b) the dashed dark blue line marks the end of the anthropogenic mode ($D_i = 0.42 \mu\text{m}$). In this case, the original size resolution of FidasL has been reduced by integrating 4 consecutive bins except for the last one that contains 3, resulting in 16 bins. The first integrated bin is not represented as the Fidas is considered efficient from the second one onward.

Figures 10.6 and 10.7 show the estimated size-resolved emitted dust number and mass fluxes calculated from Eq. 5.21 applying the v_{dep} estimated with the tuned parameterization. Results from the other two schemes are shown in Appendix D. The uncertainties (combination of random uncertainty and standard error) are shown only for the regular events for the sake of clarity. Compared to the diffusive flux,

Dry deposition flux

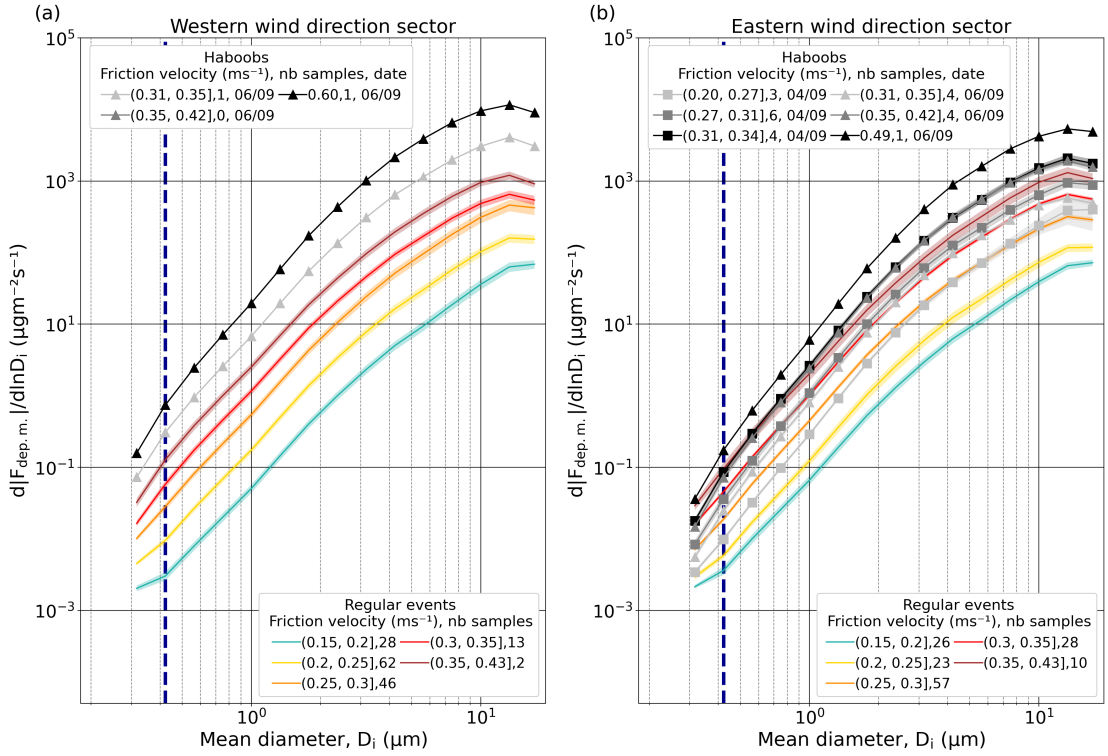


Figure 10.5: Average size-resolved mass dry deposition flux, $d|F_{dep,m}|/d\ln D_i$ ($\mu\text{g m}^{-2} \text{s}^{-1}$), estimated from the v_{dep} tuned formulation for different u_* intervals, types of events (regular or haboob), and wind directions in the range $150\text{--}330^\circ$ (a) and $330\text{--}150^\circ$ (b). Only the samples where diffusive flux is positive in all the diameter bins above the anthropogenic mode (as discussed in Sect. 8.1) have been selected. The number of available 15 min average PSDs in each u_* interval are indicated in the legend. Shaded areas around the lines depict the standard error. In (a) and (b) the dashed dark blue line marks the end of the anthropogenic mode ($D_i = 0.42 \mu\text{m}$). In this case, the original size resolution of FidasL has been reduced by integrating 4 consecutive bins except for the last one that contains 3, resulting in 16 bins. The first integrated bin is not represented as the Fidas is considered efficient from the second one onward.

the estimated emitted dust flux shows a higher proportion of particles in all size bins, but especially significant for coarse and super-coarse particles (Figs. 10.6a and b versus 8.5a and b). The normalized emitted dust flux PSDs clearly show less variability as a function of u_* , along with a lower shift towards finer dust and a lower reduction of super-coarse particles with increasing u_* (Figs. 10.6c, d, 10.7c and d), in comparison to the normalized diffusive flux PSDs (Figs. 8.5c, d, 8.6c and d). These features can be better appreciated by integrating the fractions over four size ranges in Fig. 10.8, which is analogous to Fig. 8.7 but for the estimated emitted

flux. The increase in the number fraction for $\sim 0.37 < D_i < 1 \mu\text{m}$ with increasing u_* (comparison between the u_* intervals $(0.15\text{--}0.20] \text{ m s}^{-1}$ and $(0.30\text{--}0.35] \text{ m s}^{-1}$) during regular events is reduced by $\sim 41\%$ and $\sim 28\%$ for the western and eastern sectors, respectively, in the estimated emitted dust flux in comparison with the diffusive flux (Figs. 10.8a and b versus 8.7a and b). However, the remaining difference between u_* intervals is still statistically significant (p value < 0.05) when individually considering the two smallest size bins ($0.37\text{--}0.49 \mu\text{m}$ and $0.49\text{--}0.65 \mu\text{m}$) for both wind sectors (Fig. 8.5c and d). The increase in the mass fraction for $\sim 2.5 < D_i < 10 \mu\text{m}$ and the decrease for $D_i > 10 \mu\text{m}$ with increasing u_* (comparison between the u_* intervals $(0.15\text{--}0.20] \text{ m s}^{-1}$ and $(0.30\text{--}0.35] \text{ m s}^{-1}$) during regular events are also both reduced up to $\sim 13\%$ and $\sim 18\%$, respectively, in the estimated emitted flux (Figs. 10.8c and d versus 8.7c and d). Despite the much lower decrease in super-coarse particles with increasing u_* (Figs. 10.7c and d versus 8.5c and d), the differences between the u_* intervals $(0.15\text{--}0.20] \text{ m s}^{-1}$ and $(0.30\text{--}0.35] \text{ m s}^{-1}$ are still statistically significant (p value < 0.05) for both wind sectors considering both the whole mass fraction $D_i > 10 \mu\text{m}$ (Fig. 10.8c and 10.8d) and only the last integrated size bin (Fig. 10.7c and d). Similar trends are observed for the haboob on 4 September, while those for the haboob on 6 September seem to be the opposite, consistent with the higher variability in the haboob PSDs reported in Chap. 8.3.

Table 10.1 shows the mean and standard deviation of the number and mass percentages for the four size ranges in the diffusive and emitted fluxes during regular events for each wind sector, calculated from the average values of each u_* interval shown in Figs. 8.7 and 10.8. For both wind sectors, the mean number percentage in the particle size range $\sim 0.37 < D_i < 1 \mu\text{m}$ is reduced by $\sim 9\%$ in the estimated emitted flux compared to the diffusive flux, at the expense of both an increase of $\sim 23\%$ and $> 100\%$ for the size ranges $\sim 2.5 < D_i < 10 \mu\text{m}$ and $D_i > 10 \mu\text{m}$, respectively. Mean mass percentages are reduced in the emitted flux compared to the diffusive flux for all size ranges except for $D_i > 10 \mu\text{m}$, where it increases by $\sim 29\%$, for both wind sectors.

The potential importance of dry deposition is clearly depicted in Fig. 10.9, which displays the size-resolved ratio of the estimated dry deposition flux to the emitted flux determined using the tuned v_{dep} parameterization. During regular events, dry deposition is estimated to represent up to $\sim 80\%$ of the emission for super-coarse

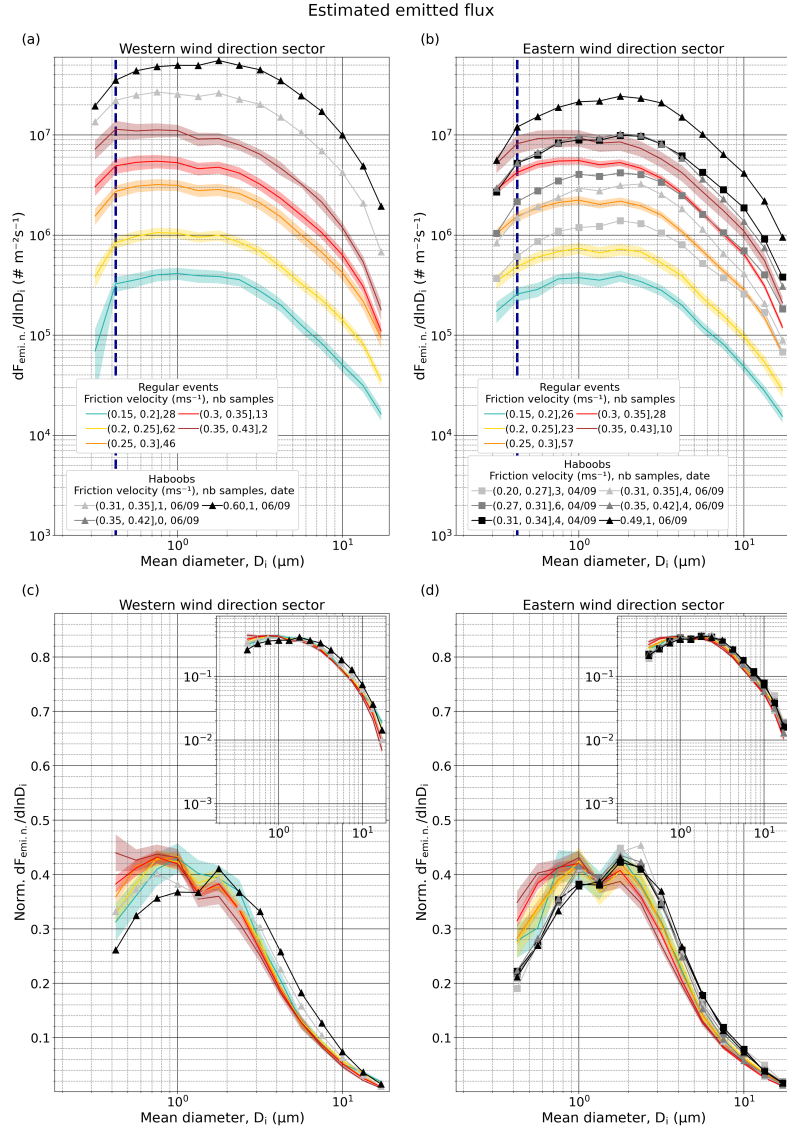


Figure 10.6: Average size-resolved number estimated emitted flux, $dF_{emi.n.}/dlnD_i$ ($\# m^{-2} s^{-1}$) from the tuned v_{dep} parameterization, for different u_* intervals, types of events (regular or haboob), and wind directions in the range $150-330^\circ$ (a) and $330-150^\circ$ (b). The number of available 15 min average PSDs in each u_* interval are indicated in the legend. Only the samples where diffusive flux is positive in all the diameter bins above the anthropogenic mode (as discussed in Sect. 3.3.1) have been selected. Panels (c)-(d) are the same as (a)-(b) but normalized ($Norm. dF_{emi.n.}/dlnD_i$) after removing the anthropogenic mode (normalization from 0.37 to $19.11 \mu m$). The insets show the same data but with logarithmic ordinate axis scaling. Shaded areas around the lines of the regular event PSDs depict the combination of random uncertainty and standard error. In (a) and (b) the dashed dark blue line marks the end of the anthropogenic mode ($D_i = 0.42 \mu m$). In this case, the original size resolution of FidasL has been reduced by integrating 4 consecutive bins except for the last one that contains 3, resulting in 16 bins. The first integrated bin is not represented as Fidas is considered efficient from the second one onward. Results are shown only for well-developed erosion conditions ($u_* > 0.15 m s^{-1}$).

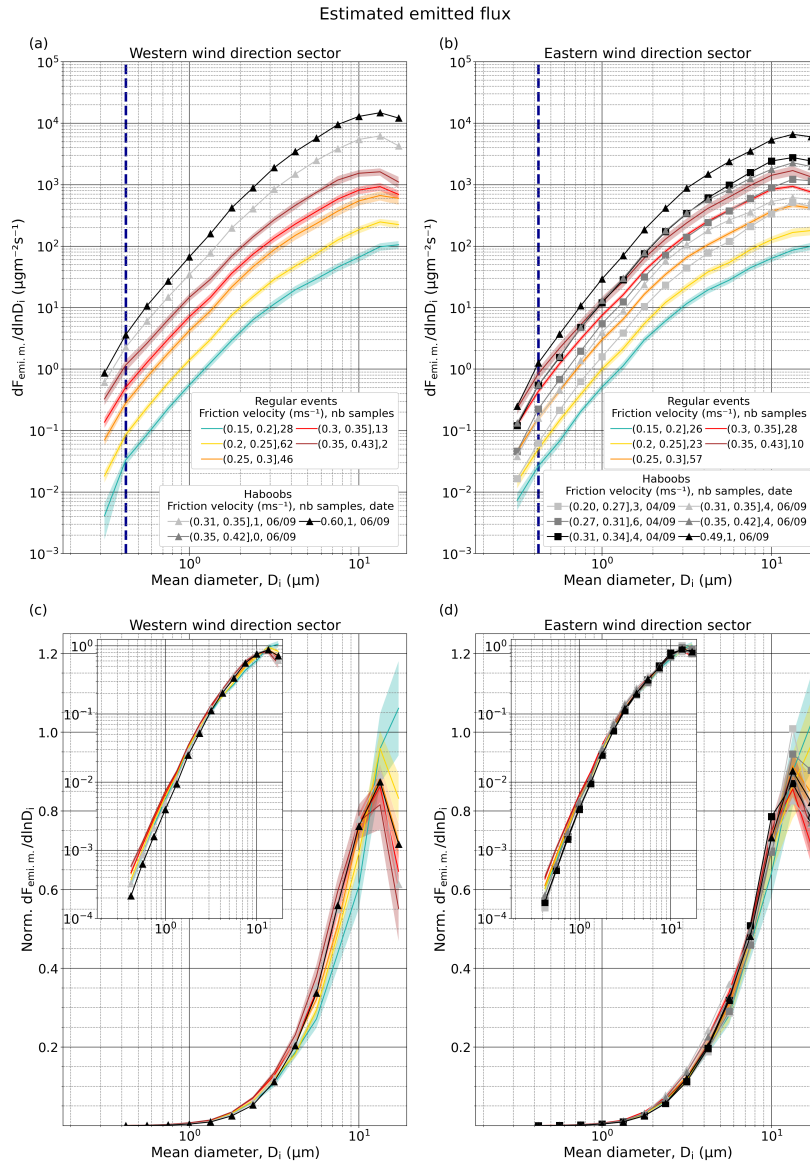


Figure 10.7: Average size-resolved mass estimated emitted flux, $dF_{emi.m.}/dlnD_i$ ($\mu\text{g m}^{-2} \text{s}^{-1}$), for different u_* intervals, types of events (regular or haboob), and wind directions in the range $150\text{--}330^\circ$ (a) and $330\text{--}150^\circ$ (b). The number of available 15 min average PSDs in each u_* class are indicated in the legend. Only the samples where diffusive flux is positive in all the diameter bins above the anthropogenic mode (as discussed in Sect. 8.1) have been selected. Panels (c)-(d) are the same as (a)-(b) but normalized ($Norm. dF_{emi.m.}/dlnD_i$) after removing the anthropogenic mode (normalization from 0.37 to $19.11 \mu\text{m}$). The insets show the same data but with logarithmic ordinate axis scaling. Shaded areas around the lines of the regular event PSDs illustrate the combination of random uncertainty and standard error. In (a) and (b) the dashed dark blue line marks the end of the anthropogenic mode ($D_i = 0.42 \mu\text{m}$). In this case, the original size resolution of FidasL has been reduced by integrating 4 consecutive bins except for the last one that contains 3, resulting in 16 bins. The first integrated bin is not represented as Fidas is considered efficient from the second one onward. Results are shown only for well-developed erosion conditions ($u_* > 0.15 \text{ m s}^{-1}$).

particles, between 55 and 60% for particles with $D_i \sim 10 \mu\text{m}$, and between 30 and 45% for particles with $D_i \sim 5 \mu\text{m}$. During the haboob events these fractions are generally higher and more variable under similar u_* intervals, reaching up to $\sim 90\%$ for super-coarse particles, up to 80% for particles with $D_i \sim 10 \mu\text{m}$, and between 50 and 65% for particles with $D_i \sim 5 \mu\text{m}$. Results obtained using the v_{dep} parameterizations F19 and Z01 are shown in Appendix F. In these cases much lower ratios are obtained.

Table 10.1: Mean and standard deviation (SD) of the number and mass percentages for the four size ranges in the diffusive and emitted fluxes during regular events for each wind sector, calculated from the average values of each u_* interval shown in Figs. 8.7 and 10.8. The average of each u_* interval contributes equally to the mean, and the standard deviation is a measure of the variability across u_* interval averages. For the estimated emitted flux we used the v_{dep} from the tuned parameterization.

		Mean \pm SD	Mean \pm SD	Mean \pm SD	Mean \pm SD
		0.37<D<1 μm	1<D<2.5 μm	2.5<D<10 μm	D>10 μm
Western wind direction sector					
Nb.	Diffusive flux	51.17 \pm 3.77	31.22 \pm 2.06	17.09 \pm 1.59	0.52 \pm 0.17
	% Emitted flux	46.61 \pm 2.45	31.42 \pm 1.44	20.92 \pm 0.89	1.05 \pm 0.23
Mass	Diffusive flux	0.52 \pm 0.12	4.95 \pm 0.62	61.52 \pm 6.34	33.01 \pm 7.07
	% Emitted flux	0.29 \pm 0.05	3.10 \pm 0.28	54.07 \pm 5.12	42.54 \pm 5.42
Eastern wind direction sector					
Nb.	Diffusive flux	47.89 \pm 3.68	33.63 \pm 1.60	17.98 \pm 1.96	0.50 \pm 0.13
	% Emitted flux	43.40 \pm 2.64	33.46 \pm 1.21	22.06 \pm 1.30	1.08 \pm 0.17
Mass	Diffusive flux	0.52 \pm 0.12	5.43 \pm 0.69	60.36 \pm 3.91	33.69 \pm 4.69
	% Emitted flux	0.28 \pm 0.04	3.25 \pm 0.24	53.03 \pm 3.28	43.45 \pm 3.55

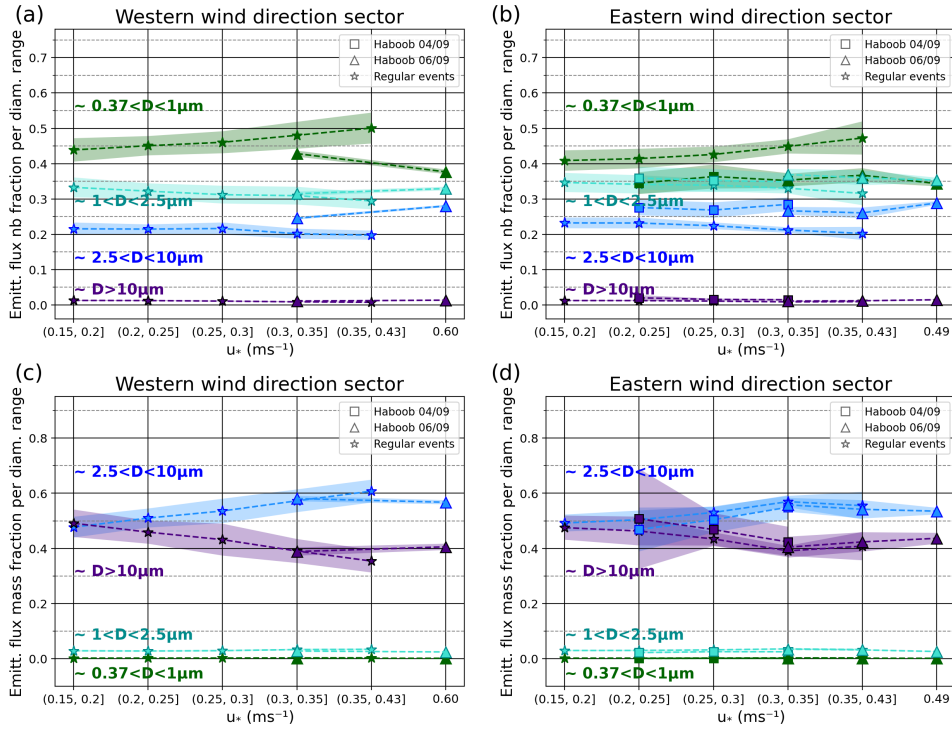


Figure 10.8: Number and mass emitted flux fractions for different u_* intervals, types of events (regular or haboob), and wind directions in the range $150\text{--}330^\circ$ (a-c) and $330\text{--}150^\circ$ (b-d)

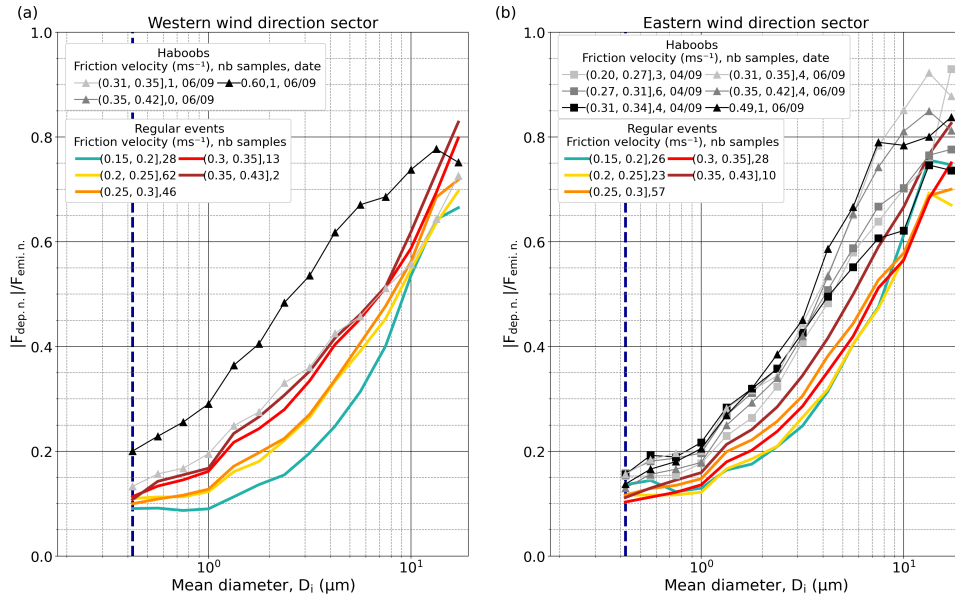


Figure 10.9: Ratio of dry deposition flux to the estimated emitted dust flux, determined using the v_{dep} tuned parameterization, for different u_* intervals, types of events (regular or haboob), and wind directions in the range $150\text{--}330^\circ$ (a) and $330\text{--}150^\circ$ (b)

Comparison with Brittle Fragmentation Theory

In this chapter, wind direction differences are sidestepped and the obtained normalized concentration, diffusive flux, and estimated emitted flux PSDs are compared with the emitted PSDs formulated in Kok (2011a) (Fig. 11.1) and Meng et al. (2022) (Fig. 11.2), both based on BFT. The former depends on the fully dispersed PSD and the latter on both the fully dispersed and aggregated soil PSDs. Here, our comparison focuses on the simplified parameterization proposed for modelling, which assumes a constant soil PSD and thus an invariant emitted PSD given the lack of spatially resolved soil PSDs.

For the sake of clarity, in Figs. 11.1 and 11.2 only two haboob PSDs are represented, corresponding to the two highest values of u_* reached during the haboob events. While our number concentration PSD is close to the PSD derived from the Kok (2011a) parameterization (dashed pink line), particularly during regular events, our measurements show a substantially higher proportion of super-micrometre particles in the diffusive flux and the estimated emitted flux PSDs (Fig. 11.1a, c and e). In terms of mass, the super-coarse fraction is much higher in our PSDs (Fig. 11.1b, d and f), especially in the estimated emitted flux. Consequently, the fine and coarse mass fractions are smaller in our measurements.

While the measured PSDs shown in Fig. 11.1 assume that dust particles are PSL latex spheres with a refractive index of $1.59+0i$, results shown in Fig. 11.2 consider a more realistic representation of the shape and composition of the measured dust particles, i.e. it assumes tri-axial ellipsoids and a refractive index of $1.49+0.0015i$. Furthermore, these transformed PSDs are compared with the updated BFT parameterization (Meng et al., 2022) (dashed blue line), which accounts for super-coarse dust and is constrained with measured PSDs harmonized to geometric diameters assuming dust is a tri-axial ellipsoid (Huang et al., 2021). The proportion of particles with $D_i \sim (0.5 - 2) \mu\text{m}$ and $D_i > \sim 14 \mu\text{m}$ is higher and that of particles with

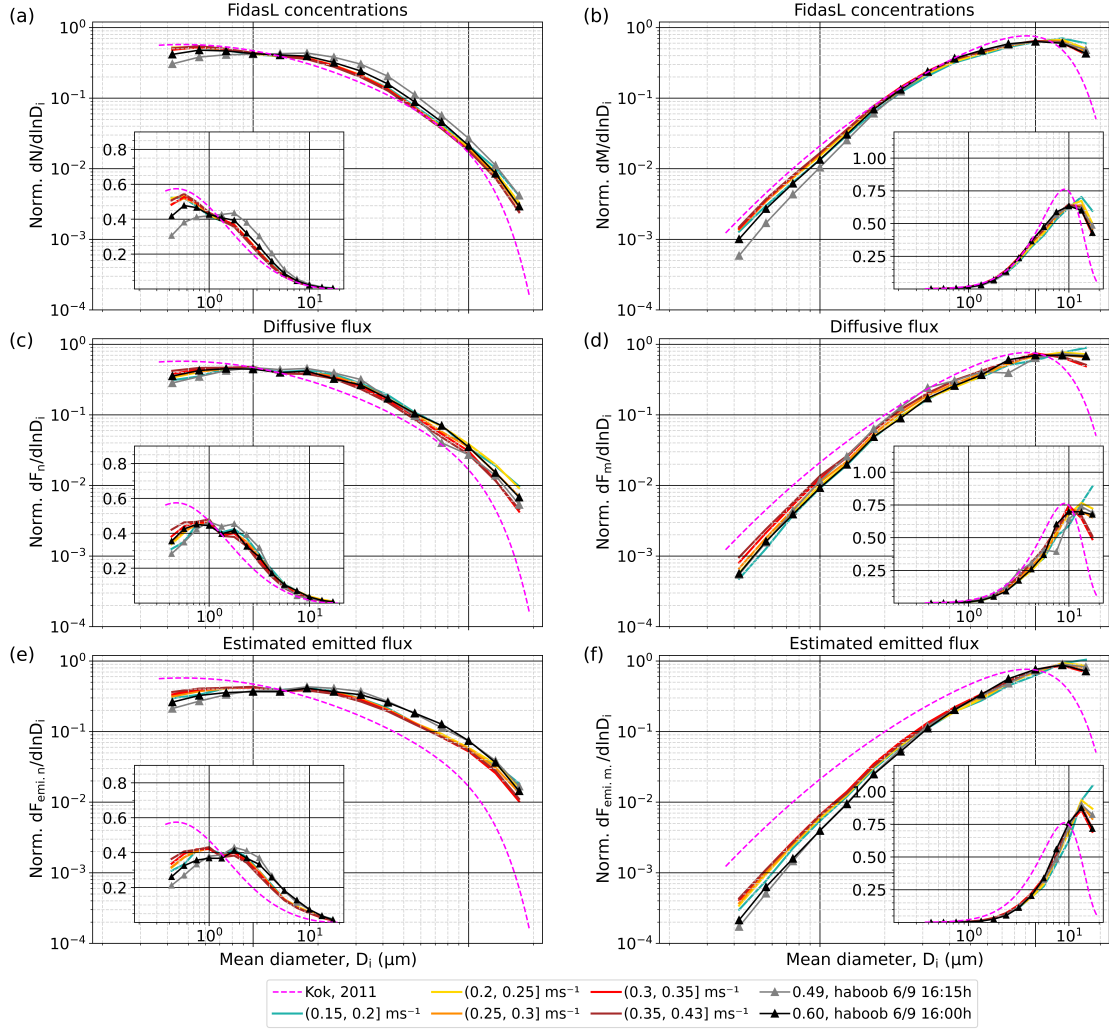


Figure 11.1: Averaged normalized PSDs considering PSL latex spheres with a refractive index of $1.59 + 0i$ removing the anthropogenic mode (normalization from 0.37 to 19.11 μm) for well-developed erosion conditions during regular events and for two PSDs during haboob events for FidasL (a-b), for diffusive flux (c-d), and for estimated emitted flux using the v_{dep} from the tuned parameterization (e-f). Panels (a,c,e) show PSDs in terms of number, and panels (b,d,f) show PSDs in terms of mass. The insets show the same data, but the scale of the ordinate is linear. Dashed pink lines represent the invariant Kok (2011a) size distribution. The original size resolution of FidasL has been reduced by integrating 4 consecutive bins, except for the last one that contains 3, resulting in 16 bins. The first integrated bin is not represented as Fidas is considered efficient from the second one onward.

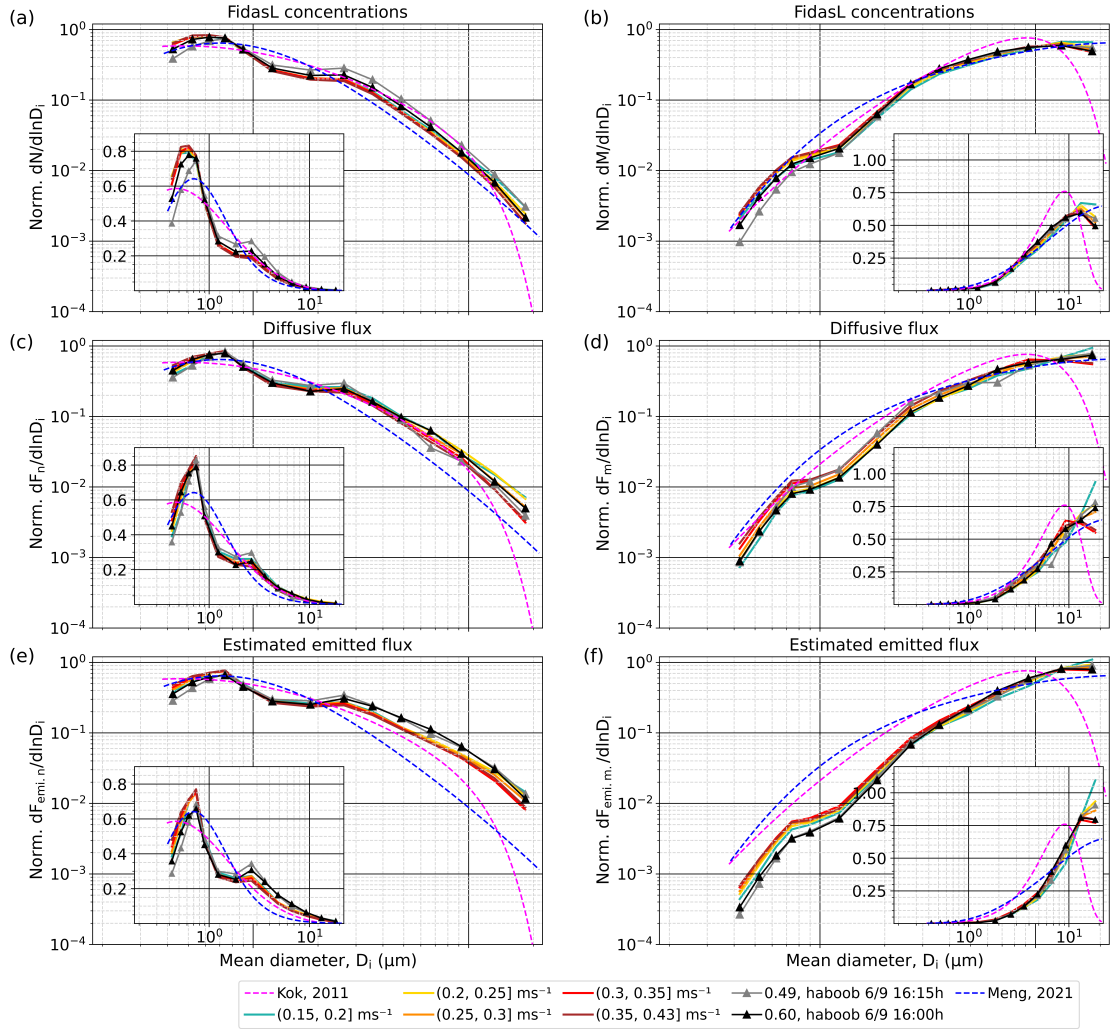


Figure 11.2: Averaged normalized PSDs considering tri-axial ellipsoids of $1.49 + 0.0015i$ removing the anthropogenic mode (normalization from 0.37 to 19.11 μm) for well-developed erosion conditions during regular events, and for two PSDs during haboob events for FidasL (a-b), for diffusive flux (c-d) and for estimated emitted flux using the v_{dep} from the tuned parameterization (e-f). Panels (a,c,e) show PSDs in terms of number, and panels (b,d,f) show PSDs in terms of mass. The insets show the same data, but the scale of the ordinate is linear. Dashed pink lines represent the invariant Kok (2011a) size distribution. Dashed blue lines represent Meng et al. (2022) data. The original size resolution of FidasL has been reduced by integrating 4 consecutive bins, except for the last one that contains 3, resulting in 16 bins. The first integrated bin is not represented as Fidas is considered efficient from the second one onward.

$D_i < \sim 0.5 \mu\text{m}$ and with $D_i \sim (2 - 14) \mu\text{m}$ is lower in the updated parameterization than in the original one (blue versus pink dashed lines in Fig. 11.2a, c and e). In terms of mass, the proportion of particles with $D_i < \sim 3 \mu\text{m}$ and $D_i > \sim 12.5 \mu\text{m}$ is higher and that of particles with $D_i \sim (3 - 12.5) \mu\text{m}$ is lower in the updated parameterization than in the original one (dashed blue versus dashed pink lines in Fig. 11.2b, d and f).

Our converted PSDs show substantial differences with respect to the Meng et al. (2022) parameterization. Firstly, our number concentration (Fig. 11.2a), diffusive flux (Fig. 11.2c) and estimated emitted PSDs (Fig. 11.2e) have a higher proportion of particles with $D_i < \sim 0.8 \mu\text{m}$. Conversely, our PSDs show a lower proportion of particles with $D_i \sim (0.8 - 2) \mu\text{m}$ and a higher proportion of particles with $D_i > \sim 2 \mu\text{m}$. The latter is more pronounced in the case of the diffusive flux PSD, and especially in the estimated emitted PSD. Secondly, the mass concentration PSD (Fig. 11.2b) show from relatively similar to lower fractions of particles with $D_i < \sim 2.5 \mu\text{m}$. The lower fractions are particularly noticeable in the range of particles with $D_i \sim (0.8 - 2.5) \mu\text{m}$. Conversely, the fractions are relatively similar to higher for particles with $\sim 2.5 < D_i < 12 \mu\text{m}$. Furthermore, depending on the type of event and u_* , there is a higher or lower fraction of dust particles with $D_i > \sim 12 \mu\text{m}$. Thirdly, the mass diffusive and estimated emitted flux PSDs (Fig. 11.2d, and f, respectively) display a similar pattern to the mass concentration PSD (Fig. 11.2b). However, they exhibit higher fractions of coarse dust (with $D_i > \sim (6 - 8) \mu\text{m}$) and generally super-coarse dust. Additionally, they show lower fractions of dust with $D_i < \sim (6 - 8) \mu\text{m}$, and a substantial reduction in the range $D_i \sim (0.8 - 2.5) \mu\text{m}$, especially in the estimated emitted flux PSD.

Table 11.1 is analogous to Table 10.1 but considering tri-axial ellipsoids. The trends in the mean number and mass fractions of the diffusive and estimated emitted fluxes are similar to those described when using the original diameters in Chap. 10. However, the mean number fractions for $\sim 0.37 < D_i < 1 \mu\text{m}$ are $\sim 22 - 24 \%$ and $\sim 25 - 27 \%$ higher for the diffusive and the estimated emitted flux, respectively, than when assuming PSL latex spheres. At the same time, the mean number fractions $\sim 2.5 < D_i < 10 \mu\text{m}$ are $\sim 41 - 43 \%$ and $\sim 38 - 40 \%$ lower for the diffusive and the estimated emitted flux, respectively. In terms of mass, the most remarkable when considering tri-axial ellipsoids is the increase of $\sim 31 - 33 \%$ and $\sim 28 - 29 \%$ in the

fraction $D_i > 10 \mu\text{m}$ of the diffusive and estimated emitted flux, respectively.

Table 11.1: Mean and standard deviation (SD) of the number and mass percentages for the four size ranges in the diffusive and emitted fluxes during regular events for each wind sector, assuming tri-axial ellipsoids. The average of each u_* interval contributes equally to the mean, and the standard deviation is a measure of the variability across u_* interval averages. For the estimated emitted flux we used the v_{dep} from the tuned parameterization.

		Mean \pm SD	Mean \pm SD	Mean \pm SD	Mean \pm SD
		0.37<D<1 μm	1<D<2.5 μm	2.5<D<10 μm	D>10 μm
Western wind direction sector					
Nb.	Diffusive flux	62.18 \pm 3.16	27.17 \pm 2.07	10.13 \pm 0.94	0.52 \pm 0.17
	% Emitted flux	58.16 \pm 2.18	27.88 \pm 1.48	12.88 \pm 0.52	1.08 \pm 0.23
Mass	Diffusive flux	0.57 \pm 0.14	6.11 \pm 0.97	50.15 \pm 7.24	43.18 \pm 8.33
	% Emitted flux	0.30 \pm 0.05	3.72 \pm 0.43	41.43 \pm 5.27	54.56 \pm 5.74
Eastern wind direction sector					
Nb.	Diffusive flux	59.32 \pm 3.52	29.86 \pm 2.20	10.33 \pm 1.22	0.50 \pm 0.13
	% Emitted flux	55.24 \pm 2.67	30.32 \pm 1.75	13.32 \pm 0.80	1.12 \pm 0.17
Mass	Diffusive flux	0.56 \pm 0.14	6.65 \pm 0.91	48.19 \pm 4.50	44.59 \pm 5.52
	% Emitted flux	0.29 \pm 0.04	3.88 \pm 0.35	39.94 \pm 3.46	55.90 \pm 3.84





IV

Conclusions and future perspectives



Conclusions and future perspectives

Atmospheric mineral dust, consisting of tiny mineral particles that are mainly produced by the wind erosion of arid and semi-arid areas, is a key component of the Earth System, and its emitted PSD partly determines its lifetime and global contribution. However, currently there is still an incomplete understanding of the physics of dust emission and the representation and variability of the dust PSD at emission. This knowledge gap is partly due to scarce and incomplete global measurements, leading to contradictory findings. These discrepancies have contributed to the development of different theoretical frameworks. This thesis aims to advance our fundamental and quantitative understanding of the emitted dust PSD and its variability based on the analysis and interpretation of intensive measurements performed during the FRAGMENT field campaign in the Moroccan Sahara in September 2019. In particular, the measurements were conducted in an ephemeral lake, whose surface consisted of paved sediments, located in the Lower Drâa Valley of Morocco surrounded by small sand dune fields.

The main outcomes obtained in each chapter of this thesis are outlined in Sect. 12.1, while the subsequent Sect. 12.2 discusses potential future research based on these findings.

12.1. Conclusions

Chapter 6 reveals that saltation and dust emission occurred regularly at our measurement site, generally following the diurnal cycles of surface winds associated to solar heating, and mostly under near-neutral atmospheric stability conditions. In addition to these “regular events”, two “haboob events” were also identified. During the campaign, dust events occurred under two prevailing wind directions, one centred around 80° (more aligned with M’hamid El Ghizlane, the closest town) and the other

one around 240° (from the Saharan desert).

Chapter 7 highlights that our site was characterized by relatively low sandblasting efficiencies in comparison to some previous studies, probably attributed to the paved sediment surface of the ephemeral lake. Nevertheless, despite the low sandblasting efficiencies, diffusive and saltation fluxes were relatively high due to frequent and intense saltation. Furthermore, sandblasting efficiency was found to decrease with increasing saltation flux and u_* . This feature is partly attributed to the observed reduction in the mass fraction of super-coarse particles in the diffusive flux with increasing u_* .

Chapter 8 evidences the presence of anthropogenic particles with diameters $<0.4\ \mu\text{m}$, which are subsequently excluded before conducting a thorough analysis of the dust PSD variability. This analysis shows differences between concentration and diffusive flux PSDs and reveals robust dependencies of these PSDs in terms of number and mass, upon u_* , wind direction, and type of event (regular versus haboob). Additionally, differences in the PSDs between regular and haboob events are identified.

Chapters 9 and 10 are closely related. They shed light on the potential major role of dry deposition in shaping the concentration and diffusive flux PSD variations, modulated by the wind-direction-dependent fetch length, and u_* . The results of this thesis support the hypothesis that the shift towards a finer diffusive flux PSD with increasing u_* is to a large extent due to an increase in the dry deposition flux of coarse and super-coarse dust with u_* . To my knowledge, this is the first time that the effect of dry deposition upon the diffusive fluxes is identified experimentally, supporting results from numerical simulations in recent studies (Dupont et al., 2015; Fernandes et al., 2019). The influence of dry deposition can invalidate the common assumption that the diffusive flux PSD is equivalent to the emitted dust PSD, particularly when including the super-coarse size range, and has consequences for the evaluation of dust emission schemes and their implementation in dust transport models. In Chap. 10 the emitted dust flux is estimated based on the diffusive flux and an estimated dry deposition flux. The findings indicate that the emitted dust PSD is coarser and its variability is smaller than that of the diffusive flux PSD. The estimation of the emitted flux must be taken with caution as in the absence of

observation-based dry deposition velocities for all u_* conditions, a resistance-based parameterization tuned with observation-based dry deposition velocities below the threshold of dust emission had to be used. Furthermore, given the large uncertainties associated with resistance-based parameterizations it cannot be discarded that our tuned parameterization partly overestimates the dry deposition velocity, thereby indirectly accounting for sampling inefficiencies of the inlet, which may affect coarse and super-coarse particles for high wind velocities. Although the Sigma-2 inlet has been designed to be efficient for coarse particles, its sensitivity upon u_* is currently ignored. Theoretically quantifying the efficiency of the Sigma-2 inlet is difficult due to its relatively complex geometry. In our location, dry deposition was estimated to represent an important portion of dust emission, up to $\sim 90\%$ for super-coarse particles, up to 80% for $10\ \mu\text{m}$ particles, and up to 65% for particles as small as $5\ \mu\text{m}$ in diameter during the haboob events. This shows that dry deposition needs to be properly accounted for, even in studies limited to the fine and coarse size ranges. The results of this thesis further imply that at least part of the variability among the diffusive flux PSDs obtained in different locations and that are used to constrain emitted dust PSD theories (e.g. Meng et al., 2022) may be due to the effect of dry deposition modulated by differences in fetch length and u_* regime.

While the reduction in super-micrometre particles with u_* was mainly attributed to the effect of dry deposition, it cannot be fully discarded that enhanced aggregate disintegration (Alfaro et al., 1997; Shao, 2001) plays an additional role in enhancing the sub-micrometre number fraction, although in the case of the haboob events there was no detectable increase in the proportion of sub-micrometre particles with increasing u_* . The clear differences observed in Chap. 8 between the haboob PSDs and the regular PSDs, notably a lower proportion of sub-micron particles for equivalent or higher u_* intervals, could be explained by a shorter “effective” fetch associated to the haboob. Also, it is observed that during the haboobs, there is an increase in both dry deposition and the variability in the coarse and super-coarse dust mass fractions with diameters $> 3\ \mu\text{m}$. This feature could be related to the effect of the moving haboob dust front, where u_* and dust emission are maximized, around our measurement site (which is equivalent to a variable fetch). This explanation is largely hypothetical and remains to be verified with targeted numerical experiments. An alternative mechanism consistent with the smaller proportion of sub-micrometre

particles would be an increased resistance of soil aggregates to fragmentation with the observed increase in relative humidity along the haboob outflow.

In **Chapter 11** our PSDs are compared with the invariant PSDs derived from the parameterization of Kok (2011a), based on BFT, and the recently updated scheme that accounts for super-coarse dust emission and uses measurements harmonized in terms of geometric diameter (Meng et al., 2022). A substantially higher proportion of super-micrometre particles is obtained in the diffusive and in particular in the estimated emitted flux PSDs in comparison with the Kok (2011a) PSDs. The comparison with the Meng et al. (2022) parameterization is performed after transforming the standard optical diameter PSDs into geometric diameter PSDs, where a more realistic index of refraction and shape of the dust particles are accounted. Despite the inclusion of super-coarse dust in the updated BFT, our PSDs show a higher proportion of particles above $\sim 2\ \mu\text{m}$ and a higher mass fraction of super-coarse particles both in the diffusive flux and estimated emitted PSDs. It is important to emphasize that this diameter transformation can be very sensitive to shape, refractive index, and wavelength (or spectrum) of the light beam. However, a detailed analysis of this sensitivity was beyond the scope of this thesis.

12.2. Future work

The work presented in this PhD thesis should serve as a starting point for coming studies aimed at better understanding the variability of dust PSD at emission. In particular, the following ideas could be implemented.

- Although this PhD thesis has focused on the variability of the PSD with u_* , wind direction, and type of event (regular vs haboob), it would be worthy also to make an exhaustive analysis of the variability of our PSDs with atmospheric stability, which has been questioned in recent years.
- Furthermore, in this PhD thesis I opted to use the u_* calculated from the law-of-the-wall method instead of the u_* derived from the eddy covariance method, due to gaps in our 3-D sonic measurements during the haboob events. Although preliminary results of u_* using both methods were largely in agreement (see Appendix B), it could be valuable to examine the impact of these methods

on the variability of both concentration and diffusive flux. Furthermore, it could be also explored the effect of this method on the resulting diffusive flux PSD.

- In this study simple correlations between our bulk measured saltation and diffusive fluxes with u_* have been calculated. However, it would be very valuable to make a detailed comparison of our measured saltation, diffusive and emitted fluxes against current parameterizations in the literature, and eventually extend them.
- Furthermore, our PSDs have been compared with the average emitted dust PSD based on Brittle Fragmentation (BFT) that is currently proposed and used in many models. This parameterization assumes an average fully-dispersed soil PSD due to the lack of reliable gridded fully-dispersed PSDs of the soil. However, during the campaign the fully-dispersed soil PSD was also measured. Hence, future studies may attempt at evaluating BFT using the specific fully dispersed and aggregated soil PSDs measured in our location.
- As we mentioned in Chap. 5.3.2 our OPCs were equipped with a Sigma-2 sampling head that has been designed to be efficient for coarse particles, and it is expected to be largely insensitive to wind intensity as it ensures a wind-sheltered, low-turbulence air volume inside the sampler. However, it is not known to what extent the transmission efficiency may decrease with friction velocity and particle size. This is clearly a potential problem for most inlets and most previous field campaigns. It is not an easy task to quantify the efficiency of this inlet to friction velocity. Experimentally it is difficult, probably only possible in the laboratory under controlled conditions, and theoretically, it is not possible to infer it due to its relatively complex geometry. We have more recently performed a dust field campaign in Iceland using this inlet in parallel with another directional inlet (which is easier to model) and their comparison may provide some insights into this issue in the future.
- This thesis has focused on the study of the size-resolved emitted dust without including the mineralogy. However, during the analyzed field campaign, unprecedentedly detailed size-resolved mineralogical, chemical and mixing state analysis of the soil and emitted dust sampled were also performed. It would be very valuable to combine all these results in order to understand and constrain

the evolution of each mineral's PSD from the parent soil to the atmosphere.

- As mentioned in Chap. 4 this thesis has been conducted within the ERC FRAGMENT project which has carried out two more intense field campaigns in Iceland and Jordan, and a soil campaign in the USA. Therefore, the findings of this thesis are expected to be highly valuable for future comparisons with the results obtained in the other campaigns.





V

Appendices



Analysis of correction for heavy particles

In Chap. 5.3.5 it was said that for this thesis it had been assumed that trajectory crossing effects (Csanady, 1963; Shao et al., 2011a) were negligible for particle diameters smaller than 20 μm , implying that $K_m=K_d$ and $\Phi_m = \Phi_d$. However, the validity of this assumption may be questionable for coarse particles.

To address this concern, I estimated the correction for heavy particles used in Shao et al. (2011a), which represents the change in the turbulent diffusivity due to the trajectory crossing effect.

The correction term for heavy particles, C_{hp} , that would multiply Eq. 5.11 is given by Eq. A.1.

$$C_{hp} = \left(1 + \frac{\beta^2 v_g^2}{\sigma_w^2}\right)^{-1/2} \quad (\text{A.1})$$

where β is a dimensionless coefficient relating the fluid Lagrangian integral time scale, the integral length scale of the Eulerian fluid velocity field and the standard deviation of the turbulent velocity. In Csanady (1963), it is said that β is very close to 1, so here it is assumed $\beta=1$. The settling velocity $v_g(D_i)$ is calculated for each size bin as $v_g(D_i) = C_c \sigma_{pa} g D_i^2 / (18\nu)$ where C_c is the Cunningham slip correction factor, $\nu = 1.45 \cdot 10^{-5} \text{ m}^2 \text{ s}^{-1}$ is the air kinematic viscosity, $g = 9.81 \text{ m s}^{-2}$ is the gravitational acceleration, D_i is the mean logarithmic diameter in bin number i , and $\sigma_{pa} = (\rho_d - \rho_{air}) / \rho_{air}$ is the particle-to-air density ratio. The unbiased variance of turbulent velocity σ_w is calculated from the w component of the 3-D sonic anemometer placed at 1 m. Figure A.1 shows the mean correction term for heavy particles per size bin only considering the periods where diffusive flux was positive in all the diameter bins above the anthropogenic mode. From the graph, it can be inferred that this correction is relatively small. Consequently, it was decided not to account for it in the analysis.

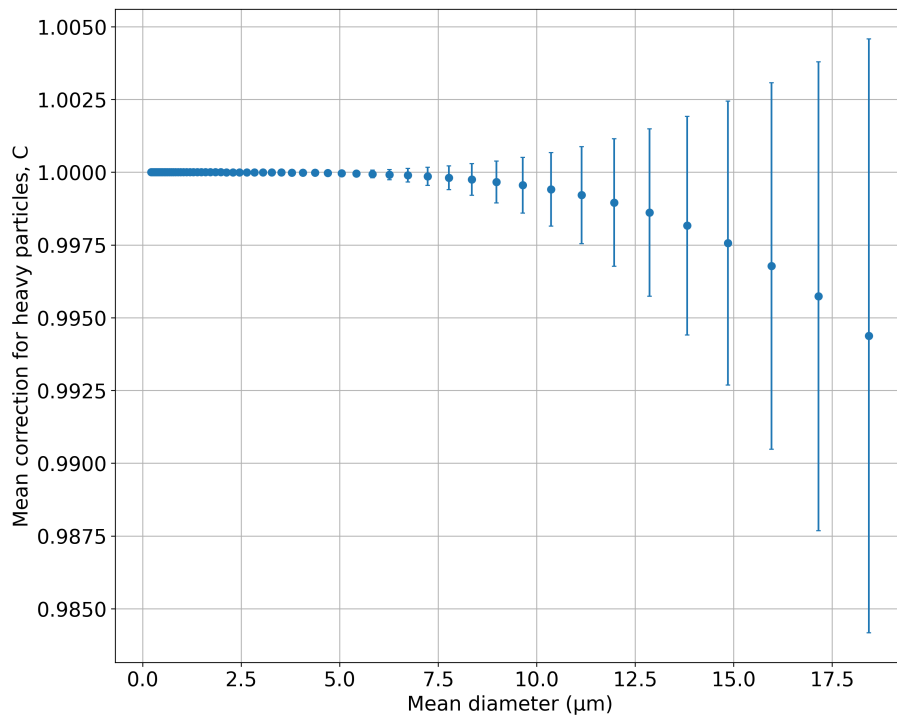


Figure A.1: Mean correction factor for heavy particles per size bin. Only the samples where diffusive flux is positive in all the diameter bins above the anthropogenic mode have been used. Error bars represent the standard deviation.

Friction velocity from the Eddy Covariance method

Although in this thesis the analysis of the PSD variability with u_* has been performed with the u_* calculated through the FG method. For verification purposes I also estimated u_* from the 3-D sonic anemometers using the EC method (Foken et al., 2011; Dupont et al., 2018) at 1 m and 3 m, and later I extrapolated it to the surface. Figure B.1 illustrates that our preliminary results of u_* from the eddy covariance were largely in agreement. Ultimately, we opted to use the u_* calculated from the FG method, due to gaps in our 3-D sonic measurements during the haboob events. In the future it would be worthy to examine the sensitivity of the results presented in this thesis to the calculation method of u_* .

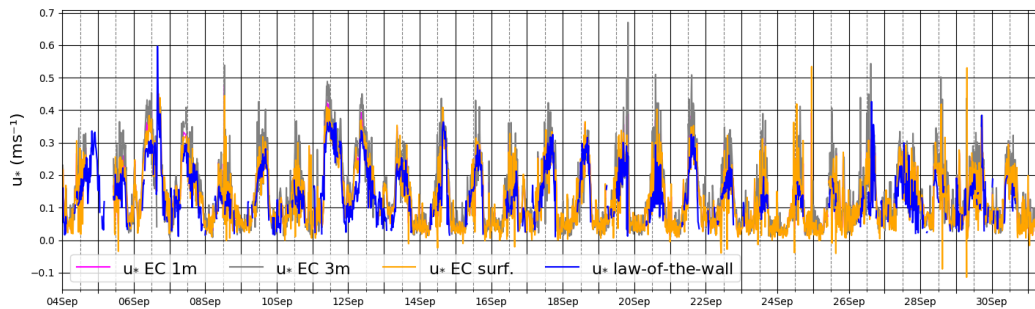


Figure B.1: Time series of u_* calculated from the law of the FG method (blue line) and EC method at 1 m (magenta line), 3 m (grey line) and extrapolated to the surface (orange line).

Additional figures related to the diffusive flux PSDs

Figures C.1 and C.2 show the same plots as Figs. 8.5 and 8.6 but including the uncertainties for each u_* range only for the haboob events. Additionally, the diffusive flux PSDs with uncertainties accounting only for standard errors are provided in Figs. C.3 and C.4. As the standard error depends inversely on the number of samples, those cases in which there is only a sample do not show any shaded areas.

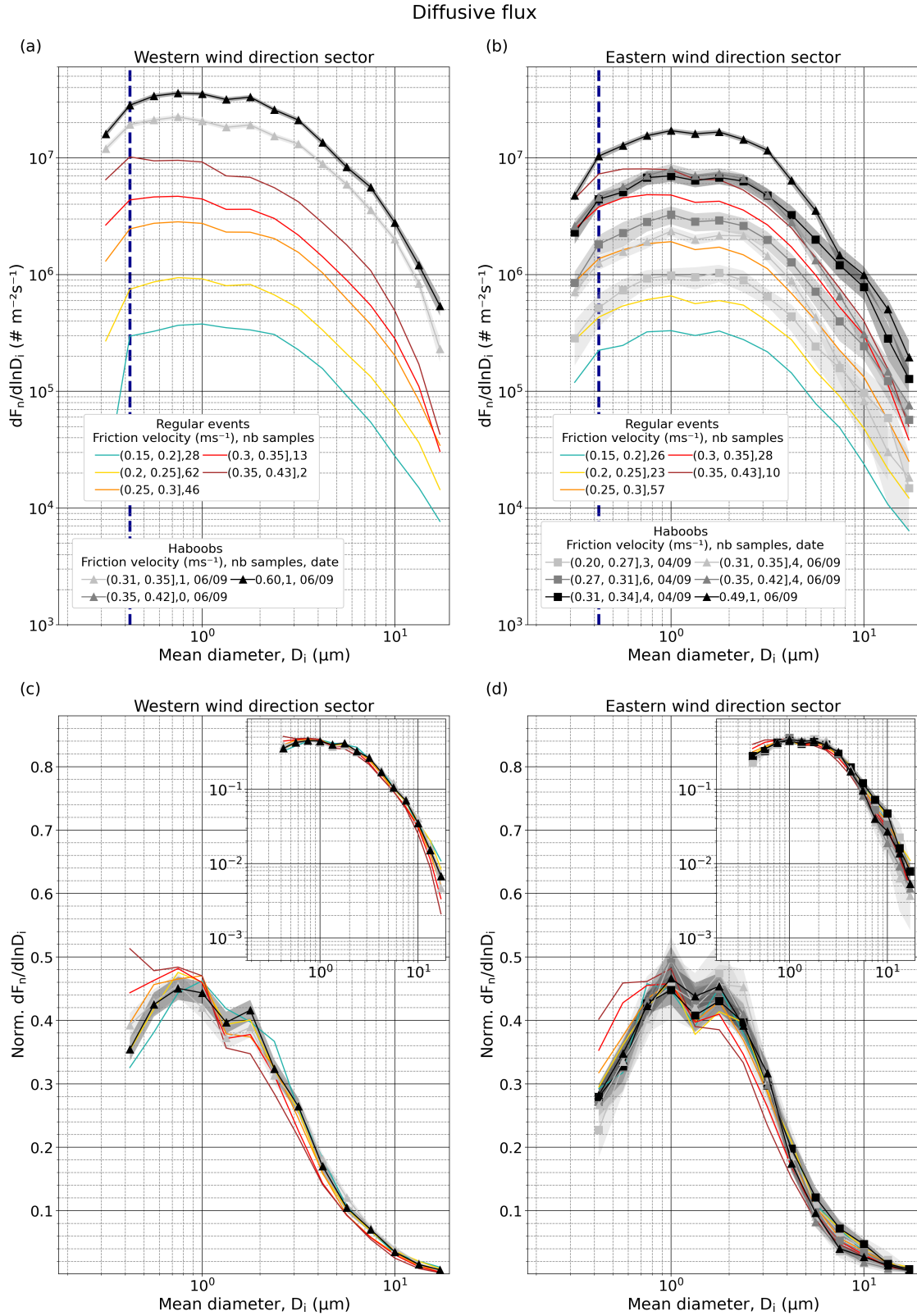


Figure C.1: Analogous to Fig. 8.5 but with shaded areas around the lines of the haboob event PSDs depicting the combination of random uncertainty and standard error.

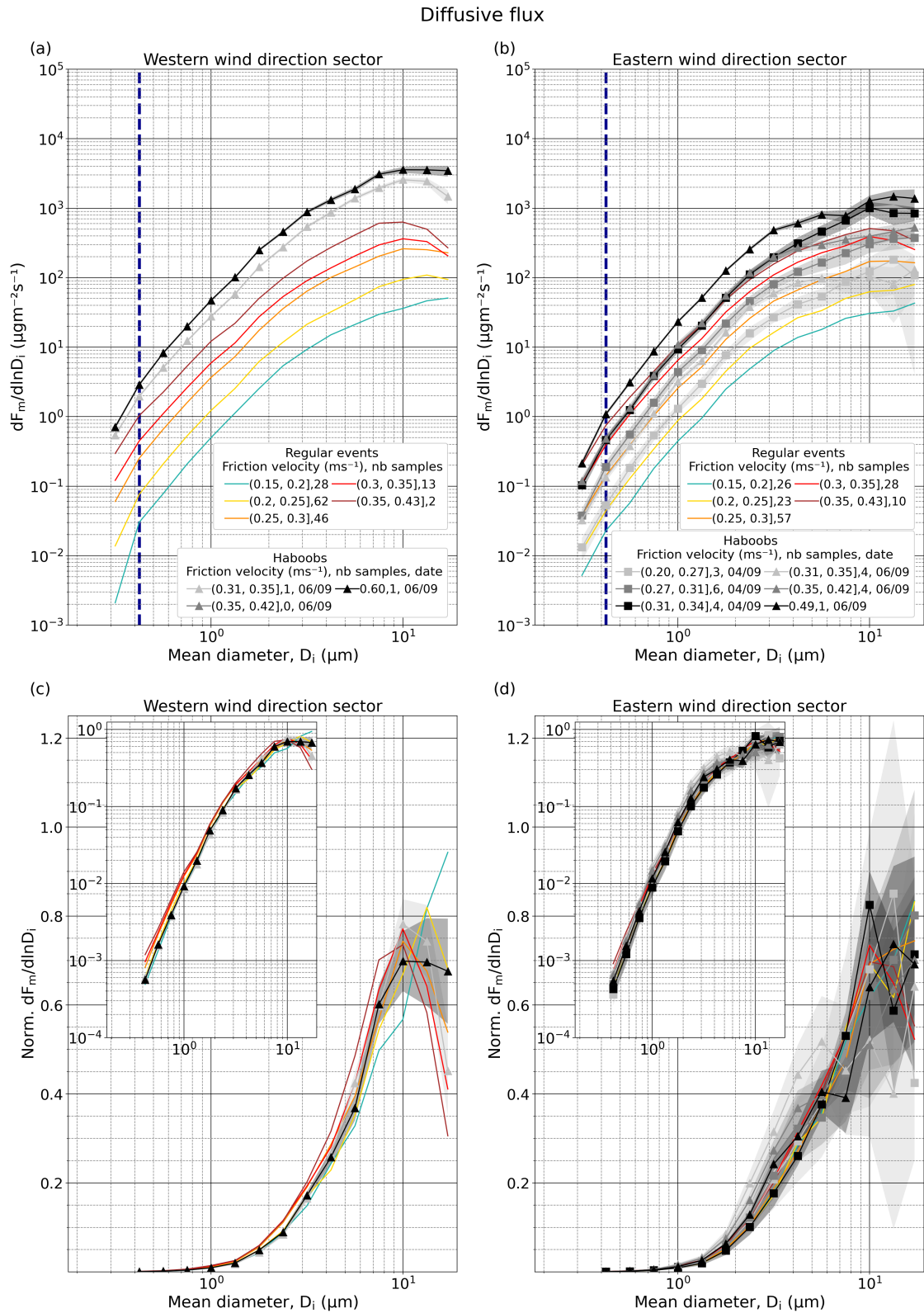


Figure C.2: Analogous to Fig. 8.6 but with shaded areas around the lines of the haboob event PSDs depicting the combination of random uncertainty and standard error.

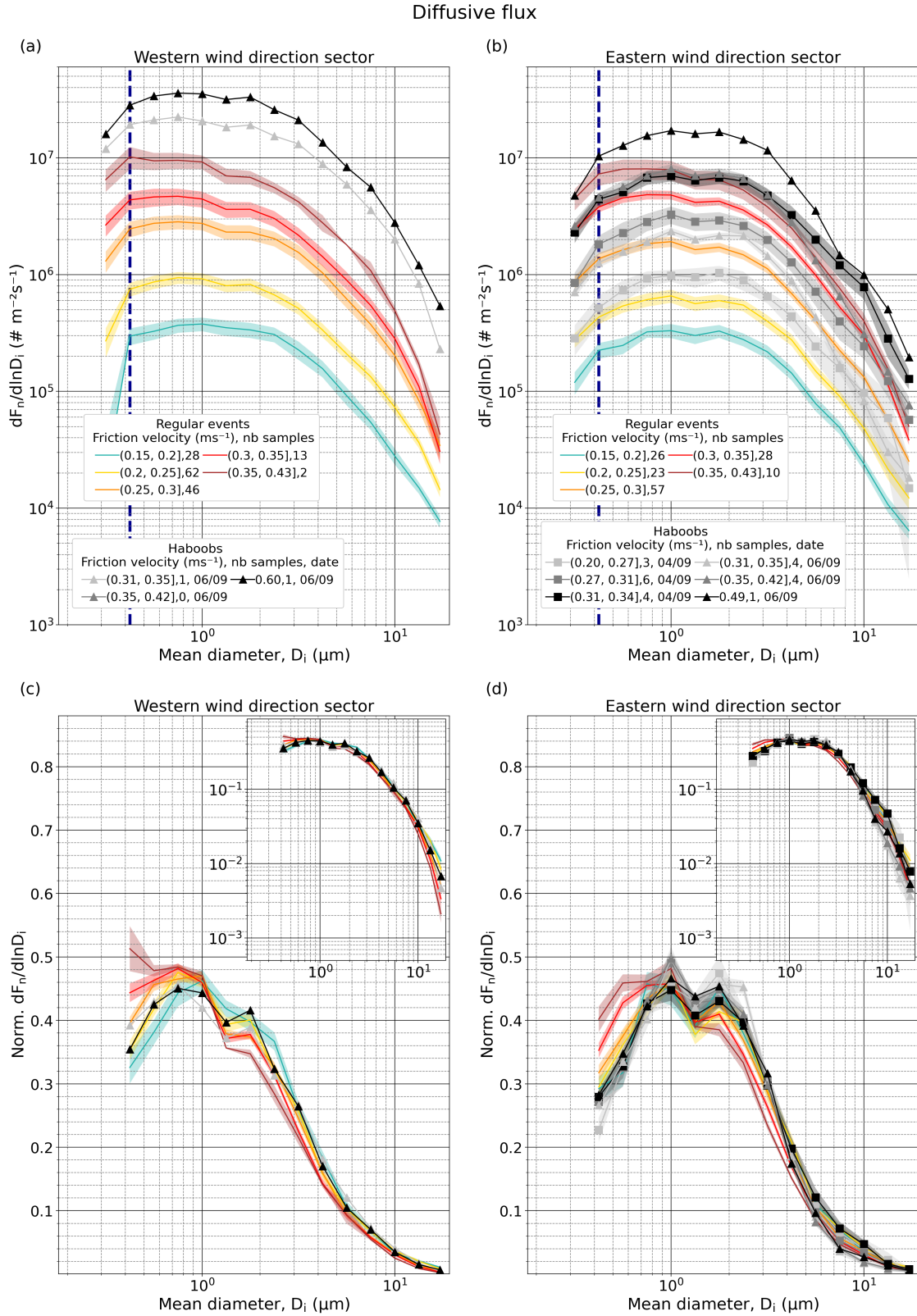


Figure C.3: Analogous to Fig. C.3 but with shaded areas around the lines depicting the standard error.

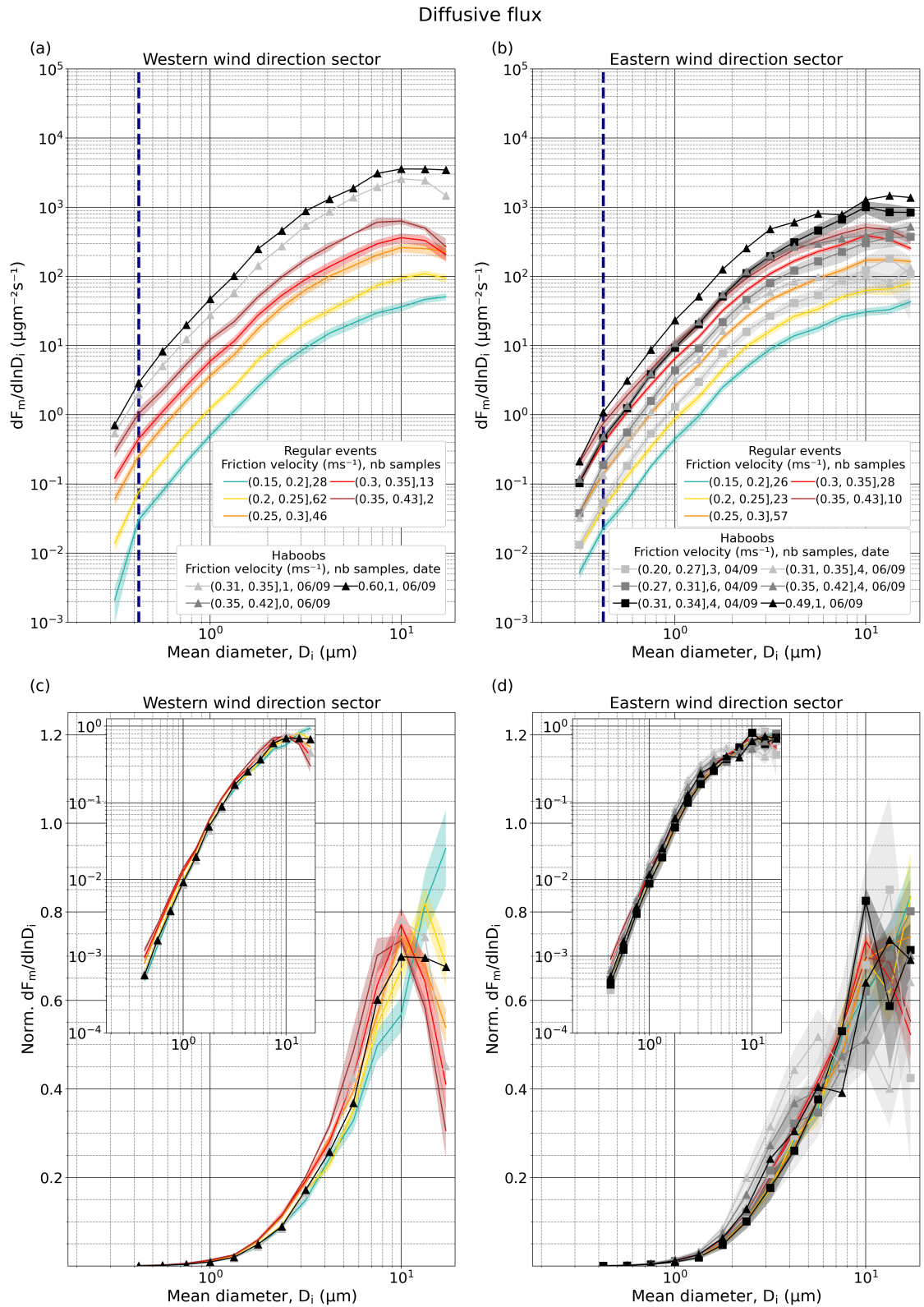


Figure C.4: Analogous to Fig. C.4 but with shaded areas around the lines depicting the standard error.

Additional figures related to the dry deposition fluxes

Chapter 10 presents the size-resolved number and mass dry deposition fluxes calculated using the v_{dep} tuned parameterization (Figs. 10.4 and 10.5). Here analogous plots obtained using F19 (Figs. D.1 and D.2) and Z01 (Figs. D.3 and D.4) are included.

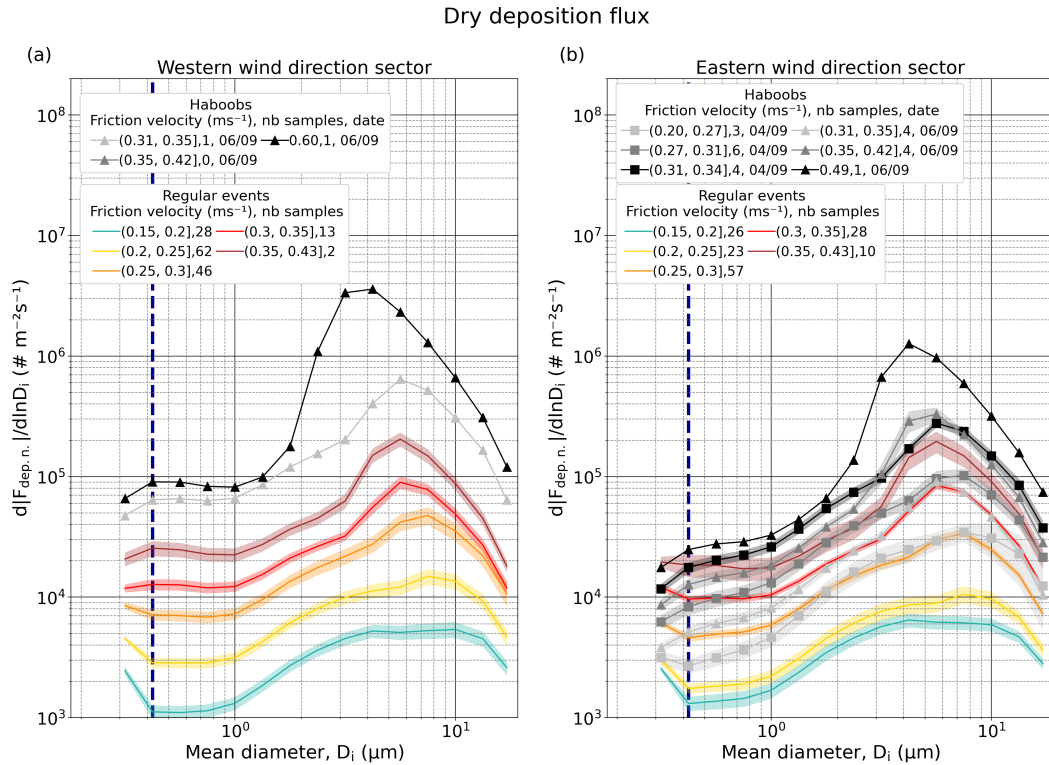


Figure D.1: Analogous to Fig. 10.4 but with v_{dep} estimated from F19.

Appendix D. Additional figures related to the dry deposition fluxes

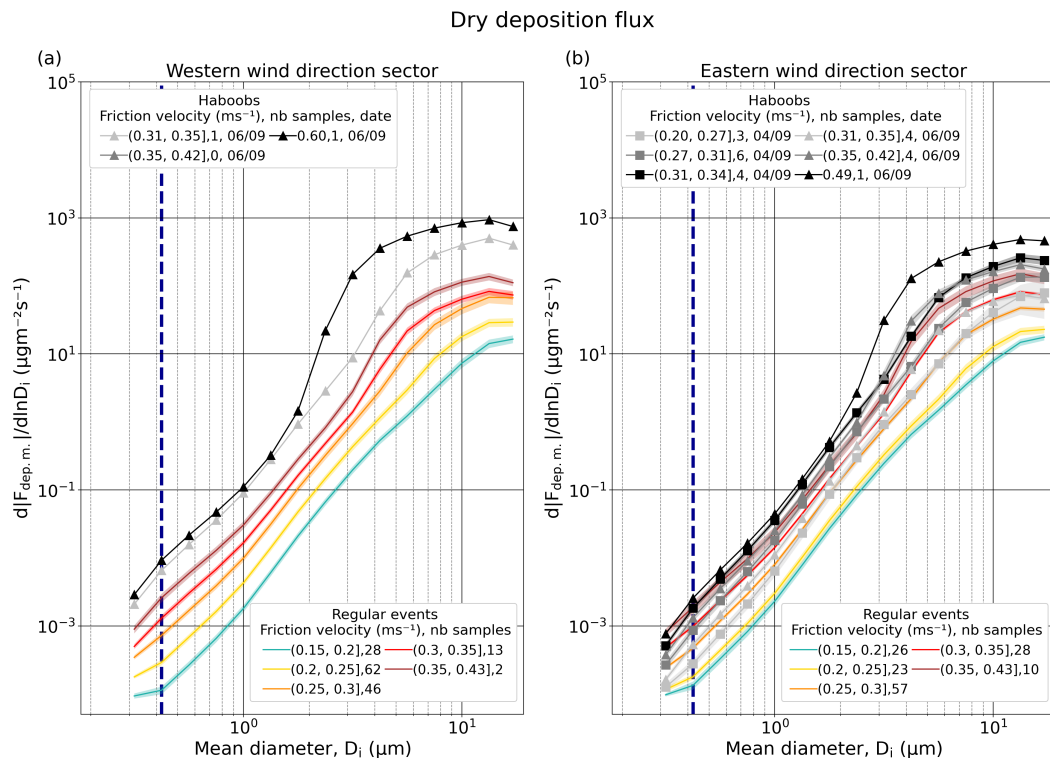


Figure D.2: Analogous to Fig. 10.5 but with v_{dep} estimated from F19.

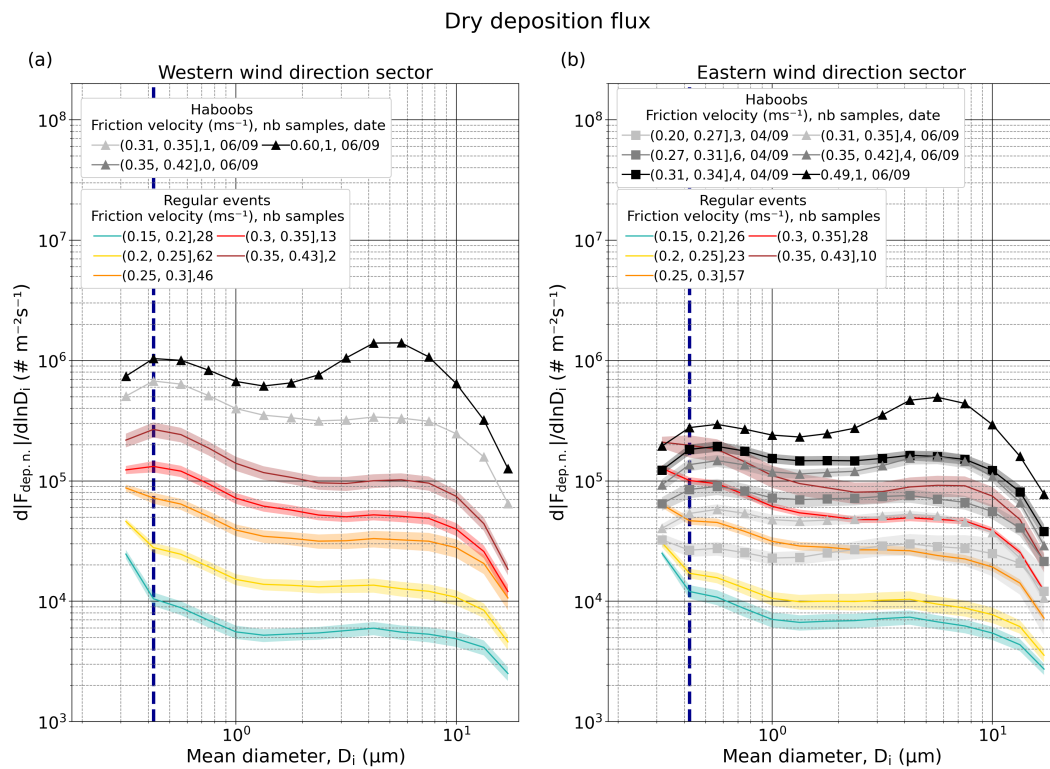


Figure D.3: Analogous to Fig. 10.4 but with v_{dep} estimated from Z01.

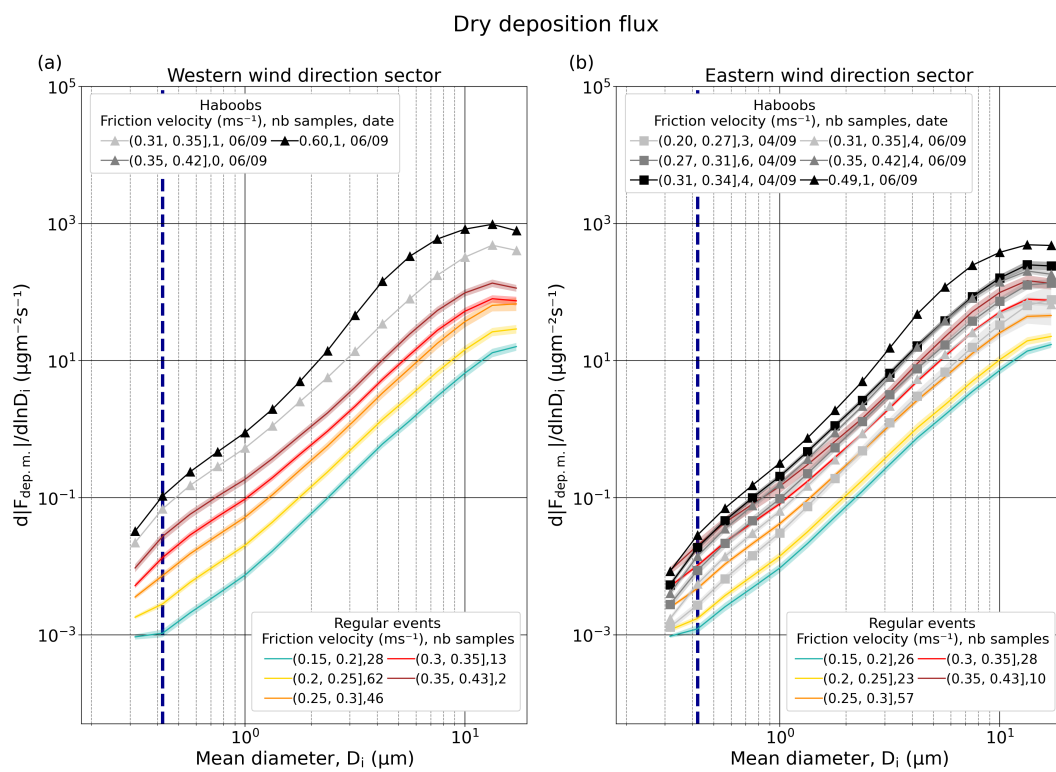


Figure D.4: Analogous to Fig. 10.5 but with v_{dep} estimated from Z01.

Additional figures related to the estimated emitted flux PSDs

Chapter 10 presents the estimated size-resolved number and mass emitted fluxes calculated using the v_{dep} tuned parameterization (Figs. 10.6 and 10.7). Here analogous plots obtained using F19 (Figs. D.1 and D.2) and Z01 (Figs. D.3 and D.4) are included. The uncertainties (combination of random uncertainty and standard error) are shown only for the regular events for the sake of clarity. The increase of particles in the estimated emitted flux compared to the diffusive flux is very subtle, almost unnoticed in logarithmic scale, when applying F19 (Figs. E.1a, b, E.2a and b) and Z01 (Figs. E.3a, b, E.4a and b), in agreement with the smaller dry deposition fluxes (see Appendix D).

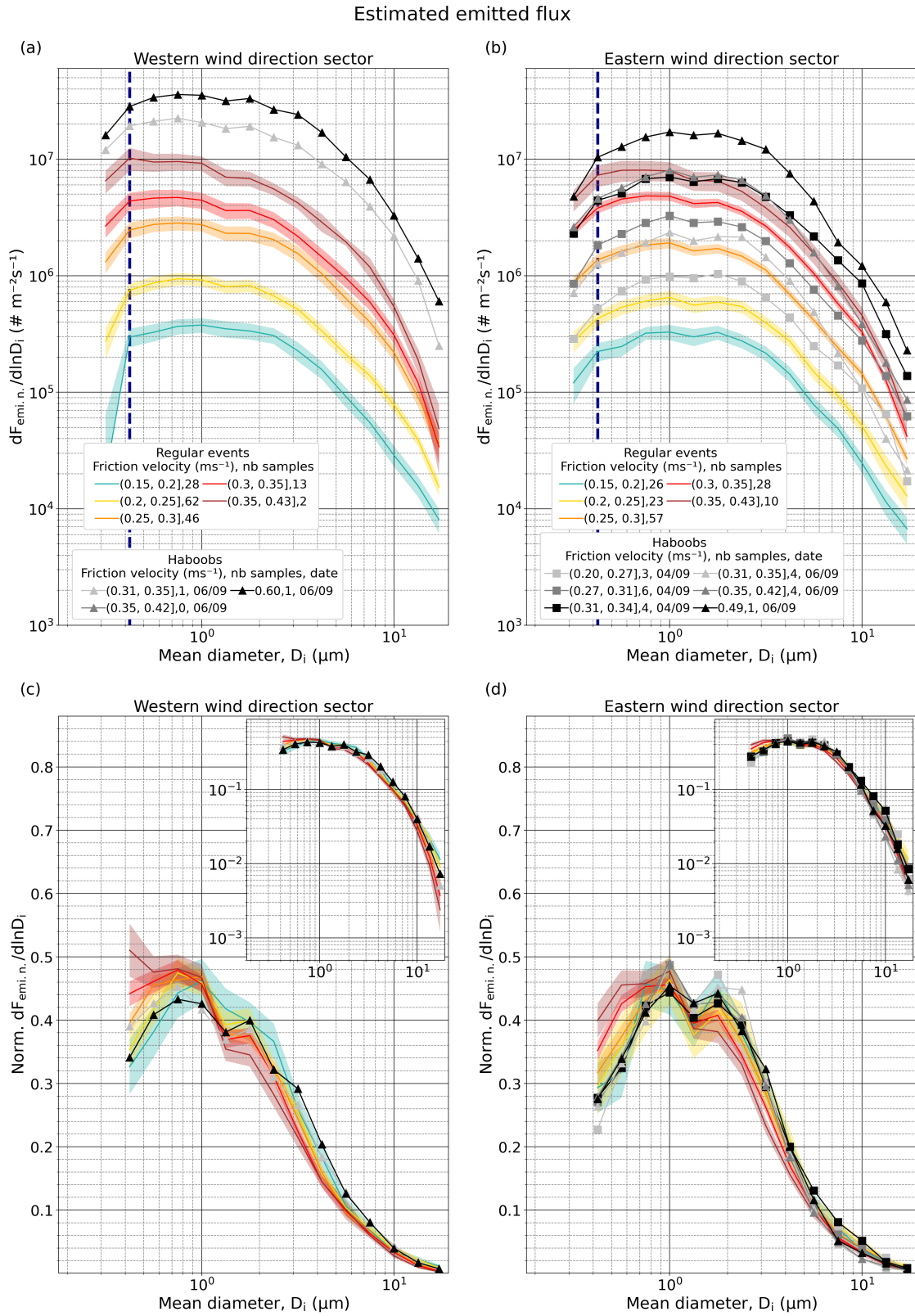


Figure E.1: Analogous to Fig. 10.6 but with v_{dep} estimated from F19.

Estimated emitted flux

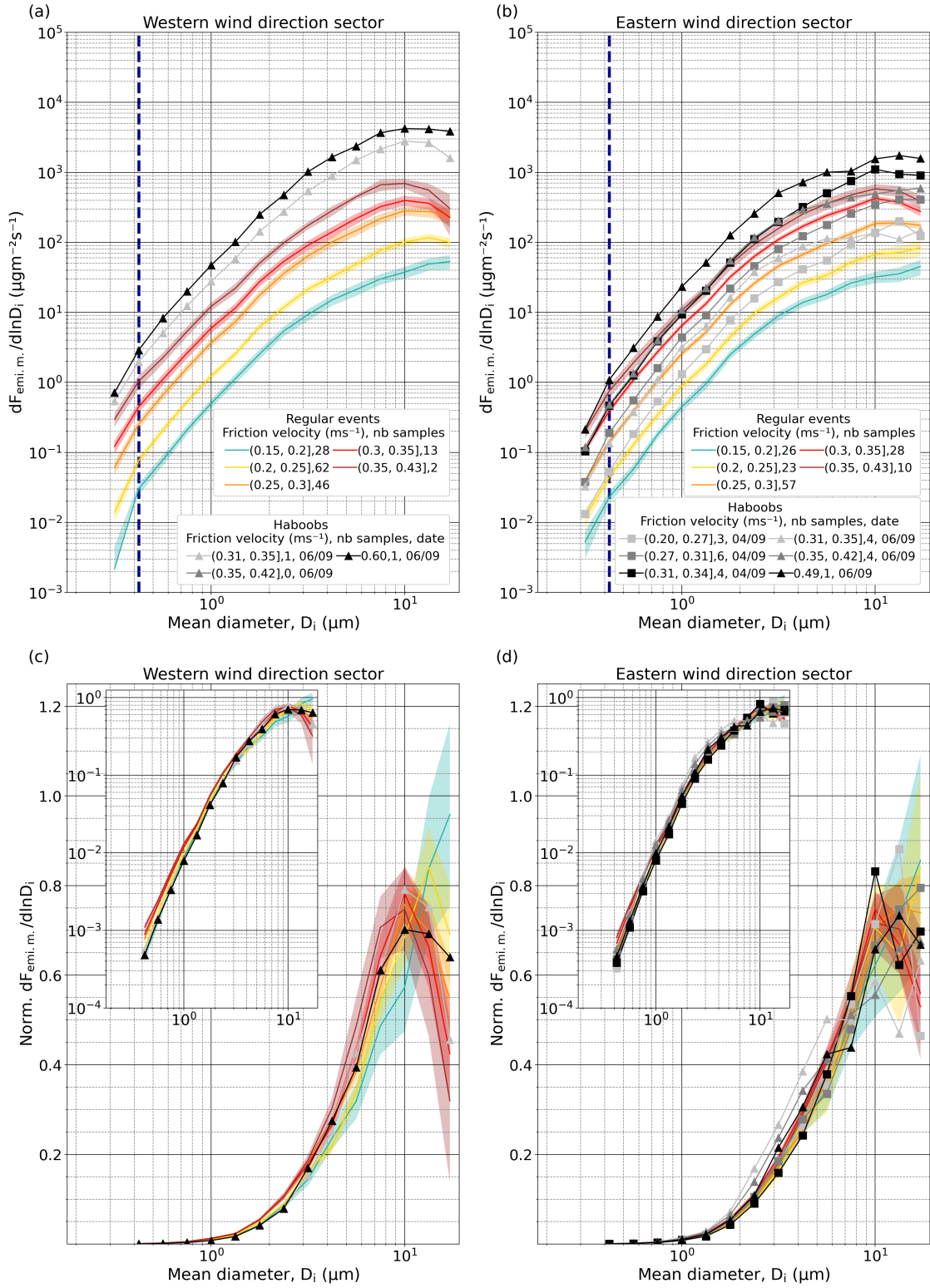


Figure E.2: Analogous to Fig. 10.7 but with v_{dep} estimated from F19.

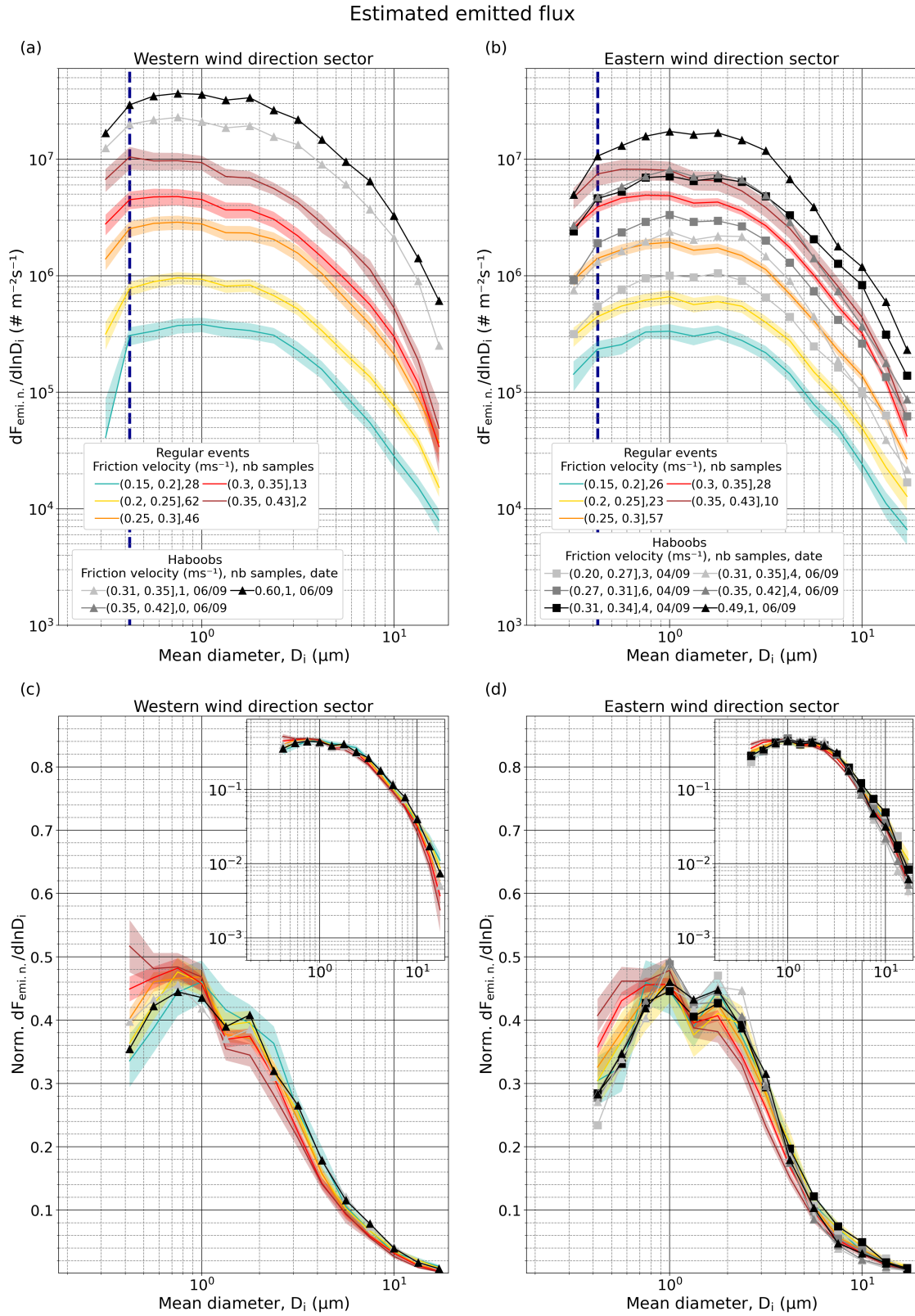


Figure E.3: Analogous to Fig. 10.6 but with v_{dep} estimated from Z01.

Estimated emitted flux

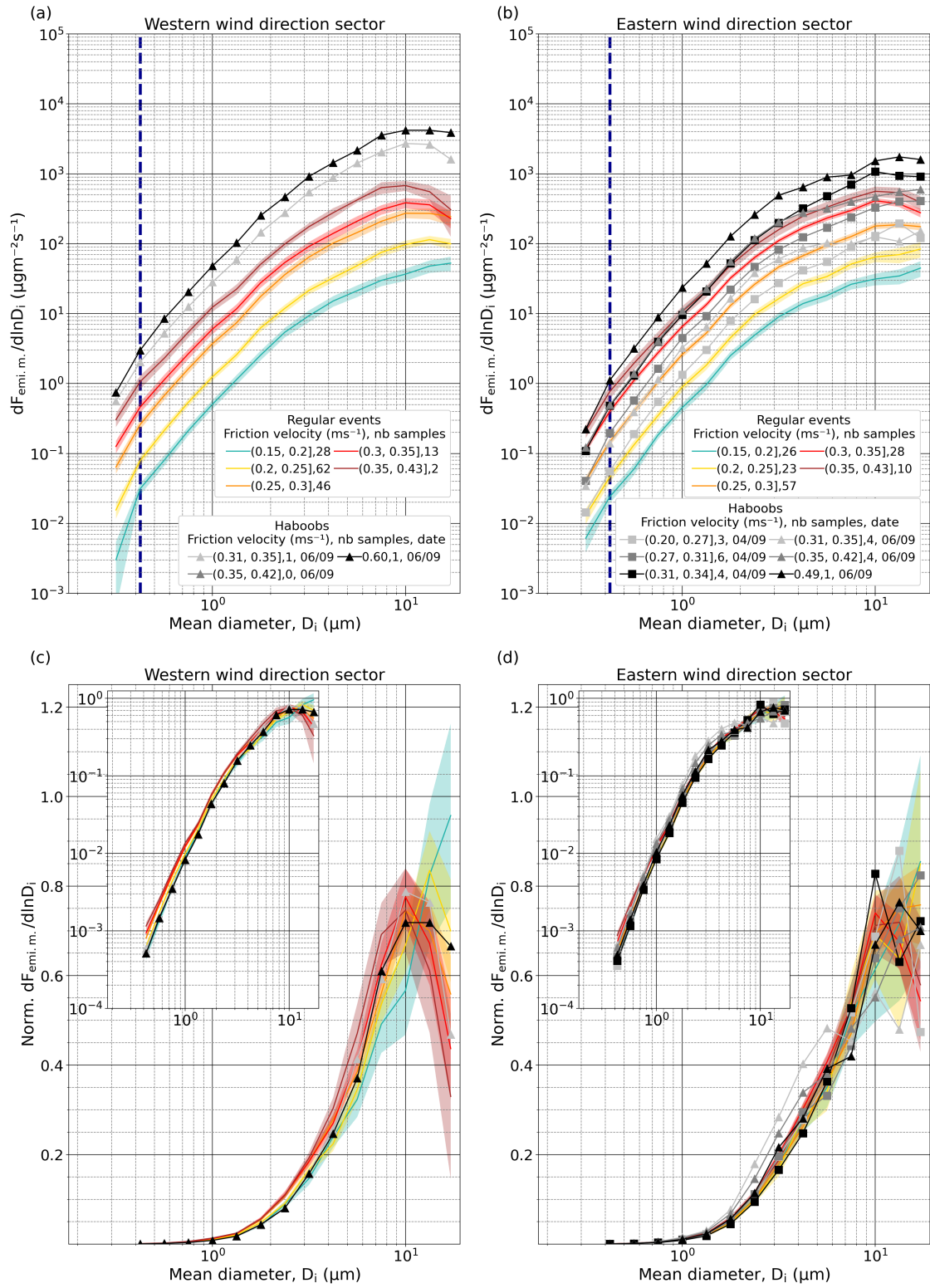


Figure E.4: Analogous to Fig. 10.7 but with v_{dep} estimated from Z01.

Additional figures related to the ratio of dry deposition flux to the estimated emitted flux

Chapter 10 presents the size-resolved ratio of dry deposition flux, calculated using the v_{dep} tuned parameterization, to the estimated emitted flux (Fig. 10.9). Here analogous plots obtained using F19 (Fig. F.1) and Z01 (Fig. F.2) are included.

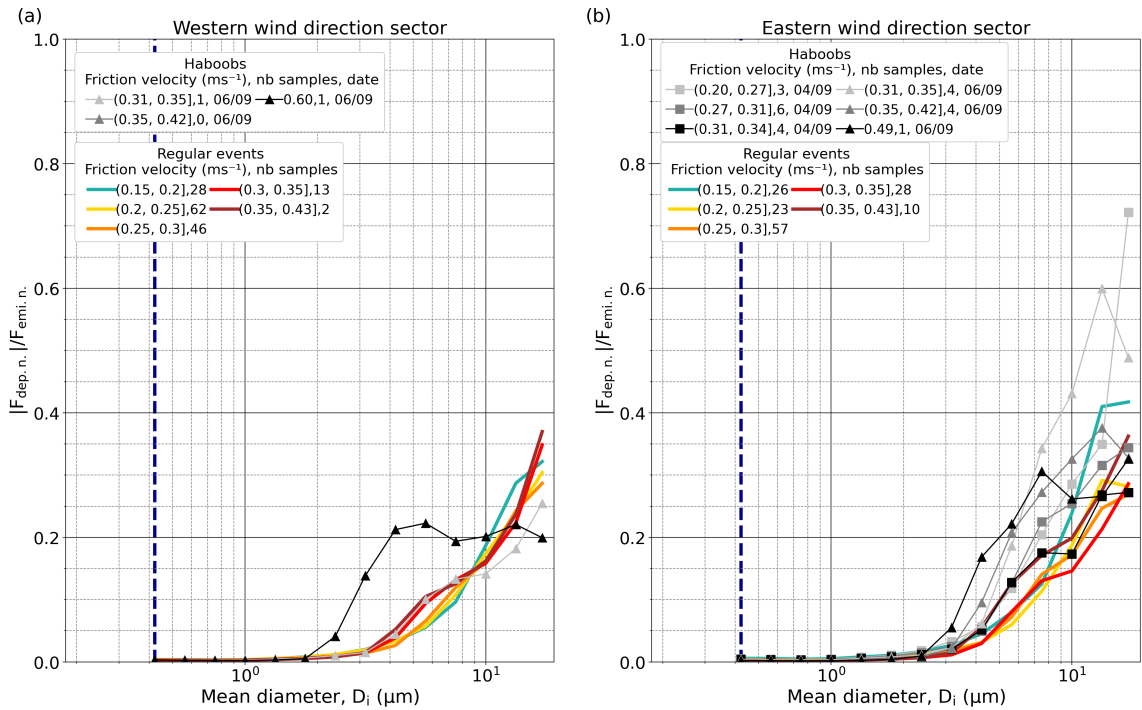


Figure F.1: Analogous to Fig. 10.9 but with v_{dep} estimated from F19.

Appendix F. Additional figures related to the ratio of dry deposition flux to the estimated emitted flux

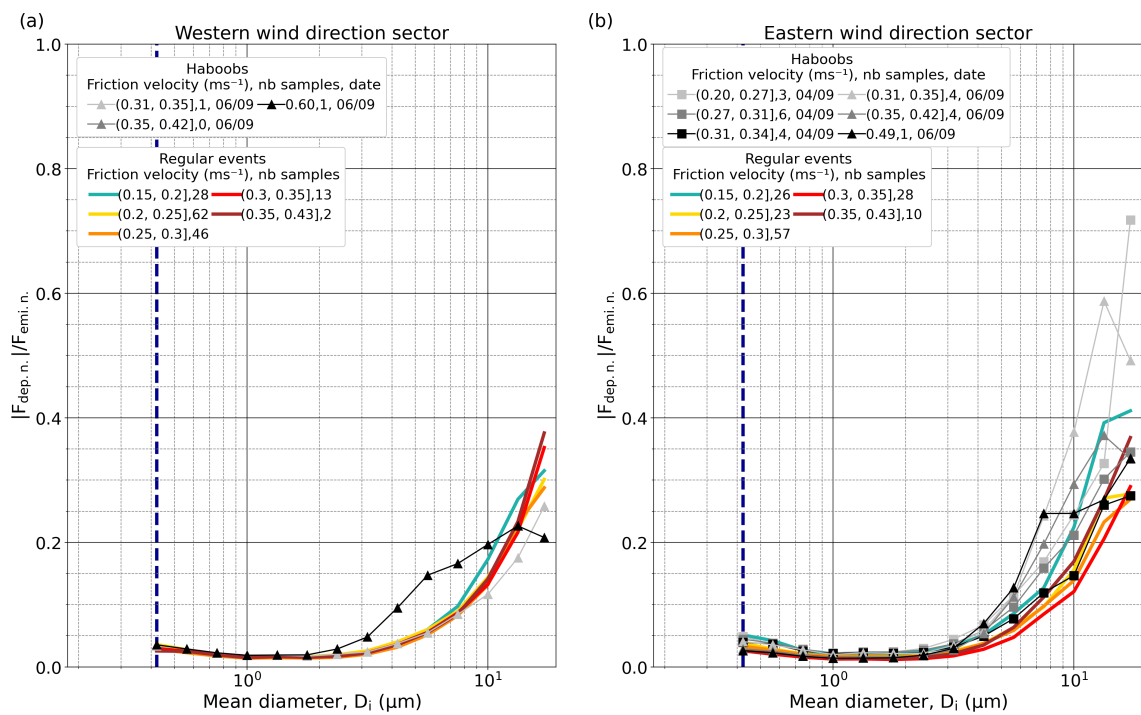


Figure F.2: Analogous to Fig. 10.9 but with v_{dep} estimated from Z01.





References

References

- Adebiyi, A., Kok, J., Murray, B., Ryder, C., Stuut, J.-B., Kahn, R., Knippertz, P., Formenti, P., Mahowald, N., Pérez García-Pando, C., Klose, M., Ansmann, A., Samset, B., Ito, A., Balkanski, Y., Di Biagio, C., Romanias, M., Huang, Y., and Meng, J. (2023). A review of coarse mineral dust in the earth system. *Aeolian Research*, 60:100849.
- Adebiyi, A. A. and Kok, J. F. (2020). Climate models miss most of the coarse dust in the atmosphere. *Science Advances*, 6(15):1–10.
- Alfaro, S., Bouet, C., Khalfallah, B., Shao, Y., Ishizuka, M., Labiadh, M., Marticorena, B., Laurent, B., and Rajot, J.-L. (2022). Unraveling the roles of saltation bombardment and atmospheric instability on magnitude and size distribution of dust emission fluxes: Lessons from the jade and wind-o-v experiments. *J. Geophys. Res. Atmos.*, 127(12):e2021JD035983.
- Alfaro, S. C. (2008). Influence of soil texture on the binding energies of fine mineral dust particles potentially released by wind erosion. *Geomorphology*, 93(3-4):157–167.
- Alfaro, S. C., Gaudichet, A., Gomes, L., and Maillé, M. (1998). Mineral aerosol production by wind erosion: aerosol particle sizes and binding energies. *Geophysical Research Letters*, 25(7):991–994.
- Alfaro, S. C., Gaudichet, A., Gomes, L., and Maillé, M. (1997). Modeling the size distribution of a soil aerosol produced by sandblasting. *J. Geophys. Res.*, 102:11239–11249.
- Alfaro, S. C. and Gomes, L. (2001). Modeling mineral aerosol production by wind erosion: Emission intensities and aerosol size distributions in source areas. *Journal of Geophysical Research: Atmospheres*, 106(D16):18075–18084.
- Alizadeh-Choobari, O., Zawar-Reza, P., and Sturman, A. (2014). The “wind of 120 days” and dust storm activity over the sistan basin. *Atmospheric research*, 143:328–341.

- Amiri-Farahani, A., Allen, R. J., Neubauer, D., and Lohmann, U. (2017). Impact of saharan dust on north atlantic marine stratocumulus clouds: importance of the semidirect effect. *Atmospheric Chemistry and Physics*, 17(10):6305–6322.
- Ansmann, A., Tesche, M., Knippertz, P., Bierwirth, E., Althausen, D., Mueller, D., and Schulz, O. (2009). Vertical profiling of convective dust plumes in southern morocco during samum. *Tellus B: Chemical and Physical Meteorology*, 61(1):340–353.
- Arnalds, O., Dagsson-Waldhauserova, P., and Olafsson, H. (2016). The icelandic volcanic aeolian environment: Processes and impacts—a review. *Aeolian Research*, 20:176–195.
- Arya, P. S. (2001). *Introduction to micrometeorology*. Academic Press, San Diego, 2 edition.
- Åström, J. (2006). Statistical models of brittle fragmentation. *Advances in Physics*, 55(3-4):247–278.
- Atkinson, J. D., Murray, B. J., Woodhouse, M. T., Whale, T. F., Baustian, K. J., Carslaw, K. S., Dobbie, S., O’Sullivan, D., and Malkin, T. L. (2013). The importance of feldspar for ice nucleation by mineral dust in mixed-phase clouds. *Nature*, 498(7454):355–358.
- Avila, A., Queralt-Mitjans, I., and Alarcón, M. (1997). Mineralogical composition of african dust delivered by red rains over northeastern spain. *Journal of Geophysical Research: Atmospheres*, 102(D18):21977–21996.
- Baddock, M. C., Mockford, T., Bullard, J. E., and Thorsteinsson, T. (2017). Pathways of high-latitude dust in the north atlantic. *Earth and Planetary Science Letters*, 459:170–182.
- Bagnold, R. (1941). *The physics of blown sand and desert dunes*. Methuen and Co. Ltd, London.
- Bagnold, R. A. (1937). The transport of sand by wind. *The Geographical Journal*, 89(5):409–438.
- Bak, P., Tang, C., and Wiesenfeld, K. (1987). Self-organized criticality: An explanation of the $1/f$ noise. *Physical review letters*, 59(4):381.

- Baker, A. and Jickells, T. (2006). Mineral particle size as a control on aerosol iron solubility. *Geophysical Research Letters*, 33(17).
- Baker, A. R. and Croot, P. L. (2010). Atmospheric and marine controls on aerosol iron solubility in seawater. *Marine Chemistry*, 120(1-4):4–13.
- Baldo, C., Formenti, P., Nowak, S., Chevaillier, S., Cazaunau, M., Pangui, E., Di Biagio, C., Doussin, J.-F., Ignatyev, K., Dagsson-Waldhauserova, P., et al. (2020). Distinct chemical and mineralogical composition of icelandic dust compared to northern african and asian dust. *Atmospheric Chemistry and Physics*, 20(21):13521–13539.
- Balsamo, G., Albergel, C., Beljaars, A., Boussetta, S., Brun, E., Cloke, H., Dee, D., Dutra, E., Muñoz-Sabater, J., Pappenberger, F., et al. (2015). Era-interim/land: a global land surface reanalysis data set. *Hydrology and Earth System Sciences*, 19(1):389–407.
- Benoit, R. (1977). On the integral of the surface layer profile-gradient functions. *J. Appl. Meteor.*, 16:859–860.
- Bergametti, G. and Foret, G. (2014). *Dust deposition*. CDordrecht, Netherlands: Springer.
- Bergametti, G., Marticorena, B., Rajot, J.-L., Foret, G., Alfaro, S., and Laurent, B. (2018). Size-resolved dry deposition velocities of dust particles: in situ measurements and parameterizations testing. *Journal of Geophysical Research: Atmospheres*, 123(19):11–080.
- Bi, L., Yang, P., Kattawar, G. W., and Kahn, R. (2009). Single-scattering properties of triaxial ellipsoidal particles for a size parameter range from the rayleigh to geometric-optics regimes. *Applied Optics*, 48(1):114–126.
- Blyth, A. M., Lasher-Trapp, S. G., Cooper, W. A., Knight, C. A., and Latham, J. (2003). The role of giant and ultragiant nuclei in the formation of early radar echoes in warm cumulus clouds. *Journal of the atmospheric sciences*, 60(21):2557–2572.
- Bonasoni, P., Cristofanelli, P., Calzolari, F., Bonafe, U., Evangelisti, F., Stohl, A., Zauli Sajani, S., Van Dingenen, R., Colombo, T., and Balkanski, Y. (2004).

References

- Aerosol-ozone correlations during dust transport episodes. *Atmospheric Chemistry and Physics*, 4(5):1201–1215.
- Boussinesq, J. (1877). Essai sur la théorie des eaux courantes. paris: Impr. nationale.
- Bowker, D. (2011). Meteorology and the ancient greeks. *Weather*, 66(9):249–251.
- Boyd, P., Mackie, D., and Hunter, K. (2010). Aerosol iron deposition to the surface ocean—modes of iron supply and biological responses. *Marine Chemistry*, 120(1-4):128–143.
- Bristow, C. S., Drake, N., and Armitage, S. (2009). Deflation in the dustiest place on earth: the bodélé depression, chad. *Geomorphology*, 105(1-2):50–58.
- Bristow, C. S., Hudson-Edwards, K. A., and Chappell, A. (2010). Fertilizing the Amazon and equatorial Atlantic with West African dust. *Geophys. Res. Lett.*, 37(14):3–7.
- Brunekreef, B. and Holgate, S. T. (2002). Air pollution and health. *The lancet*, 360(9341):1233–1242.
- Bryant, R. G., Bigg, G. R., Mahowald, N. M., Eckardt, F. D., and Ross, S. G. (2007). Dust emission response to climate in southern africa. *Journal of Geophysical Research: Atmospheres*, 112(D9).
- Bullard, J. E., Baddock, M., Bradwell, T., Crusius, J., Darlington, E., Gaiero, D., Gassó, S., Gisladdottir, G., Hodgkins, R., McCulloch, R., et al. (2016). High-latitude dust in the earth system. *Reviews of Geophysics*, 54(2):447–485.
- Bullard, J. E., Harrison, S. P., Baddock, M. C., Drake, N., Gill, T. E., McTainsh, G., and Sun, Y. (2011). Preferential dust sources: A geomorphological classification designed for use in global dust-cycle models. *Journal of Geophysical Research: Earth Surface*, 116(F4).
- Businger, J. A., Wyngaard, J. C., Izumi, Y., and Bradley, E. F. (1971). Flux-profile relationships in the atmospheric surface layer. *J. Atmos. Sci.*, 28:181–189.
- Caquineau, S., Gaudichet, A., Gomes, L., Magonthier, M.-C., and Chatenet, B. (1998). Saharan dust: Clay ratio as a relevant tracer to assess the origin of soil-derived aerosols. *Geophysical research letters*, 25(7):983–986.

- Carlson, T. N. and Prospero, J. M. (1972). The large-scale movement of saharan air outbreaks over the northern equatorial atlantic. *Journal of Applied Meteorology and Climatology*, 11(2):283–297.
- Chadwick, O. A., Derry, L. A., Vitousek, P. M., Huebert, B. J., and Hedin, L. O. (1999). Changing sources of nutrients during four million years of ecosystem development. *Nature*, 397(6719):491–497.
- Chamberlain, A. C. (1983). Roughness length of sea, sand, and snow. *Bound. Lay. Meteorol.*, 25(4):405–409.
- Charnock, H. (1955). Wind stress on a water surface. *Q. J. Roy. Meteor. Soc.*, 81(350):639–640.
- Chatziparaschos, M., Daskalakis, N., Myriokefalitakis, S., Kalivitis, N., Nenes, A., Gonçalves Ageitos, M., Costa-Surós, M., Pérez García-Pando, C., Zanoli, M., Vrekoussis, M., et al. (2023). Role of k-feldspar and quartz in global ice nucleation by mineral dust in mixed-phase clouds. *Atmospheric Chemistry and Physics*, 23(3):1785–1801.
- Chen, S., Huang, J., Li, J., Jia, R., Jiang, N., Kang, L., Ma, X., and Xie, T. (2017). Comparison of dust emissions, transport, and deposition between the taklimakan desert and gobi desert from 2007 to 2011. *Science China Earth Sciences*, 60:1338–1355.
- Chepil, W. (1945). Dynamics of wind erosion: Ii. initiation of soil movement. *Soil Science*, 60(5):397.
- Chepil, W. (1951). Properties of soil which influence wind erosion: Iv. state of dry aggregate structure. *Soil Science*, 72(5):387–402.
- Choorari, O. A., Zawar-Reza, P., and Sturman, A. (2014). The global distribution of mineral dust and its impacts on the climate system: A review. *Atmospheric Research*, 138:152–165.
- Chou, C., Formenti, P., Maille, M., Ausset, P., Helas, G., Harrison, M., and Osborne, S. (2008). Size distribution, shape, and composition of mineral dust aerosols collected during the african monsoon multidisciplinary analysis special observation period

References

- 0: Dust and biomass-burning experiment field campaign in niger, january 2006. *Journal of Geophysical Research: Atmospheres*, 113(D23).
- Christoph, M., Fink, A., Diekkruger, B., Giertz, S., Reichert, B., and Speth, P. (2008). Impetus: Implementing help in the upper ouémé basin. *Water SA*, 34(4):481–489.
- Chuang, P., Duvall, R., Shafer, M., and Schauer, J. (2005). The origin of water soluble particulate iron in the asian atmospheric outflow. *Geophysical Research Letters*, 32(7).
- Chun, Y., Cho, H.-K., Chung, H.-S., and Lee, M. (2000). The yellow-sand phenomenon recorded in the "joseon wangjosillok" (in korean). *Journal of the Korean Meteorological Society*, 36:285–292.
- Chun, Y., Cho, H.-K., Chung, H.-S., and Lee, M. (2008). Historical records of asian dust events (hwangsa) in korea. *Bulletin of the American Meteorological Society*, 89(6):823–828.
- Claquin, T., Schulz, M., and Balkanski, Y. (1999). Modeling the mineralogy of atmospheric dust sources. *Journal of Geophysical Research: Atmospheres*, 104(D18):22243–22256.
- Creysse, M., Dupont, P., El Moctar, A. O., Valance, A., Cantat, I., Jenkins, J. T., Pasini, J. M., and Rasmussen, K. R. (2009). Saltating particles in a turbulent boundary layer: experiment and theory. *Journal of Fluid Mechanics*, 625:47–74.
- Csanady, G. (1963). Turbulent diffusion of heavy particles in the atmosphere. *J. Atmos. Sci.*, 20(3):201–208.
- Cwiertny, D. M., Young, M. A., and Grassian, V. H. (2008). Chemistry and photochemistry of mineral dust aerosol. *Annu. Rev. Phys. Chem.*, 59:27–51.
- Dagsson-Waldhauserova, P., Arnalds, O., and Olafsson, H. (2014). Long-term variability of dust events in iceland (1949–2011). *Atmospheric Chemistry and Physics*, 14(24):13411–13422.
- De Deckker, P., Abed, R. M., De Beer, D., Hinrichs, K.-U., O’Loingsigh, T., Schefuß, E., Stuut, J.-B. W., Tapper, N. J., and Van Der Kaars, S. (2008). Geochemical and microbiological fingerprinting of airborne dust that fell in canberra, australia, in october 2002. *Geochemistry, Geophysics, Geosystems*, 9(12).

References

- DeMott, P. J., Sassen, K., Poellot, M. R., Baumgardner, D., Rogers, D. C., Brooks, S. D., Prenni, A. J., and Kreidenweis, S. M. (2003). African dust aerosols as atmospheric ice nuclei. *Geophysical Research Letters*, 30(14).
- Di Biagio, C., Balkanski, Y., Albani, S., Boucher, O., and Formenti, P. (2020). Direct radiative effect by mineral dust aerosols constrained by new microphysical and spectral optical data. *Geophysical Research Letters*, 47(2):e2019GL086186.
- Di Biagio, C., Banks, J. R., and Gaetani, M. (2021). Dust atmospheric transport over long distances.
- Di Biagio, C., Formenti, P., Balkanski, Y., Caponi, L., Cazaunau, M., Panguì, E., Journet, E., Nowak, S., Andreae, M. O., Kandler, K., et al. (2019). Complex refractive indices and single-scattering albedo of global dust aerosols in the shortwave spectrum and relationship to size and iron content. *Atmos. Chem. Phys.*, 19(24):15503–15531.
- Di Mauro, B., Garzonio, R., Rossini, M., Filippa, G., Pogliotti, P., Galvagno, M., Morra di Cella, U., Migliavacca, M., Baccolo, G., Clemenza, M., et al. (2019). Saharan dust events in the European Alps: role in snowmelt and geochemical characterization. *The Cryosphere*, 13(4):1147–1165.
- Dietze, V., Fricker, M., Goltzsche, M., and Schultz, E. (2006). Air quality measurement in German health resorts—part 1: Methodology and verification. *Gefahrst. Reinhalt. L.*, 66(1/2):45–53.
- Dubovik, O., Holben, B., Eck, T. F., Smirnov, A., Kaufman, Y. J., King, M. D., Tanré, D., and Slutsker, I. (2002). Variability of absorption and optical properties of key aerosol types observed in worldwide locations. *Journal of the atmospheric sciences*, 59(3):590–608.
- Dubovik, O., Sinyuk, A., Lapyonok, T., Holben, B. N., Mishchenko, M., Yang, P., Eck, T. F., Volten, H., Muñoz, O., Veihelmann, B., et al. (2006). Application of spheroid models to account for aerosol particle nonsphericity in remote sensing of desert dust. *Journal of Geophysical Research: Atmospheres*, 111(D11).
- Duce, R. A. and Tindale, N. W. (1991). Atmospheric transport of iron and its deposition in the ocean. *Limnology and oceanography*, 36(8):1715–1726.

- Dufresne, J.-L., Gautier, C., Ricchiazzi, P., and Fouquart, Y. (2002). Longwave scattering effects of mineral aerosols. *Journal of the Atmospheric Sciences*, 59(12):1959–1966.
- Dumont, M., Brun, E., Picard, G., Michou, M., Libois, Q., Petit, J., Geyer, M., Morin, S., and Josse, B. (2014). Contribution of light-absorbing impurities in snow to greenland’s darkening since 2009. *Nature Geoscience*, 7(7):509–512.
- Dumont, M., Tuzet, F., Gascoïn, S., Picard, G., Kutuzov, S., Lafaysse, M., Cluzet, B., Nheili, R., and Painter, T. (2020). Accelerated snow melt in the russian caucasus mountains after the saharan dust outbreak in march 2018. *Journal of Geophysical Research: Earth Surface*, 125(9):e2020JF005641.
- Dupont, S. (2022). On the influence of thermal stratification on emitted dust flux. *J. Geophys. Res. Atmos.*, page e2022JD037364.
- Dupont, S., Alfaro, S., Bergametti, G., and Marticorena, B. (2015). Near-surface dust flux enrichment in small particles during erosion events. *Geophys. Res. Lett.*, 42(6):1992–2000.
- Dupont, S., Rajot, J.-L., Labiadh, M., Bergametti, G., Alfaro, S., Bouet, C., Fernandes, R., Khalfallah, B., Lamaud, E., Marticorena, B., et al. (2018). Aerodynamic parameters over an eroding bare surface: reconciliation of the law of the wall and eddy covariance determinations. *J. Geophys. Res. Atmos.*, 123(9):4490–4508.
- Dupont, S., Rajot, J.-L., Labiadh, M., Bergametti, G., Lamaud, E., Irvine, M., Alfaro, S., Bouet, C., Fernandes, R., Khalfallah, B., et al. (2019). Dissimilarity between dust, heat, and momentum turbulent transports during aeolian soil erosion. *Journal of Geophysical Research: Atmospheres*, 124(2):1064–1089.
- Dupont, S., Rajot, J.-L., Lamaud, E., Bergametti, G., Labiadh, M., Khalfallah, B., Bouet, C., Marticorena, B., and Fernandes, R. (2021). Comparison between eddy-covariance and flux-gradient size-resolved dust fluxes during wind erosion events. *J. Geophys. Res. Atmos.*, 126(13):e2021JD034735.
- Durán, O., Claudin, P., and Andreotti, B. (2011). On aeolian transport: Grain-scale interactions, dynamical mechanisms and scaling laws. *Aeolian Research*, 3(3):243–270.

- Ekström, M., McTainsh, G. H., and Chappell, A. (2004). Australian dust storms: temporal trends and relationships with synoptic pressure distributions (1960–99). *International Journal of Climatology: A Journal of the Royal Meteorological Society*, 24(12):1581–1599.
- Escribano, J., Bozzo, A., Dubuisson, P., Flemming, J., Hogan, R. J., C-Labonnote, L., and Boucher, O. (2019). A benchmark for testing the accuracy and computational cost of shortwave top-of-atmosphere reflectance calculations in clear-sky aerosol-laden atmospheres. *Geosci. Model Dev.*, 12(2):805–827.
- Esworthy, R. and McCarthy, J. E. (2013). The national ambient air quality standards (naaqs) for particulate matter (pm): Epa’s 2006 revisions and associated issues. Library of Congress, Congressional Research Service.
- Etyemezian, V., Nikolich, G., Nickling, W., King, J. S., and Gillies, J. A. (2017). Analysis of an optical gate device for measuring aeolian sand movement. *Aeolian Res.*, 24:65–79.
- Evan, A. T., Flamant, C., Gaetani, M., and Guichard, F. (2016). The past, present and future of african dust. *Nature*, 531(7595):493–495.
- Evans, S., Malyshev, S., Ginoux, P., and Shevliakova, E. (2019). The impacts of the dust radiative effect on vegetation growth in the sahel. *Global Biogeochemical Cycles*, 33(12):1582–1593.
- Fécan, F., Marticorena, B., and Bergametti, G. (1999). Soil-derived dust emissions from semiarid lands: 1. parameterization of the soils moisture effect on the threshold wind friction velocities. *Ann. Geophysicae*, 17:149–157.
- Feng, Y., Wang, H., Rasch, P., Zhang, K., Lin, W., Tang, Q., Xie, S., Hamilton, D., Mahowald, N., and Yu, H. (2022). Global dust cycle and direct radiative effect in e3sm version 1: Impact of increasing model resolution. *Journal of Advances in Modeling Earth Systems*, 14(7):e2021MS002909.
- Fernandes, R., Dupont, S., and Lamaud, E. (2019). Investigating the role of deposition on the size distribution of near-surface dust flux during erosion events. *Aeolian Res.*, 37(November 2018):32–43.

- Field, J. and Pelletier, J. (2018). Controls on the aerodynamic roughness length and the grain-size dependence of aeolian sediment transport. *Earth Surf. Proc. Land.*, 43(12):2616–2626.
- Finlayson-Pitts, B. J. and Pitts Jr, J. N. (1999). *Chemistry of the upper and lower atmosphere: theory, experiments, and applications*. Elsevier.
- Flanner, M. G., Arnheim, J. B., Cook, J. M., Dang, C., He, C., Huang, X., Singh, D., Skiles, S. M., Whicker, C. A., and Zender, C. S. (2021). Snicar-adv3: a community tool for modeling spectral snow albedo. *Geoscientific Model Development*, 14(12):7673–7704.
- Fletcher, B. (1976a). The erosion of dust by an airflow. *Journal of Physics D: Applied Physics*, 9(6):913.
- Fletcher, B. (1976b). The incipient motion of granular materials. *Journal of Physics D: Applied Physics*, 9(17):2471.
- Foken, T., Aubinet, M., and Leuning, R. (2011). The eddy covariance method. In *Eddy covariance: a practical guide to measurement and data analysis*, pages 1–19. Springer.
- Foken, T. and Napo, C. (2008). *Micrometeorology*. Springer, Heidelberg, 2 edition.
- Formenti, P., Rajot, J.-L., Desboeufs, K., Caquineau, S., Chevaillier, S., Nava, S., Gaudichet, A., Journet, E., Triquet, S., Alfaro, S., et al. (2008). Regional variability of the composition of mineral dust from western africa: Results from the amma sop0/dabex and dodo field campaigns. *Journal of Geophysical Research: Atmospheres*, 113(D23).
- Formenti, P., Rajot, J.-L., Desboeufs, K., Saïd, F., Grand, N., Chevaillier, S., and Schmechtig, C. (2011a). Airborne observations of mineral dust over western africa in the summer monsoon season: spatial and vertical variability of physico-chemical and optical properties. *Atmospheric Chemistry and Physics*, 11(13):6387–6410.
- Formenti, P., Schütz, L., Balkanski, Y., Desboeufs, K., Ebert, M., Kandler, K., Petzold, A., Scheuven, D., Weinbruch, S., and Zhang, D. (2011b). Recent progress in understanding physical and chemical properties of african and asian mineral dust. *Atmospheric Chemistry and Physics*, 11(16):8231–8256.

- Forster, P., Storelvmo, T., Armour, K., Collins, W., Dufresne, J.-L., Frame, D., Lunt, D., Mauritsen, T., Palmer, M., Watanabe, M., et al. (2021). The earth's energy budget, climate feedbacks, and climate sensitivity.
- FRAGMENT team (2023). Timelapse 6 sept 2019 l'bour.
- Fratini, G., Ciccioli, P., Febo, A., Forgione, A., and Valentini, R. (2007). Size-segregated fluxes of mineral dust from a desert area of northern China by eddy covariance. *Atmos. Chem. Phys.*, 7(11):2839–2854.
- Froyd, K. D., Yu, P., Schill, G. P., Brock, C. A., Kupc, A., Williamson, C. J., Jensen, E. J., Ray, E., Rosenlof, K. H., Bian, H., et al. (2022). Dominant role of mineral dust in cirrus cloud formation revealed by global-scale measurements. *Nature Geoscience*, 15(3):177–183.
- Garcia-Carreras, L., Parker, D., Marsham, J., Rosenberg, P., Brooks, I., Lock, A., Marengo, F., McQuaid, J., and Hobby, M. (2015). The turbulent structure and diurnal growth of the saharan atmospheric boundary layer. *Journal of the Atmospheric Sciences*, 72(2):693–713.
- García-Pando, C. P., Thomson, M. C., Stanton, M. C., Diggle, P. J., Hopson, T., Pandya, R., Miller, R. L., and Hugonnet, S. (2014). Meningitis and climate: from science to practice. *Earth Perspectives*, 1:1–15.
- Gassó, S. and Torres, O. (2019). Temporal characterization of dust activity in the central patagonia desert (years 1964–2017). *Journal of Geophysical Research: Atmospheres*, 124(6):3417–3434.
- Gatz, D. F., Barnard, W. R., and Stensland, G. J. (1986). The role of alkaline materials in precipitation chemistry: A brief review of the issues. *Water, Air, and Soil Pollution*, 30:245–251.
- Ge, J. M., Liu, H., Huang, J., and Fu, Q. (2016). Taklimakan desert nocturnal low-level jet: climatology and dust activity. *Atmospheric Chemistry and Physics*, 16(12):7773–7783.
- Gillette, D. and Morales, C. (1979). Environmental factors affecting dust emission by wind erosion. *Saharan dust*, pages 71–94.

References

- Gillette, D. A. (1974a). On the production of soil wind erosion aerosols having the potential for long range transport. *J. Geophys. Res. Atmos.*, 8:735–744.
- Gillette, D. A. (1974b). On the production of soil wind erosion having the potential for long range transport. *J. Rech. Atmos.*, 8:734–744.
- Gillette, D. A. (1977). Fine particulate emissions due to wind erosion. *Trans. Am. Soc. Agricultural Engrs.*, 20:890–897.
- Gillette, D. A., Blifford Jr., I. H., and Fenster, C. R. (1972). Measurements of aerosol size distributions and vertical fluxes of aerosols on land subject to wind erosion. *J. Appl. Meteorol.*, pages 977–987.
- Gillette, D. A., Blifford Jr, I. H., and Fryrear, D. (1974). The influence of wind velocity on the size distributions of aerosols generated by the wind erosion of soils. *Journal of Geophysical Research*, 79(27):4068–4075.
- Gillette, D. A. and Chen, W. (2001). Particle production and aeolian transport from a “supply-limited” source area in the chihuahuan desert, new mexico, united states. *Journal of Geophysical Research: Atmospheres*, 106(D6):5267–5278.
- Gillette, D. A., Marticorena, B., and Bergametti, G. (1998). Change in the aerodynamic roughness height by saltating grains: Experimental assessment, test of theory, and operational parameterization. *J. Geophys. Res. Atmos.*, 103(D6):6203–6209.
- Gillette, D. A. and Passi, R. (1988). Modeling dust emission caused by wind erosion. *J. Geophys. Res. Atmos.*, 93(D11):14233–14242.
- Gillies, J. and Berkofsky, L. (2004). Eolian suspension above the saltation layer, the concentration profile. *Journal of sedimentary research*, 74(2):176–183.
- Gillies, J. A., Etyemezian, V., Nikolich, G., Nickling, W. G., and Kok, J. F. (2018). Changes in the saltation flux following a step-change in macro-roughness. *Earth Surface Processes and Landforms*, 43(9):1871–1884.
- Ginoux, P., Prospero, J. M., Gill, T. E., Hsu, N. C., and Zhao, M. (2012). Global-scale attribution of anthropogenic and natural dust sources and their emission rates based on modis deep blue aerosol products. *Reviews of Geophysics*, 50(3).

- Giorgi, F. (1986). A particle dry-deposition parameterization scheme for use in tracer transport models. *Journal of Geophysical Research: Atmospheres*, 91(D9):9794–9806.
- Gkikas, A., Proestakis, E., Amiridis, V., Kazadzis, S., Di Tomaso, E., Marinou, E., Hatzianastassiou, N., Kok, J. F., and García-Pando, C. P. (2022). Quantification of the dust optical depth across spatiotemporal scales with the midas global dataset (2003–2017). *Atmospheric Chemistry and Physics*, 22(5):3553–3578.
- Gliß, J., Mortier, A., Schulz, M., Andrews, E., Balkanski, Y., Bauer, S. E., Benedictow, A. M., Bian, H., Checa-Garcia, R., Chin, M., et al. (2021). Aerocom phase iii multi-model evaluation of the aerosol life cycle and optical properties using ground-and space-based remote sensing as well as surface in situ observations. *Atmospheric Chemistry and Physics*, 21(1):87–128.
- Gomes, L., Arrue, J., Lopez, M., Sterk, G., Richard, D., Gracia, R., Sabre, M., Gaudichet, A., and Frangi, J. (2003a). Wind erosion in a semiarid agricultural area of spain: the welsons project. *Catena*, 52(3-4):235–256.
- Gomes, L., Arrúe, J. L., López, M. V., Sterk, G., Richard, D., Gracia, R., Sabre, M., Gaudichet, A., and Frangi, J. P. (2003b). Wind erosion in a semiarid agricultural area of Spain: The WELSONS project. *Catena*, 52(3-4):235–256.
- Gomes, L., Bergametti, G., Coudé-Gaussen, G., and Rognon, P. (1990). Submicron desert dusts: A sandblasting process. *Journal of Geophysical Research: Atmospheres*, 95(D9):13927–13935.
- Gomes, L., Rajot, J. L., Alfaro, S. C., and Gaudichet, A. (2003c). Validation of a dust production model from measurements performed in semi-arid agricultural areas of Spain and Niger. *Catena*, 52(3-4):257–271.
- González-Flórez, C., Klose, M., Alastuey, A., Dupont, S., Escribano, J., Etyemezian, V., Gonzalez-Romero, A., Huang, Y., Kandler, K., Nikolich, G., et al. (2023). Insights into the size-resolved dust emission from field measurements in the moroccan sahara. *Atmospheric Chemistry and Physics*, 23(12):7177–7212.
- González-Romero, A., González-Florez, C., Panta, A., Yus-Díez, J., Reche, C., Córdoba, P., Alastuey, A., Kandler, K., Klose, M., Baldo, C., et al. (2023). Variability in grain size, mineralogy, and mode of occurrence of fe in surface sediments of

References

- preferential dust-source inland drainage basins: The case of the lower drâa valley, s morocco. *EGUsphere*, 2023:1–32.
- Goossens, D. (2004). Effect of soil crusting on the emission and transport of wind-eroded sediment: field measurements on loamy sandy soil. *Geomorphology*, 58(1-4):145–160.
- Goossens, D., Nolet, C., Etyemezian, V., Duarte-Campos, L., Bakker, G., and Riksen, M. (2018). Field testing, comparison, and discussion of five aeolian sand transport measuring devices operating on different measuring principles. *Aeolian Res.*, 32:1–13.
- Goossens, D. and Rajot, J. L. (2008). Techniques to measure the dry aeolian deposition of dust in arid and semi-arid landscapes: a comparative study in west niger. *Earth Surface Processes and Landforms: The Journal of the British Geomorphological Research Group*, 33(2):178–195.
- Gorgas, J., Cardiel, N., and J., Z. (2011). *Estadística básica para estudiantes de ciencias*. Departamento de Astrofísica y Ciencias de la Atmósfera, Universidad Complutense de Madrid.
- Goudie, A. S. (2014). Desert dust and human health disorders. *Environment international*, 63:101–113.
- Greeley, R., Balme, M. R., Iversen, J. D., Metzger, S., Mickelson, R., Phoreman, J., and White, B. (2003). Martian dust devils: Laboratory simulations of particle threshold. *Journal of Geophysical Research: Planets*, 108(E5).
- Greeley, R., Blumberg, D. G., and Williams, S. H. (1996). Field measurements of the flux and speed of wind-blown sand. *Sedimentology*, 43(1):41–52.
- Greeley, R. and Iversen, J. D. (1985). *Wind as a geological process: on Earth, Mars, Venus and Titan*. Number 4. Cambridge University Press.
- Griffin, D. W., Kellogg, C. A., and Shinn, E. A. (2001). Dust in the wind: long range transport of dust in the atmosphere and its implications for global public and ecosystem health. *Global Change and Human Health*, 2:20–33.
- Güsten, H., Heinrich, G., Mönnich, E., Sprung, D., Weppner, J., El-Din, M. R. E., Ahmed, D. M., Hassan, G. K., et al. (1996). On-line measurements of ozone surface

- fluxes: Part ii. surface-level ozone fluxes onto the sahara desert. *Atmospheric Environment*, 30(6):911–918.
- Hamidi, M., Kavianpour, M. R., and Shao, Y. (2013). Synoptic analysis of dust storms in the middle east. *Asia-Pacific Journal of atmospheric sciences*, 49:279–286.
- Hamlin, L., Green, R., Mouroulis, P., Eastwood, M., Wilson, D., Dudik, M., and Paine, C. (2011). Imaging spectrometer science measurements for terrestrial ecology: Aviris and new developments. In *2011 Aerospace conference*, pages 1–7. IEEE.
- Hand, J. L., Gill, T., and Schichtel, B. (2017). Spatial and seasonal variability in fine mineral dust and coarse aerosol mass at remote sites across the united states. *Journal of Geophysical Research: Atmospheres*, 122(5):3080–3097.
- Hansen, J., Sato, M., Ruedy, R., Nazarenko, L., Lacis, A., Schmidt, G., Russell, G., Aleinov, I., Bauer, M., Bauer, S., et al. (2005). Efficacy of climate forcings. *Journal of geophysical research: atmospheres*, 110(D18).
- Harrison, A. D., Lever, K., Sanchez-Marroquin, A., Holden, M. A., Whale, T. F., Tarn, M. D., McQuaid, J. B., and Murray, B. J. (2019). The ice-nucleating ability of quartz immersed in water and its atmospheric importance compared to k-feldspar. *Atmospheric Chemistry and Physics*, 19(17):11343–11361.
- Hawker, R. E., Miltenberger, A. K., Wilkinson, J. M., Hill, A. A., Shipway, B. J., Cui, Z., Cotton, R. J., Carslaw, K. S., Field, P. R., and Murray, B. J. (2021). The temperature dependence of ice-nucleating particle concentrations affects the radiative properties of tropical convective cloud systems. *Atmospheric Chemistry and Physics*, 21(7):5439–5461.
- Heald, C., Ridley, D., Kroll, J., Barrett, S., Cady-Pereira, K., Alvarado, M., and Holmes, C. (2014). Contrasting the direct radiative effect and direct radiative forcing of aerosols. *Atmospheric Chemistry and Physics*, 14(11):5513–5527.
- Heintzenberg, J. (1989). Fine particles in the global troposphere a review. *Tellus B: Chemical and Physical Meteorology*, 41(2):149–160.
- Heintzenberg, J. (2009). The samum-1 experiment over southern morocco: overview and introduction. *Tellus B: Chemical and Physical Meteorology*, 61(1):2–11.

References

- Hersbach, H. (2019). Global reanalysis: goodbye era-interim, hello era5. *ECMWF newsletter*, 159:17.
- Highwood, E. J. and Ryder, C. L. (2014). Radiative effects of dust. *Mineral dust: A key player in the earth system*, pages 267–286.
- Hinds, W. C. (1999). *Aerosol technology: properties, behavior, and measurement of airborne particles*. Wiley-Interscience.
- Högström, U. (1988). Non-dimensional wind and temperature profiles in the atmospheric surface layer: A re-evaluation. *Bound. Lay. Meteorol.*, 42(1-2):55–78.
- Houser, C. A. and Nickling, W. G. (2001). The factors influencing the abrasion efficiency of saltating grains on a clay-crustated playa. *Earth Surface Processes and Landforms: The Journal of the British Geomorphological Research Group*, 26(5):491–505.
- Huang, J., Li, Y., Fu, C., Chen, F., Fu, Q., Dai, A., Shinoda, M., Ma, Z., Guo, W., Li, Z., et al. (2017). Dryland climate change: Recent progress and challenges. *Reviews of Geophysics*, 55(3):719–778.
- Huang, Y., Adebisi, A. A., Formenti, P., and Kok, J. F. (2021). Linking the different diameter types of aspherical desert dust indicates that models underestimate coarse dust emission. *Geophys. Res. Lett.*, 48(6):e2020GL092054.
- Huang, Y., Kok, J. F., Kandler, K., Lindqvist, H., Nousiainen, T., Sakai, T., Adebisi, A., and Jokinen, O. (2020). Climate models and remote sensing retrievals neglect substantial desert dust asphericity. *Geophysical Research Letters*, 47(6):e2019GL086592.
- Huang, Y., Kok, J. F., Martin, R. L., Swet, N., Katra, I., Gill, T. E., Reynolds, R. L., and Freire, L. S. (2019). Fine dust emissions from active sands at coastal oceanic dunes, California. *Atmospheric Chemistry and Physics*, 19(5):2947–2964.
- Huneeus, N., Schulz, M., Balkanski, Y., Griesfeller, J., Prospero, J., Kinne, S., Bauer, S., Boucher, O., Chin, M., Dentener, F., et al. (2011). Global dust model intercomparison in aerosol phase I. *Atmospheric Chemistry and Physics*, 11(15):7781–7816.

- Hussain, A., Mir, H., and Afzal, M. (2005). Analysis of dust storms frequency over Pakistan during 1961–2000. *Pakistan Journal of Meteorology*, 2(3).
- Ishizuka, M., Mikami, M., Leys, J. F., Shao, Y., Yamada, Y., and Heidenreich, S. (2014). Power law relation between size-resolved vertical dust flux and friction velocity measured in a fallow wheat field. *Aeolian Res.*, 12:87–99.
- Ito, A., Ye, Y., Baldo, C., and Shi, Z. (2021). Ocean fertilization by pyrogenic aerosol iron. *npj Climate and Atmospheric Science*, 4(1):30.
- Iversen, J., Pollack, J. B., Greeley, R., and White, B. R. (1976). Saltation threshold on Mars: The effect of interparticle force, surface roughness, and low atmospheric density. *Icarus*, 29(3):381–393.
- Iversen, J. D. and White, B. R. (1982). Saltation threshold on Earth, Mars and Venus. *Sedimentology*, 29(1):111–119.
- Jakobs, C. L., Reijmer, C. H., van den Broeke, M. R., Van de Berg, W., and Van Wessem, J. (2021). Spatial variability of the snowmelt-albedo feedback in Antarctica. *Journal of Geophysical Research: Earth Surface*, 126(2):e2020JF005696.
- Jeong, G. Y., Kim, J. Y., Seo, J., Kim, G., Jin, H., and Chun, Y. (2014). Long-range transport of giant particles in Asian dust identified by physical, mineralogical, and meteorological analysis. *Atmospheric Chemistry and Physics*, 14(1):505–521.
- Jia, G., Shevliakova, E., Artaxo, P., Noblet-Ducoudré, N. D., Houghton, R., House, J., Kitajima, K., Lennard, C., Popp, A., Sirin, A., Sukumar, R., and Verchot, L. (2019). Land–climate interactions. *Climate Change and Land: an IPCC special report on climate change, desertification, land degradation, sustainable land management, food security, and greenhouse gas fluxes in terrestrial ecosystems [Shukla, P.R., J. Skea, E.C. Buendia, V. Masson-Delmotte, H.-O. Pörtner, D.C. Roberts, P. Zhai, R. Slade, S. Connors, R. Diemen, M. Ferrat, E. Haughey, S. Luz, S. Neogi, M. Pathak, J. Petzold, J. Portugal Pereira, E.H. P. Vyas, K. Kissick, M. Belkacemi, and J. Malley (eds.)]*.
- Jickells, T. and Moore, C. M. (2015). The Importance of Atmospheric Deposition for Ocean Productivity. *Annu. Rev. Ecol. Evol. S.*, 46:481–501.

References

- Jin, Q., Wei, J., Lau, W. K., Pu, B., and Wang, C. (2021). Interactions of asian mineral dust with indian summer monsoon: Recent advances and challenges. *Earth-Science Reviews*, 215:103562.
- Johnson, M., Meskhidze, N., Kiliyanpilakkil, V. P., and Gasso, S. (2011). Understanding the transport of patagonian dust and its influence on marine biological activity in the south atlantic ocean. *Atmospheric Chemistry and Physics*, 11(6):2487–2502.
- Journet, E., Balkanski, Y., and Harrison, S. P. (2014). A new data set of soil mineralogy for dust-cycle modeling. *Atmospheric Chemistry and Physics*, 14(8):3801–3816.
- Junge, C. E. (1963). *Air Chemistry and Radioactivity*. Academic Press.
- Kaaden, N., Massling, A., Schladitz, A., Müller, T., Kandler, K., Schütz, L., Weinzierl, B., Petzold, A., Tesche, M., Leinert, S., et al. (2009). State of mixing, shape factor, number size distribution, and hygroscopic growth of the saharan anthropogenic and mineral dust aerosol at tinou, morocco. *Tellus B*, 61(1):51–63.
- Kaimal, J. C. and Finnigan, J. J. (1994). *Atmospheric boundary layer flows: their structure and measurement*. Oxford university press.
- Kandler, K., Benker, N., Bundke, U., Cuevas, E., Ebert, M., Knippertz, P., Rodríguez, S., Schütz, L., and Weinbruch, S. (2007). Chemical composition and complex refractive index of saharan mineral dust at izaña, tenerife (spain) derived by electron microscopy. *Atmospheric Environment*, 41(37):8058–8074.
- Kandler, K., Lieke, K., Benker, N., Emmel, C., Küpper, M., Müller-Ebert, D., Ebert, M., Scheuvs, D., Schladitz, A., Schütz, L., et al. (2011). Electron microscopy of particles collected at praia, cape verde, during the saharan mineral dust experiment: particle chemistry, shape, mixing state and complex refractive index. *Tellus B: Chemical and Physical Meteorology*, 63(4):475–496.
- Kandler, K. and Scheuvs, D. (2019). Asian and saharan dust from a chemical/mineralogical point of view: differences and similarities from bulk and single particle measurements. In *E3S Web of Conferences*, volume 99, page 03001. EDP Sciences.

- Kandler, K., Schneiders, K., Heuser, J., Waza, A., Aryasree, S., Althausen, D., Hofer, J., Abdullaev, S. F., and Makhmudov, A. N. (2020). Differences and similarities of central asian, african, and arctic dust composition from a single particle perspective. *Atmosphere*, 11(3):269.
- Kandler, K., Schütz, L., Deutscher, C., Ebert, M., Hofmann, H., Jäckel, S., Jaenicke, R., Knippertz, P., Lieke, K., Massling, A., et al. (2009). Size distribution, mass concentration, chemical and mineralogical composition and derived optical parameters of the boundary layer aerosol at tinfou, morocco, during samum 2006. *Tellus B*, 61(1):32–50.
- Karanasiou, A., Moreno, N., Moreno, T., Viana, M., de Leeuw, F., and Querol, X. (2012). Health effects from sahara dust episodes in europe: literature review and research gaps. *Environ. Int.*, 47:107–114.
- Karydis, V., Kumar, P., Barahona, D., Sokolik, I., and Nenes, A. (2011). On the effect of dust particles on global cloud condensation nuclei and cloud droplet number. *Journal of Geophysical Research: Atmospheres*, 116(D23).
- Kaspari, S., Painter, T. H., Gysel, M., Skiles, S., and Schwikowski, M. (2014). Seasonal and elevational variations of black carbon and dust in snow and ice in the solu-khumbu, nepal and estimated radiative forcings. *Atmospheric chemistry and physics*, 14(15):8089–8103.
- Kelly, J. T., Chuang, C. C., and Wexler, A. S. (2007). Influence of dust composition on cloud droplet formation. *Atmospheric Environment*, 41(14):2904–2916.
- Khalfallah, B., Bouet, C., Labiadh, M. T., Alfaro, S. C., Bergametti, G., Marticorena, B., Lafon, S., Chevaillier, S., Féron, A., Hease, P., Henry des Tureaux, T., Sekrafi, S., Zapf, P., and Rajot, J. L. (2020). Influence of Atmospheric Stability on the Size Distribution of the Vertical Dust Flux Measured in Eroding Conditions Over a Flat Bare Sandy Field. *J. Geophys. Res. Atmos.*, 125(4):e2019JD031185.
- Kinne, S., Schulz, M., Textor, C., Guibert, S., Balkanski, Y., Bauer, S. E., Berntsen, T., Berglen, T., Boucher, O., Chin, M., et al. (2006). An aerocom initial assessment—optical properties in aerosol component modules of global models. *Atmospheric Chemistry and Physics*, 6(7):1815–1834.

References

- Klose, M., Gill, T. E., Etyemezian, V., Nikolich, G., Ghodsi Zadeh, Z., Webb, N. P., and Van Pelt, R. S. (2019). Dust emission from crusted surfaces: Insights from field measurements and modelling. *Aeolian Res.*, 40:1–14.
- Klose, M., Jorba, O., Gonçalves Ageitos, M., Escribano, J., Dawson, M. L., Obiso, V., Di Tomaso, E., Basart, S., Montané Pinto, G., Macchia, F., et al. (2021). Mineral dust cycle in the multiscale online nonhydrostatic atmosphere chemistry model (monarch) version 2.0. *Geosci. Model Dev.*, 14(10):6403–6444.
- Klose, M. and Shao, Y. (2012). Stochastic parameterization of dust emission and application to convective atmospheric conditions. *Atmospheric Chemistry and Physics*, 12(16):7309–7320.
- Klose, M. and Shao, Y. (2013). Large-eddy simulation of turbulent dust emission. *Aeolian Research*, 8:49–58.
- Klose, M., Shao, Y., Li, X., Zhang, H., Ishizuka, M., Mikami, M., and Leys, J. F. (2014). Further development of a parameterization for convective turbulent dust emission and evaluation based on field observations. *Journal of Geophysical Research: Atmospheres*, 119(17):10441–10457.
- Knippertz, P. and Stuut, J.-B. (2014). *Mineral Dust, A Key Player in the Earth System*. Springer, Dordrecht Heidelberg New York London.
- Knippertz, P. and Todd, M. C. (2012). Mineral dust aerosols over the sahara: Meteorological controls on emission and transport and implications for modeling. *Reviews of Geophysics*, 50(1).
- Kok, J., Mahowald, N., Fratini, G., Gillies, J., Ishizuka, M., Leys, J., Mikami, M., Park, M.-S., Park, S.-U., Van Pelt, R., et al. (2014). An improved dust emission model—part 1: Model description and comparison against measurements. *Atmospheric Chemistry and Physics*, 14(23):13023–13041.
- Kok, J. F. (2011a). A scaling theory for the size distribution of emitted dust aerosols suggests climate models underestimate the size of the global dust cycle. *Earth, Atmospheric, and Planetary Sciences*, 108(3):1016–1021.
- Kok, J. F. (2011b). Does the size distribution of mineral dust aerosols depend on the wind speed at emission? *Atmos. Chem. Phys.*, 11(19):10149–10156.

- Kok, J. F., Adebisi, A. A., Albani, S., Balkanski, Y., Checa-Garcia, R., Chin, M., Colarco, P. R., Hamilton, D. S., Huang, Y., Ito, A., et al. (2021a). Contribution of the world's main dust source regions to the global cycle of desert dust. *Atmospheric Chemistry and Physics*, 21(10):8169–8193.
- Kok, J. F., Adebisi, A. A., Albani, S., Balkanski, Y., Checa-Garcia, R., Chin, M., Colarco, P. R., Hamilton, D. S., Huang, Y., Ito, A., et al. (2021b). Improved representation of the global dust cycle using observational constraints on dust properties and abundance. *Atmos. Chem. Phys.*, 21(10):8127–8167.
- Kok, J. F., Parteli, E. J., Michaels, T. I., and Karam, D. B. (2012). The physics of wind-blown sand and dust. *Reports on progress in Physics*, 75(10):106901.
- Kok, J. F., Ridley, D. A., Zhou, Q., Miller, R. L., Zhao, C., Heald, C. L., Ward, D. S., Albani, S., and Haustein, K. (2017). Smaller desert dust cooling effect estimated from analysis of dust size and abundance. *Nat. Geosci.*, 10(4):274–278.
- Kok, J. F., Storelvmo, T., Karydis, V. A., Adebisi, A. A., Mahowald, N. M., Evan, A. T., He, C., and Leung, D. M. (2023). Mineral dust aerosol impacts on global climate and climate change. *Nature Reviews Earth and Environment*, pages 1–16.
- Kolmogorov, A. (1941). On the logarithmically normal distribution law of particle sizes at the subdivision. *Doklady Akademii Nauk SSSR*, 31(2):99–101.
- Kong, S., Sato, K., and Bi, L. (2022). Lidar ratio–depolarization ratio relations of atmospheric dust aerosols: The super-spheroid model and high spectral resolution lidar observations. *Journal of Geophysical Research: Atmospheres*, 127(4):e2021JD035629.
- Kouznetsov, R. and Sofiev, M. (2012). A methodology for evaluation of vertical dispersion and dry deposition of atmospheric aerosols. *Journal of Geophysical Research: Atmospheres*, 117(D1).
- Kramm, G., Amaya, D. J., Foken, T., et al. (2013). Hans a. panofsky's integral similarity function—at fifty. *Atmospheric and Climate Sciences*, 3(4):581–594.
- Kruse, F. A., Boardman, J. W., and Huntington, J. F. (2003). Comparison of airborne hyperspectral data and eo-1 hyperion for mineral mapping. *IEEE transactions on Geoscience and Remote Sensing*, 41(6):1388–1400.

- Kulkarni, P., Baron, P. A., and Willeke, K. (2011). *Aerosol measurement: principles, techniques, and applications*. John Wiley & Sons.
- Kumar, P., Sokolik, I., and Nenes, A. (2011). Cloud condensation nuclei activity and droplet activation kinetics of wet processed regional dust samples and minerals. *Atmospheric Chemistry and Physics*, 11(16):8661–8676.
- Lamaud, E., Chapuis, A., Fontan, J., and Serie, E. (1994). Measurements and parameterization of aerosol dry deposition in a semi-arid area. *Atmospheric Environment*, 28(15):2461–2471.
- Laskin, A., Iedema, M. J., Ichkovich, A., Graber, E. R., Taraniuk, I., and Rudich, Y. (2005). Direct observation of completely processed calcium carbonate dust particles. *Faraday Discussions*, 130:453–468.
- Leung, D. M., Kok, J. F., Li, L., Okin, G. S., Prigent, C., Klose, M., Pérez García-Pando, C., Menut, L., Mahowald, N. M., Lawrence, D. M., et al. (2023). A new process-based and scale-aware desert dust emission scheme for global climate models—part i: Description and evaluation against inverse modeling emissions. *Atmospheric Chemistry and Physics*, 23(11):6487–6523.
- Levin, Z. and Ganor, E. (1996). The effects of desert particles on cloud and rain formation in the eastern mediterranean. *The impact of Desert dust across the Mediterranean*, pages 77–86.
- Levin, Z., Teller, A., Ganor, E., and Yin, Y. (2005). On the interactions of mineral dust, sea-salt particles, and clouds: A measurement and modeling study from the mediterranean israeli dust experiment campaign. *Journal of Geophysical Research: Atmospheres*, 110(D20).
- Leys, J. and Raupach, M. (1991). Soil flux measurements using a portable wind erosion tunnel. *Soil Research*, 29(4):533–552.
- Li, F., Ginoux, P., and Ramaswamy, V. (2010). Transport of patagonian dust to antarctica. *Journal of Geophysical Research: Atmospheres*, 115(D18).
- Li, L., Mahowald, N. M., Miller, R. L., Pérez García-Pando, C., Klose, M., Hamilton, D. S., Gonçalves Ageitos, M., Ginoux, P., Balkanski, Y., Green, R. O., et al. (2021).

- Quantifying the range of the dust direct radiative effect due to source mineralogy uncertainty. *Atmospheric chemistry and physics*, 21(5):3973–4005.
- Li, X. and Bo, T. (2019). Statistics and spectra of turbulence under different roughness in the near-neutral atmospheric surface layer. *Earth Surface Processes and Landforms*, 44(7):1460–1470.
- Li-Jones, X., Maring, H., and Prospero, J. (1998). Effect of relative humidity on light scattering by mineral dust aerosol as measured in the marine boundary layer over the tropical atlantic ocean. *Journal of Geophysical Research: Atmospheres*, 103(D23):31113–31121.
- Liao, H. and Seinfeld, J. (1998). Radiative forcing by mineral dust aerosols: sensitivity to key variables. *Journal of Geophysical Research: Atmospheres*, 103(D24):31637–31645.
- Liou, K., Takano, Y., He, C., Yang, P., Leung, L., Gu, Y., and Lee, W. (2014). Stochastic parameterization for light absorption by internally mixed bc/dust in snow grains for application to climate models. *Journal of Geophysical Research: Atmospheres*, 119(12):7616–7632.
- Loosmore, G. A. and Hunt, J. R. (2000). Dust resuspension without saltation. *Journal of Geophysical Research: Atmospheres*, 105(D16):20663–20671.
- Loye-Pilot, M., Martin, J., and Morelli, J. (1986). Influence of saharan dust on the rain acidity and atmospheric input to the mediterranean. *Nature*, 321(6068):427–428.
- Lu, H. and Shao, Y. (1999). A new model for dust emission by saltation bombardment. *Journal of Geophysical Research: Atmospheres*, 104(D14):16827–16842.
- Luo, C. and Gao, Y. (2010). Aeolian iron mobilisation by dust–acid interactions and their implications for soluble iron deposition to the ocean: a test involving potential anthropogenic organic acidic species. *Environmental Chemistry*, 7(2):153–161.
- Macpherson, T., Nickling, W. G., Gillies, J. A., and Etyemezian, V. (2008). Dust emissions from undisturbed and disturbed supply-limited desert surfaces. *Journal of Geophysical Research: Earth Surface*, 113(F2).

References

- Mahowald, N., Albani, S., Kok, J. F., Engelstaeder, S., Scanza, R., Ward, D. S., and Flanner, M. G. (2014). The size distribution of desert dust aerosols and its impact on the earth system. *Aeolian Research*, 15:53–71.
- Mahowald, N. M., Kloster, S., Engelstaedter, S., Moore, J. K., Mukhopadhyay, S., McConnell, J. R., Albani, S., Doney, S. C., Bhattacharya, A., Curran, M., et al. (2010). Observed 20th century desert dust variability: impact on climate and biogeochemistry. *Atmospheric Chemistry and Physics*, 10(22):10875–10893.
- Mahowald, N. M., Rivera, G. D. R., and Luo, C. (2004). Comment on “relative importance of climate and land use in determining present and future global soil dust emission” by i. tejen et al. *Geophysical Research Letters*, 31(24).
- Mallios, S. A., Drakaki, E., and Amiridis, V. (2020). Effects of dust particle sphericity and orientation on their gravitational settling in the earth’s atmosphere. *Journal of Aerosol Science*, 150:105634.
- Marticorena, B. (2014). Dust production mechanisms. *Mineral dust: A key player in the earth system*, pages 93–120.
- Marticorena, B. and Bergametti, G. (1995). Modeling the atmospheric dust cycle: 1. design of a soil-derived dust emission scheme. *Journal of geophysical research: atmospheres*, 100(D8):16415–16430.
- Marticorena, B., Chatenet, B., Rajot, J.-L., Bergametti, G., Deroubaix, A., Vincent, J., Kouoi, A., Schmechtig, C., Coulibaly, M., Diallo, A., et al. (2017). Mineral dust over west and central sahel: Seasonal patterns of dry and wet deposition fluxes from a pluriannual sampling (2006–2012). *Journal of Geophysical Research: Atmospheres*, 122(2):1338–1364.
- Marticorena, B., Kardous, M., Bergametti, G., Callot, Y., Chazette, P., Khatteli, H., Le Hégarat-Masclé, S., Maillé, M., Rajot, J.-L., Vidal-Madjar, D., and Zribi, M. (2006). Surface and aerodynamic roughness in arid and semiarid areas and their relation to radar backscatter coefficient. *J. Geophys. Res.*, 111:1–26.
- Martin, J. H., Gordon, M., and Fitzwater, S. E. (1991). The case for iron. *Limnology and Oceanography*, 36(8):1793–1802.

- Martin, R. L. and Kok, J. F. (2017a). Equal susceptibility and size-selective mobility in aeolian saltation. *arXiv preprint arXiv:1707.09964*.
- Martin, R. L. and Kok, J. F. (2017b). Wind-invariant saltation heights imply linear scaling of aeolian saltation flux with shear stress. *Science advances*, 3(6):e1602569.
- Matsuki, A., Iwasaka, Y., Shi, G.-Y., Chen, H.-B., Osada, K., Zhang, D., Kido, M., Inomata, Y., Kim, Y.-S., Trochkin, D., et al. (2005). Heterogeneous sulfate formation on dust surface and its dependence on mineralogy: balloon-borne observations from balloon-borne measurements in the surface atmosphere of beijing, china. *Water, Air, & Soil Pollution: Focus*, 5:101–132.
- McKee, E. D. (1983). Eolian sand bodies of the world. *Developments in Sedimentology*, 38:1–25.
- McKenna-Neuman, C. and Nickling, W. (1989). A theoretical and wind tunnel investigation of the effect of capillary water on the entrainment of sediment by wind. *Canadian Journal of Soil Science*, 69(1):79–96.
- McTainsh, G., Lynch, A., and Burgess, R. (1990). Wind erosion in eastern australia. *Soil Research*, 28(2):323–339.
- Meinander, O., Dagsson-Waldhauserova, P., Amosov, P., Aseyeva, E., Atkins, C., Baklanov, A., Baldo, C., Barr, S. L., Barzycka, B., Benning, L. G., et al. (2022). Newly identified climatically and environmentally significant high-latitude dust sources. *Atmospheric Chemistry and Physics*, 22(17):11889–11930.
- Meinander, O., Dagsson-Waldhauserova, P., and Arnalds, O. (2016). Icelandic volcanic dust can have a significant influence on the cryosphere in greenland and elsewhere. *Polar Research*, 35(1):31313.
- Meng, J., Huang, Y., Leung, D. M., Li, L., Adebisi, A. A., Ryder, C. L., Mahowald, N. M., and Kok, J. F. (2022). Improved parameterization for the size distribution of emitted dust aerosols reduces model underestimation of super coarse dust. *Geophys. Res. Lett.*, 49(8):e2021GL097287. e2021GL097287 2021GL097287.
- Meng, Z., Yang, P., Kattawar, G. W., Bi, L., Liou, K., and Laszlo, I. (2010). Single-scattering properties of tri-axial ellipsoidal mineral dust aerosols: A database for application to radiative transfer calculations. *J. Aerosol Sci.*, 41(5):501–512.

References

- Miller, R., Cakmur, R., Perlwitz, J., Geogdzhayev, I., Ginoux, P., Koch, D., Kohfeld, K., Prigent, C., Ruedy, R., Schmidt, G., et al. (2006). Mineral dust aerosols in the nasa goddard institute for space sciences modele atmospheric general circulation model. *Journal of Geophysical Research: Atmospheres*, 111(D6).
- Miller, R. L., Knippertz, P., Pérez García-Pando, C., Perlwitz, J. P., and Tegen, I. (2014). Impact of dust radiative forcing upon climate. In *Mineral dust*, pages 327–357. Springer.
- Miller, S. D., Kuciauskas, A. P., Liu, M., Ji, Q., Reid, J. S., Breed, D. W., Walker, A. L., and Mandoos, A. A. (2008). Haboob dust storms of the southern arabian peninsula. *J. Geophys. Res. Atmos.*, 113(D1):D01202.
- Mills, M. M., Ridame, C., Davey, M., La Roche, J., and Geider, R. J. (2004). Iron and phosphorus co-limit nitrogen fixation in the eastern tropical north atlantic. *Nature*, 429(6989):292–294.
- Miri, A., Ahmadi, H., Ekhtesasi, M. R., Panjehkeh, N., and Ghanbari, A. (2009). Environmental and socio-economic impacts of dust storms in sistán region, iran. *International journal of environmental studies*, 66(3):343–355.
- Möhler, O., Field, P., Connolly, P., Benz, S., Saathoff, H., Schnaiter, M., Wagner, R., Cotton, R., Krämer, M., Mangold, A., et al. (2006). Efficiency of the deposition mode ice nucleation on mineral dust particles. *Atmospheric Chemistry and Physics*, 6(10):3007–3021.
- Monin, A. S. and Obukhov, A. M. (1954). Basis laws of turbulent mixing in the ground layer of the atmosphere. *Tr. Akad. Nauk SSSR Geophys.*, 24(151):163–187.
- Moosmüller, H., Engelbrecht, J. P., Skiba, M., Frey, G., Chakrabarty, R. K., and Arnott, W. P. (2012). Single scattering albedo of fine mineral dust aerosols controlled by iron concentration. *Journal of Geophysical Research: Atmospheres*, 117(D11).
- Moroni, B., Arnalds, O., Dagsson-Waldhauserová, P., Crocchianti, S., Vivani, R., and Cappelletti, D. (2018). Mineralogical and chemical records of icelandic dust sources upon ny-ålesund (svalbard islands). *Frontiers in Earth Science*, 6:187.

- Muhs, D. R., Budahn, J., Reheis, M., Beann, J., Skipp, G., and Fisher, E. (2007). Airborne dust transport to the eastern pacific ocean off southern california: Evidence from san clemente island. *Journal of Geophysical Research: Atmospheres*, 112(D13).
- Müller, T., Schladitz, A., Massling, A., Kaaden, N., Kandler, K., and Wiedensohler, A. (2009). Spectral absorption coefficients and imaginary parts of refractive indices of saharan dust during samum-1. *Tellus B: Chemical and Physical Meteorology*, 61(1):79–95.
- Murray, B., O’sullivan, D., Atkinson, J., and Webb, M. (2012). Ice nucleation by particles immersed in supercooled cloud droplets. *Chemical Society Reviews*, 41(19):6519–6554.
- Myhre, G., Shindell, D., and Pongratz, J. (2013). Anthropogenic and natural radiative forcing. *Climate Change 2013: The Physical Science Basis. Contribution of Working Group I to the Fifth Assessment Report of the Intergovernmental Panel on Climate Change [Stocker, T.F., D. Qin, G.-K. Plattner, M. Tignor, S.K. Allen, J. Boschung, A. Nauels, Y. Xia, V. Bex and P.M. Midgley (eds.)]*.
- Ndour, M., D’Anna, B., George, C., Ka, O., Balkanski, Y., Kleffmann, J., Stemmler, K., and Ammann, M. (2008). Photoenhanced uptake of no₂ on mineral dust: Laboratory experiments and model simulations. *Geophysical Research Letters*, 35(5).
- Nickling, W. (1983). Grain-size characteristics of sediment transported during dust storms. *J. Sediment. Res.*, 53(3):1011–1024.
- Nickling, W. and Gillies, J. (1989). Emission of fine-grained particulates from desert soils. *Paleoclimatology and Paleometeorology: modern and past patterns of global atmospheric transport*, pages 133–165.
- Nickling, W. and Gillies, J. (1993). Dust emission and transport in mali, west africa. *Sedimentology*, 40(5):859–868.
- Nickling, W. G., McTainsh, G. H., and Leys, J. F. (1999). Dust emission from the Channel Country of western Queensland, Australia. *Z. Geomorphol.*, 116:1–17.
- Okada, K., Heintzenberg, J., Kai, K., and Qin, Y. (2001). Shape of atmospheric mineral particles collected in three chinese arid-regions. *Geophysical Research Letters*, 28(16):3123–3126.

References

- Okin, G. S. (2008). A new model of wind erosion in the presence of vegetation. *Journal of Geophysical Research: Earth Surface*, 113(F2).
- Okin, G. S., Baker, A. R., Tegen, I., Mahowald, N. M., Dentener, F. J., Duce, R. A., Galloway, J. N., Hunter, K., Kanakidou, M., Kubilay, N., et al. (2011). Impacts of atmospheric nutrient deposition on marine productivity: Roles of nitrogen, phosphorus, and iron. *Global Biogeochemical Cycles*, 25(2).
- Okin, G. S., Mahowald, N., Chadwick, O. A., and Artaxo, P. (2004). Impact of desert dust on the biogeochemistry of phosphorus in terrestrial ecosystems. *Global Biogeochem. Cy.*, 18(2).
- Otto, S., Trautmann, T., and Wendisch, M. (2011). On realistic size equivalence and shape of spheroidal saharan mineral dust particles applied in solar and thermal radiative transfer calculations. *Atmospheric Chemistry and Physics*, 11(9):4469–4490.
- Owen, R. P. (1964). Saltation of uniform grains in air. *J. Fluid Mech.*, 20:225–242.
- Painter, T. H., Barrett, A. P., Landry, C. C., Neff, J. C., Cassidy, M. P., Lawrence, C. R., McBride, K. E., and Farmer, G. L. (2007). Impact of disturbed desert soils on duration of mountain snow cover. *Geophysical Research Letters*, 34(12).
- Panta, A., Kandler, K., Alastuey, A., González-Flórez, C., González-Romero, A., Klose, M., Querol, X., Reche, C., Yús-Díez, J., and Perez García-Pando, C. (2023). Insights into the single particle composition, size, mixing state and aspect ratio of freshly emitted mineral dust from field measurements in the moroccan sahara using electron microscopy. *Atmospheric Chemistry and Physics*, 23(6):3861–3885.
- Parajuli, S. P., Yang, Z.-L., and Lawrence, D. M. (2016). Diagnostic evaluation of the community earth system model in simulating mineral dust emission with insight into large-scale dust storm mobilization in the middle east and north africa (mena). *Aeolian Research*, 21:21–35.
- Park, M.-S., Park, S.-U., and Chun, Y. (2011). Improved parameterization of dust emission (pm₁₀) fluxes by the gradient method using the naiman tower data at the horqin desert in china. *Science of the total environment*, 412:265–277.

- Paytan, A., Mackey, K. R., Chen, Y., Lima, I. D., Doney, S. C., Mahowald, N., Labiosa, R., and Post, A. F. (2009). Toxicity of atmospheric aerosols on marine phytoplankton. *Proceedings of the National Academy of Sciences*, 106(12):4601–4605.
- Pease, P. P., Tchakerian, V. P., and Tindale, N. W. (1998). Aerosols over the arabian sea: geochemistry and source areas for aeolian desert dust. *Journal of Arid Environments*, 39(3):477–496.
- Pérez, C., Haustein, K., Janjic, Z., Jorba, O., Huneus, N., Baldasano, J., Black, T., Basart, S., Nickovic, S., Miller, R., et al. (2011). Atmospheric dust modeling from meso to global scales with the online nmmb/bsc-dust model—part 1: Model description, annual simulations and evaluation. *Atmospheric Chemistry and Physics*, 11(24):13001–13027.
- Pérez García-Pando, C., Miller, R. L., Perlwitz, J. P., Rodríguez, S., and Prospero, J. M. (2016). Predicting the mineral composition of dust aerosols: Insights from elemental composition measured at the izaña observatory. *Geophysical research letters*, 43(19):10–520.
- Perlwitz, J. P., Pérez García-Pando, C., and Miller, R. L. (2015a). Predicting the mineral composition of dust aerosols - Part 1: Representing key processes. *Atmos. Chem. Phys.*, 15(20):11593–11627.
- Perlwitz, J. P., Pérez García-Pando, C., and Miller, R. L. (2015b). Predicting the mineral composition of dust aerosols - Part 2: Model evaluation and identification of key processes with observations. *Atmos. Chem. Phys.*, 15(20):11629–11652.
- Petroff, A. and Zhang, L. (2010). Development and validation of a size-resolved particle dry deposition scheme for application in aerosol transport models. *Geoscientific Model Development*, 3(2):753–769.
- Pierre, C., Bergametti, G., Marticorena, B., Mougin, E., Bouet, C., and Schmechtig, C. (2012). Impact of vegetation and soil moisture seasonal dynamics on dust emissions over the Sahel. *J. Geophys. Res. Atmos.*, 117(6):1–21.
- Powell, J. H., Abed, A. M., and Le Nindre, Y.-M. (2014). Cambrian stratigraphy of jordan. *GeoArabia*, 19(3):81–134.

References

- Prospero, J. M., Bonatti, E., Schubert, C., and Carlson, T. N. (1970). Dust in the caribbean atmosphere traced to an african dust storm. *Earth and Planetary Science Letters*, 9(3):287–293.
- Prospero, J. M., Ginoux, P., Torres, O., Nicholson, S. E., and Gill, T. E. (2002). Environmental characterization of global sources of atmospheric soil dust identified with the nimbus 7 total ozone mapping spectrometer (toms) absorbing aerosol product. *Reviews of geophysics*, 40(1):2–1.
- Pu, B. and Ginoux, P. (2017). Projection of american dustiness in the late 21st century due to climate change. *Scientific Reports*, 7(1):5553.
- Pu, B. and Ginoux, P. (2018). How reliable are cmip5 models in simulating dust optical depth? *Atmospheric Chemistry and Physics*, 18(16):12491–12510.
- Pye, K. (1987). *Aeolian dust and dust deposits*. Academic Press.
- Querol, X., Tobías, A., Pérez, N., Karanasiou, A., Amato, F., Stafoggia, M., García-Pando, C. P., Ginoux, P., Forastiere, F., Gumy, S., et al. (2019). Monitoring the impact of desert dust outbreaks for air quality for health studies. *Environment international*, 130:104867.
- Rajot, J., Alfaro, S., Gomes, L., and Gaudichet, A. (2003). Soil crusting on sandy soils and its influence on wind erosion. *Catena*, 53(1):1–16.
- Rajot, J. L., Formenti, P., Alfaro, S., Desboeufs, K., Chevaillier, S., Chatenet, B., Gaudichet, A., Journet, E., Marticorena, B., Triquet, S., et al. (2008). Amma dust experiment: An overview of measurements performed during the dry season special observation period (sop0) at the banizoumbou (niger) supersite. *Journal of Geophysical Research: Atmospheres*, 113(D23).
- Rastogi, N. and Sarin, M. (2006). Chemistry of aerosols over a semi-arid region: Evidence for acid neutralization by mineral dust. *Geophysical Research Letters*, 33(23).
- Raupach, M., Gillette, D., and Leys, J. (1993). The effect of roughness elements on wind erosion threshold. *Journal of Geophysical Research: Atmospheres*, 98(D2):3023–3029.

- Rausch, J., Jaramillo-Vogel, D., Perseguers, S., Schnidrig, N., Grobéty, B., and Yajan, P. (2022). Automated identification and quantification of tire wear particles (twp) in airborne dust: Sem/edx single particle analysis coupled to a machine learning classifier. *Sci. Total Environ.*, 803:149832.
- Ravi, S., Zobeck, T. M., Over, T. M., Okin, G. S., and P., D. (2006). On the effect of moisture bonding forces in air-dry soils on threshold friction velocity of wind erosion. *Sedimentology*, 53(3):597–609.
- Reid, J. S., Jonsson, H. H., Maring, H. B., Smirnov, A., Savoie, D. L., Cliff, S. S., Reid, E. A., Livingston, J. M., Meier, M. M., Dubovik, O., et al. (2003). Comparison of size and morphological measurements of coarse mode dust particles from africa. *Journal of Geophysical Research: Atmospheres*, 108(D19).
- Reid, J. S., Reid, E. A., Walker, A., Piketh, S., Cliff, S., Al Mandoos, A., Tsay, S.-C., and Eck, T. F. (2008). Dynamics of southwest asian dust particle size characteristics with implications for global dust research. *J. Geophys. Res. Atmos.*, 113(D14):D14212.
- Renard, J.-B., Dulac, F., Durand, P., Bourgeois, Q., Denjean, C., Vignelles, D., Couté, B., Jeannot, M., Verdier, N., and Mallet, M. (2018). In situ measurements of desert dust particles above the western mediterranean sea with the balloon-borne light optical aerosol counter/sizer (loac) during the charmex campaign of summer 2013. *Atmospheric Chemistry and Physics*, 18(5):3677–3699.
- Rice, M., Mullins, C., and McEwan, I. (1997). An analysis of soil crust strength in relation to potential abrasion by saltating particles. *Earth Surface Processes and Landforms: The Journal of the British Geomorphological Group*, 22(9):869–883.
- Rice, M., Willetts, B., and McEwan, I. (1996a). Wind erosion of crusted soil sediments. *Earth Surface Processes and Landforms*, 21(3):279–293.
- Rice, M. A., Willetts, B. B., and McEwan, I. (1996b). Observations of collisions of saltating grains with a granular bed from high-speed cine-film. *Sedimentology*, 43(1):21–31.
- Rocha-Lima, A., Martins, J. V., Remer, L. A., Todd, M., Marsham, J. H., Engelstaedter, S., Ryder, C. L., Cavazos-Guerra, C., Artaxo, P., Colarco, P., et al.

- (2018). A detailed characterization of the saharan dust collected during the fennec campaign in 2011: in situ ground-based and laboratory measurements. *Atmospheric Chemistry and Physics*, 18(2):1023–1043.
- Römken, M. J., Helming, K., and Prasad, S. (2002). Soil erosion under different rainfall intensities, surface roughness, and soil water regimes. *Catena*, 46(2-3):103–123.
- Roney, J. A. and White, B. R. (2004). Definition and measurement of dust aeolian thresholds. *Journal of Geophysical Research: Earth Surface*, 109(F1).
- Rosenfeld, D., Rudich, Y., and Lahav, R. (2001). Desert dust suppressing precipitation: A possible desertification feedback loop. *Proceedings of the National Academy of Sciences*, 98(11):5975–5980.
- Ryder, C. L., Highwood, E. J., Walser, A., Seibert, P., Philipp, A., and Weinzierl, B. (2019). Coarse and giant particles are ubiquitous in saharan dust export regions and are radiatively significant over the sahara. *Atmos. Chem. Phys.*, 19(24):15353–15376.
- Ryder, C. L., Marenco, F., Brooke, J. K., Estelles, V., Cotton, R., Formenti, P., McQuaid, J. B., Price, H. C., Liu, D., Ausset, P., et al. (2018). Coarse-mode mineral dust size distributions, composition and optical properties from aer-d aircraft measurements over the tropical eastern atlantic. *Atmospheric Chemistry and Physics*, 18(23):17225–17257.
- Saidan, M., Albaali, A. G., Alasis, E., and Kaldellis, J. K. (2016). Experimental study on the effect of dust deposition on solar photovoltaic panels in desert environment. *Renewable Energy*, 92:499–505.
- Saito, M. and Yang, P. (2021). Advanced bulk optical models linking the backscattering and microphysical properties of mineral dust aerosol. *Geophysical Research Letters*, 48(17):e2021GL095121.
- Sanchez-Marroquin, A., Arnalds, O., Baustian-Dorsi, K., Browse, J., Dagsson-Waldhauserova, P., Harrison, A., Maters, E., Pringle, K., Vergara-Temprado, J., Burke, I., et al. (2020). Iceland is an episodic source of atmospheric ice-nucleating particles relevant for mixed-phase clouds. *Science Advances*, 6(26):eaba8137.

- Scanza, R., Mahowald, N., Ghan, S., Zender, C., Kok, J., Liu, X., Zhang, Y., and Albani, S. (2015). Modeling dust as component minerals in the community atmosphere model: development of framework and impact on radiative forcing. *Atmospheric Chemistry and Physics*, 15(1):537–561.
- Scheuvs, D., Schütz, L., Kandler, K., Ebert, M., and Weinbruch, S. (2013). Bulk composition of northern african dust and its source sediments—a compilation. *Earth-Science Reviews*, 116:170–194.
- Schroth, A. W., Crusius, J., Sholkovitz, E. R., and Bostick, B. C. (2009). Iron solubility driven by speciation in dust sources to the ocean. *Nature Geoscience*, 2(5):337–340.
- Schuepp, P., Leclerc, M., MacPherson, J., and Desjardins, R. (1990). Footprint prediction of scalar fluxes from analytical solutions of the diffusion equation. *Boundary-Layer Meteorology*, 50(1):355–373.
- Schüler, D., Wilbert, S., Geuder, N., Affolter, R., Wolfertstetter, F., Prahl, C., Röger, M., Schroedter-Homscheidt, M., Abdellatif, G., Guizani, A. A., et al. (2016). The enermena meteorological network—solar radiation measurements in the mena region. In *AIP conference proceedings*, volume 1734, page 150008. AIP Publishing LLC.
- Schultz, J. A. and Meisner, B. N. (2009). The 24 february 2007 north texas wind and dust storm: An impact weather event. *Natl. Wea. Dig*, 33:165–184.
- Schulz, O. and Fink, A. H. (2016). Meteorologic measurements in 15 minute resolution at station JHB, 2001-2011. PANGAEA. In: Schulz, O; Fink, AH (2016): Multi-year weather data in the remote semi-arid to arid mountain region of the Saharan flank of the Atlas Mountains. PANGAEA, <https://doi.org/10.1594/PANGAEA.862541>.
- Schütz, L. and Seibert, M. (1987). Mineral aerosols and source identification. *Journal of aerosol science*, 18(1):1–10.
- Sehmel, G. A. (1980). Particle and gas dry deposition: a review. *Atmospheric Environment (1967)*, 14(9):983–1011.

- Seinfeld, J. H. and Pandis, S. N. (2006). *Atmospheric chemistry and physics: from air pollution to climate change*. John Wiley & Sons.
- Shao, Y. (2001). A model for mineral dust emission. *J. Geophys. Res. Atmos.*, 106(D17):20239–20254.
- Shao, Y. (2004). Simplification of a dust emission scheme and comparison with data. *Journal of Geophysical Research: Atmospheres*, 109(D10).
- Shao, Y. (2008). *Physics and Modelling of Wind Erosion*. Springer–Verlag, Berlin, 2 edition.
- Shao, Y., Ishizuka, M., Mikami, M., and Leys, J. F. (2011a). Parameterization of size-resolved dust emission and validation with measurements. *J. Geophys. Res. Atmos.*, 116(D8).
- Shao, Y. and Klose, M. (2016). A note on the stochastic nature of particle cohesive force and implications to threshold friction velocity for aerodynamic dust entrainment. *Aeolian Research*, 22:123–125.
- Shao, Y. and Leslie, L. M. (1997). Wind erosion prediction over the Australian continent. *Journal of Geophysical Research: Atmospheres*, 102(D25):30091–30105.
- Shao, Y. and Lu, H. (2000). A simple expression for wind erosion threshold friction velocity. *Journal of Geophysical Research: Atmospheres*, 105(D17):22437–22443.
- Shao, Y., Raupach, M., and Findlater, P. (1993). Effect of saltation bombardment on the entrainment of dust by wind. *Journal of Geophysical Research: Atmospheres*, 98(D7):12719–12726.
- Shao, Y., Raupach, M. R., and Leys, J. F. (1996). A model for predicting aeolian sand drift and dust entrainment on scales from paddock to region. *Soil Research*, 34(3):309–342.
- Shao, Y., Wyrwoll, K.-H., Chappell, A., Huang, J., Lin, Z., McTainsh, G. H., Mikami, M., Tanaka, T. Y., Wang, X., and Yoon, S. (2011b). Dust cycle: An emerging core theme in Earth system science. *Aeolian Res.*, 2:181–204.

- Shao, Y., Zhang, J., Ishizuka, M., Mikami, M., Leys, J., and Huang, N. (2020). Dependency of particle size distribution at dust emission on friction velocity and atmospheric boundary-layer stability. *Atmos. Chem. Phys.*, 20:12939–12953.
- Shen, Z., Caquineau, S., Cao, J., Zhang, X., Han, Y., Gaudichet, A., and Gomes, L. (2009). Mineralogical characteristics of soil dust from source regions in northern china, *particuology*, 7, 507–512.
- Sherman, D. J. (1992). An equilibrium relationship for shear velocity and apparent roughness length in aeolian saltation. *Geomorphology*, 5(3-5):419–431.
- Shi, T., He, C., Zhang, D., Zhang, X., Niu, X., Xing, Y., Chen, Y., Cui, J., Pu, W., and Wang, X. (2022). Opposite effects of mineral dust nonsphericity and size on dust-induced snow albedo reduction. *Geophysical Research Letters*, 49(12):e2022GL099031.
- Shi, Z., Shao, L., Jones, T. P., and Lu, S. (2005). Microscopy and mineralogy of airborne particles collected during severe dust storm episodes in beijing, china. *Journal of Geophysical Research: Atmospheres*, 110(D1).
- Skiles, S. M., Flanner, M., Cook, J. M., Dumont, M., and Painter, T. H. (2018). Radiative forcing by light-absorbing particles in snow. *Nature Climate Change*, 8(11):964–971.
- Skiles, S. M. and Painter, T. H. (2018). Assessment of radiative forcing by light-absorbing particles in snow from in situ observations with radiative transfer modeling. *Journal of Hydrometeorology*, 19(8):1397–1409.
- Skiles, S. M. and Painter, T. H. (2019). Toward understanding direct absorption and grain size feedbacks by dust radiative forcing in snow with coupled snow physical and radiative transfer modeling. *Water Resources Research*, 55(8):7362–7378.
- Slinn, W. (1982). Predictions for particle deposition to vegetative canopies. *Atmospheric Environment (1967)*, 16(7):1785–1794.
- Sokolik, I. N. and Toon, O. B. (1996). Direct radiative forcing by anthropogenic airborne mineral aerosols. *Nature*, 381(6584):681–683.

References

- Sokolik, I. N. and Toon, O. B. (1999). Incorporation of mineralogical composition into models of the radiative properties of mineral aerosol from uv to ir wavelengths. *Journal of Geophysical Research: Atmospheres*, 104(D8):9423–9444.
- Sokolik, I. N., Toon, O. B., and Bergstrom, R. W. (1998). Modeling the radiative characteristics of airborne mineral aerosols at infrared wavelengths. *Journal of Geophysical Research: Atmospheres*, 103(D8):8813–8826.
- Sørensen, M. (1985). Estimation of some aeolian saltation transport parameters from transport rate profiles. In *Proceedings of International Workshop on the Physics of Blown Sand*, volume 1, pages 141–190. University of Aarhus: Aarhus, Denmark.
- Sow, M., Alfaro, S. C., Rajot, J. L., and Marticorena, B. (2009). Size resolved dust emission fluxes measured in Niger during 3 dust storms of the AMMA experiment. *Atmos. Chem. Phys.*, 9(12):3881–3891.
- Stanelle, T., Bey, I., Raddatz, T., Reick, C., and Tegen, I. (2014). Anthropogenically induced changes in twentieth century mineral dust burden and the associated impact on radiative forcing. *Journal of Geophysical Research: Atmospheres*, 119(23):13–526.
- Stefanski, R. and Sivakumar, M. (2009). Impacts of sand and dust storms on agriculture and potential agricultural applications of a sdsws. In *IOP Conference Series: Earth and Environmental Science*, volume 7, page 012016. IOP Publishing.
- Stull, R. B. (1988). *An Introduction to Boundary Layer Meteorology*. Kluwer Academic Publishers, Norwell.
- Swap, R., Garstang, M., Greco, S., Talbot, R., and Källberg, P. (1992). Saharan dust in the amazon basin. *Tellus B*, 44(2):133–149.
- Takeishi, A. and Storelvmo, T. (2018). A study of enhanced heterogeneous ice nucleation in simulated deep convective clouds observed during dc3. *Journal of Geophysical Research: Atmospheres*, 123(23):13–396.
- Tang, M., Cziczo, D. J., and Grassian, V. H. (2016). Interactions of water with mineral dust aerosol: water adsorption, hygroscopicity, cloud condensation, and ice nucleation. *Chemical reviews*, 116(7):4205–4259.

- Tegen, I., Harrison, S. P., Kohfeld, K., Prentice, I. C., Coe, M., and Heimann, M. (2002). Impact of vegetation and preferential source areas on global dust aerosol: Results from a model study. *J. Geophys. Res. Atmos.*, 107(21).
- Tegen, I., Werner, M., Harrison, S., and Kohfeld, K. E. (2004). Relative importance of climate and land use in determining present and future global soil dust emission. *Geophysical research letters*, 31(5).
- Tetens, O. (1930). Uber einige meteorologische Begriffe. *J. Geophys-Z. Geophys.*, 6:297–309.
- Textor, C., Schulz, M., Guibert, S., Kinne, S., Balkanski, Y., Bauer, S., Berntsen, T., Berglen, T., Boucher, O., Chin, M., et al. (2006). Analysis and quantification of the diversities of aerosol life cycles within aerocom. *Atmospheric Chemistry and Physics*, 6(7):1777–1813.
- Textor, C., Schulz, M., Guibert, S., Kinne, S., Balkanski, Y., Bauer, S., Berntsen, T., Berglen, T., Boucher, O., Chin, M., et al. (2007). The effect of harmonized emissions on aerosol properties in global models—an aerocom experiment. *Atmospheric Chemistry and Physics*, 7(17):4489–4501.
- Thomson, M. C., Molesworth, A. M., Djingarey, M. H., Yameogo, K., Belanger, F., and Cuevas, L. E. (2006). Potential of environmental models to predict meningitis epidemics in africa. *Tropical Medicine & International Health*, 11(6):781–788.
- Tian, Z., Kaminski, U., Sauer, J., Maschowski, C., Stille, P., Cen, K., Gieré, R., Sommer, F., Dietze, V., and Baum, A. (2017). Coarse-particle passive-sampler measurements and single-particle analysis by transmitted light microscopy at highly frequented motorways. *Aerosol Air Qual. Res.*, 17(8):1939–1953.
- Tobo, Y., Zhang, D., Matsuki, A., and Iwasaka, Y. (2010). Asian dust particles converted into aqueous droplets under remote marine atmospheric conditions. *Proceedings of the National Academy of Sciences*, 107(42):17905–17910.
- Ulanowski, Z., Bailey, J., Lucas, P., Hough, J., and Hirst, E. (2007). Alignment of atmospheric mineral dust due to electric field. *Atmospheric Chemistry and Physics*, 7(24):6161–6173.

References

- van der Does, M., Brummer, G.-J. A., van Crimpen, F. C., Korte, L. F., Mahowald, N. M., Merkel, U., Yu, H., Zuidema, P., and Stuut, J.-B. W. (2020). Tropical rains controlling deposition of saharan dust across the north atlantic ocean. *Geophysical Research Letters*, 47(5):e2019GL086867.
- Van Der Does, M., Korte, L. F., Munday, C. I., Brummer, G.-J. A., and Stuut, J.-B. W. (2016). Particle size traces modern saharan dust transport and deposition across the equatorial north atlantic. *Atmospheric Chemistry and Physics*, 16(21):13697–13710.
- van der Does, M., Pourmand, A., Sharifi, A., and Stuut, J.-B. W. (2018). North african mineral dust across the tropical atlantic ocean: Insights from dust particle size, radiogenic sr-nd-hf isotopes and rare earth elements (ree). *Aeolian research*, 33:106–116.
- VDI-2119 (2013). Ambient air measurements—sampling of atmospheric particles >2.5 m on an acceptor surface using the sigma-2 passive sampler, vdi guideline. *Beuth Verlag.*, pages 1–62.
- Vergara-Temprado, J., Murray, B. J., Wilson, T. W., O’Sullivan, D., Pringle, K. J., Ardon-Dryer, K., Bertram, A. K., Burrows, S. M., Ceburnis, D., DeMott, P. J., et al. (2017). Contribution of feldspar and marine organic aerosols to global ice nucleating particle concentrations. *Atmospheric Chemistry and Physics*, 17(5):3637–3658.
- Vickery, K. J., Eckardt, F. D., and Bryant, R. G. (2013). A sub-basin scale dust plume source frequency inventory for southern africa, 2005–2008. *Geophysical Research Letters*, 40(19):5274–5279.
- Volz, F. E. (1972). Infrared refractive index of atmospheric aerosol substances. *Applied Optics*, 11(4):755–759.
- Walton, W. (1954). Theory of size classification of airborne dust clouds by elutriation. *British Journal of Applied Physics*, 5(S3):S29.
- Wang, G., Zheng, X., and Tao, J. (2017a). Very large scale motions and pm10 concentration in a high-re boundary layer. *Physics of Fluids*, 29(6):061701.
- Wang, R., Li, Q., Wang, R., Chang, C., Guo, Z., Li, J., and Zhou, N. (2021a). Influence of wind velocity and soil size distribution on emitted dust size

- distribution: A wind tunnel study. *Journal of Geophysical Research: Atmospheres*, 126(7):e2020JD033768.
- Wang, X., Cai, D., Li, D., Lou, J., Zheng, Y., Hu, S., and Liu, F. (2021b). Dust deposition and its significance to soil nutrients in the otindag desert, china. *Journal of Arid Environments*, 194:104612.
- Wang, Z., Pan, X., Uno, I., Li, J., Wang, Z., Chen, X., Fu, P., Yang, T., Kobayashi, H., Shimizu, A., et al. (2017b). Significant impacts of heterogeneous reactions on the chemical composition and mixing state of dust particles: A case study during dust events over northern china. *Atmospheric environment*, 159:83–91.
- Washington, R., Parker, D., Marsham, J., McQuaid, J., Brindley, H., Todd, M., Highwood, E., Flamant, C., Chaboureau, J.-P., Kocha, C., et al. (2012). Fennec-the saharan climate system: an overview. In *EGU General Assembly Conference Abstracts*, page 11975.
- Waza, A., Schneiders, K., May, J., Rodríguez, S., Epple, B., and Kandler, K. (2019). Field comparison of dry deposition samplers for collection of atmospheric mineral dust: results from single-particle characterization. *Atmos. Meas. Tech.*, 12(12):6647–6665.
- Webb, N. P., LeGrand, S. L., Cooper, B. F., Courtright, E. M., Edwards, B. L., Felt, C., Van Zee, J. W., and Ziegler, N. P. (2021). Size distribution of mineral dust emissions from sparsely vegetated and supply-limited dryland soils. *Journal of Geophysical Research: Atmospheres*, 126(22):e2021JD035478.
- Webb, N. P., Okin, G. S., and Brown, S. (2014). The effect of roughness elements on wind erosion: The importance of surface shear stress distribution. *Journal of Geophysical Research: Atmospheres*, 119(10):6066–6084.
- Wei, T., Brahney, J., Dong, Z., Kang, S., Zong, C., Guo, J., Yang, L., and Qin, X. (2021). Hf–nd–sr isotopic composition of the tibetan plateau dust as a fingerprint for regional to hemispherical transport. *Environmental Science & Technology*, 55(14):10121–10132.
- Weinzierl, B., Ansmann, A., Prospero, J. M., Althausen, D., Benker, N., Chouza, F., Dollner, M., Farrell, D., Fomba, W., Freudenthaler, V., et al. (2017). The

References

- saharan aerosol long-range transport and aerosol–cloud-interaction experiment: Overview and selected highlights. *Bulletin of the American Meteorological Society*, 98(7):1427–1451.
- Weinzierl, B., Sauer, D., Esselborn, M., Petzold, A., Veira, A., Rose, M., Mund, S., Wirth, M., Ansmann, A., Tesche, M., et al. (2011). Microphysical and optical properties of dust and tropical biomass burning aerosol layers in the cape verde region—an overview of the airborne in situ and lidar measurements during samum-2. *Tellus B: Chemical and Physical Meteorology*, 63(4):589–618.
- Whitby, K. and Cantrell, B. (1976). Fine particles. In *International conference of environmental sensing and assessment, Las Vegas, NV, Institute of Electrical and Electronic Engineers*.
- Wood, W. W., Clark, D., Imes, J. L., and Councell, T. B. (2010). Eolian transport of geogenic hexavalent chromium to ground water. *Groundwater*, 48(1):19–29.
- Woodward, S. (2001). Modeling the atmospheric life cycle and radiative impact of mineral dust in the hadley centre climate model. *Journal of Geophysical Research: Atmospheres*, 106(D16):18155–18166.
- Wu, C., Lin, Z., and Liu, X. (2020). The global dust cycle and uncertainty in cmip5 (coupled model intercomparison project phase 5) models. *Atmospheric Chemistry and Physics*, 20(17):10401–10425.
- Xi, X. and Sokolik, I. N. (2016). Quantifying the anthropogenic dust emission from agricultural land use and desiccation of the aral sea in central asia. *Journal of Geophysical Research: Atmospheres*, 121(20):12–270.
- Yakobi-Hancock, J., Ladino, L., and Abbatt, J. (2013). Feldspar minerals as efficient deposition ice nuclei. *Atmospheric Chemistry and Physics*, 13(22):11175–11185.
- Yu, H., Chin, M., West, J. J., Atherton, C. S., Bellouin, N., Bergmann, D., Bey, I., Bian, H., Diehl, T., Forberth, G., et al. (2013). A multimodel assessment of the influence of regional anthropogenic emission reductions on aerosol direct radiative forcing and the role of intercontinental transport. *Journal of Geophysical Research: Atmospheres*, 118(2):700–720.

- Yu, H., Tan, Q., Chin, M., Remer, L. A., Kahn, R. A., Bian, H., Kim, D., Zhang, Z., Yuan, T., Omar, A. H., et al. (2019). Estimates of african dust deposition along the trans-atlantic transit using the decadelong record of aerosol measurements from caliop, modis, misr, and iasi. *Journal of Geophysical Research: Atmospheres*, 124(14):7975–7996.
- Yus-Díez, J., Pandolfi, M., González-Flórez, C., Escribano, J., González-Romero, J., Ivančič, M., Rigler, M., Klose, M., Kandler, K., Panta, A., Querol, X., Reche, C., Perez García-Pando, C., and Alastuey, A. (in prep.). Quantifying variations in multi-wavelength optical properties of freshly-emitted saharan dust from the lower drâa valley, moroccan sahara.
- Yusuf, N. (2007). Dust activity over the jordanian red sea coast. *Abhath Al-Yarmouk: Basic Sci. Eng*, 16:211–227.
- Zhang, J., Li, G., Shi, L., Huang, N., and Shao, Y. (2022). Impact of turbulence on aeolian particle entrainment: results from wind-tunnel experiments. *Atmospheric Chemistry and Physics*, 22(14):9525–9535.
- Zhang, J. and Shao, Y. (2014). A new parameterization of particle dry deposition over rough surfaces. *Atmospheric Chemistry and Physics*, 14(22):12429–12440.
- Zhang, L., Gong, S., Padro, J., and Barrie, L. (2001). A size-segregated particle dry deposition scheme for an atmospheric aerosol module. *Atmospheric environment*, 35(3):549–560.
- Zhang, X., Wu, G., Zhang, C., Xu, T., and Zhou, Q. (2015). What is the real role of iron oxides in the optical properties of dust aerosols? *Atmospheric Chemistry and Physics*, 15(21):12159–12177.
- Zhang, X., Zhao, L., Tong, D. Q., Wu, G., Dan, M., and Teng, B. (2016). A systematic review of global desert dust and associated human health effects. *Atmosphere*, 7(12):158.
- Zhang, X.-X., Sharratt, B., Lei, J.-Q., Wu, C.-L., Zhang, J., Zhao, C., Wang, Z.-F., Wu, S.-X., Li, S.-Y., Liu, L.-Y., et al. (2019). Parameterization schemes on dust deposition in northwest china: Model validation and implications for the global dust cycle. *Atmospheric environment*, 209:1–13.

References

- Zhang, Y. (2018). Black carbon and mineral dust in snow cover on the third pole.
- Zhao, C., Chen, S., Leung, L. R., Qian, Y., Kok, J., Zaveri, R. A., and Huang, J. (2013). Uncertainty in modeling dust mass balance and radiative forcing from size parameterization. *Atmospheric Chemistry and Physics*, 13(21):10733–10753.
- Zimbone, S., Vickers, A., Morgan, R., and Vella, P. (1996). Field investigations of different techniques for measuring surface soil shear strength. *Soil Technology*, 9(1-2):101–111.
- Zingg, A. (1952). Wind tunnel studies of the movement of sedimentary material. In *Proc. 5th Hydraulics Conf., IAHR*, pages 111–135.
- Zobeck, T. M. and Van Pelt, R. S. (2006). Wind-induced dust generation and transport mechanics on a bare agricultural field. *Journal of hazardous materials*, 132(1):26–38.



**Barcelona
Supercomputing
Center**
Centro Nacional de Supercomputación



**UNIVERSITAT POLITÈCNICA
DE CATALUNYA
BARCELONATECH**

